SKIN FRICTION AND FLUID DYNAMICS OF A PLANAR IMPINGING GAS JET

Skin Friction and Fluid Dynamics of a Planar Impinging Gas Jet

By

ADAM RITCEY, B.ENG.

A Thesis

Submitted to the School of Graduate Studies

in Partial Fulfillment of the Requirements

for the Degree Doctor of Philosophy

McMaster University

DOCTOR OF PHILOSOPHY (2018) McMaster University

(Mechanical Engineering) Hamilton, Ontario

TITLE:	Skin Friction and Fluid Dynamics of a Planar Impinging Gas Jet
SUPERVISOR(S):	Dr. Samir Ziada, Dr. Joseph McDermid
NUMBER OF PAGES:	XXVI, 230

Ask yourself what is really important.

Have the wisdom and the courage to build your life around your answer.

-Lee Jampolsky

In memory of Samir Ziada (1949-2018)

Abstract

Impinging gas jets have many engineering applications, including propulsion, cooling, drying, and coating control processes. In continuous hot-dip galvanizing, a molten zinc-based coating is applied to a steel substrate for corrosion protection. Planar impinging gas jets (industrially called air-knives) are employed to wipe the protective coating from the steel sheet to control the final coating weight. The maximum skin friction and pressure gradient developed by the impinging gas jet on the steel sheet heavily influences the final coating weight. In the thesis, the maximum skin friction developed on an rigid impingement plate positioned downstream of a planar impinging gas jet (scaled-up model air-knife) is measured using oil film interferometry (OFI). A maximum skin friction map based on the jet operating conditions is established, which can be used in conjunction with industrial coating weight models for film thickness prediction, and can be further employed in the assessment and verification of computational fluid dynamic (CFD) models.

As impinging gas jets reach higher flow velocities, inherent instabilities in the jet can amplify due to feedback loops created between the jet exit and the impingement plate. The flow field characteristics under resonance conditions are known to exhibit large amplitude jet column oscillations, and strong coherent fluid structures propagating down the impinging shear layers. This work examined the global effect

of planar impinging gas jet oscillations on the maximum mean skin friction developed in the stagnation region using external jet forcing. Reductions in maximum mean impingement plate skin friction were confirmed and found to be caused by increased levels of fluid entrainment under jet forcing conditions.

The fluctuating velocity fields under external jet forcing was also examined. The velocity fluctuations due to both the coherent motion of the jet column, and the turbulence were obtained and analyzed using fluid dynamic tools such as particle image velocimetry (PIV) and proper orthogonal decomposition (POD). The fluctuating velocity of the planar impinging gas jet displayed increased levels of fluctuation intensity and unique flow field characteristics under external forcing, as well as, exhibited similar features to that of a high speed impinging planar gas jet under fluid resonance conditions. Overall, it is determined that enhanced planar impinging gas jet oscillations (or equivalent air-knife oscillations) is associated with adverse fluid effects, which degrade the wiping performance of the jet.

Contents

List of Figures

Chapter 1

Introduction

1.1 Research Motivation

Continuous hot-dip galvanizing is a process used to apply a sacrificial metallic coating - usually zinc-based - to steel sheets in order to protect the steel from corrosion. A steel strip moving vertically ($V_s \approx 1-3\ m/s$) from a molten coating bath ($\approx 450°\ C$), and through a set of wiping air-knives is depicted in Figure 1.1. Air-knives utilize a high-speed gas (typically air, $U_{jet} \approx 100\ m/s$) exiting a high aspect ratio, thin planar nozzle ($W \approx 1\ mm$) impinging orthogonally to the steel surface, which forms a planar impinging gas jet used to wipe excess molten zinc-based coating from the steel sheet. The air-knives allow manufacturers to control the final coating thicknesses on the steel sheet. Target coating thicknesses are derived from corrosion data for various applications. For automotive, coating thickness specifications are quite thin ($7-10\ \mu$m) because of the expectation of 10 years of service in combination with paint. For culvert steel, the coating thicknesses are increased (up to $30\ \mu$m) based on 30 years of service without paint. Due to the coating thickness variability along the steel substrate, cost enters into the equation in the practice of overcoating. Overcoating ensures the final coating thicknesses do not drop below the minimum standards (customers can reject the product if minimum standards are not met). Hence, there is a strong incentive to control the accuracy and precision of coating weights along the steel sheet in continuous hot-dip galvanizing.

The physics of wiping molten coatings is complex due to the coupled nature of heat transfer, solidification, momentum transfer, film instability, and splashing. In practical engineering models for coating control, the applied wall shear stress, and pressure gradient imposed by the air-knives are the dominant process parameters that influence the wiping process. Specifically, the maximum wall shear stress, and maximum pressure gradients along the wiping surface are used as inputs in existing coating weight models, which can then be used to predict the final coating thicknesses [1, 2].

Computational fluid dynamics (CFD) also has inaccuracies associated with wall shear stress determination due to the difficulty in capturing the correct flow physics near the wall. This is due to the limitations of the small scale resolution near walls, the ad-hoc nature of wall functions, as well as, the Boussinesq approximation built into standard turbulence models applied to flows exhibiting large strain rates. Additionally, experimental skin friction data is scarce in the literature for planar impinging jets, and the skin friction data is prone to large measurement error depending on the wall shear stress measurement technique employed.

The research presented in this thesis characterizes the experimental maximum wall shear stress measured along the impingement plate of an air-knife model, using a more robust wall shear stress measurement technique for gas flows, called oil film

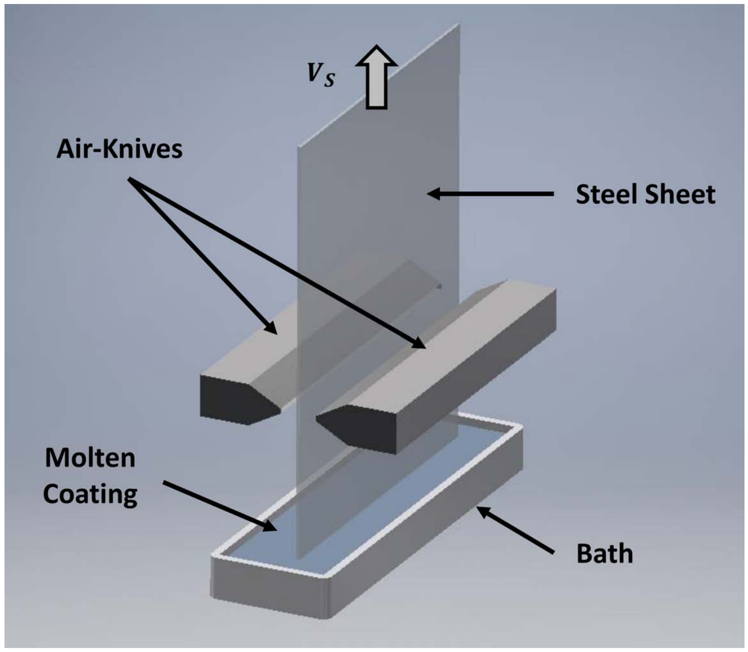

Figure 1.1: A basic schematic of the gas-jet wiping process in continuous hot-dip galvanizing. A steel sheet travels vertically from a bath containing molten coating material at velocity V_s, and then through a set of air-knives (impinging planar gas jets), which are used to wipe, and control the final coating thickness on the steel substrate.

interferometry (OFI). The maximum wall shear stress is evaluated using different air-knife velocities and standoff distances to construct a parametric maximum skin friction map. The goal and motivation of this research is to provide experimental skin friction (non-dimensional wall shear stress) inputs for coating weight models utilized in continuous hot-dip galvanizing, and to help assess current CFD models developed by Tamadonfar [3] and Yahyaee et al. [4]. Additionally, a first look at the effects of enhanced jet oscillations on the wiping ability of air-knives is considered due to the self-excited resonance conditions that have been observed in industrial hot-dip galvanizing processes. Conventional fluid dynamic tools, such as particle image velocimetry, are then used to analyze the flow field and velocity statistics under forcing conditions. The overall contributions of this thesis is intended to improve coating weight model prediction accuracy with maximum skin friction data using OFI, facilitate in the configuration and operation of air-knives in order to achieve better wiping potential, and provide the reader with a deeper understanding of the underlying impinging jet flow physics.

1.2 Scope of the Work

The experimental research in this thesis is broken down into three peer-reviewed journal papers, which comprise Chapters 3 through 5. In the first paper, **Chapter 3: The Maximum Skin Friction and Flow Field of a Planar Impinging Gas Jet**, the impingement plate skin friction and flow field produced by a planar impinging gas jet is experimentally measured under different jet standoff distances, and jet Reynolds numbers using oil film interferometry (OFI) and particle image velocimetry (PIV). This chapter constructed a parametric maximum skin friction map, which can be used as inputs to coating weight models in industrial applications. This research also compared and explained the discrepancies that exist between the current OFI data, and the skin friction data reported in the literature. In the second paper, **Chapter 4: Effect of Jet Oscillation on the Maximum Impingement Plate Skin Friction**, the effect of jet oscillations on the impingement plate fluid loading is investigated. Reductions in maximum mean skin friction and pressure gradients at the impingement plate were found when the jet is perturbed using anti-symmetric and symmetric forcing at the jet nozzle exit. This experimental work provided an initial assessment of the wiping ability of an oscillating air-knife, where impinging gas jets are known to become self-excited, and exhibit large amplitude oscillations under industrially relevant, higher flow velocity conditions. The results confirmed that the maximum skin friction reductions occur due to entrainment of the surrounding acquiescent fluid, which is influenced by gas jet column deflection, and amplification of coherent structures in the impinging shear layers. In the third paper, **Chapter 5: The Fluctuating Velocity Field of a Forced Planar Impinging Gas Jet**, the velocity statistics and fluctuating kinetic energy of the planar impinging gas jet is analyzed under forced and unforced conditions using PIV. The fluctuating velocity fields obtained by the current model air-knife was found to display similar qualitative features to that of a self-excited high-speed impinging gas jet. The results reinforce the ability of the scaled model air-knife to capture similar jet column dynamics, and flow features to that of a high-speed impinging jet under resonance conditions. Additionally, a low order reconstruction of the fluctuating velocity fields were constructed using Proper Orthogonal Decomposition (POD) to approximate the coherent velocities and turbulence fields. As a note to the reader: these three papers included in this thesis contain some overlap in the literature review, skin friction measurement technique, and experimental setup, which may be skipped without loss of continuity.

1.3 Thesis Outline

This thesis is organized starting with a brief literature review on jet flow and skin friction measurements, followed by the three peer-reviewed journal papers mentioned above, a global discussion connecting the papers, conclusions, list of contributions, and recommendations for future work. There is also five section appendix covering topics not included in the main chapters.

Chapter 2

Literature Review

2.1 The Nature of Jet Flow

Gas jets can exhibit a great deal of flow complexity and a wide range of length and time scales, depending on the state of the jet, and the location in the jet flow. In the jet shear layers, the sharp mean velocity gradient facilitates the extraction of energy from the mean flow, channeling it down to the smallest scales, where the energy can be finally dissipated by viscous action [5]. The smallest turbulent length scale in the flow η is on the order of the molecular motion of the fluid, and the largest length scale l is on the order of the jet width, with their ratio decreasing with increasing Reynolds number, where $\frac{\eta}{l} \sim Re^{-3/4}$ [5]. The time-averaged large scale features of the jet (such as the spread rate) are insensitive to jet velocity, even with a factor of 4 difference in Reynolds number, as shown in Figure 2.1 [6]. Inspection of Figure 2.1 will show that the most significant difference between the two jets was the evolution of the small turbulent scales represented by the fine-grained structure of the flow [6]. The spread rate is typically constant for axisymmetric and planar jets independent of

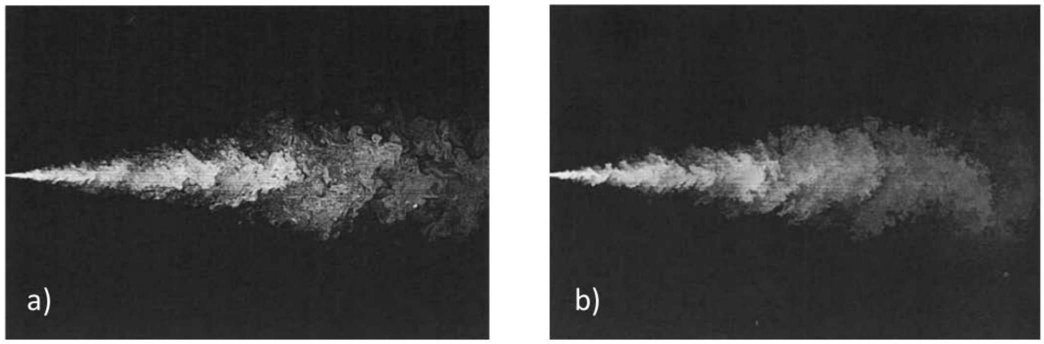

Figure 2.1: Flow visualization of a turbulent axisymmetric free jet a) Re = 5000, b) Re = 20000, reproduced from Dahm and Dimotakis [6].

jet Reynolds number, with a jet half-width span of $\theta_s \approx 6$ deg from the jet centerline [5]. The momentum equations for axisymmetric and planar jets reveal that the centerline velocity decay rate is proportional to $1/z$ and $1/\sqrt{z}$ respectively, where z represents the downstream distance from the jet exit [5]. This indicates that round jets decay, and entrain ambient surrounding fluid more effectively than planar jets.

Close to the jet nozzle exit, the free jet region is composed of a potential core (extending $\approx 5 - 6$ nozzle widths for submerged turbulent jets [7]), where the centerline velocity remains constant. In the potential core region of the jet, the shear layers are initially developing and are yet to merge laterally, as depicted in Figure 2.2. Vortices roll-up at the nozzle edge due to the unstable velocity profile, grow exponentially, and pair downstream, due to the difference in phase speed of the disturbance across the shear layer [8, 9]. Both of these factors contribute to the expansion of the shear layer, and the entrainment of the surrounding fluid. The state of the jet (determined by the initial velocity profile shape), is highly influenced by the development length of the nozzle and the jet Reynolds number [10]. Similar to flow in a pipe, velocity profiles near the jet exit can be uniform laminar (top

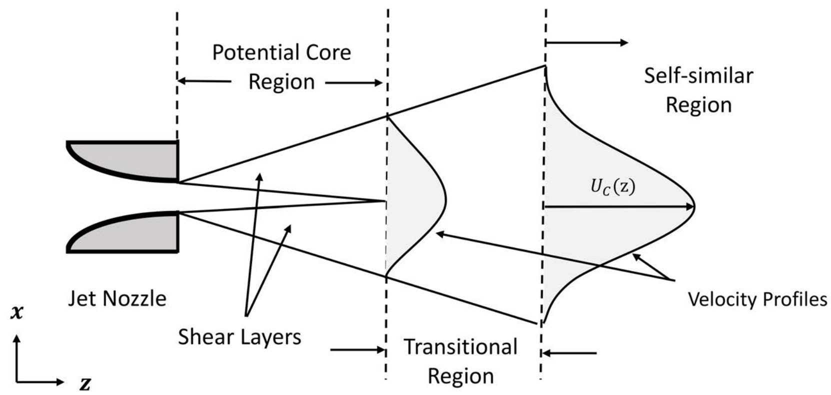

Figure 2.2: Flow regions in a free jet.

hat), developing laminar, fully developed laminar, turbulent, and fully developed turbulent, which can be roughly characterized by the shape factor ($\frac{\delta^*}{\theta} \approx 2.6$ for laminar, $\frac{\delta^*}{\theta} \approx 1.3$ for fully turbulent [11]). The velocity profile shape also dictates the jet instability characteristics and growth rates. For instance, a jet exhibiting an initial "top-hat" velocity profile will be more prone to symmetric instability modes (vortex structures appearing symmetric about the jet centerline) due to the instability characteristics of a velocity profile with relatively thin boundary layers. As the boundary layers grow downstream, anti-symmetric vortex arrangements occur with higher probability due to the instability characteristics of a more parabolic-shaped velocity profile [12].

Velocity measurements (or scalar measurements such as temperature, and species concentration) in jet flow also have unique characteristics. Intermittency in the velocity time signals become more prominent at the edges of the jet shear layer, causing large amounts of skewness ($\neq 0$) and flatness (> 3) in their probability density functions (PDF). This feature leads to the non-Gaussian characteristics of velocity PDF's in the shear layer, and non-conformity with the central limit theorem [5]. This intermittency can be circumvented with conditional-sampling techniques, however, they usually employ arbitrary threshold parameters to determine when to bin data. In the Lagrangian view of the flow field, the edge of the shear layer is defined by a thin interfacial layer, known as the viscous super-layer. This layer separates the highly disorganized jet flow, and the ambient fluid. The viscous super-layer provides a large scalar gradient across its boundary promoting diffusion, and its interface is known to be highly wrinkled, exhibiting fractal properties [5]. The process of large scale engulfment, and small scale nibbling causes this viscous super-layer to migrate outwards, entraining the surrounding ambient fluid [13].

Immediately downstream of the potential core region of the jet there is a highly intermittent region, known as the jet transition region, shown in Figure 2.2. This transition region is where the two shear layers (and super-layers) meet and interact; researchers usually avoid this region in jet studies due to the flow complexity. Many jet nozzle widths further downstream there is known to be a self-similar region. In this self-similar regime, depicted on the right of Figure 2.2, the time-averaged velocities take on a universal form if they are non-dimensionalized by their respective characteristic length, and velocity scales (usually jet half-width, and centerline velocity at the respective downstream location). Many laminar and turbulent self-similar jet properties (such mean stream-wise velocity, cross-stream velocity, jet half-width, and entrainment velocity functions), for both planar and circular nozzle geometries have been tabulated in Blevins [7]. Self-similarity in the mean velocity profiles and turbulence intensity profiles have been reported in the literature for downstream distances of roughly $\tilde{z}/D \gtrsim 70$ in circular jets [14], and for $\tilde{z}/W \gtrsim 65$ in planar jets [15]; where the tilde represents the downstream distance from the

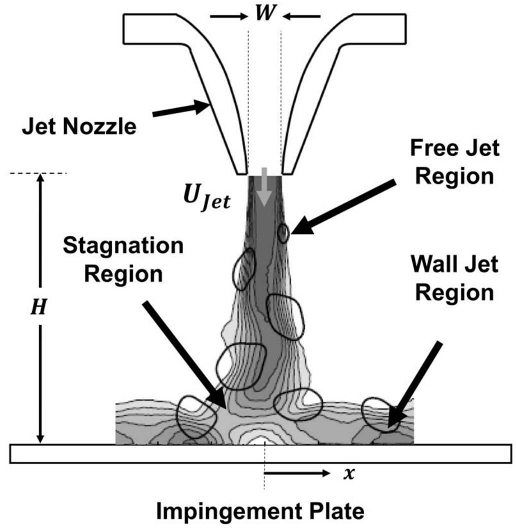

Figure 2.3: Flow regions under a planar impinging gas jet. Flow field data borrowed from Arthurs and Ziada [16].

virtual origin.

An impingement plate positioned a distance H from the jet, introduces new regions of the flow, illustrated in Figure 2.3 [16]. This configuration has many applications in engineering and manufacturing, such as propulsion, drying, cooling, and wiping processes. The stagnation region is where the fluid first encounters the wall, and is forced to change direction symmetrically about the jet stagnation point. Significant amounts of anisotropic fluid strains occur in this region, with the extent of the stagnation region roughly defined to be within the confines of the static wall pressure profile $x/W \approx \pm\ 2$ [17], and the presence of the plate heavily influencing the flow between $z/H \approx 0.75 - 1$ [18]. Acceleration of the flow in the stagnation region is due to the favourable pressure gradient generated. This flow acceleration can cause an effective laminarization of the boundary layer along the plate due to the increasing mean velocity, and "freezing" of fluctuating velocity components. Freezing of fluctuating velocity intensities has also been observed in accelerating pipe flows by Selvam et al. [19]. Within the stagnation region of the jet, the maximum wall shear stresses and the maximum rate of heat transfer is obtained, making impinging jets strong candidates for cooling, particle removal, and wiping processes. Moving away from the stagnation region and along the impingement plate, the static wall pressure subsides and the flow no longer accelerates, eventually leading to a complex state of transition. At this transition location, the boundary layer is known to evolve into a fully turbulent state, and exhibit wall jet behaviour ($x/W > 5$), where the shear stresses begin to monotonically decrease in the flow direction.

Jet stabilities is a widely studied and comprehensive subject, and only a brief description will be given here. Instabilities arising from free jet flow can be characterized by mainly two parameters. The first parameter is the momentum thickness θ of the time-averaged velocity profile at the jet exit. Lord Rayleigh showed that the existence of an inflection point in the velocity profile, allows the flow to be unstable, and susceptible to certain external frequencies [8]. These types of instabilities are known as "shear layer" instabilities. The shear layer instability frequencies are known to be correlated to the length scale of the velocity boundary layer, or more adequately by the jet exit momentum thickness. Typical values for plane jet shear layer instability frequencies are associated with the Strouhal number ranges $St_\theta = \frac{f\theta}{U_{jet}} \approx 0.01 - 0.02$ [9].

Another instability arising in jet flow is due to the full velocity profile (not simply the momentum thickness of one shear layer), and can be characterized by the nozzle spacing (W for planar jets [20], and D for circular nozzles [21]). These frequencies depend on the conditions of the applied external disturbance, exhibiting both symmetric (varicose for plane jets, ring for circular jets) and anti-symmetric (sinuous for plane jets, and helical for circular jets) arrangements [22, 23]. These inherent instabilities in the jet column are usually lower frequency than that of the shear layer mode, and are sometimes referred to as the "preferred mode". This term was proposed by Crow and Champagne [21], where the authors were exciting a cir-

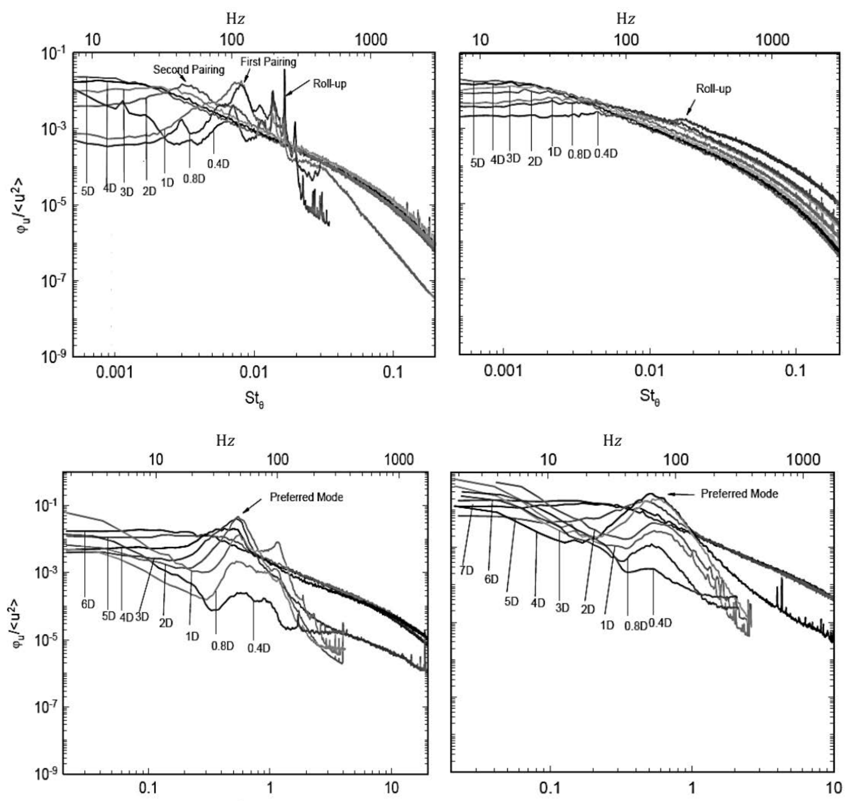

Figure 2.4: Hot-wire frequency spectrum in the shear layer r/D = 0.476 of a round jet (top left), and with an interrupter ring installed at the jet exit (top right) at different downstream positions. Hot-wire frequency spectrum at the jet centerline r/D = 0 of a round jet (bottom left), and with an interrupter ring installed at the jet exit (bottom right) at different downstream positions. Re_{jet} = 30000 for both cases. Plots reproduced from Sadeghi and Pollard [25].

cular jet with a loudspeaker inside the jet plenum to determine the most amplified frequency in the jet flow; originally reported as $St_D = \frac{fD}{U_{jet}} \approx 0.3$. The preferred mode was shown to have some relation (not well defined) to the shear layer instability frequency for laminar jets, and was shown to be independent, and separable for higher velocity jet flows [24]. This has been further examined by installing interrupter rings [25], and mesh screens [26] immediately outside the jet exit in circular nozzles to annihilate the shear layer mode growth. In Figure 2.4, four velocity frequency spectra are shown without (left plots), and with (right plots) interrupter rings installed at the jet exit of a circular free jet [25]. The top two velocity spectra were measured in the shear layer, and the two bottom velocity spectra were measured at the jet centerline. The interrupter rings were successful at removing the shear layer mode frequency (top right), but the preferred mode frequency $St_D = \frac{fD}{U_{jet}} \approx 0.56$ remained dominant at the jet centerline (bottom right). This is some experimental evidence of the decoupling of these two types of instabilities.

The discrepancy between reported preferred mode Strouhal numbers for circular jets is typically $\pm 100\%$ in the literature, and this has been attributed to jet sensitivity to background noise, and spatial coherence in different-sized jet plenums [27]. Despite these discrepancies, researchers generally agree that planar jets exhibit lower preferred mode Strouhal numbers $St_W \approx 0.15$ [22] compared to circular jets, and are more susceptible to anti-symmetric forcing at the jet nozzle exit. To minimize the literature review overlap with those in the thesis papers, self-excited instabilities on high-speed impinging jets will be reserved to Chapters 4 and 5.

2.2 Impingement Plate Skin Friction

A large body of fluid dynamics literature has been devoted to measuring wall shear stress, mainly due to its importance in wiping, particle removal, and drag. The difficulty in measuring viscous wall shear stress distributions arises in its definition, where the velocity gradient of the fluid needs to be evaluated deep within the inner regions of the boundary layer at the solid surface.

As the fluid velocity parallel to the plate becomes appreciable in realistic flows, this inner region, or viscous sublayer in the case of turbulent flow, becomes extremely small; on the order of microns scaling with $\sim 1/U_{jet}$. Large measurement errors ($> 15\%$) are associated with measuring wall shear stresses using the velocity gradient technique, and are further detailed in Section 3.1. Many other indirect wall shear stress measuring techniques have been discussed in the literature based on heat transfer (hot-film or infrared), mass transfer (electrochemical or particle removal), and momentum transfer (Preston or Stanton tubes) analogies. There are also other less common techniques such as liquid crystal, laser Doppler wall sensors, and micro-displacement sensors discussed in the literature. A thorough review of all the above techniques can be found in Naughton and Sheplak [28]. For brevity, only the semi-empirical wall shear stress correlations, electrochemical, and Preston/Stanton tube techniques will be discussed in this chapter. Oil film interferometry will be discussed in detail in Chapter 3.2.

2.2.1 Semi-Empirical Wall Shear Stress Correlations

Semi-empirical wall shear stress correlations for circular and planar jets are given in the literature for various jet Reynolds numbers $Re_{jet}=\frac{U_{jet}W}{\nu}$, and impingement ratios H/W introduced by Phares et al. [29]. These correlations are termed "semi-empirical" due to their combined numerical, empirical, and analytical approach, with original methodologies formulated by Polhausen as detailed in Schlichting [30]. Free stream velocities $U_\infty(x)$ were numerically solved using stream functions in an inviscid stagnation flow domain with an influx velocity profile boundary condition [31]. These influx profiles can be obtained from experimental velocity data, or from Tollmein's solution for jet flow [32]. An illustration of this numerical flow domain with its empirical influx velocity profile is shown in Figure 2.5. A lam-

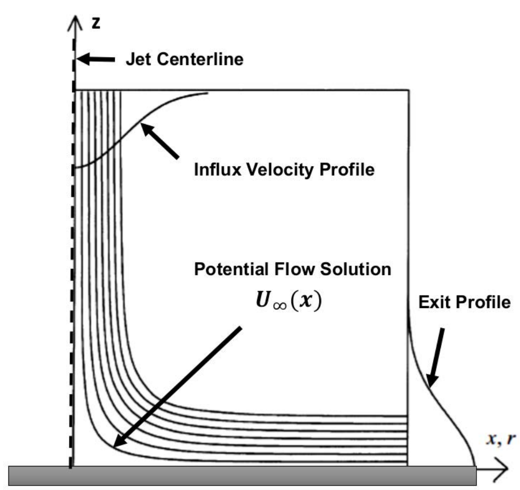

Figure 2.5: Computational domain with empirical influx velocity profile to determine the potential flow solution near the impingement plate in the stagnation region. Modified from Phares et al. [29].

inar polynomial velocity profile, and a pressure gradient shape parameter Λ were employed at the impingement plate, which are presented as a function of unknown variables in Equations 2.1 and 2.2, respectively. The pressure gradient shape parameter has an influence on the curvature of the velocity profile, which can exhibit inflection points, and can take on positive or negative values depending on whether the pressure gradient is favourable or adverse, respectively. The velocity profile can also exhibit separation conditions under heavily adverse pressure gradients [30].

$$u = f(\delta, U_\infty, \Lambda) \tag{2.1}$$

$$\Lambda = \frac{\delta^2}{\nu} \cdot \frac{dU_\infty}{dx} = f(\delta, \frac{dU_\infty}{dx}) \tag{2.2}$$

Using this laminar boundary layer profile, with an unknown boundary layer thickness δ, the corresponding displacement and momentum thickness equations can be described by Equations 2.3 and 2.4, respectively.

$$\delta^* = f(\delta, U_\infty, \Lambda) \tag{2.3}$$

$$\theta = f(\delta, U_\infty, \Lambda) \tag{2.4}$$

The final two equations are the wall shear stress definition (velocity gradient evaluated at the wall) in Equation 2.5, and Von Kármán's momentum integral equation given in Equation 2.6, which is obtained by integrating the momentum equation across the boundary layer in the z -direction.

$$\tau_w = \mu \frac{\partial u}{\partial z}\bigg|_{z=0} = f(\delta, U_\infty, \Lambda) \tag{2.5}$$

$$\tau_w = \rho\left[U_\infty^2 \frac{d\theta}{dx} + (2\theta + \delta^*)\cdot U_\infty \frac{dU_\infty}{dx}\right] = f\left(\delta, \delta^*, \theta, U_\infty, \frac{dU_\infty}{dx}\right) \tag{2.6}$$

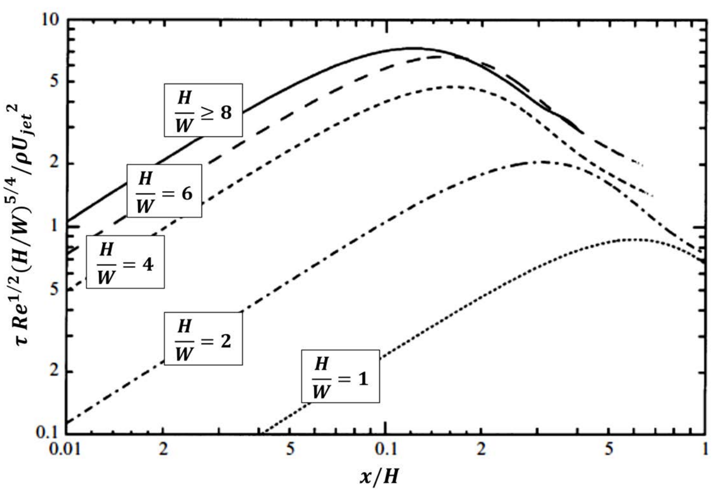

Figure 2.6: Semi-empirical wall shear stress correlations for different impingement ratios H/W for a planar impinging jet. Figure modified from Phares et al. [29].

Knowing the free stream velocity U_∞, and velocity gradient $\frac{dU_\infty}{dx}$ distribution along the impingement plate from the inviscid computations, this problem comprises six equations (2.1, 2.2, 2.3, 2.4, 2.5, 2.6) and six unknowns (u, δ, δ^*, θ, Λ, τ_w). One solution approach to this problem involves solving a non-linear differential equation, detailed in Schlichting [30], to obtain the resulting wall shear stress τ_w distributions. The final results using this methodology are the curves, and correlations given by Phares et al. [29], where the 2D planar impinging jet case is reproduced in Figure 2.6. Although theoretically and mathematically sound, there is little direct experimental evidence showing that these wall shear stress approximations agree with experimental planar gas jet data; details will be examined in

Section 3.6.3. This is mainly due to the difficulty and poor reliability of measured wall shear stress data in impinging gas flows. One of the primary objectives of the present research is to provide accurate wall shear stress data for coating weight models used in continuous hot-dip galvanizing, and compare the results with the aforementioned semi-empirical wall shear stress correlations.

2.2.2 Electrochemical Method for Liquid Jets

The electrochemical method is used to determine wall shear stresses under liquid impinging jets [34, 35, 33, 36] by estimating the velocity gradient at the wall using mass transfer relations. This method was originally designed to measure mass transfer rates [37] and requires a liquid electrolyte, usually potassium ferri/ferrocyanide dissolved in an aqueous solution of sodium hydroxide. The impinging jet rig can be submerged in a closed loop electrolytic bath that circulates the working fluid through the jet and onto the impingement plate, as illustrated in Figure 2.7. On the

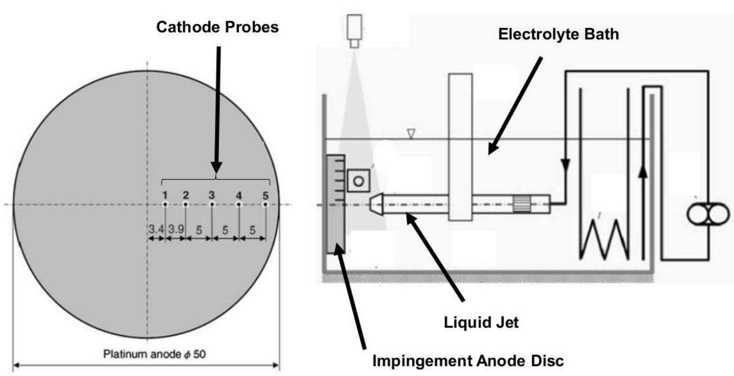

Figure 2.7: Electrochemical setup with a submerged circular impinging liquid jet in an electrolytic solution (right). The impingement disc that serves as an anode with embedded cathodic electrodes (left). Modified from El Hassan et al. [33].

.

impingement surface, there are small (order of $\sim 1\ mm$) embedded and circumferentially insulated cathodes positioned at different positions downstream from the point of jet stagnation. The impingement surface, which is the platinum disc shown in Figure 2.7, served as an anode in the experiments by El Hassan et al. [33]. The embedded cathodes were accessible through the back side of the impingement surface, where an external electric current was applied. The limiting diffusion current, I, through these electrodes has been studied extensively [38, 39], and can be varied by the flow of electrolyte over the cathode and the anode surfaces. In other words, the limiting diffusion current can be related to the mass transfer coefficient of the ions, and to the velocity gradient of the electrolytic solution at the wall by a form of the Lévêque solution. The wall shear stress can be calculated by:

$$\tau_w = \mu \cdot \frac{8}{3} \cdot \left[\frac{L}{D^2}\right] \cdot \left[\frac{I \cdot n \cdot \Gamma(4/3)}{FCA}\right]^3 \tag{2.7}$$

where μ is the dynamic viscosity of the fluid, D is the diffusivity of the active ions, C is the ion bulk concentration, F is Faraday's constant, n is the number electrons transferred in the reaction (n =1 for potassium ferri/ferrocyanide systems), Γ is the gamma function, A is the cathode surface area, I is the limiting diffusion current, and L is the cathode dimension in the stream-wise direction. For circular cathodes an equivalent length formula can be used L_e = $0.8136\ D$ [39]. For liquid jets, this method of wall shear stress measurement is in reasonable agreement with the semi-empirical correlations shown in Figure 2.8.

The experiments of Alekseenko and Markovich [34], Kataoka and Mizushina [40], and Kataoka et al. [35] are plotted against the semi-empirical correlations of Phares et al. [29] in Figure 2.8. The left plot represents data for impingement ratios

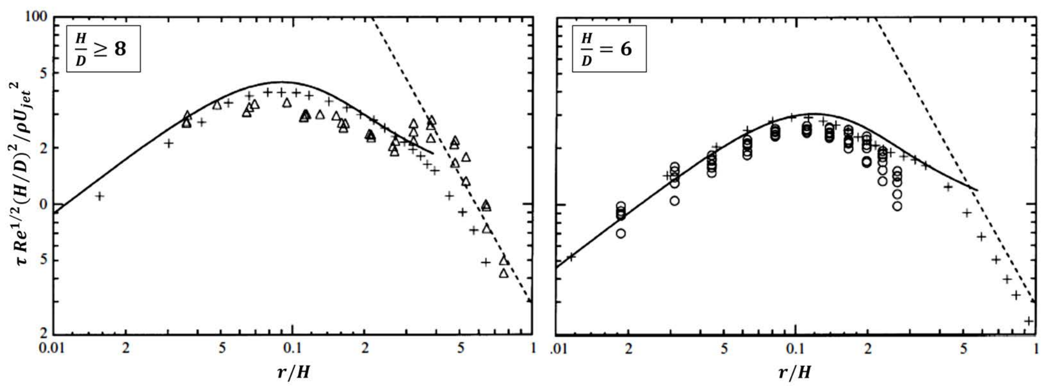

Figure 2.8: Wall shear stress measurements under circular impinging liquid jets using the electrochemical method modified from Phares et al. [29]. Impingement ratios $H/D \geq 8$ (left), and $H/D = 6$ (right). Solid and dashed lines are the semi-empirical wall shear stress correlations. Alekseenko and Markovich [34] [$+$] $Re_{jet} = 41600$, Kataoka and Mizushina [40] [$\triangle$] $Re_{jet} = 10600 - 36200$, Kataoka et al. [35] [$\circ$] $Re_{jet} = 4000 - 15000$.

$H/D \geq 8$, and the right plot for $H/D = 6$. There are a few details worth noting about these logarithmic plots of Phares et al. [29]. First, there was an over-estimation of the wall shear stress versus the experimental data plotted in Figure 2.8 by the semi-empirical correlations. Second, the electrochemical method is only viable for liquid jet experiments. In particular, all of the experimental work in Figure 2.8 was taken from circular impinging liquid jets. The work of the present research concerns planar gas jets, and so this section serves only as a useful comparison between the experiments of circular impinging liquid jets and the shear stress predictions of Phares et al. [29], as well as a validation of the laminar boundary assumption used in these semi-empirical models.

2.2.3 Preston Tube Method for Gas Jets

The Preston tube was originally developed by Preston [41] as a method for determining skin friction in wall bounded flows. The Preston tube operates in a similar manner to a Pitot tube, but is relatively small (hypodermic [<1 mm] in most cases or flattened) and are situated close to the wall, as shown in Figure 2.9.

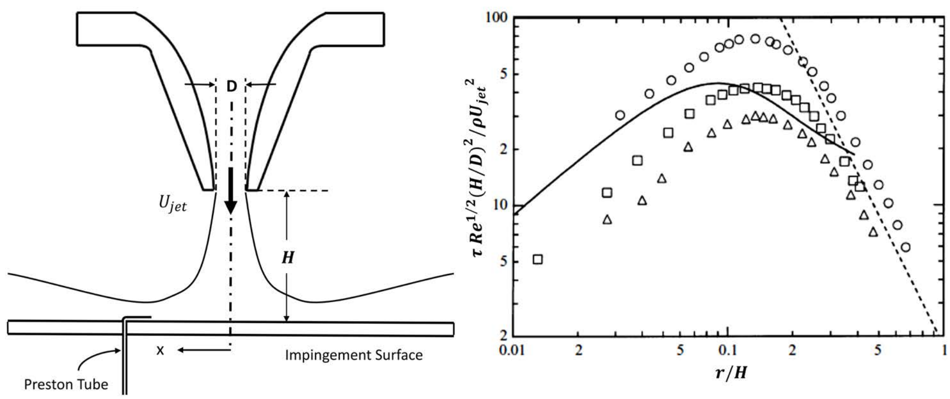

Figure 2.9: Preston tube in situ under an impinging gas jet (left). Wall shear stress measurements for circular impinging gas jets in literature modified from Phares et al. [29] (right). Beltaos and Rajaratnam [42] $Re_{jet} = 80400$ H/D = 21.1 [□], $Re_{jet} = 30000$ H/D = 65.7 [△], Bradshaw and Love [43] $Re_{jet} = 150000$ H/D = 18 [○].

Preston tubes measure the flow stagnation pressure at a defined wall location. A subsequent static pressure measurement at the same location will allow one to calculate the dynamic pressure. The dynamic pressure can be used to evaluate the effective momentum near the wall, which in theory has some correlation to the amount of wall shear stress experienced by that surface. The razor blade technique (or Stanton probes) operates in a similar manner as the Preston tube, where the stagnation pressure is measured by placing the sharp edge of the razor blade over a small static pressure hole [44]. The Preston tube method has been used for many years in fully developed turbulent flows, and serves as a simple skin friction measuring technique.

The calibration of Preston tubes is typically performed in a "known" flow condition, such as fully developed turbulent pipe or channel flow. After calibration, the Preston tube is then placed in an unknown flow condition and can be used to evaluate the skin friction, such as stagnation flows. Wall shear stress measurements from the literature using Preston tubes under circular impinging gas jets are shown on the right of Figure 2.9. The lines in this figure are the semi-empirical correlations of Phares et al. [29], and the data points were taken from the work of Beltaos and Rajaratnam [42] and Bradshaw and Love [43]. The above scatter in the wall shear stress measurements for impinging gas jets raises some obvious questions and concerns. The accuracy of the Preston tube probe relies heavily on the universality of the log-law region in the turbulent boundary layer. Any deviations from this "universal" profile, which can be caused by boundary layer development, pressure gradients (both favorable and adverse), laminarization, and/or non-similar flow conditions have been shown to induce significant measurement error [45, 46].

Skin friction measurements have also been shown to be sensitive to probe size [47], and orientation [44]. The skin friction distributions shown at the top of Figure 2.10 are taken from Tu and Wood [48] for $Re_{jet} = 6300$ and $H/W = 20.6$. Note that the smaller probe sizes induce a higher skin friction measurement in the stagnation region when using Preston and Stanton tubes. Phares et al. [29] analyzed these results by plotting the probe height relative to both laminar and turbulent flow conditions for this set of experimental conditions, as shown in the bottom of Figure 2.10. Also the maximum skin friction was computed using the semi-

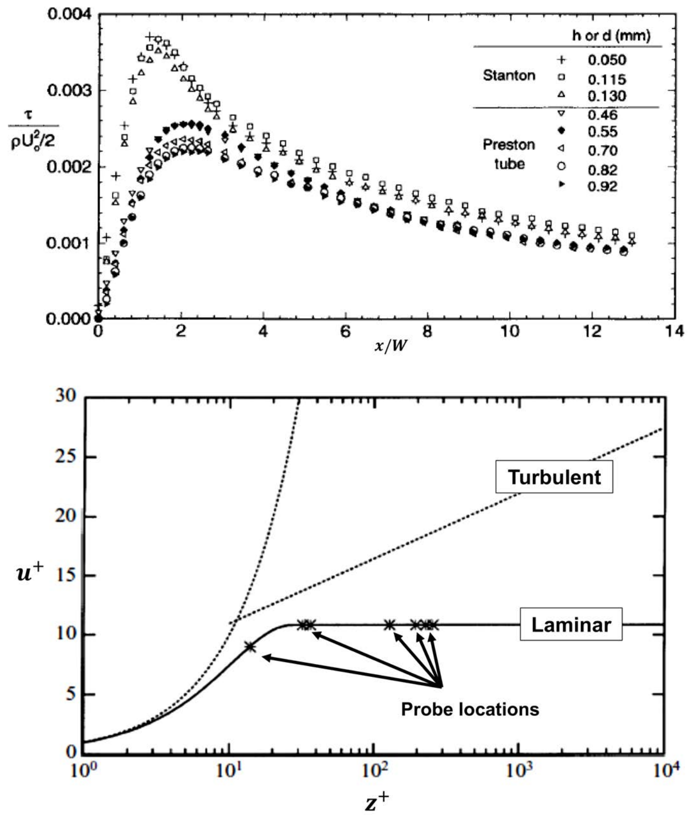

Figure 2.10: Preston/Stanton tube measurements from Tu and Wood [48] with different probe sizes for a planar impinging gas jet; Re_{jet} = 6300 and H/W = 20.6 (top). Probe measurement locations move closer to the wall with smaller probe sizes, as indicated by wall-normalized velocity profiles modified from Phares et al. [29] (bottom).

empirical correlations to be $C_f \approx 0.004$ for this case. Phares et al. [29] argued that if the velocity profile in the stagnation region was laminar and the probe was calibrated for turbulent flow, then as the probe size became smaller, the deviations between the laminar and turbulent profiles would become smaller, and the skin friction measurement would become more accurate. The bottom of Figure 2.10 shows a non-dimensionally scaled laminar and turbulent velocity profile along with the corresponding Preston tube measurement location in the boundary layer for each of the skin friction distributions shown at the top of Figure 2.10. The skin friction factor C_f appears to be asymptotically approaching $C_f \approx 0.004$, agreeing with this conjecture. Despite these efforts to explain the inconsistencies in the experimental data, there is still a clear need for accurate wall shear stress measurements for impinging gas jets.

2.3 Summary and Open Issues

Despite the various wall shear stress measuring techniques, and the large body of literature devoted to impinging jet wall shear stresses, there is still a clear need to produce reliable experimental data for planar impinging gas flows. This is evident by the lack of experimental wall shear stress data for impinging gas flows, and the discrepancies between the existing data (shown in Figure 2.9). Chapter 3 will help expand this scarce experimental data set, and provide accurate wall shear stress measurements using a measurement technique that is not subject to the inconsistencies and limitations of mass transfer, heat transfer, or momentum transfer analogies. To help facilitate the measurement of wall shear stress, a scaled-up model of an air-knife (planar impinging gas jet) is designed and tested.

Additionally, planar impinging gas jets are prone to fluid instabilities, some of which were discussed previously in Section 2.1. These jet instabilities can result in a highly oscillatory jet response under a selected range of disturbance/forcing frequencies. The effects of wiping under jet instability conditions were previously inconclusive and unknown. Chapter 4 will determine the effects of jet oscillations on the fluid loading on the plate, by introducing perturbations at the nozzle exit of the model air-knife using planar synthetic jets, while directly measuring the wall shear stress and pressure gradient at the impingement plate.

Chapter 5 will further analyze the fluctuating velocity fields and fluctuating kinetic energy of the model air-knife, determined using PIV, under forced and unforced conditions. Fluctuating jet velocity data is quite restricted in the literature, and is mostly limited to discrete locations in the flow, such as at the jet nozzle exit or along the jet centerline. The obtained fluctuating velocity fields will also be decomposed into their respective coherent and stochastic components, with the intention of explaining some of the unique flow field features observed under external forcing. The velocity statistics of the current low-speed model air-knife will be paralleled with a high-speed planar impinging gas jet tested previously, more akin to an industrial air-knife utilized in continuous hot-dip galvanizing.

Chapter 3

The Maximum Skin Friction and Flow Field of a Planar Impinging Gas Jet

Complete Citation:

Ritcey, A., McDermid, J.R., and Ziada, S., 2017."The maximum skin friction and flow field of a planar impinging gas jet". *Journal of Fluids Engineering*, 139(10), p.101204. *doi: 10.1115/1.4036717*

Copyright

Preface

This study determined the maximum impingement plate skin friction developed by a scaled air-knife model (planar impinging gas jet) using oil film interferometry (OFI) under different jet Reynolds numbers (Re_{jet} = $11000 - 40000$) and impingement ratios (H/W = $4, 6, 8, 10$). A parametric skin friction map based on the air-knife operating condition was constructed, and can be used to provide experimental inputs to coating weight models applied to continuous hot-dip galvanizing. The OFI skin friction data was compared to other skin friction studies in the literature, and the flow field of the air-knife model was assessed using particle image velocimetry (PIV) to characterize the jet exit conditions, and downstream behaviour of the flow near the impingement plate. All experimental measurements, data analysis, and technical writing was completed by the first author under the supervision of advisors: Dr. McDermid and Dr. Ziada.

The Maximum Skin Friction and Flow Field of a Planar Impinging Gas Jet

Adam Ritcey, Joseph McDermid, Samir Ziada

McMaster University
Department of Mechanical Engineering
1280 Main Street West
Hamilton, Ontario L8S 4L7

Abstract

The maximum skin friction and flow field is experimentally measured on a planar impinging gas jet using oil film interferometry (OFI) and particle image velocimetry (PIV), respectively. A jet nozzle width of $W = 15\ mm$, impingement ratios $H/W = 4, 6, 8, 10$, and a range of jet Reynolds numbers $Re_{jet} = 11000 - 40000$ is tested to provide a parametric map of the maximum skin friction. The maximum skin friction predictions of Phares et al. (2000, "The Wall Shear Stress Produced By the Normal Impingement of a Jet on a Flat Surface," J.Fluid Mech., **418**, pp. 351-375) for plane jets agree within $5\ \%$ of the current OFI results for $H/W = 6$, but deviates upwards of $28\ \%$ for other impingement ratios. The maximum skin friction is found to be less sensitive to changes in the impingement ratio when the jet stand-off distance is roughly within the potential core length of the jet. PIV measurements show turbulence transition locations moving towards the nozzle exit with increasing Reynolds number, saturation in the downstream evolution of the maximum axial turbulence intensity before reaching a maximum peak upon impingement, followed by sudden damping at the plate surface. As the flow is redirected, there is an or-

thogonal redistribution of the fluctuating velocity components, and local peaks in both the axial and transverse turbulence intensity distributions at the plate locations of the maximum skin friction.

3.1 Introduction

Wall shear stress τ_w is an important fluid flow parameter in many engineering applications. It serves as a scaling parameter in wall bounded flows, manifests itself in the formation of viscous drag on moving bodies, and has applications in mass transfer and coating control processes [1]. In particular, the maximum wall shear stress is an input parameter in coating weight models used in continuous hot-dip galvanizing [2]. Wall shear stress has also been quite an elusive parameter, where its magnitude and distribution is difficult to measure at appreciable Reynolds numbers. The difficulty arises due to the small turbulent scales introduced into the continually shrinking viscous sublayer, and the limited resolution of the measuring equipment being probed very close to the wall. Even computational fluid dynamic (CFD) models have difficulty capturing the near-wall physics at the impingement plate and are known to provide inaccurate predictions of wall shear stresses. The wall shear stresses presented here will also be used to help validate CFD models for impinging flows in the future. Despite the many years of jet research, and books written on the subject [3, 4], there is very little experimental data available for wall shear stress distributions under planar impinging gas jets; especially in the stagnation region. The stagnation region under the jet is of interest to researchers because this is where steep pressure gradients, minimum and maximum wall shear stresses (separated by Hiemenz flow relations), maximum rates of heat transfer, high streamline curvature, and high rates of fluid strain occur.

Early wall shear stress measuring techniques were indirect and relied on the relationship between the wall shear stress and the dynamic wall pressure measured with Preston tubes, Stanton tubes, and razor blade techniques. Several impinging jet studies have used this approach to estimate the wall shear stresses along the impingement plate [2, 5, 6, 7]. The downfall of these measuring techniques is the large scatter in the relationship between the dynamic wall pressure and wall shear stress among different flows (pipe flow versus impinging flows). This scatter concerns the accuracy of the probe calibration, in addition to being strongly affected by existing pressure gradients [8]. Analogies between the wall heat transfer and wall shear stresses have also been considered [9, 10]. The same problems and inaccuracies arise in the calibration and indirect nature of the hot-film sensors. Along the wall surface under an impinging jet flow, there is an increase in wall shear stress from the stagnation point, whereas the opposite trend is true for the Nusselt number. In fact the maximum Nusselt number seems to occur at the line of jet symmetry [11], which is the location of zero wall shear stress. This is an example where the analogy breaks down. The velocity gradient at the wall can also be used to determine the wall shear stress in a Newtonian fluid using Equation 3.1.

$$\tau_w = \mu_a \frac{\partial v}{\partial z}\bigg|_{z=0} \tag{3.1}$$

Measuring the velocity gradient in the viscous sublayer is considered a direct wall shear stress measuring technique, however, on top of the limited spatial resolution of this layer in higher Reynolds number flows, there is the challenge of measuring hot-wire to wall distances accurately [12], low velocity hot-wire calibration [13], and wall interference [14, 15], which is known to impose a fictitious velocity reading on the hot-wire. Zhe and Modi [16] determined wall shear stresses using hot-wire measurements on a planar impinging air jet for $Re_{jet} = 10000 - 30000$ and $H/W = 2 - 9$. Their jet was scaled up ($W = 40\ mm$) to increase spatial resolution, and they attempted to compensate for wall interference by calibrating the probe in a known laminar flow. Due to discrete measurement locations on the impingement plate with their single wire probe, it is uncertain if the maximum wall shear stress locations were resolved, and all the wall shear stress measurements were at least one slot width away from the jet stagnation point. Near-wall PIV measurements have also been used to determine wall shear stresses (using Equation 3.1) produced by circular and elliptical impinging liquid jets [17, 18]. The jet flow velocities were very low ($U_{jet} \approx 0.11\ m/s$) in these studies to accommodate the needed spatial resolution in the boundary layer. Also in the literature, the electrochemical method uses the relationship between the measured diffusion current across a surface-mounted anode and cathode and the mass transfer of ions in the electrolytic fluid to determine the wall shear rate. Impinging jet studies using the electro-chemical/diffusion technique [19, 20, 21, 22] have claimed to provide accurate wall shear stress measurements, however, these studies have only been performed on liquid round submerged jets where an electrolyte can be implemented. Other modern wall shear stress measuring techniques include particle removal studies [23], micro-electro mechanical systems (MEMS), laser Doppler wall sensors, and liquid crystal methods, which can be found in a thorough review by Naughton and Sheplak [24]. The current study implements oil film interferometry (OFI) to measure wall shear stress on a planar impinging gas jet. This technique has made great progress in the recent years due to better cameras, equipment, and processing techniques. A review of impingement plate wall shear stress studies using oil film interferometry are reserved until Section 3.2.4.

Important non-dimensional numbers will now be defined. For impinging gas jets, the jet Reynolds number incorporates the jet nozzle width W and jet exit velocity U_{jet} given in Equation 3.2, and the wall shear stress is non-dimensionalized to form the skin friction factor in Equation 3.3.

$$Re_{jet} = \frac{U_{jet}W}{\nu_a} \tag{3.2}$$

$$C_f = \frac{\tau_w}{\frac{1}{2}\rho_a U_{jet}^2} \tag{3.3}$$

In the impinging jet literature their exists semi-empirical wall shear stress correlations for axisymmetric and planar jets, for various jet Reynolds numbers Re_{jet} and impingement ratios H/W, introduced by Phares et al. [25]. Free stream velocities were numerically solved using stream functions in a stagnating flow domain with an influx velocity profile, which serves as a boundary condition [26]. These influx profiles can be obtained from experimental velocity data or known correlations, and together with the laminar boundary layer assumption, one can numerically obtain wall shear stresses for different Re_{jet} and H/W. Equation 3.4 gives the maximum wall shear stress predicted for plane jets given by Phares et al. [25]:

$$\tau_{max} = \alpha\rho U_{jet}^2 {Re_{jet}}^{-0.5}\left(\frac{H}{W}\right)^{-1.25} \tag{3.4}$$

The constant value α = 7.3 for $H/W \geq 8$, α = 6.6 for H/W = 6, and α = 4.8 for H/W = 4, can be obtained from the prediction curves provided in Phares et al. [25]. One of the tasks in this study is to compare our experimental maximum skin friction data with these semi-empirical prediction curves.

Flow field measurements on impinging jets using PIV have also been reported in the literature. Maurel and Solliec [27] analyzed a planar impinging gas jet at Re_{jet} = 27000 and H/W = $5 - 50$. They identified different flow zones in the jet, presented velocity decay and Reynolds stress data, and provided qualitative features of the downstream turbulence statistics. Hammad and Milanovic [28] performed flow field measurements using PIV on a round impinging liquid jet for Re_{jet} = 15895 and H/W = $1 - 8$. They presented both radial and axial velocity profiles, along with turbulence statistics at the nozzle exit and in the vicinity of the impingement plate. Some of the flow field features in these studies will be compared with our current impinging jet facility.

3.2 Oil Film Interferometry

3.2.1 Development and Theory

Equation 3.5 is the simplified one-dimensional laminar analytical equation that governs the motion and forces on a thin oil film. A complete derivation can be found in Naughton and Sheplak [24].

$$\frac{\partial h}{\partial t} + \frac{\partial}{\partial x}\left[\frac{\tau_w h^2}{2\mu}\right] = 0 \qquad (3.5)$$

The thin oil film equations were originally developed by Squire [29], but it wasn't until Tanner and Blows [30] realized that these equations could also be used to calculate the wall shear stress if the oil height was known as a function of space and time. The thin film equations have also been analyzed and implemented for radial and rotational flows [30, 31]. Today, the common oil film interferometry method requires an oil (with known index of refraction n and dynamic viscosity μ) to be placed on a surface where the shear stress is to be measured. A light source is then used to illuminate the oil and the image recorded with an angled camera as shown in Figure 3.1. The light rays being reflected from the oil surface, and the light rays being transmitted through the oil and reflecting off of the solid surface meet back up at the camera at different phases from each other. If only one wavelength of light is recorded using a narrow bandpass filter (532 nm), a unique interference pattern can be observed. The images of the interference patterns are called interferograms. The fringe spacing in the interference pattern reveals the spatial distribution of the oil height using the optics relation in Equation 3.6.

$$h = \frac{\lambda\phi}{4\pi}\left(\frac{1}{\sqrt{n^2 - n_a^2 sin^2\theta}}\right) \tag{3.6}$$

The governing partial differential equation of the oil film (Equation 3.5) can now be analytically solved using the oil height distributions in space and time.

3.2.2 Single and Dual Image Analysis

The simplest solution to Equation 3.5 is the constant shear stress solution given by Equation 3.7.

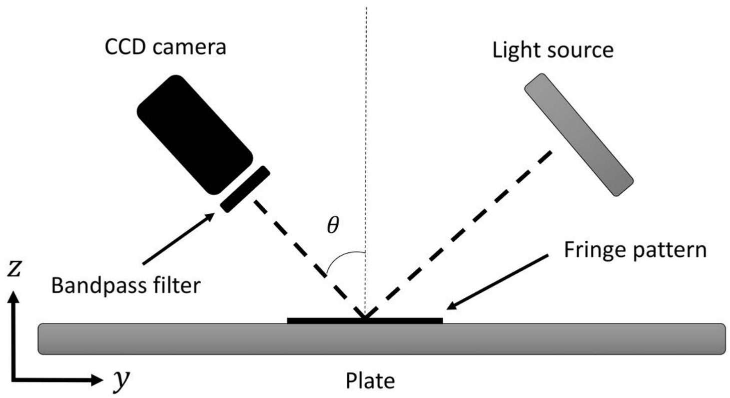

Figure 3.1: Light and camera setup at image station indicating the coordinate system. Flow direction (x) on plate is normal to page.

$$\tau_w = \frac{\mu x'}{ht} \tag{3.7}$$

Note h is the height of the oil at a distance measured from the leading edge x' at time t. This equation can be solved using a single interferogram knowing the experiment duration. Since the computation of the oil film height was calculated in this study using only the second bright fringe from the leading edge (at every y-direction slice across the angled oil line), assuming constant shear stress in this small x-direction (Refer to Figure 3.2) region proved to be a reasonable assumption. This was verified by using different camera lens magnifications and different experiment times. Another technique for computing the oil film height distribution is using the dual-image process [32]. Equation 3.5 can be numerically solved using Equation 3.8 [33]. Two interferograms at two different times (subscript 0 and 1 respectively) are needed to compute the change in height temporally. Within each interferogram, the oil film height distribution can be calculated at each downstream location from the oil leading edge (subscript i).

$$\tau_i = \frac{\left[\frac{(h_0 - h_1)_i}{\Delta t} + \left(\frac{\tau h_0 h_1}{2\mu \Delta x}\right)_{i-1}\right]}{\left(\frac{h_0 h_1}{2\mu \Delta x}\right)_i} \tag{3.8}$$

The dual image technique was experimented for a large scaling of the jet (camera and lighting could be placed in situ of the planar jet and impingement surface) to ensure agreement between both single and dual image methods. Preliminary OFI experiments were also performed on simple flat plates in parallel wind-tunnel flows, and agreement was confirmed between the skin friction measurements and well-known flat plate skin friction correlations in the literature.

3.2.3 Photogrammetry and Image Processing

Camera space (mm) is mapped to image space ($pixels$) using a direct linear transformation and a calibration grid placed over the impingement surface. Skin friction measurements were compared against different angles ψ of oil lines to ensure perspective distortion had no effect. For the current OFI experiments, an oil line placed at $\psi \approx 45°$ along the impingement plate was used. The removable impingement plate was slid onto the traverse mounting bracket, with the wind-tunnel running (to eliminate start-up time). As the jet flow impinges on the plate, the oil is spread out over the plate symmetrically about the stagnation line shown in Figure 3.2. This stagnation line can be determined from the interferogram and used as a reference distance for the skin friction measurements. The spreading of the oil varied in time between 5 minutes to 90 minutes depending on the test case and flow velocity of the jet. The interferogram was then processed in MATLAB to compute the skin friction along the angled oil-line in the image. If the image is crisp and clear (free of dust particles and debris), then approximately 500 data points can be obtained in one image with minimal scatter. Each test case (specified jet Reynolds number and impingement ratio) was composed of two separate OFI experiments, therefore each skin friction profile provided in this paper is composed of approximately 1000 data points. These profiles can be averaged to obtain mean skin friction distributions.

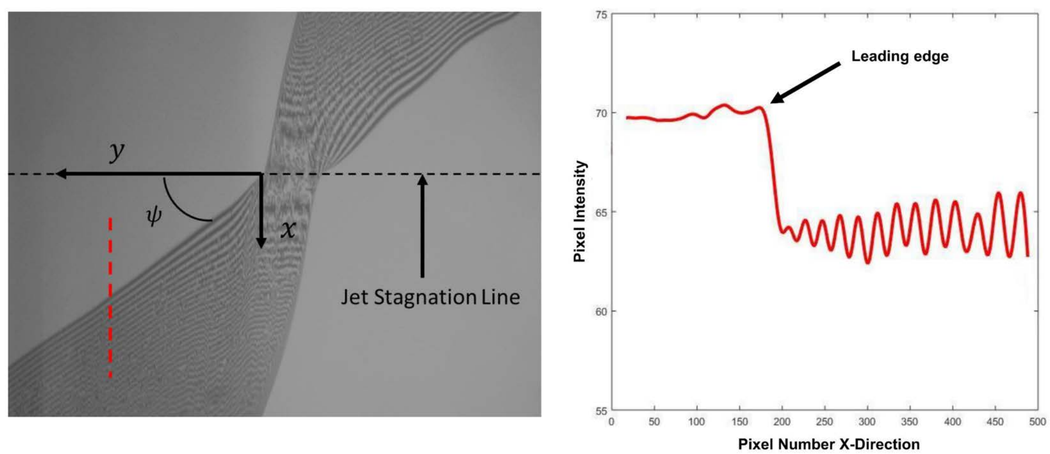

Figure 3.2: The interferogram obtained on the impingement plate surface (left). The oil is applied at an angle to the flow $\psi \approx 45°$ to obtain the entire skin friction distribution with one image, similar to the technique of Dogruoz et al. [34]. Note the line of symmetry along the jet stagnation line (left). The corresponding pixel intensity distribution along the vertical dashed line in the interferogram, which is used to determine fringe spacing (right).

3.2.4 OFI Studies

Skin friction measurements on a planar impinging gas jet for Re_{jet} = 36000 and H/W = 4 using OFI was presented by Dogruoz et al. [34]. Different angled oil lines (ψ = $30°$ and $60°$) were used to confirm negligible changes in the presented skin friction distributions. Stanton gauge (0.1 mm in height) measurements were also performed on their impingement plate for the same case, and an approximate 40

$\%$ reduction in the measured maximum skin friction was noted. These comparisons confirm the problem with Stanton gauges; the probes are indirect measurement devices and are size dependent. Due to their study mainly focusing on jet heat transfer characteristics, no OFI processing details or oil temperature calibrations were mentioned. The goal of our current study is to include these details, along with more skin friction data; providing a parametric map of the maximum skin friction for different Re_{jet} and H/W. Skin friction measurements on a round impinging gas jet for Re_{jet} = 33000 and H/W = 16 and 20 using OFI was presented by Young et al. [35]. For their compressible flow cases (U_{jet} = 136 m/s, $Ma \approx 0.4$), the challenge was to measure skin friction in the stagnation region using radially spreading concentric fringes on their impingement plate. Multiple interferograms were taken in their study and processed in MATLAB, with similar techniques to identify the oil leading edge and fringe locations. Other skin friction studies using OFI in the literature are on wall jet flows [36], supersonic flows [37], rotating blades [31], in-flight measurements on airfoils [38]. Additionally, OFI can also be used in streamline, shock wave, and transition detection.

3.3 Experimental Jet Setup

A large scale impinging planar air jet was designed at the exit of a wind-tunnel at McMaster university. A schematic of the experimental jet setup is shown in Figure 3.3. The open loop wind-tunnel is comprised of a size 19 Sheldons blower with a Toshiba 575 speed controller allowing incremental control of the output flow rate. Planar jet nozzle inserts are placed at the exit of the wind-tunnel and provide an 18:1

contraction ratio along an elliptical contour. The nozzle inserts were constructed from aluminum sheet placed over laser-cut birch support ribs and cedar stock. The elliptical profile follows a major/minor axis ratio of 2.4:1 in this experiment. The aspect ratio of the planar jet (length/slot) at W = 15 mm is 40:1, thus ensuring two dimensional behaviour along the center of the impingement plate. The impingement plate was constructed from 122 cm x 61 cm x 12.7 mm thick smoke-tinted acrylic plate, which allowed for suitable fringe photography and proper cleaning of the silicon oil in between tests. The impingement plate was mounted vertically on a sturdy Isel three-axis traverse, which allowed the impingement plate to be removed and the impingement ratio to be altered in between oil film interferometry tests. Air temperature measurements were made at the jet exit to monitor the temperature of the experiment and the flow velocity at the jet exit recorded with a pitot tube attached to a Fluke 922 micro-manometer. Immediately after each experiment, the impingement plate was removed from the traverse and brought over to the image station (shown in Figure 3.1), and placed horizontal, where a TSI Powerview Plus CCD camera equipped with a 50 mm lens mounted on a 360 degree rotary and steel portable tripod was used to capture the interferograms. The external light source was provided by two halogen lamps mounted on their respective tripods along with a white soft-core backdrop to increase light intensity levels in the measurement area. The camera lens was equipped with a manufacturer-tested high quality Omega Optical 532 nm bandpass filter to allow capturing of a unique interference pattern.

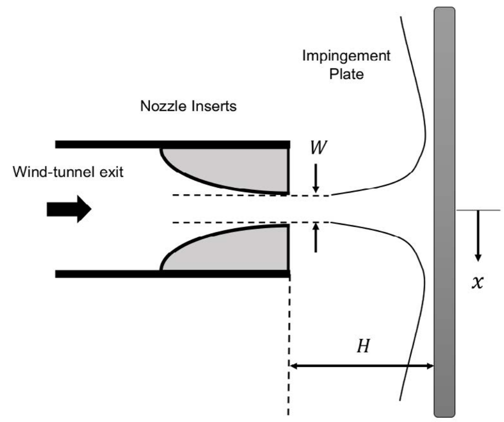

Figure 3.3: Schematic of the experimental impinging air jet setup at the wind-tunnel exit.

3.4 Oil Calibration

Dow Corning 50 cSt silicon oil was used in the OFI experiments. The oil supplier's data indicated 50 ± 2.5 cSt at a single temperature (25 deg C). The oil viscosity was independently calibrated with temperature prior to experiments with a vertical capillary viscometer in a constant temperature bath. The temperature of the water bath was maintained throughout the course of the experiments using a built-in VWR digital temperature controller. Steady state temperature times were calculated using transient conduction Heisler charts for the viscometer's spherical reservoir bulb. The silicon oil was calibrated over the operating range of 19-31 deg C (Figure 3.4) by measuring the drainage times over a series of trials. The weight of 20 mL oil samples was measured on a Mettler Toledo precision balance to compute the density. The density and the kinematic viscosity at each temperature was used to obtain the dynamic viscosity μ, an important input in Equation 3.5.

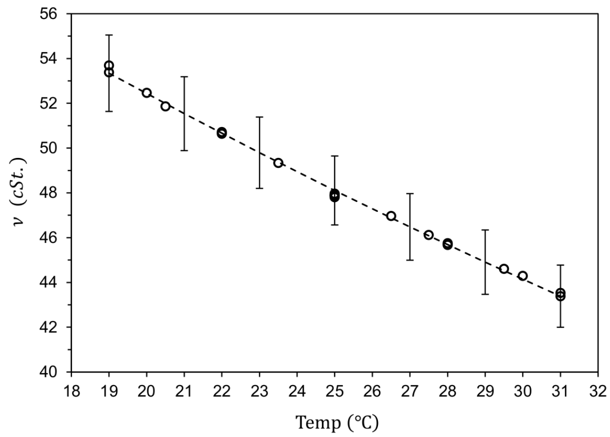

Figure 3.4: Kinematic viscosity versus temperature calibration curve for 50 cSt. silicon oil performed with a capillary viscometer in a temperature controlled bath.

3.5 Jet Flow Field Measurements

Two-dimensional particle image velocimetry (PIV) was performed to capture the flow field between the jet and the impingement plate for H/W = 8 and Re_{jet} = 11000, 20000, 30000, 40000. The purpose of measuring the flow field is to assess the jet flow behaviour and the jet exit conditions of our current experimental setup. To be very clear, the flow field measurements cannot be used to determine the skin friction on the impingement plate due to the poor spatial resolution in the boundary layer (discussed in the introduction), and the near wall inadequacies of PIV. The velocity field in the vicinity of the impingement plate is subject to higher error due to plate reflection and seeding buildup at that location. To accommodate for this, the flow field is slightly cropped ($\approx 1\ mm$) using the PIV mask at the plate surface. The origin of the z coordinate will be placed at the nozzle exit for the flow field measurements.

3.5.1 Measuring Equipment

The PIV system is composed of a $532\ nm$ New Wave Solo 120XT pulsed Nd:YAG laser, an Edmund's $45°$ high power laser mirror mounted on a custom made light-arm, a single TSI Powerview 4MP CCD camera with a 12 bit dynamic range, a Nikon AF Nikkor 50 mm lens, and a Edmund's $532\ nm$ bandpass filter. The $45°$ laser mirror allows us to view the flow in vertical planes, so that the laser can remain horizontal due to the limitations of its internal cooling system. The jet flow was seeded with a bis(2-ethylhexyl) sebacate via a Laskin aerosol generator, which creates a dispersion of particles with a mean diameter of $1\ \mu m$. The PIV velocities were checked against pitot measurements in the potential core using a Fluke 922 micro-manometer with a manufacturers accuracy of $\pm\ 5\ \%$. A schematic of the PIV setup for the impinging planar gas jet is shown in Figure 3.5.

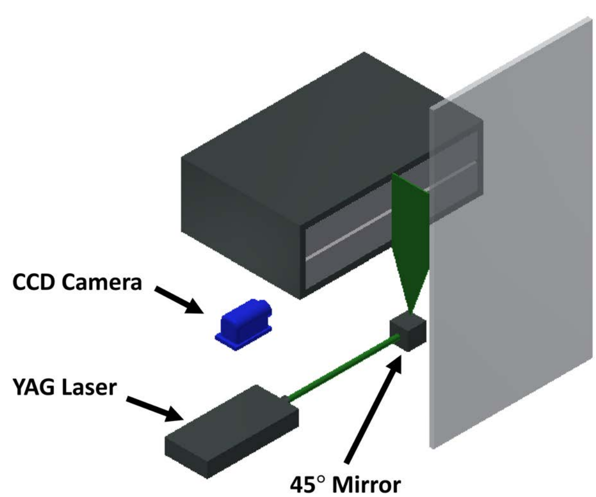

Figure 3.5: PIV setup for capturing flow field.

3.5.2 Jet Flow Field

The flow field of the impinging planar gas jet was captured by ensemble averaging 500 images with 99 percent vector validation rate for each case. Typical time-averaged velocity magnitudes for $Re_{jet} = 11000$ and $Re_{jet} = 40000$ for $H/W = 8$ are shown in Figure 3.6. Both Reynolds number cases indicate a potential core length of approximately $5 - 6$ nozzle widths with comparable spread of the jet column. Reynolds number independence in spread rates is well documented and observed in round free jets [39]. The centerline air velocity u_c remains constant throughout the potential core, followed by a rapid reduction in the impingement zone as the plate redirects the fluid motion. Equation 3.9 is an approximate centerline decay function used by Beltaos and Rajaratnam [5] for planar impinging jets in the impingement zone ($0.75 < z/H < 1$) near the plate:

$$\frac{u_c}{U_{jet}}\sqrt{\frac{H}{W}} = 5.5 \cdot \sqrt{1 - \frac{z}{H}} \tag{3.9}$$

The PIV data for Re_{jet} = 11000, 20000, 30000, 40000 and H/W = 8 in the impingement zone are plotted in Figure 3.7 and agrees well with Equation 3.9 given by the dashed line. For larger impingement ratios ($H/W > 20$), the velocity profiles are known to become self-similar and collapse in the intermediate z/H regions [27].

The time-averaged turbulence intensities in both the axial $\sqrt{\overline{u'u'}}/U_{jet}$ and transverse $\sqrt{\overline{v'v'}}/U_{jet}$ directions for Re_{jet} = 11000 and Re_{jet} = 40000 are shown in Figure 3.8 and 3.9 respectively. For both cases, the air exits the jet nozzle with velocity fluctuations that are primarily in the axial direction due to the jet nozzle contraction. Further downstream the axial and transverse turbulence intensities

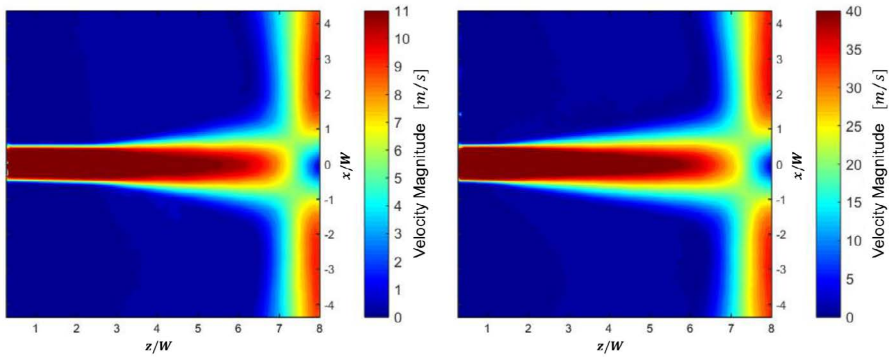

Figure 3.6: Particle image velocimetry of the velocity magnitude for $Re_{jet} = 11000$ $H/W = 8$ (left) and $Re_{jet} = 40000$ $H/W = 8$ (right).

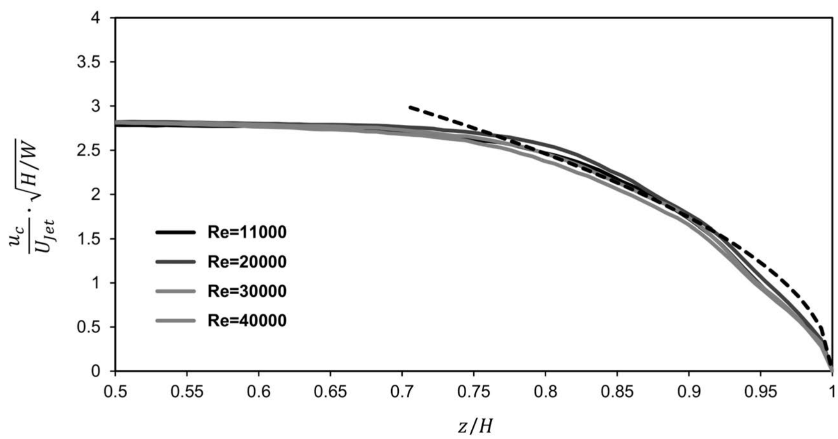

Figure 3.7: Centerline velocity decay for Re_{jet} = 11000, 20000, 30000, 40000 and $H/W = 8$. The dashed line represents Equation 3.9 developed by Beltaos and Rajaratnam [5].

grow rapidly at the turbulent transition location. The initial jet transition location can clearly be seen in Figure 3.8 at $z/W \approx 2.5$, where the turbulence intensity in the shear layers suddenly expand in the transverse direction. Figures 3.10 and 3.11 represent the maximum axial and transverse turbulence intensities within the jet column region ($-1.5 < x/W < 1.5$) as a function of the downstream z direction. For Re_{jet} = 20000, 30000, and 40000, the axial turbulence intensities start increasing rapidly at the transition location, and then saturate at $\sqrt{\overline{u'u'}}/U_{jet} \approx 17$ $\%$. Zhe and Modi [16] and Dogruoz et al. [34] reported turbulence intensities of ≈ 17.5 $\%$ at 5.4 slot widths, and ≈ 15.5 $\%$ at 8 slot widths from their jet nozzles, respectively. For downstream distances $z/H > 0.9$, the axial velocity fluctuations experience a maximum $\sqrt{\overline{u'u'}}/U_{jet} \approx 19$ $\%$ and then rapidly decrease in the vicinity of the impingement plate. A maximum peak in the axial velocity fluctuations within one nozzle distance from the plate was also observed by Maurel and Solliec [27] in plane jets (values not given) and Hammad and Milanovic [28] in round liquid jets ($\sqrt{\overline{u'u'}}/U_{jet} \approx$ upwards of 16 $\%$ from their flood plots for Re_{jet} = 15895 and H/W = 8). Figures 3.10 and 3.11 also show that the transition location migrates closer to the jet exit as the jet Reynolds number is increased. The turbulent transition location is known to change with initial conditions in round jets [40], where the fully developed turbulent case has immediate transition outside the nozzle exit. The transverse turbulence intensities for Re_{jet} = 20000, 30000, 40000 also start increasing after the transition point, reaching $\sqrt{\overline{v'v'}}/U_{jet} \approx 14-18$ $\%$, and then slightly decreasing over the impingement length shown in Figure 3.11. Increasing the jet Reynolds number appears to increase the transverse fluctuating velocities, but lower the overall transverse turbulence intensity levels. These changes in fluctuating velocities relative to the jet exit velocities may be attributed to the ongoing development of the jet.

For Re_{jet} = 11000 we observe much higher turbulence intensities (but lower fluctuating velocities), with the transverse fluctuating component outweighing the axial fluctuating component in some downstream locations. This may be due to organized Kelvin Helmholtz vortex structures migrating down the shear layers, causing apparent flapping of the jet column. Instantaneous smoke visualizations done

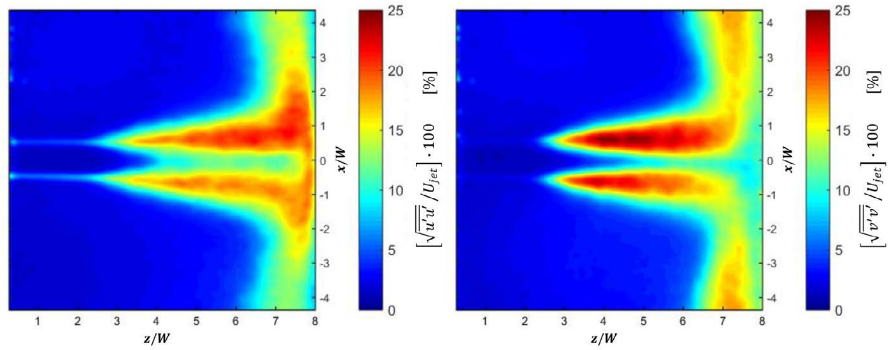

Figure 3.8: Particle image velocimetry of the axial turbulence intensities (left) and transverse turbulence intensities (right) for $Re_{jet} = 11000$ and $H/W = 8$.

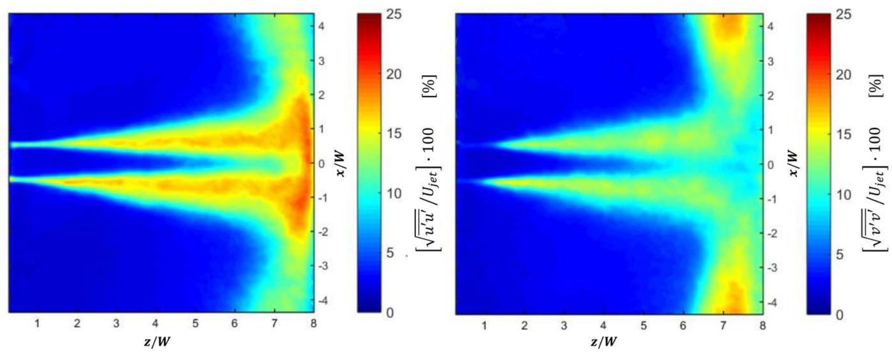

Figure 3.9: Particle image velocimetry of the axial turbulence intensities (left) and transverse turbulence intensities (right) for $Re_{jet} = 40000$ and $H/W = 8$.

at Re_{jet} = 11000 and Re_{jet} = 20000 reveal some evidence of this shown in Figure 3.12. At low flow velocities, the unsteady flow coherence is more preserved over longer downstream distances allowing the vortical structures to grow to higher intensity levels before being dissipated into small scale turbulence. At high velocities, however, the coherence of flow structures breakdown sooner into broadband turbulence. The smoke visualization image for the Re_{jet} = 20000 case (right of Figure 3.12) shows breakup of the these organized structures, more turbulence, and smaller length scales typical of higher velocity air jets.

The maximum axial and transverse turbulence intensities in the vicinity of the

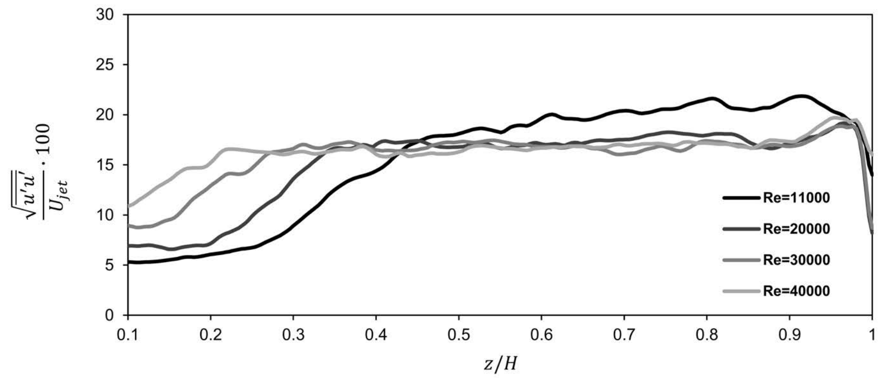

Figure 3.10: The maximum axial turbulence intensity in the jet column region ($-1.5 < x/W < 1.5$) as a function of downstream distance for $Re_{jet} = 11000$, 20000, 30000, 40000 and $H/W = 8$.

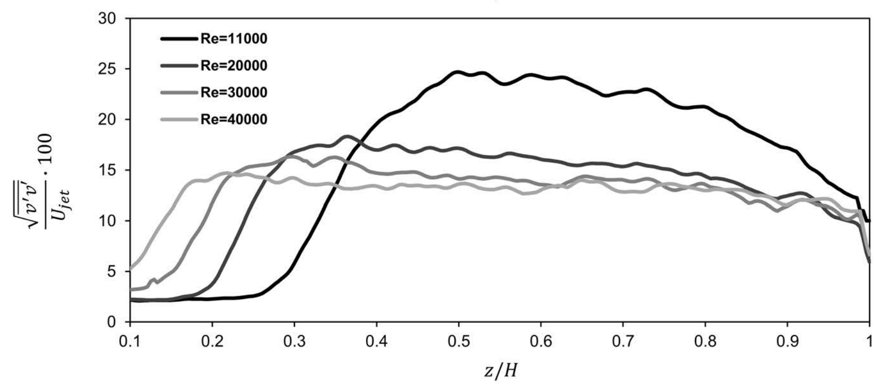

Figure 3.11: The maximum transverse turbulence intensity in the jet column region ($-1.5 < x/W < 1.5$) as a function of downstream distance for $Re_{jet} = 11000$, 20000, 30000, 40000 and $H/W = 8$.

wall ($7 < z/W < 8$) are displayed as a function of cross-stream flow direction in Figures 3.13 and 3.14. As the flow is directed through the stagnation zone and along the impingement plate, the maximum axial fluctuations begin to subside due to impingement plate damping, and the transverse fluctuations become dominant, aligning with the flow direction. The same redistribution phenomenon was observed by [28] with axial and radial turbulence intensities in the near-wall region of their

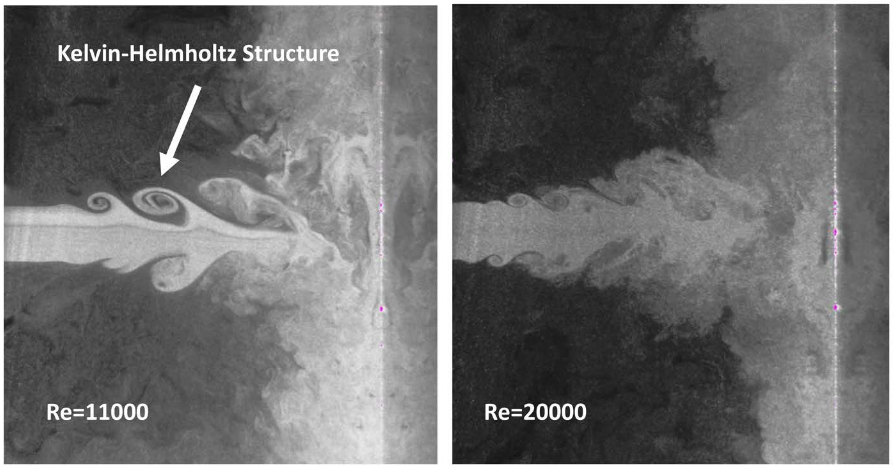

Figure 3.12: Instantaneous smoke visualizations of the planar impinging gas jet for $Re_{jet} = 11000$ (left) and $Re_{jet} = 20000$ (right) for $H/W = 8$. Flow is moving from the left (jet exit) to the right (impingement plate) in each image.

round impinging liquid jet. For each jet Reynolds number case in Figures 3.13 and 3.14, there is a local maxima in the axial and transverse turbulence intensities around $x/W \pm 1$, which also corresponds roughly to the location of maximum impingement plate skin friction; discussed more in Section 3.6.

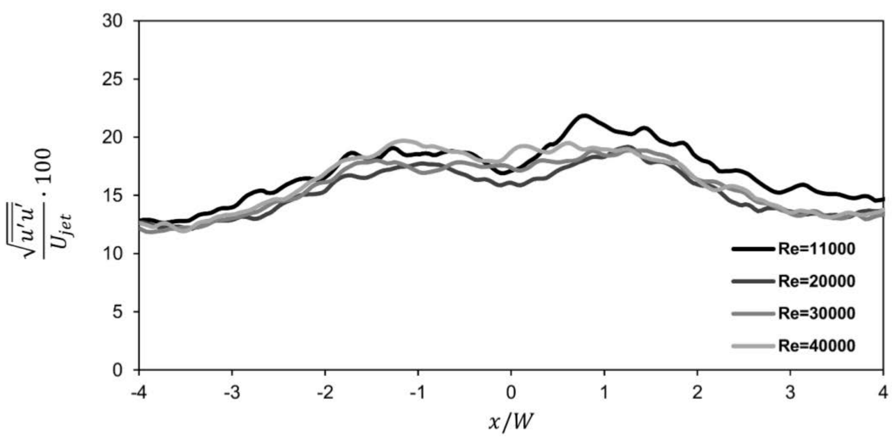

Figure 3.13: The maximum axial turbulence intensity in the impingement plate region ($7 < z/W < 8$) as a function of impingement plate distance for $Re_{jet} = 11000$, 20000, 30000, 40000 and $H/W = 8$.

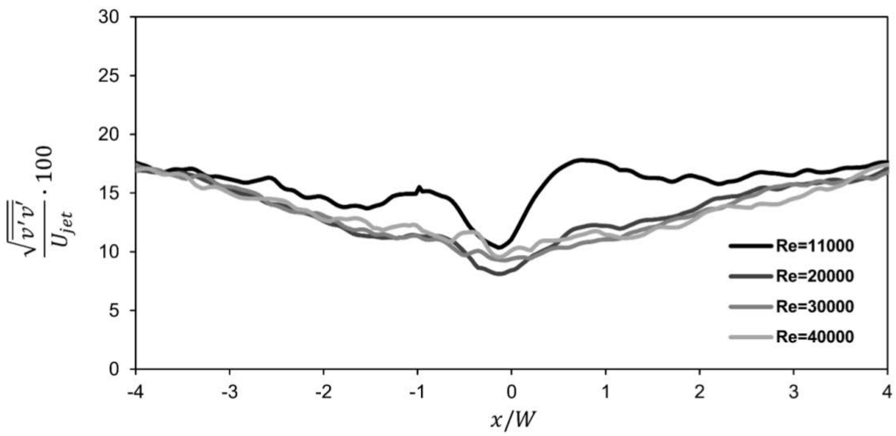

Figure 3.14: The maximum transverse turbulence intensity in the impingement plate region ($7 < z/W < 8$) as a function of impingement plate distance for $Re_{jet} =$ 11000, 20000, 30000, 40000 and $H/W = 8$.

3.5.3 Jet Exit Conditions

The mean velocities and turbulence intensities close to the nozzle exit (z/W = 0.8 or $z/H = 0.1$) are given for the planar impinging gas jet in Figure 3.15. PIV data much closer to the jet nozzle are subject to higher measurement error caused by laser light reflection off of these solid surfaces and lower vector counts, even with image subtraction and post-processing. The axial velocity profiles have a "top-hat" appearance and collapse very well over the entire range of jet Reynolds numbers, shown on the left of Figure 3.15. The velocity profile data in this figure is not differentiated to limit marker clutter, and reveal the curvature of the velocity profile at this location. On the right of Figure 3.15, the turbulence intensity level in the shear layers is increasing with increasing jet Reynolds number, indicating that the jet is not yet fully developed for our current wind-tunnel setup. At one nozzle width away from the jet exit, Hammad and Milanovic [28] and Dogruoz et al. [34] have reported maximum turbulence intensities of ≈ 7 % at Re_{jet} = 15895, and ≈ 5 %

at Re_{jet} = 21500, respectively. The current results show a maximum turbulence intensity of $\approx 5 - 6$ % between Re_{jet} = 11000 and 20000 at the same shear layer location of x/W $\pm$ 0.5. Additionally, turbulence intensities have been known to vary with jet nozzle curvature [41], jet nozzle length [40], and the jet plenum facility itself, due to different numbers of flow conditioning screens, honeycombs, and contraction ratios.

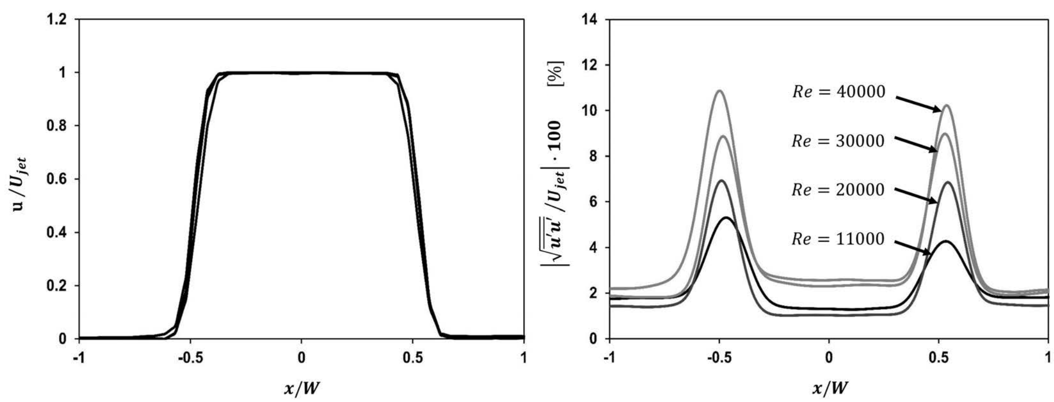

Figure 3.15: Particle image velocimetry of the velocity profiles (left) and axial turbulence intensity levels (right) at the jet exit z/W=0.8 (z/H=0.1) for Re_{jet} = $11000, 20000, 30000, 40000$ and H/W=8.

3.6 Impingement Plate Skin Friction Measurements

3.6.1 Effect of Jet Reynolds Number

Skin friction measurements were made on the impingement plate surface for Re_{jet} = $11000 - 40000$ shown in Figure 3.16. The centered markers along each of the distributions represent the binned averages (bin width x/W = 0.1) of the plotted data. Data points more than two standard deviations from the mean skin friction were labeled as outliers and removed. The average skin friction distributions are found to decrease with jet Reynolds number, which is a characteristic of most drag coefficient plots for bluff bodies. The peaks in the skin friction distributions remain in the same location ($x/W \approx 1$) roughly independent of Reynolds number. This independence is consistent with the investigation of Phares et al. [25], and can be further reasoned from the insignificant changes in the velocity magnitude plots in Figures 3.6 between various Reynolds numbers. Skin friction data points less than $0.25W$ from the stagnation point could not obtained due to the limited resolution of the fringe spacing in this region. The camera can be positioned closer with higher magnification (and smaller field of view) to resolve a few more data points in this region, but the resolution issue is a continuing and asymptotic process, as the wall shear stress approaches zero at the stagnation point. Since the maximum skin friction was of primary interest in this study, these regions of the distributions were omitted. Similarly for $x/W > 4$, the skin friction was measured for only a few cases to ensure the decreasing behaviour of the skin friction distributions along the impingement plate.

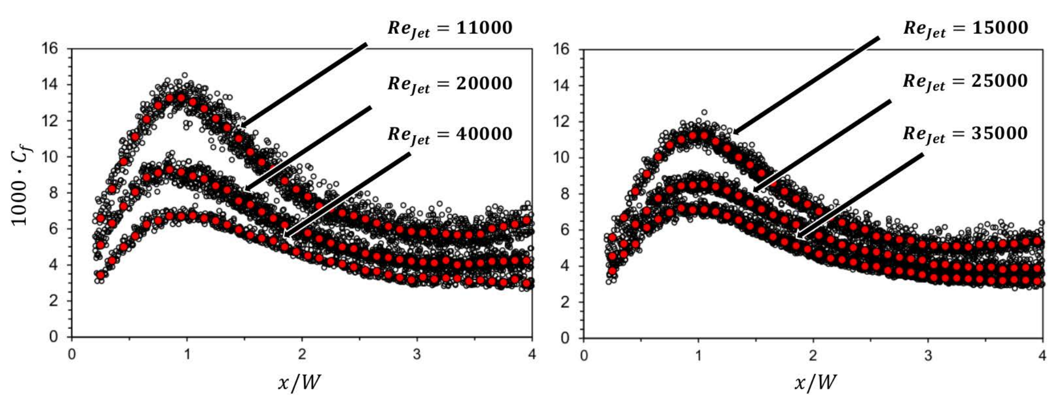

Figure 3.16: Effect of Re_{jet} on skin friction distribution for H/W=4. The centered markers are binned averages of the plotted data.

3.6.2 Effect of Impingement Ratio

The impingement ratio of the jet was varied in this study from $H/W = 4 - 10$ for each jet Reynolds number and the skin friction results for $Re_{jet} = 11000$ are presented in Figure 3.17. As the impingement ratio is increased beyond the jet potential core ($H/W > 6$), there is a reduction in the peaks of the skin friction distributions, which is attributed to jet velocity decay caused by entrainment. The jet spread with increasing impingement ratio also causes the peaks of the distribution to migrate away from the stagnation point as seen in Figure 3.17. The migration distance is small ($x/W \approx 0.5$) in Figure 3.17 between distributions $H/W = 4$ and $H/W = 10$. Phares et al. [25] suggests the location of the maximum skin friction for a fully developed jet is $x/W = 0.96$ for $H/W = 8$, which is within $10\ \%$ of the results shown here. As the impingement ratio is further increased, the skin friction distributions become flatter with less pronounced broader peaks. A smaller secondary peak can also be seen in the skin friction distribution at $x/W \approx 4 - 5$ for the $H/W = 4$ case in Figure 3.17. This secondary peak is thought to be a turbulent transition marker that becomes more pronounced at lower impingement ratios and jet Reynolds numbers [25]. The secondary peak location is similar to the skin friction distributions measured by Zhe and Modi [16] at $x/W \approx 5$ for their lowest impingement ratios ($H/W = 2, 3, 4$).

3.6.3 Maximum Skin Friction

The maximum skin friction values for all the measured OFI results are plotted with jet Reynolds number and impingement ratio in Figure 3.18. The solid curves in

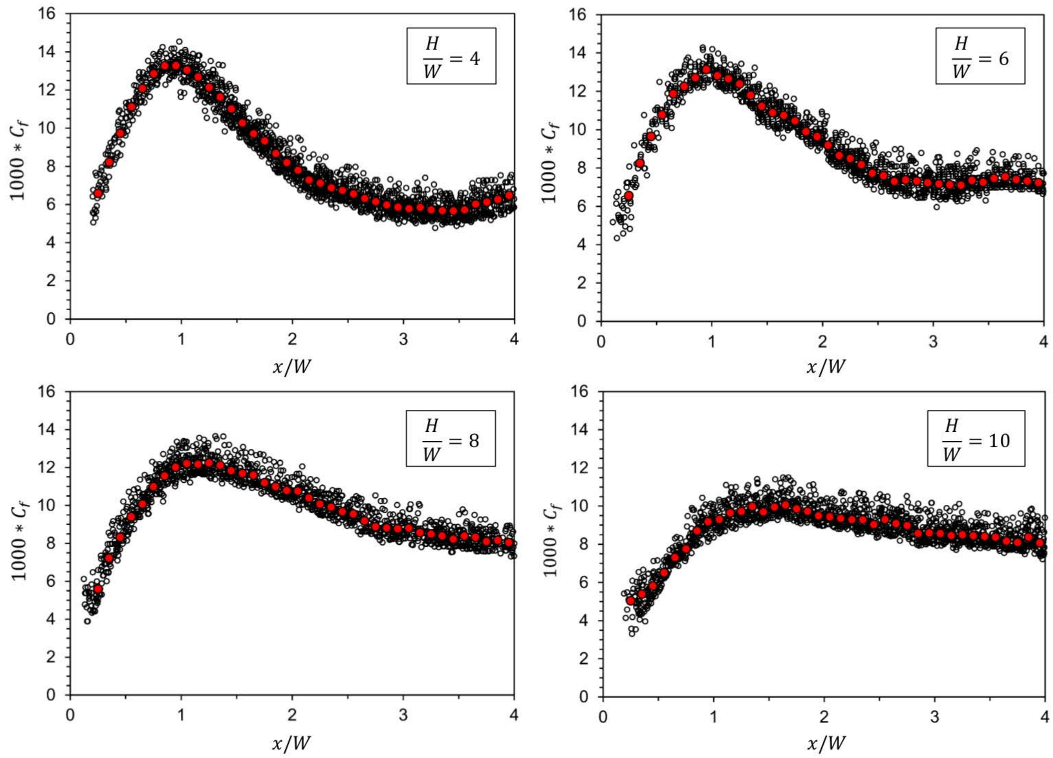

Figure 3.17: Skin friction distributions at Re_{jet} = 11000 for different jet impingement ratios, H/W = 4, H/W = 6, H/W = 8, H/W = 10. The centered markers are binned averages of the skin friction data.

the figure, represent the maximum skin friction predictions of Phares et al. [25] for plane jets, given by Equation 3.4. In Figure 3.18, we have also included some single interferogram low Reynolds number cases (Re_{jet} = 6000 and 8500) to confirm the larger skin friction coefficients at low Reynolds numbers. The maximum skin friction predictions of Phares et al. [25] for plane jets agree within 5 % of the current OFI data for H/W = 6. However, the data remains below the prediction curves for H/W = 4, and above the prediction curves for H/W = 8, and H/W = 10, indicating that the changes in the measured maximum skin friction is not as sensitive to changes in impingement ratio as predicted by Equation 3.4. The OFI experiments indicate that the maximum skin friction (and oil spreading rate) remains fairly constant when the jet standoff distance is roughly within the potential core length of the jet ($H/W \approx 4 - 6$). This result seems reasonable, due to the similar centerline air velocities approaching the plate for these impingement ratios. Zhe and Modi [16] also show minor changes in their measured skin friction for close impingement ratios ($1000{\cdot}C_f \approx 6$ for Re_{jet} = 20000, x/W = 1, H/W = $2 - 5$). As the plate is moved further away from the jet, beyond the potential core length ($H/W > 6$), the maximum skin friction decreases due to velocity decay in the jet column.

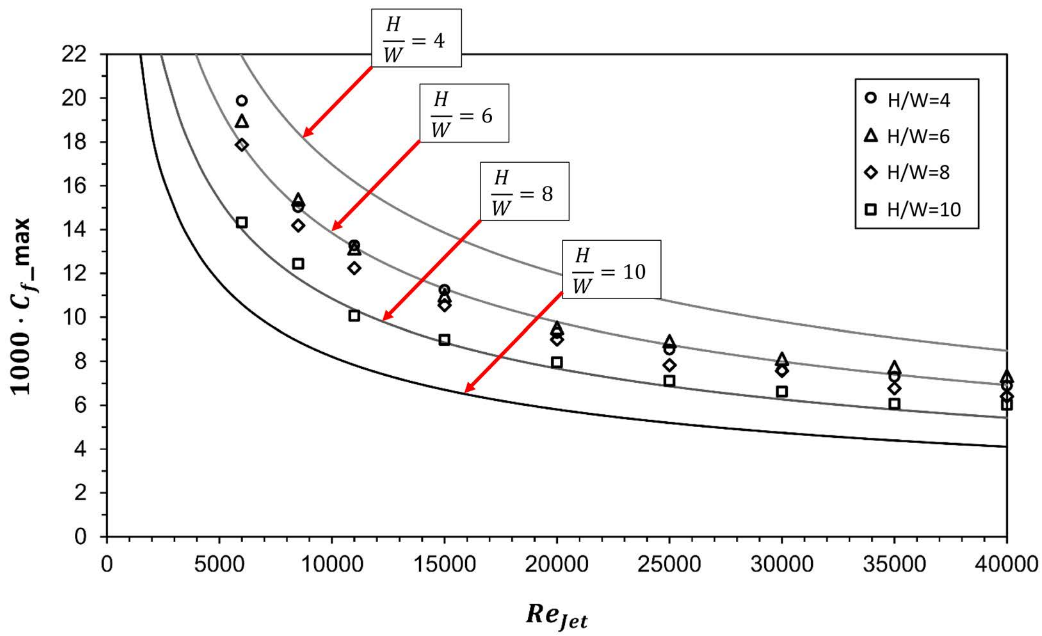

Figure 3.18: The maximum skin friction as a function of jet Reynolds number Re_{jet} for different impingement ratios H/W. The data points are the maximum skin friction values obtained from the current OFI experiments. The solid lines on the plot represent the maximum skin friction predictions of Phares et al. [25] using Equation 3.4 for two-dimensional impinging jets.

Although good agreement was observed for the H/W = 6 case, the maximum skin friction predictions of Phares et al. [25] deviates upwards of 28 % from the data obtained at other impingement ratios. In Figure 3.18, most of the OFI data seems to cluster along a band roughly within the maximum prediction curves of $H/W = 6$ and $H/W = 8$. Large discrepancies in maximum skin friction was also observed in a comparison made by Phares et al. [25], where electro-chemical studies on round impinging liquid jets by Kataoka and Mizushina [42] ($Re_{jet} = 10600 - 36200$, $H/W \geq 8$) and Kataoka et al. [19] ($Re_{jet} = 4000 - 15000$, $H/W = 6$), showed skin friction data approximately 20 % lower than the predicted maximum skin friction values. The deviations in the prediction models may be attributed to the jet turbulence statistics playing a role in impingement plate skin friction generation, or the laminar boundary layer assumption not holding under all jet Reynolds numbers and impingement ratios. We have also yet to establish the effect of Mach number on these maximum skin friction values, due to our current OFI experiments being in the lower Mach number range ($Ma = 0.03 - 0.1$). Despite these discrepancies, the changes in maximum skin friction data with jet Reynolds number follow the same decreasing trends as the prediction curves (scaling with $Re^{-1/2}$), where the maximum skin friction approaches a relatively constant value at higher jet Reynolds numbers, given a certain impingement ratio. This is analogous to the friction factors obtained from a Moody diagram for pipe flow given a certain pipe roughness. The maximum skin friction prediction values also seem to have agreed within 10 % for compressible, fully-developed, round impinging gas jet experiments [35], as well as trends in shear stress thresholds observed in gas jet particle removal experiments [25].

Maximum skin friction variability can also be attributed to certain indirect skin friction measurement devices implemented in the planar gas jet literature. The maximum skin friction obtained by Tu and Wood [6] (Re_{jet} = 6300, H/W = 20.6) and Guo and Wood [7] (Re_{jet} = 88850, H/W = 4) using Preston tubes and Stanton gauges is 14 % and 21 % lower, respectively, than the predicted maximum skin friction value of Phares et al. [25]. The razor blade technique was used to determine the maximum skin friction produced by a plane impinging air jet (Re_{jet} = 4500, H/W = 8) by Lancanette at al. [2], and their experimental maximum skin friction magnitudes ($1000{\cdot}C_f \approx 10.5$) were 35 % below the predictions of Phares et al. [25]. Lower Stanton gauge measurements were also confirmed by Dogruoz et al. [34] in their study, revealing a 40 % drop in the maximum skin friction between their Stanton gauge measurements and OFI measurements. It was shown in experiments by Tu and Wood [6], and further discussed by Phares et al. [25], that using smaller and smaller Preston tubes or Stanton gauges, increased the measured maximum skin friction as the probe sat lower in the inner-wall regions of the flow. These results indicate that Preston tubes and Stanton gauges are unreliable skin friction meters in stagnating flow due to their dependency on probe size, pressure gradient influences, and calibration technique, which is usually performed in fully developed turbulent flow.

Dogruoz et al. [34] uses OFI on a planar impinging gas jet, and presents a maximum skin friction value $1000{\cdot}C_f \approx 10$ for the single test condition of Re_{jet} = 36000 and H/W = 4. This experimental measurement is 12 % higher than the predicted maximum skin friction value of Phares et al. [25]. However, no oil calibration with temperature was mentioned in their paper, for which we found in our study can induce systematic errors in the skin friction of approximately $1.75\%/^{\circ}C$. Additionally the Mach number was more than two times higher (Ma = 0.25, U_{jet}

$\approx 85\ m/s$) than the current OFI experiments, where the effects of Mach number is yet to be determined. The skin friction measurements in the stagnation region by Zhe and Modi [16] using hot-wire anemometers show values $\approx 37\ \%$ lower than the current OFI results ($1000{\cdot}C_f \approx 6$ for Re_{jet} = 20000, x/W = 1, H/W = $2-5$), however, it is uncertain if the maximum skin friction was resolved due to discrete measurement locations along the impingement plate. Additionally, these probes are subject to major inadequacies mentioned in the introduction.

Computational fluid dynamics for impinging planar jets are known to give mixed results for impingement plate skin friction. Numerical studies using the standard κ-ϵ model with wall functions by Elsaadawy et al. [43] present skin friction results ($1000{\cdot}C_f$ = 2.7, Re_{jet} = 11000, H/W = 8) that are over $70\ \%$ lower for both those predicted by Phares et al. [25] and the current OFI results. The κ-ϵ turbulence model without wall functions implemented by Kweon and Kim [44] show skin friction results ($1000{\cdot}C_f \approx 5.25$, $Re_{jet} \approx$ 23000, H/W = 8) that are approximately 26 $\%$ lower than Phares et al. [25] and 37 $\%$ lower than the current OFI measurements. Studies by Kubacki and Dick [45] used large eddy simulations (LES) with limiters on the turbulent kinetic energy to compute skin friction ($1000{\cdot}C_f \approx 5.75$, Re_{jet} = 20000, H/W = 9.2) approximately $11\ \%$ lower than that of Phares et al. [25], and κ-ω with skin friction results ($1000{\cdot}C_f \approx 9.5$, Re_{jet} = 20000, H/W = 9.2) 47 $\%$ higher than that of Phares et al. [25]. Standard CFD codes with Reynolds averaged Navier-Stokes (RANS) equations and turbulence models (such as κ-ϵ or κ-ω) are typically implemented to solve for the velocity gradients near the impingement plate. The production of turbulent kinetic energy grows quadratically with the large strains (instead of linearly) experienced in stagnating flows due to the Boussinesq approximation in these models [46]. Thus, the turbulent kinetic energy and eddy viscosity is over-predicted, which smooths out the velocity gradients, increases the boundary layer thicknesses, and underestimates the computed skin friction. To circumvent this issue, CFD codes usually resort to implementing unphysical limiters on the turbulent kinetic energy or eddy viscosity, or by simply replacing the near-wall grid with "tuned" wall functions to achieve reasonable results at the impingement plate. Even LES has to model the small scales near the impingement plate with similar ad-hoc schemes, whereas direct numerical simulation (DNS) would be far superior, however, computationally unfeasible for any appreciable Reynolds number.

From this analysis, it is clear that there is a lack of agreement between the current OFI data, the semi-empirical predictions of Phares et al. [25], CFD results, and the limited experimental data found in the literature for planar impinging gas jets. This problem has motivated us to perform the current study, and contribute additional experimental data using OFI, which can be, in our opinion, a more robust and direct technique for measuring skin friction.

3.7 Order of Magnitude Analysis

The complete one-dimensional motion of the thin oil film can be governed by Equation 3.10.

$$\frac{\partial h}{\partial t} + \frac{\partial}{\partial x}\left[\frac{\tau_w h^2}{2\mu} - \frac{h^3}{3\mu}\left(\frac{\partial P}{\partial x} - \frac{\partial}{\partial x}\left(\kappa\frac{\partial^2 h}{\partial x^2}\right) - \rho g_x\right)\right] = 0 \tag{3.10}$$

The terms in the thin film equation can be analyzed by their order of magnitude to determine their corresponding significance in the skin friction computation. A similar derivation and analysis of the thin film equations has been presented in Naughton and Sheplak [24]. This will also help validate the assumptions in neglecting certain terms and allow simplification of the thin film equation in this study. Some important assessments that need to be made are to determine whether the effects of gravity (having the impingement plate vertical) are important, as well as how the motion of the oil film is affected by the presence of a pressure gradient. Pressure gradients are typically much higher under impinging jets compared to other simple flows such as flat plates and wall jets. Taking the highest velocity U_{jet} = $40\ m/s$ for the "worst" case scenario ($Re_{jet} = 40,000$ and H/W = 4), and values of film height at the second fringe $h \approx 532\ nm$, oil dynamic viscosity μ = $0.048\ Pa{\cdot}\, s$, g = $9.81\ m^2/s$, oil density ρ = $960\ kg/m^3$, oil surface tension κ = $0.025\ N/m$, skin friction $1000 \cdot C_f \approx 6.8$, wall shear stress τ_w = $\frac{1}{2}\rho_a C_f U_{jet}^2$ = $6.5\ Pa$, jet stagnation pressure P_{stag} = $\frac{1}{2}\rho_a U_{jet}^2$ = $960\ Pa$, and maximum pressure gradient value ($\frac{\partial P}{\partial x} \approx 58000\ Pa/m$) obtained from a Gaussian distribution that tapers off at $x/W \approx 2$. Plugging these values into Equations 3.11, 3.12, 3.13, and 3.14.

$$\frac{\tau_w h^2}{2\mu} = o\left(10^{-11}\ m^2/s\right) \tag{3.11}$$

$$\frac{h^3}{3\mu}\frac{\partial P}{\partial x} = o\left(10^{-14}\ m^2/s\right) \tag{3.12}$$

$$\frac{h^3}{3\mu}\rho g_x = o\left(10^{-15}\ m^2/s\right) \tag{3.13}$$

$$\frac{h^3}{3\mu}\frac{\partial}{\partial x}\left(\kappa\frac{\partial^2 h}{\partial x^2}\right) = o\left(10^{-19}\ m^2/s\right) \tag{3.14}$$

The corresponding shear term in Equation 3.11 is three orders of magnitude greater than the pressure gradient term in Equation 3.12 for the planar impinging jet case, and thus the pressure gradient is neglected in the study. More insignificantly, the gravitational pull on the thin film, in Equation 3.13 is four orders of magnitude less than the viscous shear and is neglected in this vertical plate study. Surface tension effects are negligible as apparent in Equation 3.14. The thin film equation can be simplified to Equation 3.5 without appreciable loss of accuracy.

3.8 Detailed Uncertainty Analysis on the Wall Shear Stress

The propagation of uncertainties in the wall shear stress was analyzed using the methods described in Coleman and Steele [47] using Equation 3.7 as the data reduction equation. The subscript w will be dropped from τ_w for the wall shear stress in the following analysis. The normally distributed relative random error s_τ in the mean wall shear stress sampling distribution was statistically determined using Equation E.3 with the sample standard deviation σ and the sampling size B of the OFI data.

$$\hat{s}_\tau = \frac{\sigma}{\sqrt{B}} \tag{3.15}$$

Quantifying the random errors in the wall shear stress calculations obviously varied in each experiment depending on average bin size and scatter in the OFI data. However, typically in the maximum skin friction regions, and due to the large sample sizes used the experiments, the relative random error in the mean wall shear stress $s_\tau = \frac{\hat{s}_\tau}{\tau}$ x $100 \approx 2$ %. Assuming the relative systematic error in the wall shear stress b_τ is also normally distributed, the contribution of systematic error was calculated using the Taylor Series Method described in Coleman and Steele [47].

$$b_\tau = \sqrt{\left(\frac{\mu}{\tau}\cdot\frac{\partial\tau}{\partial\mu}\right)^2\cdot(b_\mu)^2 + \left(\frac{\lambda}{\tau}\cdot\frac{\partial\tau}{\partial h}\cdot\frac{\partial h}{\partial\lambda}\right)^2\cdot(b_\lambda)^2} \qquad (3.16)$$

This method uses partial derivatives in Equation 3.16 to evaluate the propagation of errors from the data reduction equation. The data reduction equation in Equation 3.7 has main systematic error contributions by the oil film height h measurements and the oil dynamic viscosity μ measurements. The oil film height measurements can be related to Equation 3.7 by Equation 3.6. The relative systematic error in the wavelength of the light $b_\lambda \approx 1.9$ % was given by the bandpass filter manufacturer and the relative error in the oil viscosity measurements $b_\mu \approx 3.2$ % was calculated using a viscometer relation analysis, similar to Equation 3.16, with the oil calibration data. Evaluating the partial derivatives of Equation 3.7 and substituting into Equation 3.16, we see that for this particular linear data reduction equation, Equation 3.16 can be simplified to Equation 3.17.

$$b_\tau = \sqrt{(b_\mu)^2 + (b_\lambda)^2} \qquad (3.17)$$

Combining the random and systematic components of the error into a total uncertainty δ_τ in Equation 3.18 reveals a total relative uncertainty for the average wall shear stress $\delta_\tau \approx 8\ \%$.

$$\delta_\tau = 2 \cdot \sqrt{(s_\tau)^2 + (b_\tau)^2} \tag{3.18}$$

3.9 Novelty & Contributions

1. Experimental skin friction data is provided for a planar impinging gas jet using OFI. This skin friction measuring technique is known to be more robust than the previous indirect methods commonly employed in the impinging gas jet literature. Additionally, the current OFI study has incorporated oil viscosity calibration, and previous skin friction measurements were performed on simple flat plates placed in parallel flows, to verify skin friction agreement with well-known flat plate skin friction correlations.

2. A parametric map of the maximum skin friction is provided for various jet Reynolds numbers Re_{jet} and impingement ratios H/W. The maximum skin friction is an input parameter to certain coating weight models used in gas-jet wiping for different air-knife operating conditions (velocities and standoff distances). Previous skin friction studies commonly include only a few skin friction distributions.

3. Two component flow field information on the experimental planar impinging gas jet is obtained using PIV. It is common in many jet studies to only include single hot-wire (one component) velocity and turbulence intensity measure-

ments at discrete locations in the jet flow.

3.10 Conclusions

Maximum skin friction factors are implemented in coating weight models to predict final coating weights for different air-knife configurations in gas-jet wiping applications. Accurate skin friction measurements can also be used to validate CFD models on impinging jets due to large errors in turbulence modeling in the near-wall region. In this study, the maximum skin friction factors were measured along the impingement plate using OFI for impingement ratios $H/W = 4, 6, 8, 10$, and jet Reynolds numbers $Re_{jet} = 11000 - 40000$. The oil used in the OFI experiments was additionally calibrated for viscosity at different temperatures. The maximum skin friction predictions of Phares et al. [25] agree within 5 % of the current OFI results for $H/W = 6$, but deviations of upwards of 28 % are found for other impingement ratios. The OFI experiments indicate that the maximum skin friction is less sensitive to changes in the impingement ratio when the jet standoff distance is roughly within the potential core length of the jet, and most of the maximum skin friction data cluster along a band between the prediction curves of $H/W = 6$ and $H/W = 8$. Due to the limited experimental skin friction data in the literature, this work ultimately provides an experimental parametric map for the maximum skin friction produced by a planar impinging gas jet. Future tests will investigate the effect of Mach number on these skin friction measurements, due to compressibility effects experienced on full-scale industrial air-knife assemblies. Additionally, PIV measurements were used to characterize the flow field and jet exit conditions of the experimental setup. The PIV measurements show jet transition locations moving towards the nozzle exit with increasing jet Reynolds number, a fairly level maximum axial turbulence intensity evolution in the downstream direction before reaching a maximum peak upon impingement (with the exception of the Re_{jet} = 11000 case), followed by sudden damping at the plate surface. As the flow is redirected, there is an orthogonal redistribution of the turbulence intensities, and local peaks are observed in both the axial and transverse turbulence intensity distributions at the plate locations of the maximum skin friction.

List of symbols

b	Relative systematic error
C	Celsius
C_f	Skin friction factor $\tau_w/\frac{1}{2}\rho_a U_{jet}^2$
g	Gravitational acceleration
h	Oil film height
H	Jet standoff distance
Ma	Mach number
n	Index of refraction of oil
P_{Stag}	Jet stagnation pressure
Re_{jet}	Jet Reynolds number $U_{jet}W/\nu_a$
s	Relative random error
$\hat{s}$	Absolute random error
t	Time
u	Velocity component in the z-direction
u'	Fluctuating velocity component in the z-direction
U_{jet}	Mean jet exit velocity
v	Velocity component in the x-direction
v'	Fluctuating velocity component in the x-direction
W	Jet nozzle width
x	Flow direction parallel to plate
x'	Distance from leading edge of oil film
z	Plate normal direction
α	Maximum skin friction constant
δ	Total combined relative uncertainty
θ	Incident angle of light
κ	Surface tension of oil
λ	Wavelength of light
μ	Dynamic viscosity of oil
ν	Kinematic viscosity of oil
ρ	Density of oil
σ	Sample standard deviation
τ	Shear stress
ϕ	Phase difference
ψ	Angle of oil film from jet stagnation line

Subscripts

$0, 1$	Numbering of time steps
a	Based on properties of air
c	Measured at jet centerline
i	Spatial increment in flow direction
max	Maximum
w	Wall conditions
λ	Related to wavelength of light
μ	Related to dynamic viscosity
τ	Related to shear stress

References

[1] Ellen, C., and Tu, C., 1984. "An analysis of jet stripping of liquid coatings". *Journal of fluids engineering,* **106**(4), pp. 399–404.

[2] Lacanette, D., Gosset, A., Vincent, S., Buchlin, J.-M., and Arquis, É., 2006. "Macroscopic analysis of gas-jet wiping: Numerical simulation and experimental approach". *Physics of Fluids,* **18**(4), p. 042103.

[3] Rajaratnam, N., 1976. *Turbulent jets*. Elsevier.

[4] Abramovich, G. N., Girshovich, T., Krasheninnikov, S. I., Sekundov, A., and Smirnova, I., 1984. "The theory of turbulent jets". *Moscow Izdatel Nauka,* **1**.

[5] Beltaos, S., and Rajaratnam, N., 1973. "Plane turbulent impinging jets". *Journal of Hydraulic Research,* **11**(1), pp. 29–59.

[6] Tu, C., and Wood, D., 1996. "Wall pressure and shear stress measurements beneath an impinging jet". *Experimental thermal and fluid science,* **13**(4), pp. 364–373.

[7] Guo, Y., and Wood, D., 2002. "Measurements in the vicinity of a stagnation point". *Experimental thermal and fluid science,* **25**(8), pp. 605–614.

[8] Patel, V., 1965. "Calibration of the preston tube and limitations on its use in pressure gradients". *Journal of Fluid Mechanics,* **23**(01), pp. 185–208.

[9] Baines, W., and Keffer, J., 1976. "Shear stress and heat transfer at a stagnation point". *International Journal of Heat and Mass Transfer,* **19**(1), pp. 21–26.

[10] Rudolph, I., Reyer, M., and Nitsche, W., 2009. "Infrared-based visualization of wall shear stress distributions". In *Imaging Measurement Methods for Flow Analysis*. Springer, pp. 237–246.

[11] Gardon, R., and Akfirat, J. C., 1966. "Heat transfer characteristics of impinging two-dimensional air jets". *Journal of Heat Transfer,* **88**(1), pp. 101–107.

[12] Tay, C., Khoo, B., and Chew, Y., 2012. "Determination of hot-wire position from a solid wall in an opaque channel". *Measurement Science and Technology,* **23**(8), p. 085305.

[13] Guellouz, M., and Tavoularis, S., 1995. "A simple pendulum technique for the calibration of hot-wire anemometers over low-velocity ranges". *Experiments in fluids,* **18**(3), pp. 199–203.

[14] Shi, J.-M., Breuer, M., Durst, F., and Schafer, M., 2003. "An improved numerical study of the wall effect on hot-wire measurements". *Journal of heat transfer,* **125**(4), pp. 595–603.

[15] Krishnamoorthy, L., Wood, D., Antonia, R., and Chambers, A., 1985. "Effect of wire diameter and overheat ratio near a conducting wall". *Experiments in fluids,* **3**(3), pp. 121–127.

[16] Zhe, J., and Modi, V., 2001. "Near wall measurements for a turbulent impinging slot jet (data bank contribution)". *Journal of fluids engineering,* **123**(1), pp. 112–120.

[17] New, T., and Long, J., 2015. "Dynamics of laminar circular jet impingement upon convex cylinders". *Physics of Fluids,* **27**(2), p. 024109.

[18] Long, J., and New, T., 2016. "Vortex dynamics and wall shear stress behaviour associated with an elliptic jet impinging upon a flat plate". *Experiments in Fluids,* **57**(7), pp. 1–18.

[19] Kataoka, K., Kamiyama, Y., Hashimoto, S., and Komai, T., 1982. "Mass transfer between a plane surface and an impinging turbulent jet: the influence of surface-pressure fluctuations". *Journal of fluid Mechanics,* **119**, pp. 91–105.

[20] El Hassan, M., Assoum, H. H., Sobolik, V., Vétel, J., Abed-Meraim, K., Garon, A., and Sakout, A., 2012. "Experimental investigation of the wall shear stress and the vortex dynamics in a circular impinging jet". *Experiments in fluids,* **52**(6), pp. 1475–1489.

[21] El Hassan, M., Assoum, H., Martinuzzi, R., Sobolik, V., Abed-Meraim, K., and Sakout, A., 2013. "Experimental investigation of the wall shear stress in a circular impinging jet". *Physics of Fluids (1994-present),* **25**(7), p. 077101.

[22] Alekseenko, S., and Markovich, D., 1994. "Electrodiffusion diagnostics of wall shear stresses in impinging jets". *Journal of applied electrochemistry,* **24**(7), pp. 626–631.

[23] Smedley, G., Phares, D., and Flagan, R., 1999. "Entrainment of fine particles from surfaces by gas jets impinging at normal incidence". *Experiments in Fluids,* **26**(4), pp. 324–334.

[24] Naughton, J. W., and Sheplak, M., 2002. "Modern developments in shear-stress measurement". *Progress in Aerospace Sciences,* **38**(6), pp. 515–570.

[25] Phares, D. J., Smedley, G. T., and Flagan, R. C., 2000. "The wall shear stress produced by the normal impingement of a jet on a flat surface". *Journal of Fluid Mechanics,* **418**, pp. 351–375.

[26] Phares, D. J., Smedley, G. T., and Flagan, R. C., 2000. "The inviscid impingement of a jet with arbitrary velocity profile". *Physics of Fluids (1994-present),* **12**(8), pp. 2046–2055.

[27] Maurel, S., and Solliec, C., 2001. "A turbulent plane jet impinging nearby and far from a flat plate". *Experiments in Fluids,* **31**(6), pp. 687–696.

[28] Hammad, K. J., and Milanovic, I., 2011. "Flow structure in the near-wall region of a submerged impinging jet". *Journal of Fluids Engineering,* **133**(9), p. 091205.

[29] Squire, L. C., 1961. "The motion of a thin oil sheet under the steady boundary layer on a body". *Journal of Fluid Mechanics,* **11**(02), pp. 161–179.

[30] Tanner, L., and Blows, L., 1976. "A study of the motion of oil films on surfaces in air flow, with application to the measurement of skin friction". *Journal of Physics E: Scientific Instruments,* **9**(3), p. 194.

[31] Schülein, E., 2014. "Optical method for skin-friction measurements on fast-rotating blades". *Experiments in fluids,* **55**(2), pp. 1–10.

[32] Naughton, J., and Hind, M., 2013. "Multi-image oil-film interferometry skin friction measurements". *Measurement Science and Technology,* **24**(12), p. 124003.

[33] Desse, J.-M., 2003. "Oil-film interferometry skin-friction measurement under white light". *AIAA journal,* **41**(12), pp. 2468–2477.

[34] Dogruoz, M. B., Ortega, A., and Westphal, R. V., 2015. "Measurements of skin friction and heat transfer beneath an impinging slot jet". *Experimental Thermal and Fluid Science,* **60**, pp. 213–222.

[35] Young, R. M., Hargather, M., and Settles, G., 2013. "Shear stress and particle removal measurements of a round turbulent air jet impinging normally upon a planar wall". *Journal of Aerosol Science,* **62**, pp. 15–25.

[36] Johansson, T. G., Mehdi, F., Shiri, F., and Naughton, J. W., 2005. "Skin friction measurements using oil film interferometry and laser doppler anemometry". *AIAA Paper,* **4673**, p. 2005.

[37] Davy, C., Alvi, F., and Naughton, J., 2002. "Surface flow measurements of micro-supersonic impinging jets". In Proceedings of the 22nd AIAA Aerodynamic Measurement Technology and Ground Testing Conference, pp. 24–26.

[38] Drake, A., and Kennelly, R. A., 1999. "In-flight skin friction measurements using oil film interferometry". *Journal of aircraft,* **36**(4), pp. 723–725.

[39] Dahm, W. J., and Dimotakis, P. E., 1990. "Mixing at large schmidt number in the self-similar far field of turbulent jets". *Journal of Fluid Mechanics,* **217**, pp. 299–330.

[40] Kozlov, G., Grek, G., Sorokin, A., and Litvinenko, Y. A., 2008. "Influence of initial conditions at the nozzle exit on the structure of round jet". *Thermophysics and Aeromechanics,* **15**(1), p. 55.

[41] Deo, R. C., Nathan, G., and Mi, J., 2007. "The influence of nozzle-exit geometric profile on statistical properties of a turbulent plane jet". *Experimental Thermal and Fluid Science*.

[42] Kataoka, K., and Mizushina, T., 1974. "Local enhancement of the rate of heat-transfer in an impinging round jet by free-stream turbulence". In Heat transfer 1974; Proceedings of the Fifth International Conference, Tokyo, Volume 2, Vol. 2, pp. 305–309.

[43] Elsaadawy, E., Hanumanth, G., Balthazaar, A., McDermid, J., Hrymak, A., and Forbes, J., 2007. "Coating weight model for the continuous hot-dip galvanizing process". *Metallurgical and Materials Transactions B,* **38**(3), pp. 413–424.

[44] Kweon, Y.-H., and Kim, H.-D., 2011. "Study on the wiping gas jet in continuous galvanizing line". *Journal of Thermal Science,* **20**(3), pp. 242–247.

[45] Kubacki, S., and Dick, E., 2010. "Simulation of plane impinging jets with k–ω based hybrid rans/les models". *International Journal of Heat and Fluid Flow,* **31**(5), pp. 862–878.

[46] Durbin, P. A., and Reif, B. P., 2011. *Statistical theory and modeling for turbulent flows*. John Wiley & Sons.

[47] Coleman, H. W., and Steele, W. G., 2009. *Experimentation, validation, and uncertainty analysis for engineers*. John Wiley & Sons.

Chapter 4

Effect of Jet Oscillation on the Maximum Impingement Plate Skin Friction

Complete Citation:

Ritcey, A., McDermid, J.R., and Ziada, S., 2017.“Effect of Jet Oscillation on the Maximum Impingement Plate Skin Friction”. *Journal of Fluids Engineering*, 140(9), p.091201. *doi: 10.1115/1.4039515*

Copyright

Preface

This study determined the effect of jet column oscillation on the maximum skin friction developed on the impingement plate of our air-knife model using oil film interferometry (OFI). Jet column oscillation was achieved by planar synthetic jet forcing at the nozzle exit using different frequencies (f = $36, 70, 100$ Hz corresponding to St_H = $0.39, 0.76, 1.1$, respectively), and forcing amplitudes (1%, 10% of U_{jet}). The forcing frequencies implemented in this study were based off of Strouhal numbers previously found in far-field microphone signals on high-speed self-excited planar impinging gas jets. A maximum mean skin friction reduction, and a maximum mean pressure gradient reduction, was confirmed under all jet forcing conditions compromising the wiping performance of the model air-knife. Phase-locked particle image velocimetry (PIV) was also employed to assess the dynamics of the jet under forcing. All experimental measurements, data analysis, and technical writing was completed by the first author under the supervision of advisors: Dr. McDermid and Dr. Ziada.

Effect of Jet Oscillation on the Maximum Impingement Plate Skin Friction

Adam Ritcey, Joseph McDermid, Samir Ziada

McMaster University
Department of Mechanical Engineering
1280 Main Street West
Hamilton, Ontario L8S 4L7

Abstract

The maximum impingement plate skin friction and flow field is measured for an acoustically-forced planar impinging gas jet using oil film interferometry (OFI) and particle image velocimetry (PIV), respectively. The study is performed at a jet Reynolds number of Re_{jet} = 11000 and an impingement distance H, which is set to eight times the nozzle width W. The planar impinging gas jet is forced at the jet nozzle exit using Strouhal numbers St_H = 0.39, 0.76, and 1.1, which are similar to those associated with the jet-plate tones measured in air-knife wiping experiments. The flow field measurements indicate that the jet column oscillates at the applied forcing frequency, and depending on the forcing frequency, organized vortex structures can be identified in the shear layers that impinge on the plate surface. Both of these jet oscillation features result in a reduction in the time-averaged maximum impingement plate skin friction. This skin friction reduction is attributed to momentum loss at the jet centerline caused by increased levels of fluid entrainment and mixing of the surrounding quiescent fluid.

4.1 Introduction

Air-knives in continuous hot-dip galvanizing are planar impinging gas jets employed to wipe excess molten zinc-aluminum coating material from a vertical moving steel substrate. Process parameters, such as air-knife exit velocity, air-knife standoff distance, and substrate speed are commonly selected to achieve the desired final coating weights. It is well known that planar impinging gas jets can exhibit self-excited oscillations of the jet column under various Mach numbers and impingement ratios. During fluid resonance conditions (Ma > 0.56-0.78 dependent on H/W), strong jet column oscillations have been observed, accompanied by amplified coherent structures propagating down the jet shear layers, and excessive sound pressure levels ($>$ 130 dB) radiating from the impingement region [1]. The jet dynamics under these conditions may play a role in coating non-uniformity, and affect air-knife wiping efficiencies. The goal of the current study is not to reproduce this high-speed self-excited phenomenon, but instead test the effect of planar jet oscillation on the maximum skin friction for a scaled-up, low speed air-knife model. The present study is a first step to provide some insight about the wiping characteristics of high-speed oscillating air-knives in gas-jet wiping operations.

4.2 Literature Review

4.2.1 Non-Dimensional Numbers

The following important non-dimensional numbers will be introduced:

$$Re_{jet} = \frac{U_{jet}W}{\nu_a} \tag{4.1}$$

$$C_f = \frac{\tau_w}{\frac{1}{2}\rho_a U_{jet}^2} \tag{4.2}$$

$$St_\zeta = \frac{f\zeta}{U_{jet}} \tag{4.3}$$

Equations 4.1, 4.2, 5.1 represent the jet Reynolds number, skin friction factor along the impingement plate, and the Strouhal number, respectively. The length scale ζ in the Strouhal number will employ the jet exit momentum thickness θ, nozzle width W, or jet standoff distance H, depending on the instability frequency being discussed.

4.2.2 Self-Excited Impinging Jets $\zeta = H$

Impinging gas jets are known to oscillate at selected frequencies dependent on the flow conditions; primarily Mach number and impingement plate distance. Early investigations of self-excited impinging jets were predominantly on the more popular circular jet geometry [2, 3, 4, 5], and then later in more recent studies on the planar jet geometry [1, 6, 7], due to its application in gas-jet wiping. These jet oscillation frequencies, or jet-plate tones, have also been measured and identified on galvanizing simulators by Arthurs et al. [8].

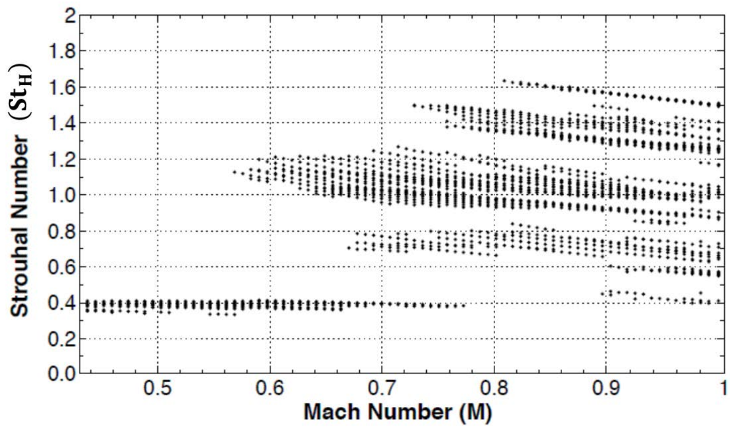

Figure 4.1: The dominant acoustic tone expressed as St_H produced by a self-excited oscillating planar impinging gas jet as a function of Mach number for various impingement ratios (H/W = $2 - 32$). Figure reproduced with permission from Arthurs and Ziada [1].

Fluid Dynamic Regime

Self-excited planar impinging gas jet instabilities can be roughly categorized into two regimes based on the underlying fluid dynamics. For lower Mach numbers ($Ma < 0.56$ for $H/W \approx 8$) on planar impinging gas jets, there is the fluid dynamic regime where the jet column rocks back and forth at the dominant acoustic tone [1]. This jet-plate frequency is broadband in far-field microphone measurements at incompressible Mach numbers, but becomes more tonal in the compressible flow regime. Generally, the microphone spectra also reveal a wide range of lower amplitude subharmonics and superharmonics. Phase-locked PIV measurements, using the dominant acoustic tone as a trigger, show no discernible vortex structures in the flow field at this rocking frequency [1]. The frequencies associated with the fluid dynamic regime are far lower than the jet shear layer mode, and vortex passage frequencies on planar free jets. The presence of the impingement plate not only lowers the dominant oscillation frequency, but also the oscillation frequency decreases with increasing jet to plate distances [6], thus the appropriate scaling in the Strouhal number takes the impingement distance H as the characteristic length. The existing literature shows that the dominant acoustic tone produced in this fluid dynamic regime resides around $St_H \approx 0.4$ across impingement distances H/W = $2 - 32$ for planar impinging gas jets, shown in Figure 4.1. Due to the relatively constant Strouhal number, Arthurs and Ziada [1] also describe this fluid dynamic regime as the "linear regime" because the frequency is an approximate linear function of velocity $f \approx 0.4 \cdot U_{jet}/H$. The fluid dynamic regime is thought to be governed by a Rossiter mode (similar to other impinging shear layer flows, such as cavities, jet-edge, jet-slot systems [9]), where fluid disturbances in the jet impinge downstream at the plate, transmit information upstream (due to the elliptical nature of the Navier-Stokes), and influence the initial conditions at the jet nozzle exit.

Fluid Resonant Regime

As the Mach number is further increased ($Ma > 0.56$ for $H/W \approx 8$), the fluid resonant regime is entered, and the dominant acoustic tone (or one of its harmonics) begins to excite the resonant frequency of the air volume trapped between the jet and the plate surface. This process induces an acoustic standing wave, which couples with the original Rossiter mode, "locking-in" the dominant acoustic tone frequency. The physics of the fluid resonance mechanism can be described in the following manner: Large vortex structures in the jet shear layers impinge downstream on the plate surface, and produce an intense pressure wave that travels back upstream. These pressure waves force the jet nozzle exit at a high amplitude, and low frequency, giving rise to a condition known as collective interaction [4, 10]. The large amplitude, low frequency, forcing present due to the collective interaction mechanism causes many smaller higher frequency vortices (from the shear layer mode) to roll up into one large vortex. An instantaneous image of this collective interaction phenomenon can be seen in a flow visualization study by Kopiev et al. [11]. This synchronization of the upstream and downstream disturbances in the flow field leads to the onset of a global instability, which couples with the acoustic trapped modes between the jet and the plate, thus amplifying the jet response. This strong synchronization of the flow field produces a very tonal noise signal, high sound pressure levels, and a different number of coherent vortex structures between the jet exit and the plate (hydrodynamic modes) during one phase of the oscillation cycle. These different hydrodynamic modes correspond to frequency jumps in the dominant acoustic tone, represented as slightly decreasing Strouhal number bands, shown in Figure 4.1. In Figure 4.2, we show an instantaneous image of a self-excited impinging planar gas jet in the fluid resonant regime (Ma = 0.87 and H/W = 10), exhibiting strong jet column oscillations, and anti-symmetric vortex structures propagating down the impinging shear layers.

4.2.3 Externally-Excited Jet Studies

Disturbances in turbulent shear flow tend to be random in nature and are not often spatially and temporally coherent. One of the most common ways to study jet instabilities is to selectively enhance the development of these natural disturbances using externally forced excitation, which removes the random jitter, and organizes the "hidden" large scale structures in the jet flow. Some of the early studies of

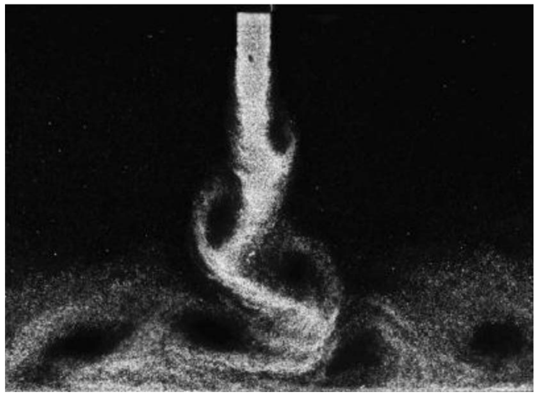

Figure 4.2: An instantaneous image of a self-excited oscillating planar impinging gas jet in the fluid resonant regime Ma = 0.87, H/W = 10, W = 3 mm, $f \approx 9.5$ kHz. Figure reproduced with permission from Arthurs and Ziada [7].

jet sensitivity to sound was investigated by Brown [12], who observed increased jet spread and organization of coherent structures in the jet shear layers. There is a long list of seminal papers, which include studies by Sato [13], Michalke [14], Freymuth [15], Crow and Champagne [16], Hussain and Zaman [17], and many others, that have investigated the shear layer mode instability ($\zeta = \theta$), jet preferred mode ($\zeta = W$ or $\zeta = D$), mode of stable pairing, and these will not be discussed here in detail. Many studies have also incorporated external excitation in their experimental jet facility, either by placing loudspeakers in the jet plenum [16, 17, 18, 19, 20, 21, 22, 23, 24], loudspeakers focused at the jet exit [25, 26, 27], loudspeakers outside the jet shear layer [13, 28, 29, 30], mechanical actuation [31, 32, 33], and most recently by using plasma actuation [34, 35, 36, 37]. The low energy input, high amplitude output, and high bandwidth features of plasma actuators make them ideal for high-speed jet flows. Most of the planar gas jet studies incorporating external forcing are in the free jet configuration.

Hussain and Thompson [18] studied the response of a planar gas jet with acoustic excitation using a loudspeaker inside the jet plenum over a range of jet Reynolds numbers Re_{jet} = $8000 - 31000$. With symmetric acoustic excitation (in-phase disturbance introduced around jet nozzle periphery), the preferred mode in a plane jet was reported at $St_W \approx 0.18$. Despite exciting the jet at this maximum response frequency, the resultant changes in the turbulence levels, centerline velocity decay, and spread rate were reported to be less affected by acoustic excitation than compared to the previously documented excited circular jet [16]. As a result, plane jets were found to have weaker vortex interactions due to line vortices being less energetic, and less spatially coherent, than toroidal vortices in circular jets. Rajagopalan and Ko [21] excited a plane free jet (Re_{jet} = 10000, W = $15\ mm$) inside the jet plenum facility with a loudspeaker at their reported shear layer mode Strouhal number St_θ = 0.012 and preferred mode Strouhal number of St_W = 0.36. They observed a reduction in stream-wise turbulence levels with shear layer mode excitation, and an increase in rms (root mean square) turbulence, and spread rate, with preferred mode excitation. The discrepancy in the reported preferred mode Strouhal numbers between different jet studies is not uncommon. The Strouhal number of the preferred mode in circular jets has been documented to have a wide range of values (St_D = $0.24 - 0.64$) [38], owing to background noise influences, measurement location, and spatial coherence in different-sized jet plenums.

External forcing on planar gas jets can also be applied in a anti-symmetric manner, by focusing loudspeakers out-of-phase at the nozzle exit to enhance the jet flapping motion. Iio et al. [27] focused out-of-phase loudspeakers at the nozzle exit of their planar free jet (Re_{jet} = 6700), and documented an increase in spread rate and large roller structures at a Strouhal number of St_W = 0.15. Their corresponding flow visualization images showed that the jet was less responsive to other excitation Strouhal numbers (St_W = 0.3, 0.55). Using a loudspeaker positioned outside the jet flow, a recent study by Kozlov et al. [39] showed similar jet response characteristics, with large anti-symmetric roller structures in their laminar planar free jet (Re_{jet} = 1700) over a range of excitation Strouhal numbers (St_W = $0.12 - 0.19$). A symmetric arrangement of vortex structures also became apparent under higher excitation Strouhal numbers (St_W = 0.35).

4.2.4 Impingement Plate Skin Friction

Skin friction measurements have been performed on impinging planar gas jets by numerous investigators [40, 41, 42, 43, 44, 45]. It is generally found that Preston and Stanton tube measuring techniques commonly under-predict the maximum skin friction in the stagnation region due to the probe size dependency [41], pressure gradient sensitivity [46], and previous calibration in non-similar flows. Zhe and Modi [42] measured the velocity gradient with hot-wire probes to determine the wall shear stress on the impingement plate of a large scale impinging planar gas jet for Re_{jet} = $10000 - 40000$ and H/W = $2 - 9$. The accuracy of hot-wire measurements are subject to spatial resolution issues with increasing jet Reynolds number (viscous sublayer having comparable length-scale to hot-wire diameter), hot-wire to wall interference, and low velocity calibration issues. Velocity gradient measurements used in conjunction with PIV also have spatial resolution limitations, and are limited to low Reynolds number flows (thicker boundary layers) due to laser light reflection at the impingement surface. Recent studies by New and Long [47] investigated wall shear stress using the velocity gradient PIV data obtained for a laminar circular liquid jet ($U_{jet} = 0.11\ m/s$, $Re_{jet} = 2200$) impinging upon convex cylinders. They found local skin friction reduction with impingement plate surface curvature compared to that of a flat plate. Long and New [48] investigated the wall shear stress produced by a laminar elliptical impinging liquid jet (Re_{jet} = 2100) using the velocity gradient PIV data, and found the instantaneous skin friction increases upon vortex impingement and a reduction observed during vortex separation from the surface. Elastic deformation film-based sensors have also been recently developed [49], however, spatial averaging poses a major problem in non-constant shear stress environments, such as stagnation regions under impinging jets. Wall shear stress measurements appear to have better repeatability (less scatter) in impinging liquid jet studies using the electro-chemical/diffusion technique [50]. This method uses a mass transfer analogy, which relates the measured diffusion current across a surface-mounted anode and cathode, and the mass transfer of ions in the electrolytic fluid, to the wall shear rate at the impingement plate. More recent studies using the electro-chemical/diffusion technique by El Hassan et al. [51, 52] measured wall shear stress on circular impinging liquid jets (Re_{jet} = 1260 and 2450). They determined that the maximum in the time-averaged wall shear stress distribution aligned with the location of primary vortex structure impingement, and the subsequent downstream decrease in the time-averaged wall shear stress coincides with areas of large-scale structure detachment from the wall. They also performed time-resolved flow field measurements, and combined the instantaneous wall shear stress signals with the vortex structure dynamics. El Hassan et al. [52] were able to correlate increases in instantaneous wall shear stress with primary vortex structure impingement, along with instantaneous wall shear stress decreases during vortex ejection/separation events.

Janetzke at al. [32] investigated the qualitative wall shear stress using oil paint removal, and heat transfer on an impinging circular gas jet array (Re_{jet} = 7280, $H/D = 2$), excited with an in-line pulsating actuator (symmetric excitation). For excitation Strouhal numbers around $St_D \approx 0.82$, which corresponds to the jet column mode of stable pairing in circular jets [53], strong toroidal vortices were present in the flow field, along with increased oil paint removal at the impingement plate, and heat transfer enhancements of $20\ \%$. The qualitative oil paint removal results would suggest that an accompanying increase in wall shear stress must be present under these forcing conditions. In a later study, Janetzke et al. [54] also reported an increase in the fluctuating wall shear stress component using surface-mounted hot-wires for their $St_D \approx 0.82$ excitation conditions.

A relevant study by Alekseenko et al. [22] used the electro-chemical/diffusion technique to measure wall shear stress at the impingement surface, with the addition of acoustic modulation in the jet plenum, and different mass fraction of air bubbles introduced in the jet flow. The jet used in the study was a circular impinging liquid jet (Re_{jet} = 6700-46200). The results of this study showed a minor decrease in the time-averaged maximum wall shear stress ($\approx 8\ \%$), and a two-fold increase in the fluctuating wall shear stress, when an acoustic modulation of f = 150 Hz (St_D = 0.59) was applied. Interestingly, increasing the mass fraction of air in the liquid jet flow (without any acoustic modulation) had the opposite, and more drastic, effect of increasing the time-averaged maximum wall shear stress, and reducing the fluctuating wall shear stress. Usually introducing air bubbles near solid surfaces have skin friction reduction capabilities [55], however, the author discusses the complexity of bubble dynamics and its subsequent interaction with fluid turbulence.

In recent years, the number of OFI studies have grown substantially, and OFI has generally been accepted as more of a direct wall shear stress measurement in gas flows. Skin friction measurements on a circular impinging gas jet (Re_{jet} = 33000 and H/W = 16 and 20) using OFI was presented by Young et al. [56]. Using radially spreading concentric fringes on their impingement plate, they resolved the maximum skin friction in the stagnation region for their compressible flow cases ($U_{jet} \approx 136\ m/s$, $Ma \approx 0.4$). Skin friction measurements on a planar impinging gas jet for Re_{jet} = 36000 and H/W = 4 using OFI was presented by Dogruoz et al. [45] using angled oil lines ($\psi \approx 30°$ and $60°$) on their impingement plate. The maximum skin friction on a planar impinging gas jet was analyzed for various jet Reynolds numbers (Re_{jet} = $11000-40000$) and impingement ratios (H/W = $4-10$) using the OFI technique by Ritcey et al. [57]. Other skin friction studies using OFI in the literature involve supersonic impinging microjets [58, 59], skin friction near a cylinder [60], jets in cross-flow [61], wall jet flows [62], channel flows [63], rotating propeller blades [64], and in-flight skin friction measurements on airfoils [65].

4.3 Experimental Setup

4.3.1 Jet Facility

The current experimental planar impinging gas jet is designed at the outlet of an open loop wind-tunnel. A cross-sectional schematic of the facility is illustrated in Figure 4.3. Two converging planar jet nozzle inserts, constructed from aluminum sheet wrapped over laser-cut birch framing, is positioned at the wind-tunnel exit providing an 18:1 contraction ratio. The nozzle profile follows an elliptical contour with a 2.4 major/minor axis ratio. The jet nozzle width at the exit is set to W = 15 mm, and jet exit velocity U_{jet} = 11 m/s, generating a jet Reynolds number of Re_{jet} = 11000. The aspect ratio of the planar jet (jet span L: nozzle width W) is 50:1. A large 122 cm x 61 cm x 12.7 mm smoke-tinted acrylic plate is mounted vertically on an Isel three-axis traverse and positioned in front of the jet, which serves as a stationary impingement plate. A stationary impingement plate is incorporated in this study as a simplification to the gas-jet wiping model, due to the current industrial air-knife gas velocities ($U_{jet} \approx 100$ m/s) typically being much higher than the steel strip velocities ($\approx 1 - 3$ m/s). All skin friction and flow field experiments in this paper utilize a jet stand-off distance of H = 120 mm, or an impingement ratio of H/W = 8. Two laser-cut birch speaker boxes, with rectangular dimensions 60 cm x 26 cm x 9 cm, each house two 8 inch 500 Watt Pyle sub-woofers, and are placed both on the top and bottom of the jet facility. The outlet of each speaker box (form a planar synthetic jet) has a gap spacing of d = 3 mm, and is used to force the jet column with acoustic particle velocity u'' orthogonal to the jet exit flow. The amplitude and frequency of the speakers are controlled using a remotely wired Sony AV multi-channel receiver and a BK frequency generator.

4.3.2 Particle Image Velocimetry (PIV)

The flow field is captured using particle image velocimetry (PIV) with the setup shown in Figure 4.4. The PIV system utilizes a 532 nm New Wave Solo 120XT pulsed Nd:YAG laser, an Edmund's $45°$ high power laser mirror mounted on a custom made light-arm, a TSI Powerview 4MP (2048 x 2048 pixel^2) CCD camera with

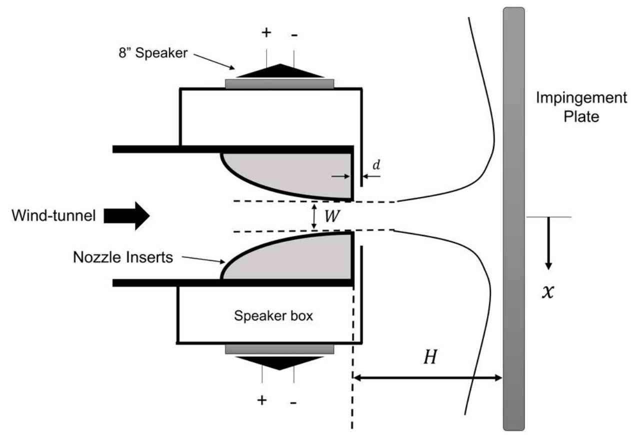

Figure 4.3: Cross-sectional schematic of the experimental planar impinging gas jet facility.

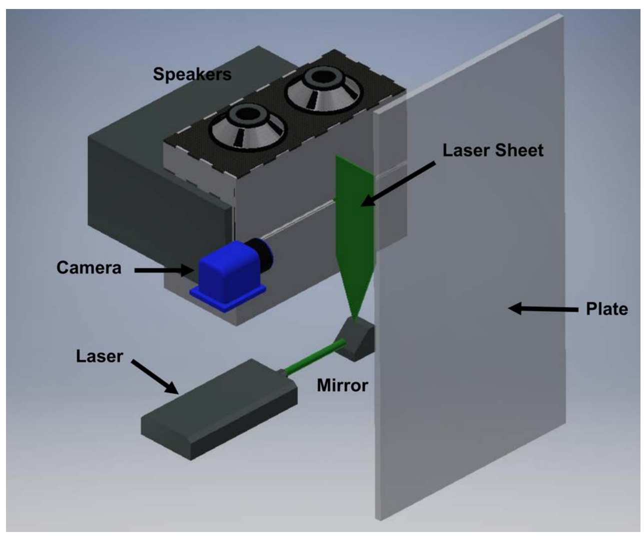

Figure 4.4: PIV setup for capturing planar impinging gas jet flow field.

a 12 bit dynamic range, a Nikon AF Nikkor 50 mm lens, and an Edmund's 532 nm narrow bandpass filter. The $45°$ laser mirror allows for flow measurements in the vertical plane of the jet, so that the laser can remain horizontal due to internal cooling system limitations. A TSI LaserPulse 610035 synchronizer with a custom made trigger was used to obtain phase-locked PIV images of the flow field at eight points in the cycle ($45°$ spacing), using the frequency generator signal as a clock. Image subtraction and vector field processing was performed using TSI InSight 4G software. An interrogation window area of 16 x 16 pixels^2, spatial resolution 11.8 pixels/mm, and a laser pulse time delay of Δt = 23 μs was set during the measurements, which allowed flow particles to travel ≈ 25 % of the interrogation window during consecutive laser pulses. The jet flow was seeded with a bis(2-ethylhexyl) sebacate via a Laskin aerosol generator, which creates a dispersion of spherical particles with a mean diameter of d_p = 1 μm. These seeding particles are small enough for sufficient spatial tracking, and large enough to scatter light with a high signal-to-noise ratio. For high density ratio turbulent flow (ρ_p/ρ_a = 760), with particle Reynolds number Re_p = $U_{jet}d_p/\nu_a$ = 0.73, Stokes number S_k = $d_p\sqrt{2\pi/\tau_k\nu_a}$ = 0.07, and maximum frequency based on the Kolmogorov timescales $1/\tau_k$ = 13 kHz, a fluctuating velocity error $|\sqrt{u_p'^2} - \sqrt{u_a'^2}|/\sqrt{u_a'^2}$ x 100 of ≈ 2.9 % can be estimated [66]. Displacement gradient methods of Scarano and Riethmuller [67] were also used at downstream location z/W = 4 to estimate the relative mean $\overline{u}$-velocity error, which was calculated to be $\delta_{\overline{u}} < 1\%$. Low errors in the velocity measurements is expected due to the ample spatial resolution of the jet flow-field.

4.3.3 Oil Film Interferometry (OFI)

Basic Description

Skin friction distributions were obtained on the impingement plate surface using oil film interferometry (OFI). This method uses the height changes of a thinning oil film to determine the applied wall shear stress. Equation 4.4 is the simplified one-dimensional governing equation of the motion of a thin oil film:

$$\frac{\partial h}{\partial t} + \frac{\partial}{\partial x}\left[\frac{\tau_w h^2}{2\mu}\right] = 0 \tag{4.4}$$

where h is the height of the oil film, μ is the dynamic viscosity of the oil, and τ_W is the applied wall shear stress from the external flow. A complete derivation of the thin oil film equation is given by Naughton and Sheplak [68]. The OFI procedure operates as follows: 1) An oil with known viscosity and index of refraction (μ, n) is placed on a solid surface and exposed to a gas flow. 2) The oil is illuminated by a light source, and the oil surface is recorded with a camera positioned at an angle θ_i shown in Figure 4.5 b). As the oil thins, it forms an approximate wedge shape, and a fraction of the incident light will reflect off the oil surface and reach the camera, while a fraction of the light will also transmit through the oil, and reflect off the solid surface below. When these two different light rays meet back up at the camera, a varying phase relationship exists between them. The local phase difference in the light rays is dependent on the local oil height. Regions of constructive and destructive interference of the light rays can be discerned as bright and dark fringes along the oil surface. If one wavelength of light is isolated using a narrow bandpass filter in front of the camera (in this case $\lambda \approx 532 \pm 10\ nm$), or with a monochromatic light source, then a unique interference pattern can be captured. These unique images are called interferograms (shown in Figure 4.5 a)). The spatial change in the oil height h can now be related to the phase difference ϕ in the interferogram using Equation 4.5:

$$h = \frac{\lambda\phi}{4\pi}\left(\frac{1}{\sqrt{n^2 - n_a^2 sin^2\theta_i}}\right) \tag{4.5}$$

where λ is the wavelength of light, θ_i is the incident angle of light from the plate normal direction, and n and n_a is the index of refraction of the oil and air, respectively. Knowing the evolution of the oil height (using Equation 4.5) and its viscosity μ, Equation 4.4 can be solved using different approaches. For skin friction distributions that exhibit local maximas and minimas, increases and decreases in the oil height cannot be differentiated from consecutive fringe spaces without the use of white light OFI [69]. White light OFI uses the spectral colour distribution of the fringes to determine the direction of oil height changes. Since large gradients in the skin friction distribution are present in the stagnation region of a planar impinging gas jet, the current study can resolve these features using standard OFI and the angled oil line technique [45, 57]. The angled oil line technique implements a constant wall shear stress solution (for small downstream x distances) and attempts to reconstruct the skin friction distribution from every oil leading edge location across the two-dimensional jet flow. The constant wall shear stress solution is given by Equation 4.6:

$$\tau_w = \frac{\mu x'}{ht} \tag{4.6}$$

where h represents the height of the oil film measured at a distance x' from the oil leading edge at time t. Equation 4.6 can be derived by solving Equation 4.4 using separation of variables and the Riccati equation, along with assuming constant wall shear stress for small x' distances, and the initial condition: h = ∞ at t

= 0. With this technique, the entire wall shear stress distribution can be obtained using a single interferogram. Single image or single interferogram methods have shown to agree with the more rigorous in-situ multi-image methods for wind-tunnel flows [70]. The effects of forcing on Equation 4.4 and 4.6 should also be assessed. The smallest introduced perturbation wavelength on the oil surface due to the disturbances traveling in the jet flow ($\lambda_d \approx \frac{U_{jet}}{f} \approx \frac{11m/s}{100Hz} \approx 110$ mm) would be much larger than distances we are performing the OFI slope measurements over ($x' <$ 10 mm), and the three-dimensionality of the flow during forcing was found to be negligible away from the edges of the speaker boxes ($\frac{u''}{U_{jet}}$ deviations $> 5\%$ from the centerline measurements for span-wise distances $y{>}0.8L$). All the OFI and PIV measurements were taken in the vicinity of the jet centerline (y = 0).

OFI Setup & Procedure

A 50 cSt Dow Corning silicon oil is used in the OFI measurements, with the oil supplier's data indicating 50 ± 2.5 cSt at a single temperature (25 deg C). The silicon oil was also independently calibrated in the lab to measure the viscosity at different temperatures using an insulated water bath, equipped with a VWR digital temperature controller, and a vertical capillary viscometer. Before each OFI experiment, an angled oil line ($\psi \approx 45°$) is placed over the clean impingement plate, and then mounted vertically on the traverse with the wind-tunnel running to eliminate start-up time. As the air impinges on the plate, the oil is spread symmetrically about the jet stagnation line, where the stagnation line is shown in Figure 4.5 a). Symmetry of the oil line cannot be seen in Figure 4.5 a) because of the perspective distortion, and cropping of the interferogram. Each test duration (one interferogram) required approximately 15 minutes to obtain ideal fringe resolution on the oil surface. To eliminate dust particles, which can contaminate interferograms by producing wakes in the fringes, proper facility cleaning, and filters were installed at the wind-tunnel inlet. During the OFI experiments, the jet exit air temperature was also monitored, and used to approximate the oil temperature on the impingement plate. After each experiment, the impingement plate is immediately taken over to a separate image station, where the camera and lighting is situated and the impingement plate is placed horizontally (schematic shown in Figure 4.5 b)). At the image station, a TSI Powerview 4MP CCD camera with a 12 bit dynamic range, a Nikon AF Nikkor 50 mm lens, and a Edmund's 532 nm narrow bandpass filter is mounted on an angled tripod support stand. The interference pattern is illuminated using Halogen lighting, similar to the OFI study by Pailhas et al. [71], along with an angled white soft-core backdrop to increase light intensity. The camera angle is set using a Wixey digital angle gauge (least count 0.1°). Image space is mapped to pixel space using a direct linear transformation and a calibration grid placed over the impingement plate. This was done after every OFI test to ensure no movement between the interferogram and calibration frames. The interferograms are then processed in MATLAB by taking pixel intensity distributions in the x-direction at every discrete y-direction slice. The bright fringe locations can be isolated in the pixel intensity distributions, and the distances between fringes can be determined. The constant wall shear stress solution in Equation 4.6 was implemented using the distance between the oil leading edge and the second bright fringe at every y-direction slice in each interferogram.

By performing the OFI analysis on the second bright fringe from the oil leading edge location (instead of the first fringe), the relative random error in the wall shear

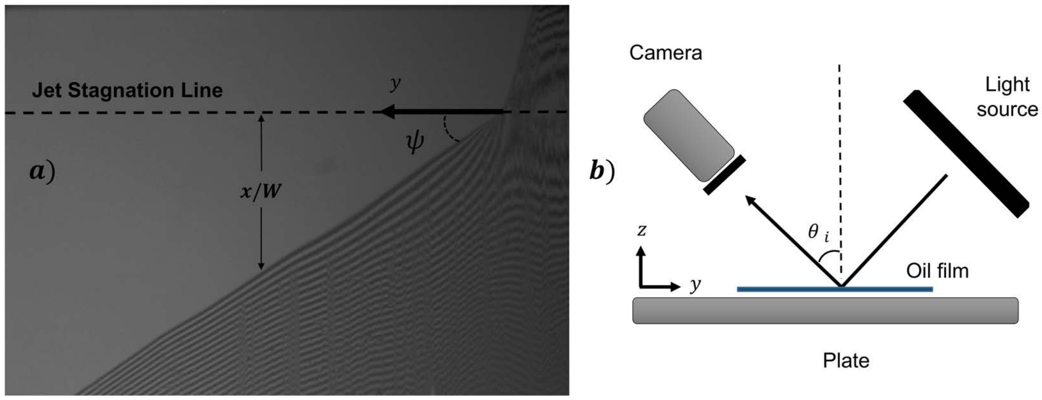

Figure 4.5: a) Interferogram obtained on the impingement plate of a planar impinging gas jet. b) Light and camera setup at image station.

stress measurements can be reduced. This is due to better spatial resolution in the x' distance measurement in Equation 4.6. Additionally, a study by Segalini et al. [72] has shown that is best to avoid fringes in the vicinity of the oil leading edge due to possible pressure field alterations at the viscous stagnation point. However, using fringes downstream from the actual measurement location in this case, comes at the expense of introducing a systematic error in the skin friction distribution due to spatial averaging. As the number of fringes used in the OFI analysis is increased (or the x' distance becomes large), spatial averaging has the effect of systematically decreasing the time-averaged maximum wall shear stress. For the OFI cases performed here, an approximation for the spatial averaging error b_{SA} was assessed using the time-averaged wall shear stress from the first fringe analysis, along with an asymmetric systematic error procedure outlined in Appendix E of Coleman and Steele [73]. Total uncertainties for the maximum wall shear stress using the second bright fringe in the OFI analysis is estimated at $\delta_\tau \approx 9$ %, using Equation 4.7, which is derived using the Taylor Series Method (TSM) [73], and

Equation 4.6 as the data reduction equation. Equation 4.7 shows the final form of the total uncertainty of the mean maximum wall shear stress, which includes the relative random error in the time-averaged maximum wall shear measurements $s_\tau = \frac{\sigma}{\sqrt{B}}/\tau \approx 2\ \%$, the systematic error in the oil viscosity calibration $b_\mu \approx 3.2\ \%$, the systematic error in the wavelength of light (given by the narrow bandpass filter manufacturer) $b_\lambda \approx 1.9\ \%$, and the systematic error due to spatial averaging $b_{SA} \approx 2\ \%$.

$$\delta_\tau = 2 \cdot \sqrt{{s_\tau}^2 + {b_\mu}^2 + {b_\lambda}^2 + {b_{SA}}^2} \tag{4.7}$$

Preliminary OFI experiments were also performed in our facility on simple flat plates in parallel wind-tunnel flows with tripped turbulent boundary layers. Agreement was confirmed between the OFI skin friction measurements and standard turbulent flat plate skin friction relations [74]. Skin friction measurements using the current OFI technique has been investigated on an unexcited planar impinging gas jet by Ritcey et al. [57]. Each OFI test case in the current study consisted of averaging two separate OFI experiments, totaling approximately 1000 data points in each skin friction distribution.

4.4 Experimental Conditions

The forcing frequencies in the current jet study were chosen based on jet-plate tones observed in previous high-speed self-excited jet studies [1, 6, 7, 8], where the experimental conditions are mapped in Figure 4.1. The dominant acoustic tone bands, shown in Figure 4.1, were approximated in this study using excitation Strouhal numbers St_H = 0.39, 0.76, and 1.1. These Strouhal number bands are indicative of different jet hydrodynamic modes at high speeds, where a different number of vortex structures exist between the jet exit and the impingement plate. For the current study at low Mach number, the planar impinging jet exhibits weak self-excited oscillations, therefore, external acoustic excitation is used to enhance/simulate the jet oscillations at the Strouhal numbers observed during high-speed air-knife wiping experiments. Also due to the low jet velocities, it is expected that upstream pressure waves from vortex structure impingement will contribute negligible affects to the synthetic jet forcing in this study. The Strouhal numbers St_H = 0.39, 0.76, and 1.1 correspond to the scaled excitation frequencies of 36 Hz, 70 Hz, and 100 Hz. Since Strouhal numbers are assembled using different length scales across the jet literature, Table 4.1 summarizes the various Strouhal numbers corresponding to the three frequencies used in this study.

Table 4.1: Strouhal numbers based on experimental frequencies.

f (Hz)	36	70	100
St_H	0.39	0.76	1.1
St_W	0.049	0.095	0.14
St_θ	9.2×10^{-4}	0.0018	0.0025

The amplitude levels of the acoustic forcing is measured using a single hot-wire probe positioned at the nozzle edge, and at the outlet of the speaker boxes, indicated by the circular dot in Figure 4.6 d). With the jet flow off (U_{jet} = 0), and with the speaker boxes operating at their respective frequencies, the gain of the receiver is adjusted to obtain the desired level of acoustic forcing from the hot-wire signal. The acoustic particle velocity u'' is defined as the average maximum velocity experienced by the hot-wire, which provides an order of magnitude estimation of the acoustic forcing to the jet column (i.e $\frac{u''}{U_{jet}} \cdot 100 \approx 1\%, 10\%$). Other definitions could have been specified, such as the overall mean, or standard deviation of the hot-wire time signal. The acoustic particle velocity is adjusted to order 1 percent of the jet exit velocity, and the corresponding time signals are shown for each frequency in Figure 4.6 a)-c). One cycle of the speaker diaphragm results in two cycles of the velocity signal from the hot-wire, due to the inability of the hot-wire to measure flow directionality. The hot-wire signal also exhibits a mean velocity component (never exhibits u'' = $0\ m/s$ in the time signal), which is consistent with synthetic jet behaviour [75] due to entrainment caused by vortex shedding at the speaker box outlet. The speaker box outlets were also offset by $3\ mm$ from the jet nozzle edge to ensure that speaker box alignment and surface discontinuities at the exit would not affect experiment repeatability, or interfere with the natural flow separation at the nozzle edge. If the speaker box gap spacing (d = 3 mm) was changed, or the speaker boxes were moved closer or further from the jet nozzle edge, one would expect the acoustic particle velocity, and thus the excitation amplitude to be affected as well. The current study is suited for acoustically forced excitation because the loudspeakers and speaker boxes behave as low pass filters, and thus constant excitation levels can be achieved with amplifier power adjustments for the low frequency range in this study. Excitation at higher frequencies would require much more power to overcome the losses in the speaker-box assembly, and a level of $1\ \%$ forcing for frequencies above 200 Hz was not achievable during testing. High amplitude and high frequency forcing on jets is more feasible by means of plasma excitation [37].

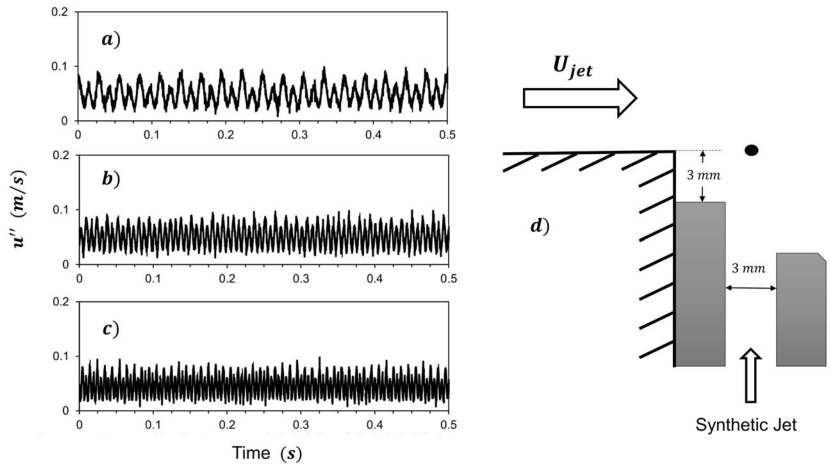

Figure 4.6: Time signals of the acoustic particle velocity measured with a single hot-wire probe at the jet nozzle exit for frequencies a) 36 Hz, b) 70 Hz, and c) 100 Hz. All signals obtained with U_{jet} = 0. Inset d) shows a cross-sectional schematic of speaker box outlet positioned at the jet nozzle edge. The solid dot represents the measurement location of the hot-wire probe.

4.5 PIV Flow Field Measurements

PIV is performed on the impinging jet flow field for Re_{jet} = 11000 and H/W = 8 under different frequencies of excitation: 36 Hz, 70 Hz, and 100 Hz. Each flow field image is an ensemble average of 200 images with 99 percent vector validation rate processed with TSI Insight 4G. The flow field is slightly cropped near the plate surface ($\approx 1\ mm$) due to laser light reflection from the impingement plate, as well as near the jet nozzle exit, due to the protrusion of the speaker boxes. For the flow field measurements, the origin of the z coordinate will be taken from the jet nozzle exit.

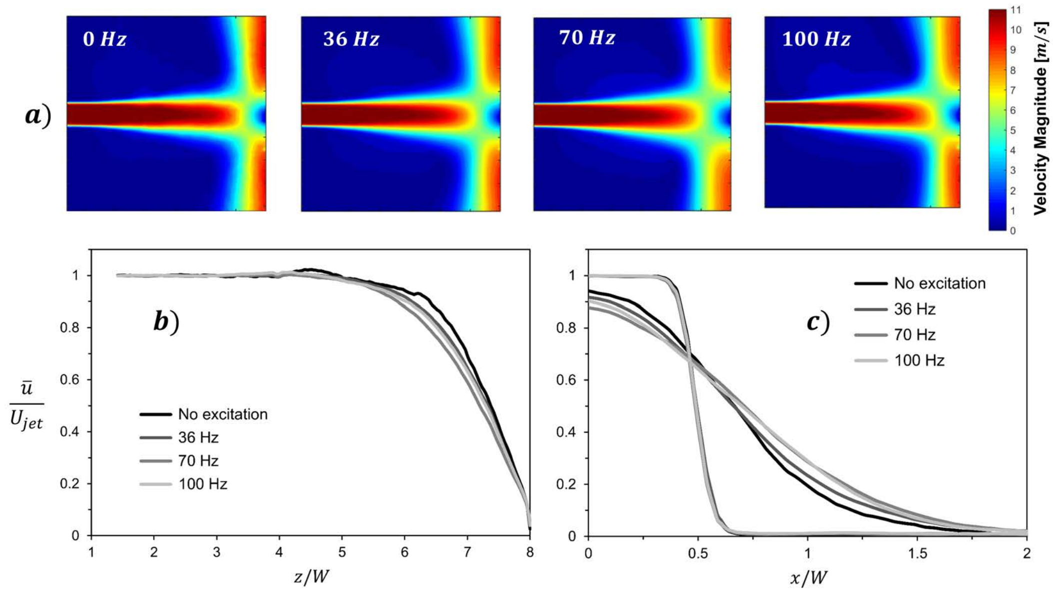

Figure 4.7: a) The velocity magnitude flood plots for the no-excitation, 36 Hz, 70 Hz, and 100 Hz anti-symmetric 1% amplitude cases. b) The centerline $\overline{u}$-component velocity as a function of downstream z/W distance. c) Transverse $\overline{u}$-component velocity profiles at downstream locations z/W = 2 and z/W = 6 for the test cases. The wider profiles measured at the z/W = 6 location.

4.5.1 Velocity Magnitude Fields

The ensemble average of the velocity magnitude for the no excitation (0 Hz), and excited cases (36 Hz, 70 Hz, 100 Hz), are presented in the flood plots in Figure 4.7 a). Due to the low level of anti-symmetric forcing ($\frac{u''}{U_{jet}} \cdot 100 \approx 1$ %), the flood plots appear similar in shape, however, a slight decrease in the impingement plate shear layer velocities can be noted for the excited cases. Upon closer inspection in Figure 4.7 b), the centerline $\overline{u}$-component of the velocity decays faster in the downstream direction for the excited cases, with potential core lengths ≈ 5 nozzle widths. In the acoustically-excited planar free jet study by Hussain and Thompson [18], sharp drops in the centerline velocity occurred at ≈ 5.5 nozzle widths, for both the forced and unforced cases. In Figure 4.7 c), $\overline{u}$-component velocity profiles are shown at downstream locations z/W = 2 and z/W = 6. The wider profiles being at the z/W = 6 location. The $\overline{u}$-component velocity collapses well for all cases at z/W = 2, however, further downstream, the z/W = 6 profiles are slightly lower and wider for the excited cases, verifying faster centerline velocity decay, and larger jet spread. Increases in jet spread were also observed when exciting a planar free jet symmetrically at St_W = 0.36 by Rajagopalan and Ko [21] and anti-symmetrically at St_W = 0.15 by Iio [27].

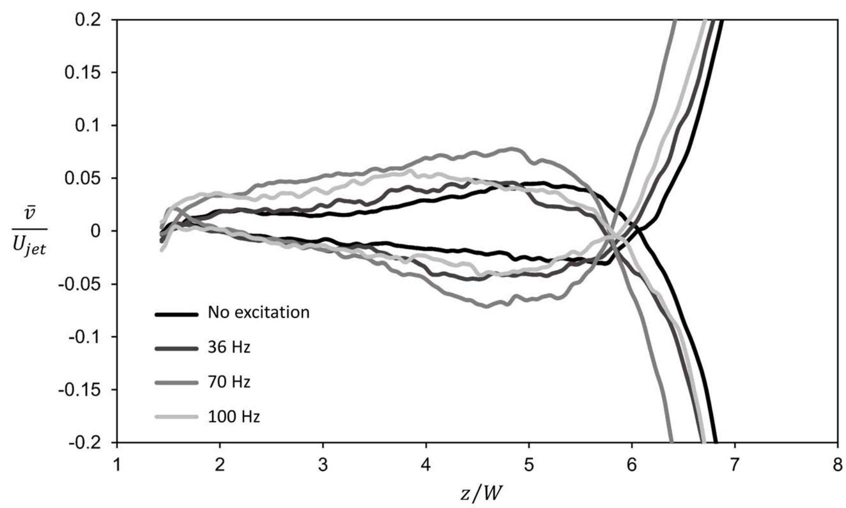

Figure 4.8: The cross-stream $\overline{v}$-component of velocity as a function of downstream z/W distance. The upper curves that sweep downwards in the plot are measured at x/W = -1.5 below the lower jet shear layer, and the lower curves that sweep upwards in the plot are measured at x/W = $+1.5$ above the upper jet shear layer, for the no-excitation, 36 Hz, 70 Hz, and 100 Hz anti-symmetric 1% amplitude cases.

The centerline $\overline{u}$-velocity decay and jet spread is a result of fluid entrainment into the jet column, and we have attempted to quantify the amount of entrainment with the PIV data. The PIV cross-stream velocities ($\overline{v}$-component) at constant x/W $\pm$ 1.5 is plotted as a function of downstream distance z/W in Figure 4.8, for the no excitation, 36 Hz, 70 Hz, and 100 Hz anti-symmetric $1\ \%$ amplitude cases. In Figure 4.8, the upper curves in the plot that sweep downwards near the impingement plate are measured along $x/W = -1.5$ (below the lower jet shear layer), and the lower curves in the plot that sweep upwards near the impingement plate are measured along $x/W = +1.5$ (above the upper jet shear layer). The sign of the $\overline{v}$-component cross-stream velocities indicate that there are regions in the flow where there is an inward mass flux, representing entrainment into the jet column region. To quantify this entrainment, the $\overline{v}$-component cross-stream velocities were numerically integrated from $z/W = 2$ to the downstream location where the cross-stream velocities reach zero ($\overline{v} = 0$), before the flow is redirected in the stagnation region. This operation was performed on the upper and lower cross-stream velocity curves for each test case, added together, and multiplied by a constant density, to obtain the total entrainment rate per unit width. To non-dimensionalize this total entrainment rate for each test case, we divided the result by the total mass flux per unit width from the jet nozzle exit ($\rho_a U_{jet} W$). In Table 4.2, the non-dimensionalized total entrainment rate is expressed as a percentage for each test case. The entrainment rate for the non-excited jet was checked using an entrainment velocity relation from Blevins [76], which was given as $\overline{v}(z) = 0.053 \cdot \overline{u}(z)$, where the $\overline{u}(z)$ is measured at the jet centerline. This entrainment velocity relation was applied to our centerline PIV velocity data for the non-excited jet case. The total entrainment velocity relation from Blevins [76] is only valid for a non-excited fully-developed turbulent planar free jet in the self-similar region, however, despite these differences in our current jet setup, the total entrainment rate obtained using the relation is within 20% of our no excitation case, presented in Table 4.2. The PIV results confirm that there is an increased amount of entrainment during jet forcing conditions, where the maximum entrainment occurs for the 70 Hz case.

Table 4.2: Non-dimensional total entrainment rate percentages for each test case.

Case	Entrainment rate [%]
Blevins	21.3
0 Hz	17.2
36 Hz	20.5
70 Hz	35.1
100 Hz	23.3

4.5.2 Turbulence Intensity Fields

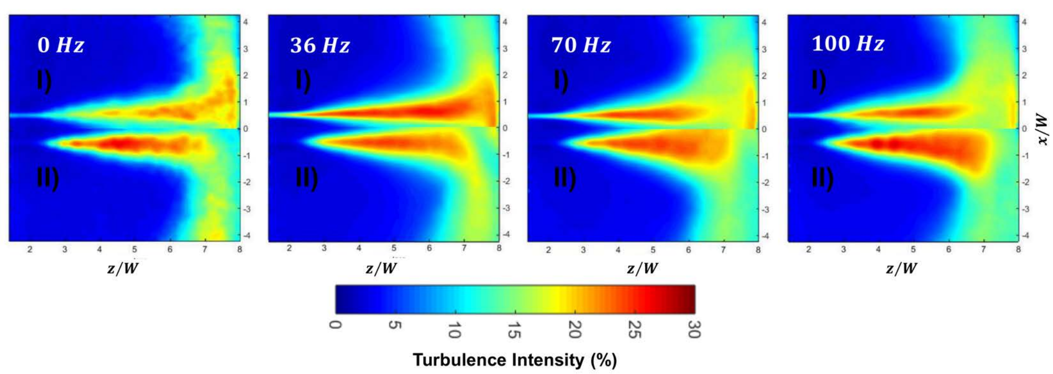

Figure 4.9: The turbulence intensity flood plots for the no-excitation, 36 Hz, 70 Hz, and 100 Hz anti-symmetric 1% amplitude cases. I) Upper sections represent the stream-wise turbulence intensity field expressed as a percentage $\frac{\sqrt{u'u'}}{U_{jet}} \cdot 100$, and II) lower sections represent the cross-stream turbulence intensity fields expressed as a percentage $\frac{\sqrt{v'v'}}{U_{jet}} \cdot 100$.

The standard deviation of the stream-wise (u-component) and cross-stream (v-component) velocity fields are represented as a turbulence intensity, expressed as a percentage of U_{jet} in Figure 4.9. The upper sections of the plots I) represent the

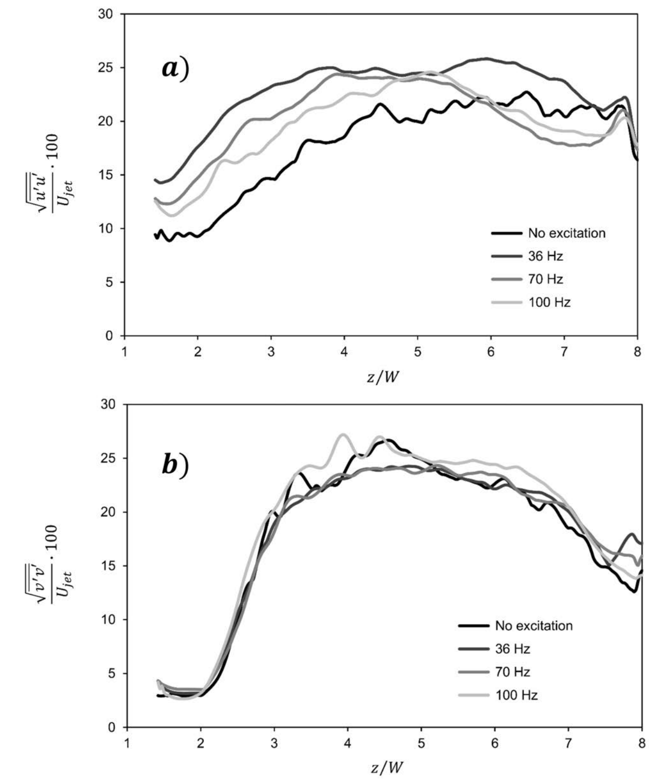

Figure 4.10: a) The maximum stream-wise turbulence intensity magnitude, and b) maximum cross-stream turbulence intensity magnitude within the jet column region ($-1.5 < x/W < 1.5$) as a function of downstream z/W distance for all test cases.

stream-wise turbulence intensity $\frac{\sqrt{\overline{u'u'}}}{U_{jet}}\cdot 100$, and the lower sections II) represent the cross-stream turbulence intensity $\frac{\sqrt{\overline{v'v'}}}{U_{jet}}\cdot 100$. Increases in stream-wise turbulence levels can be noted across all of the excited cases, which is similar to the preferred mode excitation response of a planar free jet [21]. For the 36 Hz excitation case, the stream-wise turbulence intensity field forms a concentrated band in the jet shear layers that extends most of the impingement distance. At excitation frequencies 70 Hz and 100 Hz, this concentrated band shortens and becomes more prominent in the center of the impingement distance (approximately $3 < z/W < 6$), while the cross-stream turbulence intensity bands widen in the shear layers at further downstream locations. Both of these features in the fluctuating velocity fields for the 70 Hz and 100 Hz excitation cases also appear in the PIV data of Arthurs [77] during self-excited resonant conditions at high subsonic Mach numbers (Ma = 0.9, H/W = 10.5). The growth of vortex structures in the jet shear layers redistribute the turbulent kinetic energy from the stream-wise fluctuating velocity component to the cross-stream fluctuating velocity component as the structures propagate downstream [77]. In Figure 4.10 a) and b), the downstream evolution of the maximum stream-wise turbulence intensity magnitude, and maximum cross-stream turbulence intensity magnitude is plotted in the jet column region ($-1.5 < x/W < 1.5$), respectively. Increases in the stream-wise turbulence levels can again be noted with acoustic excitation, as well as, a sudden reduction in stream-wise turbulence levels for the 70 Hz and 100 Hz cases, as the flow approaches the impingement plate z/W ≈ 7. Due to laser light reflections at the impingement plate surface, the PIV data in the vicinity of the wall ($\approx 1\ mm$) is lost, and the sharp gradients in the turbulence intensities are not resolved. Besides the spatial widening of the cross-stream turbulence intensity fields in Figure 4.9, the maximum cross-stream turbulence intensity levels is similar for all test cases shown in Figure 4.10 b). Turbulence transition in the jet also occurs at downstream location $z/W \approx 2-3$ for all cases, as the shear layers suddenly grow in the cross-stream direction, shown in Figures 4.9 and 4.10 b). For the non-excited impinging jet, the maximum turbulence intensity levels reach $20-25$ %, which is comparable to the $15-25$ % intensity levels measured in the acoustically-excited planar free jet studies of Hussain and Thompson [18].

4.5.3 Phase-Locked Vorticity Fields

Phase-locked vorticity fields are obtained by taking the curl of the velocity data obtained by the PIV. Each phase of the velocity fields consisted of an ensemble-average of 200 vector fields. The laser and camera were triggered using the output frequency generator sine wave signal (as the sine wave crosses its zero value) using a custom-made trigger circuit. In Figure 4.11, 4.12, and 4.13 the phase-locked vorticity plots are shown for eight points in the forcing cycle ($45°$ spacing) for the 36 Hz, 70 Hz, 100 Hz excitation cases, respectively.

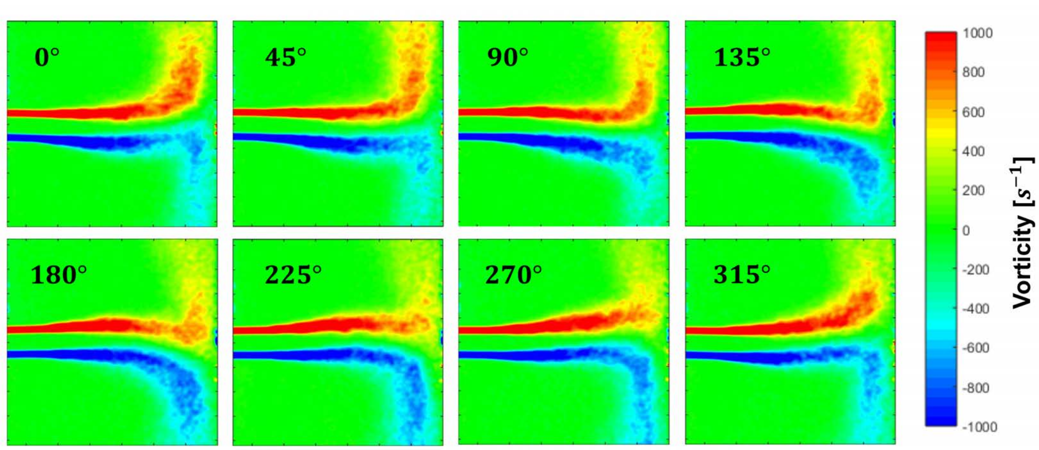

Figure 4.11: Phase-locked PIV vorticity fields for the 36 Hz excitation case.

Forcing the jet anti-symmetrically at 36 Hz induces a notable rocking motion of the jet column at that particular excitation frequency. This is consistent with the jet-plate tone frequency ($St_H \approx 0.4$) observed naturally at lower Mach numbers on impinging planar gas jets, shown in Figure 4.1, and has been previously characterized as the "linear regime/rocking mode" by Arthurs and Ziada [1]. Preliminary far-field microphone measurements for the current no-excitation case indicate

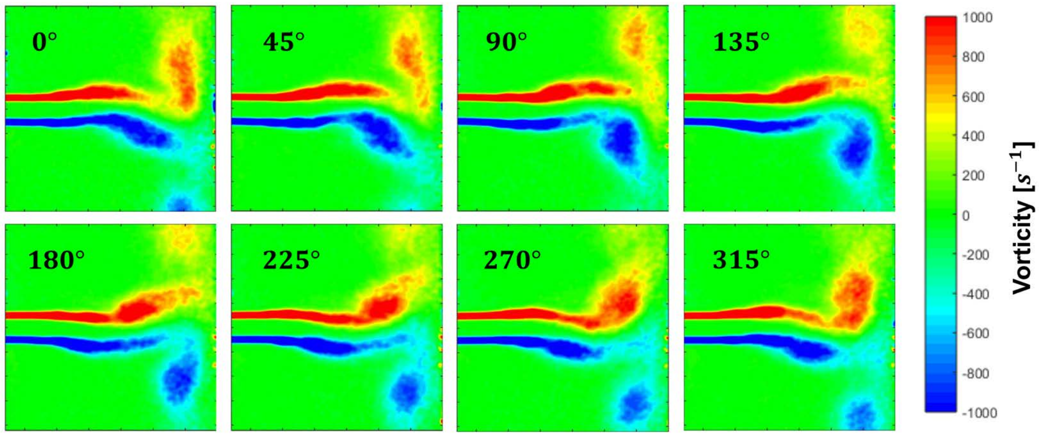

Figure 4.12: Phase-locked PIV vorticity fields for the 70 Hz excitation case.

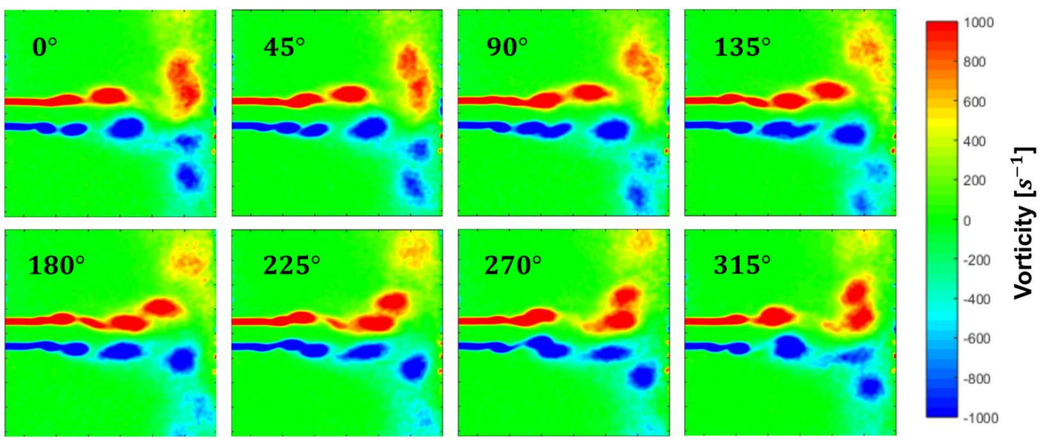

Figure 4.13: Phase-locked PIV vorticity fields for the 100 Hz excitation case.

a very broad shaped peak about this rocking frequency $St_H \approx 0.4$, whereas under external excitation conditions, the 36 Hz frequency becomes extremely tonal in the microphone spectrum. For the 70 Hz forcing case, a rocking motion of the jet column is also observed, combined with downstream vortex roll-up, shown in Figure 4.12. This vortex roll-up occurs anti-symmetrically (from side to side), propagating along either side of the jet stagnation line. Finally, for the anti-symmetric 100 Hz case, propagation of vortex structures seem to dominate the flow field in the vorticity plots, along with alternate vortex pairing on each side of the jet, as the structures approach the impingement plate. In Figure 4.13, the pairing event appears to be absent and/or weaker on the underside of the jet, however, at higher excitation amplitudes ($\frac{u''}{U_{jet}} \cdot 100 \approx 10$ %), stronger alternate pairing is observed, which occurred earlier upstream and greatly increased the jet spread rate (Phase $0°$ will be shown later in Figure 4.19). This increased jet column spread is consistent with the smoke visualization results of Iio et al. [27] at St_W = 0.15 using anti-symmetric excitation. The pairing phenomenon observed in the jet shear layer is also similar to the excitation of a free shear layer at its subharmonic frequency [10], suggesting that there are vortices naturally present in the flow-field around 200 Hz. Hot-wire spectra (not shown) also confirmed a maximum peak in the non-excited jet flow field at 213 Hz near the end of the potential core, and a dominant shear layer mode frequency $\approx$ 494 Hz in the vicinity of the nozzle exit.

For high-speed planar impinging gas jets in the fluid resonant regime, vortex pairing is not found to be present, and the Strouhal number bands in Figure 4.1 provide different numbers of vortex structures between the jet and the plate for: St_H = 0.39, 0.76, and 1.1 [1]. These hydrodynamic modes are not captured in the current PIV data, and therefore the results suggest that different flow dynamics occur. However, the jet response at 36 Hz seems to be similar to the fluid dynamic regime behaviour, which only produces anti-symmetric rocking of the jet column. Additionally, the 70 Hz and 100 Hz excitation cases also show anti-symmetric behaviour, and the corresponding Strouhal numbers are near the range $St_W \approx 0.12 - 0.16$. This range of Strouhal numbers has been argued to be the most unstable anti-symmetric column mode for planar free gas jets [13, 27, 39, 78]. Despite the differences in vortex structure arrangement, anti-symmetric oscillations of the jet column is achieved for all cases, along with distinguishable vortex structures propagating in the impinging shear layers for the phase-locked 70 Hz and 100 Hz excitation cases.

4.6 Impingement Plate Pressure Measurements

Static pressure measurements were also made along the impingement plate surface using a Fluke 922 micro-manometer connected to the back of the impingement surface using a flush-mounted pressure tap. The impingement plate was traversed across the jet flow to obtain time-averaged pressure distributions. In Figure 4.14 a) the static pressure distributions are displayed for the no excitation, anti-symmetric 36 Hz, 70 Hz, and 100 Hz cases. The pressure measurements are non-dimensionalized using the jet dynamic pressure $P_{jet} = \frac{1}{2}\rho_a U_{jet}^2$. The static pressure measurements show pressure reductions for the excited cases, which corroborate with the $z/W = 6$ velocity profiles presented in Figure 4.7 c). The excitation cases exhibit a wider static pressure profile, and a lower maximum pressure, due to momentum loss near the jet centerline caused by entrainment of the surrounding fluid. A Gaussian curve fit was taken with the static pressure data, followed by the analytical derivative, to obtain the non-dimensional pressure gradient distributions. These pressure gradient distributions are presented in Figure 4.14 b). During jet excitation at 36 Hz, 70 Hz, and 100 Hz, there is also a reduction in the maximum pressure gradient when compared to the unexcited case. Maximum pressure gradients in the jet stagnation region also play an important role in coating weight models, where larger pressure gradients increase wiping efficiency, and provide lighter coating weights

[44, 79].

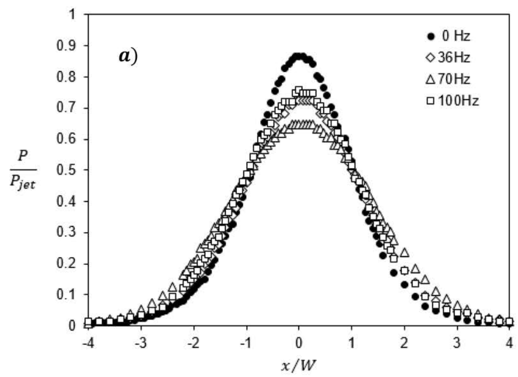

Figure 4.14: a) Static pressure distributions obtained along the impingement plate for the unexcited 0 Hz, 36 Hz, 70 Hz, and 100 Hz cases. b) Pressure gradient distributions along the impingement plate for the unexcited 0 Hz, 36 Hz, 70 Hz, and 100 Hz cases.

4.7 OFI Skin Friction Measurements

The OFI skin friction distribution obtained on the impingement plate during the no excitation case is presented in Figure 4.15. The red centered markers in the skin friction distributions are binned averages of the plotted data, with bin width x/W = 0.1. The maximum skin friction obtained in this test case ($1000{\cdot}C_f \approx$ 12) will be used as a comparison measurement for the excited cases with the same jet geometry and impingement plate configuration. The location of the maximum skin friction in this unexcited case has shown to also closely align with the location of the maximum pressure gradient ($x/W \approx \pm$ 1) plotted in Figure 4.14 b). Next to the OFI skin friction distribution in Figure 4.15 is the corresponding PIV velocity magnitude plot as a reference to the jet column behaviour.

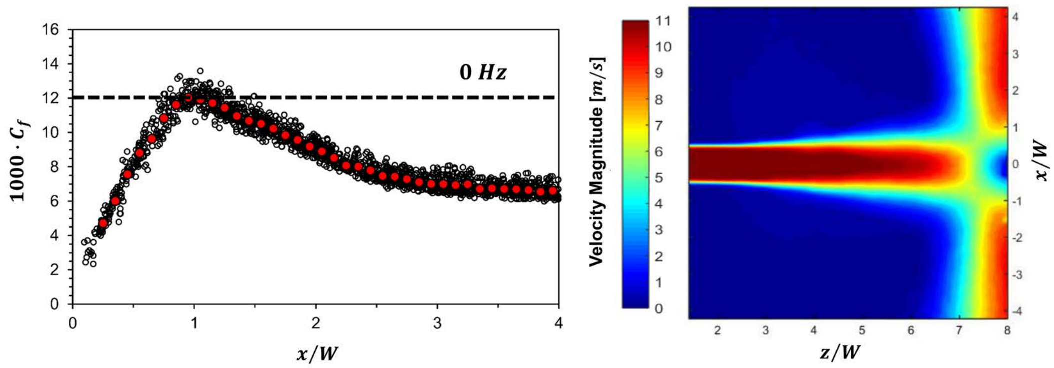

Figure 4.15: The skin friction distribution obtained using OFI for the no-excitation case (left), with the dashed line representative of the maximum skin friction value used for reference. The velocity magnitude plot for the no-excitation case (right).

4.7.1 Anti-Symmetric Forcing

At the bottom of Figure 4.16, three skin friction distributions are shown for the 36 Hz, 70 Hz, and 100 Hz anti-symmetric excitation cases, with forcing amplitude $\frac{u''}{U_{jet}} \cdot 100 \approx 1\ \%$. The dashed line above the skin friction distributions represent the maximum skin friction for the non-excited case. All three excitation cases experience a reduction in the maximum skin friction, with a reduction of 16%, 25%, and 21% for the 36 Hz, 70 Hz, and 100 Hz cases, respectively. Jet column oscillations are also captured in the phase $0°$ velocity magnitude plots displayed above the skin friction distributions in Figure 4.16. Note that the phase is with respect to the frequency generator output signal.

4.7.2 Increasing Forcing Amplitude

As the speaker excitation level is increased to $\frac{u''}{U_{jet}} \cdot 100 \approx 10\ \%$, there is a further reduction in the maximum skin friction values shown at the bottom of Figure 4.17.

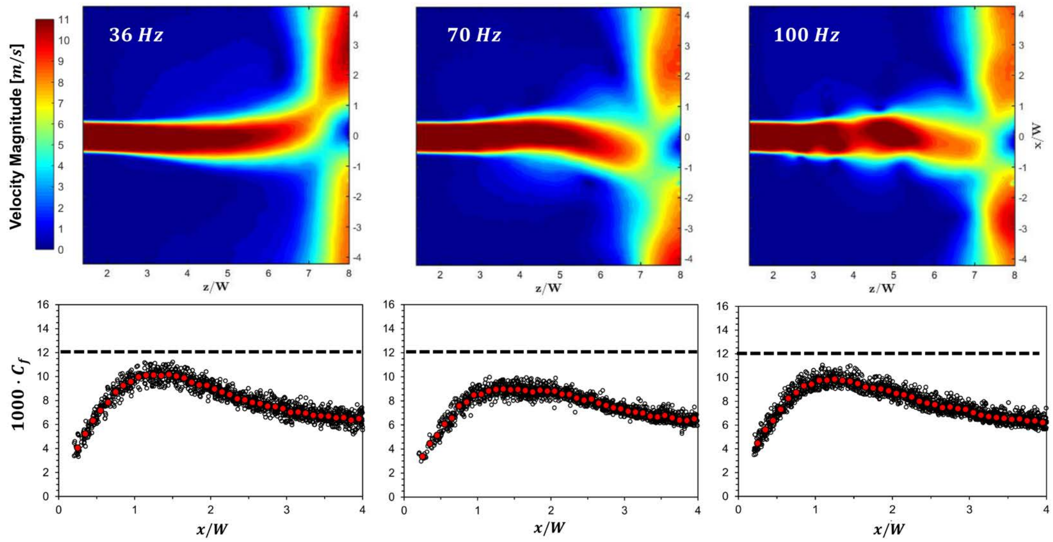

Figure 4.16: Phase-locked PIV velocity magnitude plots (Phase $0°$) for $\frac{u''}{U_{jet}} \cdot 100 \approx 1$ % (top), and corresponding OFI skin friction distributions (bottom) for 36 Hz, 70 Hz, and 100 Hz anti-symmetric excitation, respectively. The horizontal dashed line indicates the magnitude of maximum skin friction with no excitation for reference.

The location of the maximum skin friction also migrates further from the jet stagnation line; indicating a greater jet column spread rate for the current excitation amplitude levels. The corresponding phase $0°$ velocity magnitude plots are also shown at the top of Figure 4.17 to confirm the increased interactions between the jet column and the forcing frequencies. For these anti-symmetric, 10 % amplitude level cases, the maximum skin friction reductions correspond to approximately 33%, 38%, and 28%, for the 36 Hz, 70 Hz, and 100 Hz excitation frequencies, respectively.

4.7.3 Symmetric Forcing

Under some high Mach number, and low impingement ratio configurations, impinging planar gas jets have shown to produce symmetric fluid resonance modes

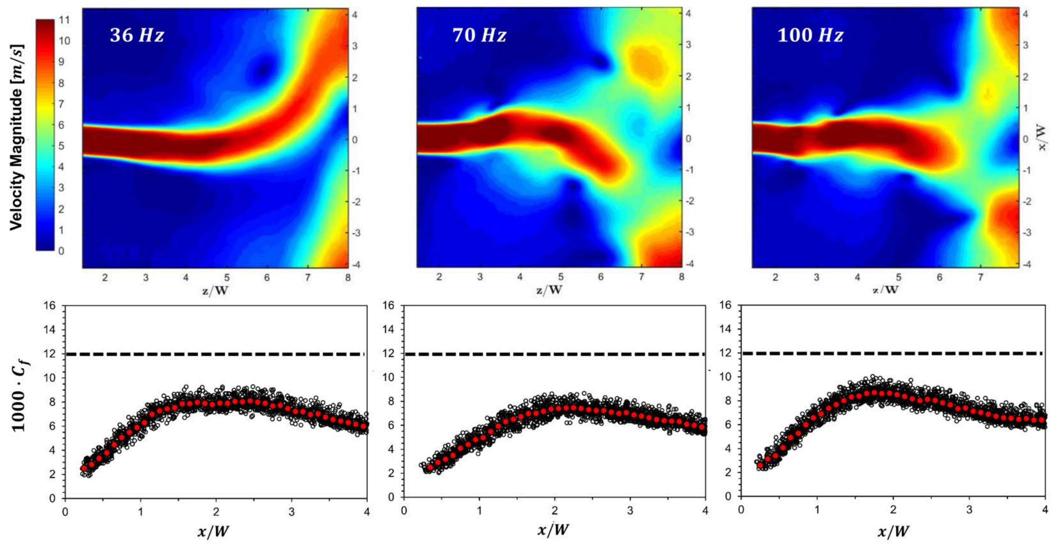

Figure 4.17: Phase-locked PIV velocity magnitude plots (Phase $0°$) for $\frac{u''}{U_{jet}} \cdot 100 \approx 10\ \%$ (top), and corresponding OFI skin friction distributions (bottom) for 36 Hz, 70 Hz, and 100 Hz anti-symmetric excitation, respectively. The horizontal dashed line indicates the magnitude of maximum skin friction with no excitation for reference.

[1]. Symmetric modes consist of strong vortex structures that remain aligned on either side of the jet centerline as they approach the impingement plate. By switching the polarity of the speaker wires in our experimental apparatus, we were able to also test the maximum skin friction and flow field during symmetric forcing. In Figure 4.18, the OFI and PIV for the $\frac{u''}{U_{jet}} \cdot 100 \approx 10\ \%$ symmetrically forced cases are presented. During symmetric forcing, the jet column in all these cases experience minimal lateral deflection throughout one cycle, compared to the anti-symmetric cases, and exhibit a pulsing behaviour in the phase-locked flow field images (not shown). The enhancement of vortex structures using symmetric excitation will be shown later in the maximum skin friction reduction maps in Figure 4.20. The maximum skin friction reductions for these $10\ \%$ amplitude, symmetrically forced cases, correspond to approximately 7%, 10%, and 15% for the 36 Hz, 70 Hz, and 100 Hz

excitation frequencies, respectively.

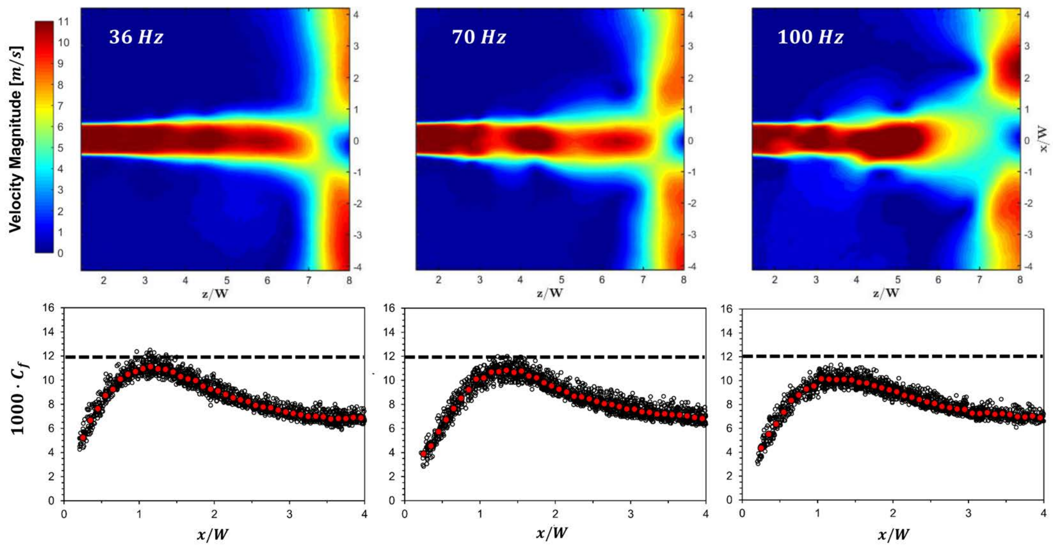

Figure 4.18: Phase-locked PIV velocity magnitude plots (Phase 0°) for $\frac{u''}{U_{jet}} \cdot 100 \approx 10$ % (top), and corresponding OFI skin friction distributions (bottom) for 36 Hz, 70 Hz, and 100 Hz symmetric excitation, respectively. Horizontal dashed line indicates magnitude of maximum skin friction with no excitation for reference.

4.7.4 Discussion

A couple items need to be clarified at this point. First, the OFI skin friction distributions are representative of the time-averaged skin friction along the impingement plate. Although the fluctuating skin friction (which cannot be measured with OFI) may increase during excitation, the overall time-averaged maximum skin friction decreases. Thus, the silicon oil used in the OFI testing took longer to spread, yielding thicker coatings and smaller fringe spacings in the same time frame. Secondly, it may seem intuitive that the maximum skin friction reduction is a simple fact that the jet is spreading the oil for only half the time, as the jet column moves from side to side of the stagnation line. This argument could hold, however, conservation of momentum would also dictate that twice the momentum should be experienced when the jet is on the measurement side of the stagnation line.

The maximum skin friction reductions are best explained by the process of entrainment. Increased rates of entrainment have been confirmed during jet forcing conditions in Section 5.1. Jet column entrainment results in faster centerline velocity decay (shown in Figure 4.7 c)), and seems to occur by two mechanisms during our testing. The first way to increase entrainment, and contribute to maximum skin friction reductions, is by lateral jet column deflection. At the lowest frequency of 36 Hz, the jet acts as a wave guide as jet column rocks back and forth at this excitation frequency, promoting mixing of the surrounding fluid. As the excitation level increases, so does the lateral deflection of the jet column. In fact, in the $10\ \%$ amplitude level case, at 36 Hz, the jet column centerline deflects past the location of the maximum skin friction of the non-excited case ($x/W \approx 1$). Thus, if the jet column centerline overshoots the non-excited location of maximum skin friction, then there will be indeed a large reduction in skin friction there. The second mechanism for entrainment is caused by coherent structures. These structures can be identified in the phase-locked vorticity plots as concentrated, and correlated, clumps of vorticity in Figures 4.12 and 4.13, which propagate down the impinging shear layers, and eventually become swept along the impingement plate. Coherent structures are well known to increase entrainment in free shear layers [80]. Additionally, studies on resonating impinging supersonic jets have revealed substantial lift losses associated with increased entrainment rates caused by amplified vortical structures in the flow field [81, 82]. These results corroborate with the current PIV, and impingement plate pressure measurements.

The trends in our OFI results, and the electro-chemical wall shear stress results of Alekseenko et al. [22], do not corroborate with the qualitative oil paint visualizations of Janetzke et al. [32], who observed increased oil paint removal under their mode of stable pairing condition of St_D = 0.82. Increased oil paint removal would qualitatively suggest increases in the accompanying wall shear stress at the impingement plate during jet excitation. Although their jet geometry (circular), and instability condition, is much different than the cases studied here, large toroidal vortices were present in their flow field, which would also indicate increased fluid entrainment, and momentum loss due to mixing in the impingement region. The current OFI results investigated on our impinging planar gas jet indicate that the maximum time-averaged skin friction on the impingement plate is greatly affected by momentum loss, and results in thicker oil coatings in the OFI testing.

A quantitative summary of the skin friction reduction percentages (from the non-excited reference case) for different levels of acoustic excitation are shown in Figures 4.19 and 4.20, for the anti-symmetric and symmetric cases, respectively. Also shown for each data point in the maximum skin friction reduction maps is the phase $0°$ vorticity field. The vorticity fields help depict the coherent structure behaviour in the flow field for each particular test case. For the anti-symmetric 36 Hz excitation frequency, skin friction reductions in the stagnation region can be observed by deflecting the jet column back and forth, in a rocking manner. For the 1% excitation level, no clear vortex structures were observed in the phase-locked vorticity plots, which is dynamically similar to the "linear regime/rocking mode" observed in the self-excited fluid dynamic regime by Arthurs and Ziada [1]. As the forcing amplitude is increased to 10% for the 36 Hz case, the deflection of the jet column even sweeps past the location of the maximum skin friction of the non-excited jet case ($x/W \approx 1$), and large rollers become apparent in the phase-locked vorticity plot. For the anti-symmetric 70 Hz, 1% excitation level case, a combination of rocking and alternate vortex roll-up is observed in the flow field. As the forcing level is increased to 10%, this rocking and vortex roll-up causes a very non-linear response in the vorticity field, shown in Figure 4.19. For this case, the alternate pairing of vortices move closer towards the jet nozzle exit, resulting in an increased jet column spread rate. For all the 1% and 10% amplitude levels tested, the 70 Hz excitation frequency produces the greatest peak skin friction reduction due to the combination of these previously mentioned entrainment effects. For the 100 Hz excitation cases, organization of vortex structures seems to be prevalent in the phase-locked vorticity plots, and similar to the 70 Hz case, increases in forcing amplitude are accompanied by increases in jet column spread, with alternate pairing moving closer to the jet exit. Interestingly, the level of forcing had less of an effect on the maximum skin friction reductions for the anti-symmetric 100 Hz case. This feature in the data may be explained by the excitation frequency also aligning with the most unstable anti-symmetric column mode of the planar jet ($St_W \approx 0.14$), as mentioned in Section 4.5.3. A characteristic of a global (or marginally global) instability is the systems disregard to input levels of the disturbance [83]. It is likely that the strong jet column oscillations, and vortex structures in the self-excited fluid resonant regime, shown in Figure 4.2, would also result in greater momentum loss near the jet centerline, and thereby lead to substantial reductions in the impingement plate shear stress.

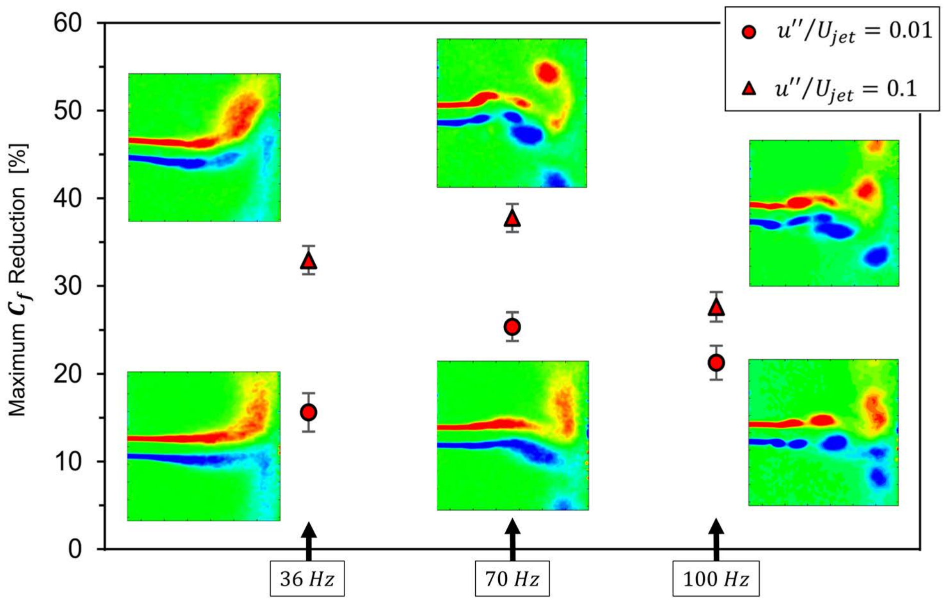

Figure 4.19: The maximum skin friction reduction percentage as a function of the three excitation frequencies tested (36 Hz, 70 Hz, 100 Hz) under different anti-symmetric excitation levels. Each data point is complemented with its corresponding phase 0° vorticity plot.

For the symmetrically forced cases, the maximum skin friction reductions and phase 0° vorticity fields are depicted in Figure 4.20. In all the symmetrically forced cases, less lateral deflection of the jet column was noted and vortex structures remained aligned on either side of the jet centerline. The organization of vortex structures becomes more pronounced in the jet shear layers for the $\frac{u''}{U_{jet}} \cdot 100 \approx 10\ \%$ amplitude cases. The results from the symmetrically forced experiments would suggest that the lateral deflection of the jet column is the main contributor to the reduction of the maximum time-averaged skin friction on the impingement plate.

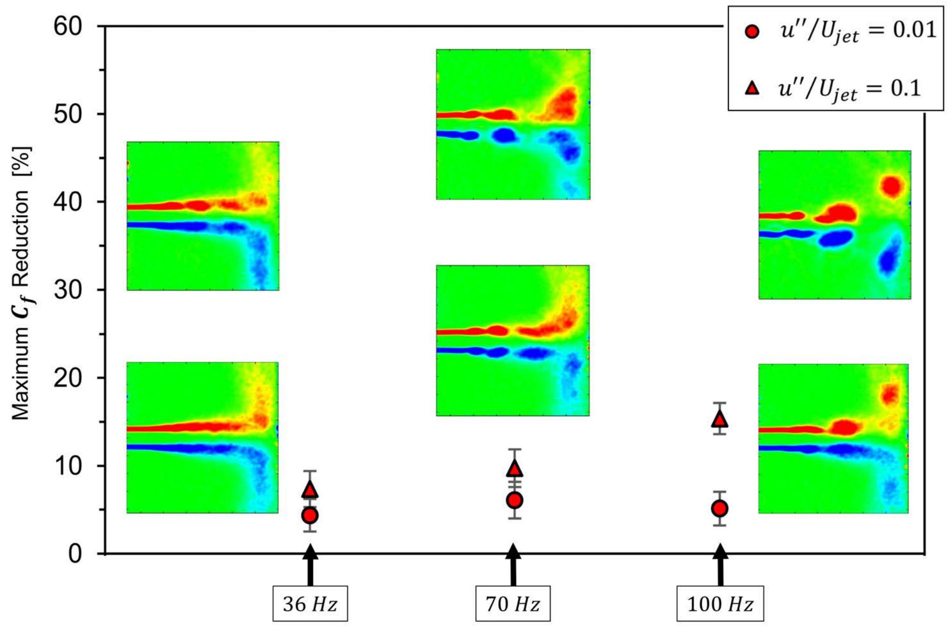

Figure 4.20: The maximum skin friction reduction percentage as a function of the three excitation frequencies tested (36 Hz, 70 Hz, 100 Hz) under different symmetric excitation levels. Each data point is complemented with its corresponding phase $0°$ vorticity plot.

4.8 Conclusions

The maximum impingement plate skin friction and flow field is investigated on an acoustically-forced planar impinging gas jet for $Re_{jet} = 11000$ and $H/W = 8$. During anti-symmetric acoustic excitation at 36 Hz ($St_H = 0.39$), the rocking mode of the jet column in the fluid dynamic regime is enhanced, with no discernible vortex structures observed in the impinging shear layers at low forcing amplitudes. For the 70 Hz ($St_H = 0.76$) and 100 Hz ($St_H = 1.1$) cases, coherent vortex structures are observed in the phase-locked vorticity fields, but with different structure arrangement than that associated with the high-speed self-excited fluid resonant regime. The growth, arrangement, and pairing of vortex structures in the current study may be attributed to the excitation frequency being near the most unstable anti-symmetric jet column mode ($St_W \approx 0.12 - 0.16$), or may be viewed as forced-induced pairing near the subharmonic of one of the shear layer mode frequencies. The shear layer mode and jet column mode are known to be related under low speed, laminar jet conditions [84]. The current OFI results indicate that the time-averaged maximum skin friction experiences a reduction for all cases tested. This reduction is attributed to increased entrainment caused by lateral jet column deflection and/or vortex structure enhancement during jet forcing conditions. Increased entrainment is verified using the PIV cross-stream velocities in the jet column region, which has the effect of widening the downstream velocity, and impingement plate pressure profiles. Entrainment also has the effect of reducing the maximum centerline velocity, and maximum impingement plate stagnation pressure. Anti-symmetric excitation has also been shown to provide a greater time-averaged maximum skin friction reduction than symmetric excitation for the same forcing frequency and amplitude. This would indicate that jet column deflection is a larger contributor to mixing and entrainment, compared to the organization/enhancement of vortex structures in the impinging shear layers. The maximum skin friction, and maximum pressure gradient, are influential factors in determining the wiping ability of air-knives. The reductions in the time-averaged maximum skin friction and pressure gradient during external forcing, would also suggest a reduction in the jet wiping ability under these conditions. This study may give qualitative insight into the wiping characteristics of high-speed air-knives that exhibit strong self-excited oscillations. With efforts in maintaining optimal wiping conditions, operating air-knives outside the fluid resonant regime, and/or eliminating planar jet oscillations all together, would appear to be beneficial in coating control applications.

List of Symbols

b	Relative systematic error
B	Skin friction data bin size
c	Speed of sound
C_f	Skin friction factor $\tau_w/\frac{1}{2}\rho_a U_{jet}^2$
d	Synthetic jet gap spacing
d_p	Mean diameter of seeding particle
D	Diameter of circular jet nozzle
f	frequency
g	Gravitational acceleration
h	Oil film height
H	Impingement distance
H/W	Impingement ratio
L	Jet span (y-direction)
Ma	Mach number U_{jet}/c
n	Index of refraction of oil
P_{jet}	Jet dynamic pressure
Re_{jet}	Jet Reynolds number $U_{jet}W/\nu_a$
s	Relative random error
St_ζ	$f\zeta/U_{jet}$
t	Time
u	Velocity component in the z-direction
u'	Fluctuating velocity component in the z-direction
u''	Acoustic particle velocity
U_{jet}	Jet exit velocity
v	Velocity component in the x-direction
v'	Fluctuating velocity component in the x-direction
W	Jet nozzle width
x	Flow direction along plate (origin at jet stagnation line)
x'	Distance from leading edge of oil film
y	Span-wise direction

z	Plate normal direction (origin at jet nozzle exit)
δ	Total combined relative uncertainty
ζ	Characteristic length
θ	Momentum thickness
θ_i	Incident angle of light
λ	Wavelength of light
μ	Dynamic viscosity of oil
ν	Kinematic viscosity of oil
ρ	Density of oil
σ	Sample standard deviation
τ	Shear stress
ϕ	Phase difference
ψ	Angle of oil film from jet stagnation line

Subscripts

a	Based on properties of air
d	Related to the disturbance
k	Kolmogorov scale
max	Maximum
p	Pertaining to seeding particle
SA	Spatial averaging
w	Wall conditions
λ	Related to wavelength of light
μ	Related to dynamic viscosity
τ	Related to shear stress

References

[1] Arthurs, D., and Ziada, S., 2012. "Self-excited oscillations of a high-speed impinging planar jet". *Journal of Fluids and Structures,* **34**, pp. 236–258.

[2] Marsh, A. H., 1961. "Noise measurements around a subsonic air jet impinging on a plane, rigid surface". *The Journal of the Acoustical Society of America,* **33**(8), pp. 1065–1066.

[3] Neuwerth, G., 1974. "Acoustic feedback of a subsonic and supersonic free jet which impinges on an obstacle". *NASA TT F-15719.*

[4] Ho, C.-M., and Nosseir, N. S., 1981. "Dynamics of an impinging jet. part 1. the feedback phenomenon". *Journal of Fluid Mechanics,* **105**, pp. 119–142.

[5] Nosseir, N. S., and Ho, C.-M., 1982. "Dynamics of an impinging jet. part 2. the noise generation". *Journal of fluid mechanics,* **116**, pp. 379–391.

[6] Arthurs, D., and Ziada, S., 2011. "The planar jet-plate oscillator". *Journal of Fluids and Structures,* **27**(1), pp. 105–120.

[7] Arthurs, D., and Ziada, S., 2014. "Effect of nozzle thickness on the self-excited impinging planar jet". *Journal of Fluids and Structures,* **44**, pp. 1–16.

[8] Arthurs, D., Ziada, S., and Goodwin, F., 2012. "Noise generation by the gas wiping jets of continuous galvanizing lines". *Journal of Fluids and Thermal Sciences,* **1**(2), p. 85.

[9] Rockwell, D., and Naudascher, E., 1979. "Self-sustained oscillations of impinging free shear layers". *Annual Review of Fluid Mechanics,* **11**(1), pp. 67–94.

[10] Ho, C.-M., and Huang, L.-S., 1982. "Subharmonics and vortex merging in mixing layers". *Journal of Fluid Mechanics,* **119**, pp. 443–473.

[11] Kopiev, V. F., Zaitsev, M. Y., Inshakov, S. I., and Guriashkin, L. P., 2003. "Visualization of the large-scale vortex structures in excited turbulent jets". *Journal of visualization,* **6**(3), pp. 303–311.

[12] Brown, G. B., 1935. "On vortex motion in gaseous jets and the origin of their sensitivity to sound". *Proceedings of the Physical Society,* **47**(4), p. 703.

[13] Sato, H., 1960. "The stability and transition of a two-dimensional jet". *Journal of Fluid Mechanics,* **7**(01), pp. 53–80.

[14] Michalke, A., 1964. "On the inviscid instability of the hyperbolictangent velocity profile". *Journal of Fluid Mechanics,* **19**(04), pp. 543–556.

[15] Freymuth, P., 1966. "On transition in a separated laminar boundary layer". *Journal of Fluid Mechanics,* **25**(04), pp. 683–704.

[16] Crow, S. C., and Champagne, F., 1971. "Orderly structure in jet turbulence". *Journal of Fluid Mechanics,* **48**(3), pp. 547–591.

[17] Hussain, A. F., and Zaman, K., 1981. "The preferred modeof the axisymmetric jet". *Journal of Fluid Mechanics,* **110**, pp. 39–71.

[18] Hussain, A., and Thompson, C., 1980. "Controlled symmetric perturbation of the plane jet: an experimental study in the initial region". *Journal of Fluid Mechanics,* **100**(2), pp. 397–431.

[19] Cohen, J., and Wygnanski, I., 1987. "The evolution of instabilities in the axisymmetric jet. part 1. the linear growth of disturbances near the nozzle". *Journal of Fluid Mechanics,* **176**, pp. 191–219.

[20] Raman, G., Zaman, K. B., and Rice, E. J., 1989. "Initial turbulence effect on jet evolution with and without tonal excitation". *Physics of Fluids A: Fluid Dynamics,* **1**(7), pp. 1240–1248.

[21] Rajagopalan, S., and Ko, N., 1996. "Velocity and spanwise vorticity measurements in an excited mixing layer of a plane jet". *Experiments in fluids,* **20**(5), pp. 346–357.

[22] Alekseenko, S., Markovich, D., and Semenov, V., 2002. "Turbulent structure of a gas-liquid impinging jet". *Fluid dynamics,* **37**(5), pp. 684–694.

[23] Olsen, J., Rajagopalan, S., and Antonia, R., 2003. "Jet column modes in both a plane jet and a passively modified plane jet subject to acoustic excitation". *Experiments in fluids,* **35**(3), pp. 278–287.

[24] Birbaud, A.-L., Durox, D., Ducruix, S., and Candel, S., 2007. "Dynamics of free jets submitted to upstream acoustic modulations". *Physics of Fluids (1994-present),* **19**(1), p. 013602.

[25] Hsiao, F.-B., and Huang, J.-M., 1990. "On the evolution of instabilities in the near field of a plane jet". *Physics of Fluids A: Fluid Dynamics (1989-1993),* **2**(3), pp. 400–412.

[26] Ziada, S., 1995. "Feedback control of globally unstable flows: impinging shear flows". *Journal of Fluids and Structures,* **9**(8), pp. 907–923.

[27] Iio, S., Hirashita, K., Katayama, Y., Haneda, Y., Ikeda, T., and Uchiyama, T., 2013. "Jet flapping control with acoustic excitation". *Journal of Flow Control, Measurement & Visualization,* **1**(02), p. 49.

[28] Chambers, F., and Goldschmidt, V., 1982. "Acoustic interaction with a turbulent plane jet: effects on mean flow". *AIAA Journal,* **20**(6), pp. 797–804.

[29] Huang, J.-M., and Hsiao, F.-B., 1999. "On the mode development in the developing region of a plane jet". *Physics of fluids,* **11**(7), pp. 1847–1857.

[30] Kozlov, G., Grek, G., Sorokin, A., and Litvinenko, Y. A., 2008. "Influence of initial conditions at the nozzle exit on the structure of round jet". *Thermophysics and Aeromechanics,* **15**(1), pp. 55–68.

[31] Azevedo, L., Webb, B., and Queiroz, M., 1994. "Pulsed air jet impingement heat transfer". *Experimental Thermal and Fluid Science,* **8**(3), pp. 206–213.

[32] Janetzke, T., Nitsche, W., and Täge, J., 2008. "Experimental investigations of flow field and heat transfer characteristics due to periodically pulsating impinging air jets". *Heat and Mass Transfer,* **45**(2), pp. 193–206.

[33] Yeh, Y.-L., Hsu, C.-C., Chiang, C.-H., and Hsiao, F.-B., 2009. "Vortical structure evolutions and spreading characteristics of a plane jet flow under anti-symmetric long-wave excitation". *Experimental Thermal and Fluid Science,* **33**(4), pp. 630–641.

[34] Samimy, M., Kim, J.-H., Kastner, J., Adamovich, I., and Utkin, Y., 2007. "Active control of high-speed and high-reynolds-number jets using plasma actuators". *Journal of Fluid Mechanics,* **578**, pp. 305–330.

[35] Sinha, A., Alkandry, H., Kearney-Fischer, M., Samimy, M., and Colonius, T., 2012. "The impulse response of a high-speed jet forced with localized arc filament plasma actuators". *Physics of Fluids,* **24**(12), p. 125104.

[36] Crawley, M. B., Kuo, C.-W., and Samimy, M., 2016. "Vortex dynamics and sound emission in an excited high-speed jet". In 22nd AIAA/CEAS Aeroacoustics Conference, p. 2985.

[37] Kuo, C.-W., Cluts, J., and Samimy, M., 2017. "Effects of excitation around jet preferred mode strouhal number in high-speed jets". *Experiments in Fluids,* **58**(4), p. 35.

[38] Gutmark, E., and Ho, C.-M., 1983. "Preferred modes and the spreading rates of jets". *Physics of Fluids (1958-1988),* **26**(10), pp. 2932–2938.

[39] Kozlov, V. V., Grek, G. R., and Litvinenko, Y. A., 2016. "Plane jets affected by initial conditions and acoustic perturbations". In *Visualization of Conventional and Combusting Subsonic Jet Instabilities*. Springer, pp. 51–63.

[40] Beltaos, S., and Rajaratnam, N., 1973. "Plane turbulent impinging jets". *Journal of Hydraulic Research,* **11**(1), pp. 29–59.

[41] Tu, C., and Wood, D., 1996. "Wall pressure and shear stress measurements beneath an impinging jet". *Experimental thermal and fluid science,* **13**(4), pp. 364–373.

[42] Zhe, J., and Modi, V., 2001. "Near wall measurements for a turbulent impinging slot jet (data bank contribution)". *Journal of fluids engineering,* **123**(1), pp. 112–120.

[43] Guo, Y., and Wood, D., 2002. "Measurements in the vicinity of a stagnation point". *Experimental thermal and fluid science,* **25**(8), pp. 605–614.

[44] Lacanette, D., Gosset, A., Vincent, S., Buchlin, J.-M., and Arquis, É., 2006. "Macroscopic analysis of gas-jet wiping: Numerical simulation and experimental approach". *Physics of Fluids,* **18**(4), p. 042103.

[45] Dogruoz, M. B., Ortega, A., and Westphal, R. V., 2015. "Measurements of skin friction and heat transfer beneath an impinging slot jet". *Experimental Thermal and Fluid Science,* **60**, pp. 213–222.

[46] Patel, V., 1965. "Calibration of the preston tube and limitations on its use in pressure gradients". *Journal of Fluid Mechanics,* **23**(01), pp. 185–208.

[47] New, T., and Long, J., 2015. "Dynamics of laminar circular jet impingement upon convex cylinders". *Physics of Fluids,* **27**(2), p. 024109.

[48] Long, J., and New, T., 2016. "Vortex dynamics and wall shear stress behaviour associated with an elliptic jet impinging upon a flat plate". *Experiments in Fluids,* **57**(7), pp. 1–18.

[49] Amili, O., Hind, M. D., Naughton, J. W., and Soria, J., 2016. "Evaluation of a film-based wall shear stress measurement technique in a turbulent channel flow". *Experimental Thermal and Fluid Science,* **70**, pp. 437–442.

[50] Phares, D. J., Smedley, G. T., and Flagan, R. C., 2000. "The wall shear stress produced by the normal impingement of a jet on a flat surface". *Journal of Fluid Mechanics,* **418**, pp. 351–375.

[51] El Hassan, M., Assoum, H. H., Sobolik, V., Vétel, J., Abed-Meraim, K., Garon, A., and Sakout, A., 2012. "Experimental investigation of the wall shear stress and the vortex dynamics in a circular impinging jet". *Experiments in fluids,* **52**(6), pp. 1475–1489.

[52] El Hassan, M., Assoum, H., Martinuzzi, R., Sobolik, V., Abed-Meraim, K., and Sakout, A., 2013. "Experimental investigation of the wall shear stress in a circular impinging jet". *Physics of Fluids (1994-present),* **25**(7), p. 077101.

[53] Zaman, K., and Hussain, A., 1980. "Vortex pairing in a circular jet under controlled excitation. part 1. general jet response". *Journal of fluid mechanics,* **101**(03), pp. 449–491.

[54] Janetzke, T., and Nitsche, W., 2009. "Time resolved investigations on flow field and quasi wall shear stress of an impingement configuration with pulsating jets by means of high speed piv and a surface hot wire array". *International Journal of Heat and Fluid Flow,* **30**(5), pp. 877–885.

[55] Ceccio, S. L., 2010. "Friction drag reduction of external flows with bubble and gas injection". *Annual Review of Fluid Mechanics,* **42**, pp. 183–203.

[56] Young, R. M., Hargather, M., and Settles, G., 2013. "Shear stress and particle removal measurements of a round turbulent air jet impinging normally upon a planar wall". *Journal of Aerosol Science,* **62**, pp. 15–25.

[57] Ritcey, A., McDermid, J. R., and Ziada, S., 2017. "The maximum skin friction and flow field of a planar impinging gas jet". *Journal of Fluids Engineering,* **139**(10), p. 101204.

[58] Davy, C., Alvi, F., and Naughton, J., 2002. "Surface flow measurements of micro-supersonic impinging jets". In Proceedings of the 22nd AIAA Aerodynamic Measurement Technology and Ground Testing Conference, pp. 24–26.

[59] Naughton, J. W., Schabron, B., Hind, M. D., and Alvi, F., 2011. "Improved wall shear stress measurements on a supersonic microjet impingement surface". *AIAA Paper,* **1096**.

[60] Naughton, J. W., and Brown, J. L., 1997. "Skin-friction distribution near a cylinder mounted on a flat plate". *AIAA Paper*, pp. 97–1783.

[61] Peterson, S. D., and Plesniak, M. W., 2004. "Surface shear stress measurements around multiple jets in crossflow using the fringe imaging skin friction technique". *Experiments in fluids,* **37**(4), pp. 497–503.

[62] Johansson, T. G., Mehdi, F., Shiri, F., and Naughton, J. W., 2005. "Skin friction measurements using oil film interferometry and laser doppler anemometry". *AIAA Paper,* **4673**, p. 2005.

[63] Zanoun, E.-S., Nagib, H., and Durst, F., 2009. "Refined cf relation for turbulent channels and consequences for high-re experiments". *Fluid dynamics research,* **41**(2), p. 021405.

[64] Schülein, E., 2014. "Optical method for skin-friction measurements on fast-rotating blades". *Experiments in fluids,* **55**(2), pp. 1–10.

[65] Drake, A., and Kennelly, R. A., 1999. "In-flight skin friction measurements using oil film interferometry". *Journal of aircraft,* **36**(4), pp. 723–725.

[66] Melling, A., 1997. "Tracer particles and seeding for particle image velocimetry". *Measurement Science and Technology,* **8**(12), p. 1406.

[67] Scarano, F., and Riethmuller, M. L., 2000. "Advances in iterative multigrid piv image processing". *Experiments in Fluids,* **29**, pp. S051–S060.

[68] Naughton, J. W., and Sheplak, M., 2002. "Modern developments in shear-stress measurement". *Progress in Aerospace Sciences,* **38**(6), pp. 515–570.

[69] Desse, J.-M., 2003. "Oil-film interferometry skin-friction measurement under white light". *AIAA journal,* **41**(12), pp. 2468–2477.

[70] Naughton, J., and Hind, M., 2013. "Multi-image oil-film interferometry skin friction measurements". *Measurement Science and Technology,* **24**(12), p. 124003.

[71] Pailhas, G., Barricau, P., Touvet, Y., and Perret, L., 2009. "Friction measurement in zero and adverse pressure gradient boundary layer using oil droplet interferometric method". *Experiments in fluids,* **47**(2), pp. 195–207.

[72] Segalini, A., Rüedi, J.-D., and Monkewitz, P. A., 2015. "Systematic errors of skin-friction measurements by oil-film interferometry". *Journal of Fluid Mechanics,* **773**, pp. 298–326.

[73] Coleman, H. W., and Steele, W. G., 2009. *Experimentation, validation, and uncertainty analysis for engineers*. John Wiley & Sons.

[74] Pritchard, P. J., 2011. *Fox and McDonald's Introduction to Fluid Mechanics*, Vol. 8. John Wiley & Sons New York, pg.440.

[75] Smith, B. L., and Glezer, A., 1998. "The formation and evolution of synthetic jets". *Physics of fluids,* **10**(9), pp. 2281–2297.

[76] Blevins, R. D., 1984. *Applied Fluid Dynamics Handbook*. Transactions of the ASME, New York, Van Nostrand Reinhold Co., pg. 236.

[77] Arthurs, D., 2012. "Self-excited oscillations of the impinging planar jet". *PhD Thesis*.

[78] Yu, M.-H., and Monkewitz, P. A., 1993. "Oscillations in the near field of a heated two-dimensional jet". *Journal of fluid mechanics,* **255**, pp. 323–347.

[79] Ellen, C., and Tu, C., 1984. "An analysis of jet stripping of liquid coatings". *Journal of fluids engineering,* **106**(4), pp. 399–404.

[80] Hussain, A. F., 1986. "Coherent structures and turbulence". *Journal of Fluid Mechanics,* **173**, pp. 303–356.

[81] Krothapalli, A., Rajkuperan, E., Alvi, F., and Lourenco, L., 1999. "Flow field and noise characteristics of a supersonic impinging jet". *Journal of Fluid Mechanics,* **392**, pp. 155–181.

[82] Alvi, F. S., Shih, C., Elavarasan, R., Garg, G., and Krothapalli, A., 2003. "Control of supersonic impinging jet flows using supersonic microjets". *AIAA journal,* **41**(7), pp. 1347–1385.

[83] Huerre, P., and Monkewitz, P. A., 1990. "Local and global instabilities in spatially developing flows". *Annual review of fluid mechanics,* **22**(1), pp. 473–537.

[84] Ho, C.-M., and Hsiao, F.-B., 1983. "Evolution of coherent structures in a lip jet". In *Structure of Complex Turbulent Shear Flow*. Springer, pp. 121–136.

Chapter 5

The Fluctuating Velocity Field of a Forced Planar Impinging Gas Jet

Complete Citation:

Ritcey, A., McDermid, J.R., and Ziada, S., 2017."The Fluctuating Velocity Field of a Forced Planar Impinging Gas Jet". *Journal of Turbulence*. *doi:10.1080/14685248.2018.1513137*

Preface

The fluctuating velocity fields of the model air-knife was analyzed under forcing conditions using particle image velocimetry (PIV) and proper orthogonal decomposition (POD). Under air-knife forcing, increased fluctuation intensities and unique flow field characteristics emerged in the ensemble PIV data. The coherent and turbulence fields were determined using a triple decomposition, and were further approximated using a low order reconstruction of the fluctuating velocity field with the first two most energetic POD modes. The unique features in the fluctuating velocity field under forced conditions was found to be caused by the periodic motion of the jet. Additionally, under the 70 Hz and 100 Hz forced conditions tested, the current low speed air-knife model displayed similar qualitative features to that of a self-excited high-speed planar impinging gas jet. All experimental measurements, data analysis, and technical writing was completed by the first author under the supervision of advisors: Dr. McDermid and Dr. Ziada.

The Fluctuating Velocity Field of a Forced Planar Impinging Gas Jet

Adam Ritcey, Joseph McDermid, Samir Ziada

McMaster University
Department of Mechanical Engineering
1280 Main Street West
Hamilton, Ontario L8S 4L7

Abstract

The fluctuating velocity field of a planar impinging gas jet is studied using Particle Image Velocimetry (PIV), while anti-symmetrically forcing the jet column at the nozzle exit using planar synthetic jets. The jet exit velocity is set to U_{jet} = 11 m/s providing a jet Reynolds number of Re_{jet} = 11000, and the impingement distance is held constant at eight times the nozzle width W. Under forcing conditions near unstable frequencies, both the stream-wise and cross-stream fluctuating velocity fields of the jet have very different characteristics than that of the unforced jet. The fluctuating velocity fields reported here were also found to have qualitatively similar features to that of a high speed self-excited impinging jet. For the highly periodic flow conditions tested, a triple decomposition, and a low order reconstruction of the fluctuating velocity field using Proper Orthogonal Decomposition (POD) is employed. These methods allow for the extraction of the coherent velocity and turbulence fields from the forced planar impinging gas jet.

5.1 Introduction

Impinging gas jets have many engineering applications, including drying operations, erosion testing, turbine blade and circuit board cooling, vertical take-off and landing (VTOL) vehicles, and coating control applications. Relatively recent gas jet studies have investigated the impingement plate pressure [1, 2], skin friction distributions [3, 4, 2, 5, 6, 7], heat transfer [8, 9, 2], and inherent instability mechanisms within the jet flow field [10, 11, 12]. This study focuses on the fluctuating velocity fields of an externally forced planar impinging gas jet under a constant jet exit velocity (U_{jet} = $11\ m/s$), and an impingement distance set to eight times the nozzle width W. The impinging jet is anti-symmetrically forced under three frequencies (36 Hz, 70 Hz, and 100 Hz) to analyze the changes in fluctuating flow quantities. The experimental conditions reported in the current study are similar to those employed by Ritcey et al. [13], used to investigate the effects of jet forcing on the maximum pressure gradient, and skin friction distributions along the impingement plate. Mean flow fields, and phase-locked vorticity time series of the jet dynamics can also be found in that study. The particle image velocimetry (PIV) analysis in the current study attempts to impart a deeper understanding of the fluctuating velocity evolution in a forced planar impinging gas jet. The jet fluctuation intensity, fluctuating kinetic energy, coherent velocity, and turbulence will be investigated during forced and unforced conditions. The most energetic POD modes of the fluctuating velocity field will also be analyzed in Section 5. The following sections will briefly discuss the present literature on forced gas jets (Section 5.1.1), self-excited impinging gas jets (Section 5.1.2), and jet velocity statistics (Section 5.1.3) as an introduction to the performed experiments.

5.1.1 Forced Gas Jets

Gas jets are known to be sensitive to sound, as well as possess many dominant frequencies in their flow characteristics depending on measurement location, and jet operating conditions, such as impingement plate stand-off distance, and jet exit Mach number. The use of acoustic forcing is commonly employed to enhance or amplify certain susceptible frequencies to manipulate the jet flow behaviour, and/or study the inherent instability mechanisms. To characterize these important frequencies, the Strouhal number is commonly employed as a dimensionless frequency parameter in the following equation:

$$St_\zeta = \frac{f\zeta}{U_{jet}} \tag{5.1}$$

The length scale represented in the Strouhal number uses the jet exit momentum thickness ζ=θ when studying the shear layer instability [14, 15], the jet nozzle width ζ=W when concerning the preferred mode instability [16, 17, 12], or the impingement plate stand-off distance ζ=H when investigating the self-excited instability [18, 1, 19, 20]. Due to the vastness of the literature on this subject, in-depth reviews on all these jet instabilities will not be given here.

Most forced gas jet studies have been performed in the free jet configuration (as opposed to the impinging jet configuration), and have employed external forcing using loudspeakers situated inside the jet plenum [16, 21, 17, 22, 23, 24, 25, 26, 27], loudspeakers situated in the far-field of the jet [28, 29, 30, 31], and loudspeakers focused at the jet nozzle exit [32, 33, 11]. External forcing has also been employed using mechanical actuation devices [34, 35], and more recently using plasma actuators along the nozzle periphery [36, 37, 12]. These Localized-Arc Filament Plasma Actuators (LAFPAs) are high frequency (upper limit of 200 kHz), high amplitude, and low power usage (time-averaged power of 20 W per actuator), having the ability to manipulate high-speed gas jets [36]. An early jet response study by Hussain and Thompson [21] forced a planar free jet from inside the jet plenum using symmetric excitation (perturbation in phase about the nozzle perimeter) over a jet Reynolds number range of $Re_{jet} = 8000 - 31000$. The preferred mode frequency in this study (previously defined by Crow and Champagne [16] as the most amplified forcing frequency measured at the jet centerline, and at the end of the potential core), was determined to reach levels of 11 % of the jet exit velocity for a forcing Strouhal number of $St_W = 0.18$. The preferred mode Strouhal number reported by Hussain and Thompson [21] is lower than the previously, and thoroughly, investigated the preferred mode of a circular jet $St_D \approx 0.3$. Over the many decades of research on the preferred mode Strouhal for the circular jet, there remains large scatter in the result ($\pm$ 100 % in St_D) reported in Gutmark and Ho [38]. This scatter is predominantly due to jet sensitivity to background noise levels, nozzle geometry, and spatial coherence in different-sized jet plenums. Despite the difference in these reported Strouhal numbers, the planar free jet is generally less responsive to plenum excitation than the circular jet. During jet forcing conditions, the amplification of the forcing frequency was reported to reach ≈ 60 % of the total turbulence in the planar jet, compared to that of 97 % in circular free jets [21]. To clarify, the "total turbulence" is defined as the root mean square (rms) of the entire velocity time signal, as opposed to the rms of only the forcing frequency at a particular location in the flow field (usually measured at the jet centerline, and at the end of the potential core).

A study by Iio [11] forced a planar free gas jet (Re_{jet} = 6700) anti-symmetrically using focused planar synthetic jets on each side of the planar jet nozzle, and were able to manipulate the jet column behaviour. At an excitation Strouhal number of St_W = 0.15, large organized anti-symmetric vortex structures were seen in their instantaneous smoke visualization images, and wider spread rates could be determined by comparing their results to the unforced case. Although only single hot-wire measurements were made along the jet centerline, the amplification of the forcing frequency was shown to be highest (rms $\approx 8\%$ of U_{jet}) just before the end of the potential core ($z/W \approx 3-4$) during St_W=0.15 forcing conditions. A study by Kozlov et al. [39] forced a planar free jet (Re_{jet} = 1700) using a loudspeaker positioned outside the jet shear layer. Large organized anti-symmetric vortex structures were also observed in their laser sheet smoke visualizations for St_W = $0.12 - 0.19$, enhancing the spread rate of the jet. Large-scale organization of the jet appeared under anti-symmetric forcing conditions, regardless of the initial conditions at the jet nozzle exit; independent of a laminar or turbulent exit velocity profile. In many of these forced gas jet studies, comprehensive fluctuating velocity fields are absent, or measured data is only provided along the jet centerline, or at discrete flow field locations.

5.1.2 Self-Excited Impinging Gas Jets

Jet-plate tones, or jet noise, in past years have been a major motivation for impinging gas jet research, stemming from early studies by Marsh [40], Neuwerth

[41], Ho and Nossier [18], and Nossier and Ho [42], up to more recent studies by Arthurs and Ziada [1, 43, 20]. The presence of the impingement plate effectively allows downstream pressure fluctuations from the gas jet to feedback upstream, thus perturbing the initial conditions at the jet nozzle. These pressure fluctuations, or "jet-plate tones", scale with the impingement plate distance H; tonal frequencies decrease with increasing plate distance. In a study by Arthurs and Ziada [19], the dominant acoustic tone measured with a far-field microphone has been linked to the oscillation of the jet column, and in some cases with the collision of strong coherent vortex structures at the impingement plate, confirmed with phase-locked PIV. The next section will describe the two different regimes for self-excited planar impinging gas jets: the fluid dynamic regime, and the fluid resonant regime.

Fluid Dynamic Regime

The fluid dynamic regime constitutes the lower Mach number range (Ma < 0.56-0.78 dependent on H/W), where the fluid dynamic feedback from the impingement plate influences the initial conditions at the nozzle exit, and governs the global oscillation frequency of the jet. Phase-locked PIV measurements (locked to the dominant acoustic tone in the microphone signal) show that the jet oscillates, or rocks back and forth, once in an acoustic cycle. Phase-locked vorticity plots show no organized vortex structures in the jet shear layers at this frequency due to the disturbance wavelengths (speed of the disturbance/frequency of the disturbance) being approximately greater, or equal, to the jet impingement distance. Arthurs and Ziada [19] describe this fluid dynamic regime as the "linear regime or rocking mode", due to the approximate linear increase in the dominant acoustic tone frequency with velocity (constant Strouhal number $St_H \approx 0.4$, or $f \approx 0.4 \cdot U_{jet}/H$), and the rocking behaviour of the jet column.

Fluid Resonant Regime

As the jet Mach number is further increased, additional effects occur in the jet flow field. First, the fundamental jet oscillation frequency (or one of its harmonics) can excite the resonant frequency of the air volume trapped between the jet and the plate. When this trapped acoustic mode becomes excited, an acoustic standing wave is formed in this jet-plate region. Secondly, pressure fluctuations from the resonant acoustic mode become dominant (i.e. stronger than the feedback from the plate), providing large amplitude forcing at the nozzle exit. Large amplitude forcing is a requirement for a phenomenon called "collective interaction" [18, 44], which causes large-amplitude, low frequency, upstream traveling waves from the impingement plate to perturb the nozzle in a way that effectively rolls up the downstream-propagating high frequency shear layer vortices. This synchronization of the upstream and downstream disturbances establishes one global low-frequency disturbance wave, coupling the hydrodynamics and acoustics in the impinging jet flow field. This resonance condition is known to produce very high sound pressure levels in the far-field of the jet (> 130 dB), enhanced jet column oscillations, and large coherent vortex structures propagating down the impinging shear layers. The acoustic standing wave can also take on different harmonics, or trapped acoustic modes, which in turn reveal a different number of vortex structures between the jet and the plate (different hydrodynamic modes). These jumps in frequency have been well documented in other impinging flows (such as cavities, jet-plate, jet-edge, jet-hole configurations) by Rockwell [45] and is sometimes referred to as frequency "staging". Arthurs and Ziada [19] have experimentally determined many different Mach number and impingement ratio combinations, which excite various hydrodynamic, and trapped acoustic modes in the fluid resonant regime. Similar resonant feedback loops can exist even without the presence of the impingement plate on supersonic free jets, known as the jet screech phenomenon [46]. Jet screech results from disturbance waves propagating from the jet nozzle and interacting with the downstream shock cell structures, thus providing upstream acoustic waves that reinforce the conditions at the jet nozzle exit.

5.1.3 Jet Velocity Statistics

The instantaneous velocity field can be separated into a mean velocity field, and the fluctuating velocity field via a Reynolds decomposition in the following equation:

$$u = \overline{U} + u' \tag{5.2}$$

The fluctuating velocity field can also be further decomposed into a coherent velocity u'_c (periodic), and a turbulence field u'_t (non-periodic), if there is a dominant frequency component in the flow. This is known as a triple decomposition and will be reserved until Section 5.4. We will begin our analysis of the fluctuating velocity field as an overall grouping of the periodic, and non-periodic fluctuations by calculating the total rms (root mean square) of the instantaneous velocity field using 200 random PIV images. Fluctuating velocity, and turbulence measurements on impinging jets have been previously reported using hot-wire probes placed at discrete locations in the flow field [47, 2], or using PIV [48, 49]. PIV has obvious advantages in capturing entire flow field measurements simultaneously, while resolving different directional components of velocity, thus allowing accurate resolution of the normal, and shear Reynolds stresses (see Section 5.2.2 for PIV uncertainty).

The state of the jet is defined based on the jet exit velocity profile (laminar or turbulent), which is influenced by the jet Reynolds number, jet nozzle geometry, surface roughness of the nozzle, and prior upstream flow conditioning. The evolution of the jet exit velocity profile due to different nozzle lengths, and due to turbulizer inserts, can be found in a circular free jet study by Kozlov et al. [31]. Due to different initial flow conditions, maximum jet exit fluctuation intensity levels can vary. From impinging gas jet experiments, the u-velocity fluctuations and the v-velocity fluctuations have been reported at $5-10$ % of the jet exit velocity [47, 48, 2]. In unforced gas jets, it is assumed that the velocity fluctuation levels are representative of the turbulence due to their broad-ranged velocity spectra. As gas exits the jet, the sharp velocity gradient in the jet shear layer produces turbulent kinetic energy (TKE), thus providing energy to the turbulence from the mean flow. In laminar gas jets, transition to turbulence occurs after some downstream distance, whereas in a fully-developed turbulent gas jet, turbulence characteristics exist immediately outside the nozzle exit.

Turbulence transition locations in laminar jets can be established using different definitions [28], however, it was shown by Ritcey et al. [7] that turbulence transition can be denoted by downstream regions of rapidly increasing turbulence intensity levels. This region of rapidly increasing turbulence intensity has shown to migrate closer to the nozzle exit with increasing jet Reynolds numbers. The turbulence intensity evolves downstream, and eventually becomes saturated in amplitude after a certain distance. The maximum u-velocity turbulence between the nozzle exit and the impingement plate have been reported in the range of $15 - 30$ % of the jet exit velocity [47, 48, 2, 7]. As the gas propagates in the middle of the impingement distance, the maximum turbulence intensity remains fairly constant, exhibiting another local peak just before impingement ($z/H \approx 0.95$). The maximum v-turbulence also seem to remain fairly constant over the impingement length, saturating at similar amplitudes as the u-turbulence, and then slightly decreasing as the impingement plate is approached. Eventually as the flow stagnates, the u-velocity fluctuations are dampened, and the turbulent kinetic energy is transferred into the v-velocity fluctuations, as the flow is re-directed. This orthogonal transfer of the velocity fluctuations in the stagnation region have been reported by Ritcey et al. [7] in planar impinging jets, and Hammad and Milanovic [48] in circular impinging jets. The fluctuating velocity intensity evolution in a non-excited planar impinging gas jet will be further investigated in the current study.

There is little experimental data in the literature on the fluctuating velocity characteristics of self-excited planar impinging gas jets. Note that, in the case of forcing, or the existence of strong feedback, there is a dominant frequency component in the flow. This fluctuating velocity field now is a combination of the turbulence, and coherent velocity fields. Arthurs [49] show the u and v-velocity fluctuation intensities over different points in the oscillation cycle of a self-excited impinging planar gas jet using PIV in Figure 5.1. The intensity $|u'|$ and $|v'|$ in Figure 5.1 is defined by taking the maximum velocity, subtracting the minimum velocity, and dividing by two, at each particular location in the flow field to determine the fluctuating veloc-

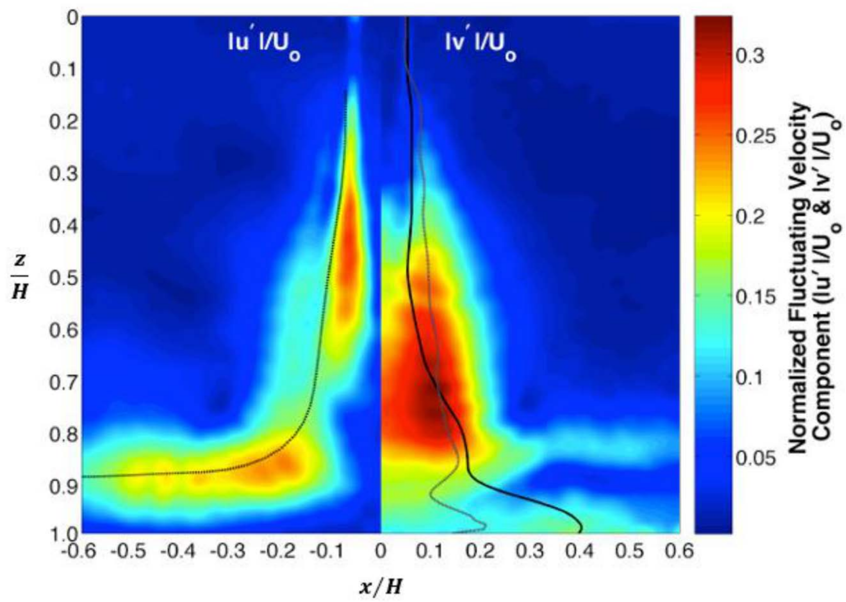

Figure 5.1: Downstream u-velocity fluctuation intensity (left) and cross-stream v-velocity fluctuation intensity (right) on a self-excited planar impinging gas jet in the fluid resonant regime (Ma = 0.9, H/W = 10.5, and W = 3 mm). The velocity fluctuations here are normalized by their jet exit velocity U_0. The dotted line in the left plot indicates the path of the coherent vortex structures, and the black and gray line in the right plot represent the location of the maximum stream-wise and cross-stream velocity fluctuations, respectively. Reproduced with permission from Arthurs [49].

ity amplitude. In Figure 5.1, the Mach number is set to Ma=0.9, impingement ratio H/W=10.5, and nozzle width W=3 mm, which are conducive to self-excited fluid resonant conditions. The z and x coordinates in Figure 5.1 depict distances away from the jet nozzle exit and along the impingement plate, respectively. These distances are non-dimensionalized with the nozzle width W, and velocity fluctuations non-dimensionalized with their jet exit velocity U_0. The dotted gray line in the left plot of Figure 5.1 represents the path of coherent vortex structures in the jet flow field, and the black and gray line in the right plot represent the spatial locations of the maximum amplitude of the u and v-velocity fluctuations, respectively. During self-excitation, the u-velocity fluctuation intensity distribution effectively shortens in the impinging shear layer, concentrating mostly near the center of the impingement distance ($z/H \approx 0.45$). The v-velocity fluctuation intensity distribution in the impinging shear layer becomes wider, diffusing inwards towards the jet centerline, and expanding outwards spatially as the impingement plate is approached, shown in Figure 5.1. In Arthurs [49], this feature was argued to be caused by the jet column dynamics, and coherent vortex structures present in the flow field.

5.2 Experimental Facility

5.2.1 Jet Setup

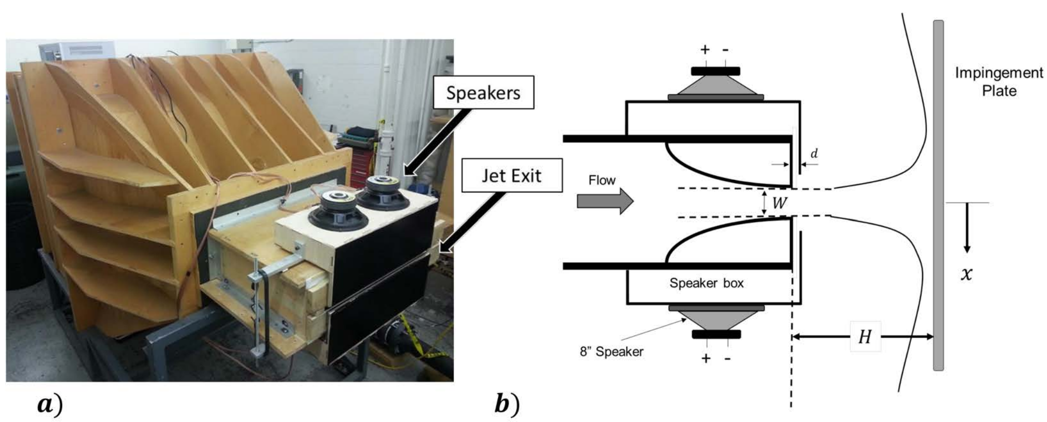

Figure 5.2: a) Planar gas jet with speaker boxes depicted at exit of wind-tunnel. b) Cross-sectional schematic of the planar impinging gas jet, indicating x-coordinate. The y-coordinate is into the page.

The experimental planar impinging gas jet setup is constructed from nozzle inserts positioned at the outlet of an open-loop wind-tunnel shown in Figure 5.2 a).

The jet nozzle inserts were manufactured from laser-cut birch ribs with smooth formed sheet metal surfaces creating a converging elliptical contour with a minor to major axis ratio of 2.4:1. The jet nozzle width is set to W = 15 mm, and the jet exit flow velocity to U_{jet} = 11 m/s, thus maintaining a constant jet Reynolds number Re_{jet} = $U_{jet}W/\nu_a$ = 11000. The aspect ratio of the planar jet (jet span L: nozzle width W) is 50:1, to ensure two-dimensional behaviour. A cross-sectional schematic of the planar impinging gas jet setup is provided in Figure 5.2 b). On the top and bottom of the planar gas jet, two speaker boxes are installed that have focused planar synthetic jet actuators near the nozzle exit. Each speaker box holds two eight inch diameter 500 Watt sub-woofers, which are controlled by an external Sony AV multi-channel amplifier and BK frequency generator. A large 122 cm x 61 cm x 12.7 mm acrylic plate mounted on an Isel three-axis traverse situated in front of the planar gas jet serves as an impingement plate, with an impingement distance set to a constant eight times the nozzle width. A schematic of the synthetic jet arrangement near the nozzle exit is shown in Figure 5.3 a). The synthetic jet nozzle spacing is set to d = 3 mm, and can provide anti-symmetric forcing to the main jet column. Time traces of the synthetic jet actuator output signal are shown in Figure 5.3 b), c), and d) for the 36 Hz, 70 Hz, and 100 Hz forcing cases. These measurements were taken at the edge of the shear layer (black circle indicated in Figure 5.3 a)) with the main jet flow off (U_{jet} = 0 m/s). Due to the non-linearity of the synthetic jet signals, the forcing amplitudes were defined as the average maximum acoustic particle velocity u'' exposed to the jet column, and were adjusted to order 1 % the jet exit velocity for all cases ($\frac{u''}{U_{jet}} \cdot 100 \approx 1\%$). Some common features of synthetic jets are unequal pushing and pulling (non-linear features seen in the time signal), and a mean velocity component due to entrainment effects at the actuator exit (u'' never equals zero). Also note that one cycle of the speaker diaphragm results in two cycles of the velocity signal from the hot-wire, due to the inability of the hot-wire to measure flow directionality.

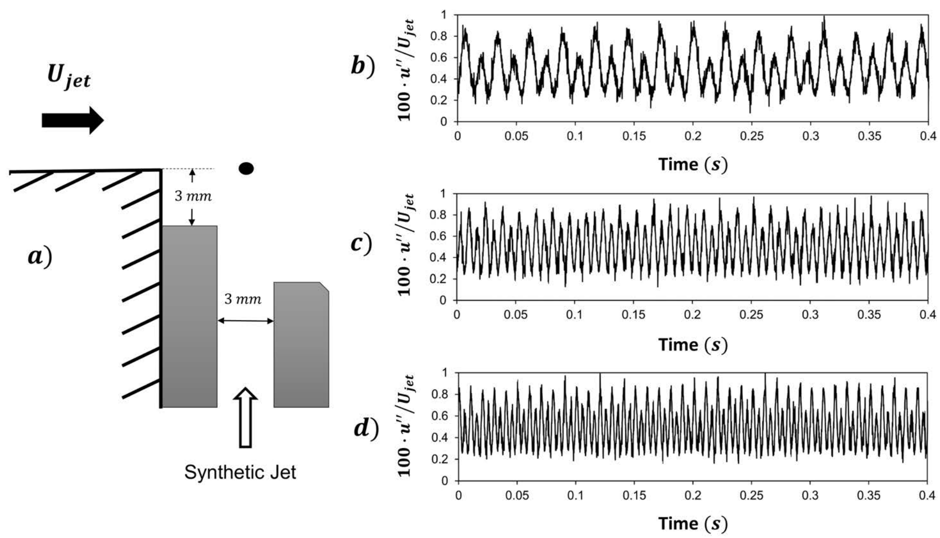

Figure 5.3: a) Schematic of the synthetic jet arrangement at the nozzle exit. Time traces of the synthetic jet signal measured at the edge of the shear layer (solid black dot in a)) for the b) 36 Hz, c) 70 Hz, and d) 100 Hz 1 % amplitude cases. u'' represents the acoustic particle velocity measured using a single hot-wire probe with the main jet flow off ($U_{jet} = 0\ m/s$).

5.2.2 Particle Image Velocimetry (PIV)

PIV was performed to obtain fluctuating velocity measurements between the jet exit and the impingement plate. The z and x coordinates represent the distances away from the jet nozzle exit and along the impingement plate, respectively. These distances will be non-dimensionalized by the nozzle width W. The field of view is slightly cropped near the impingement plate surface because of laser light reflection (≈ 1 mm), and at the jet exit due to the protrusion of the speaker boxes. The use of black colored non-reflective masking on the speaker box surfaces was implemented to minimize these laser light reflections, shown in Figure 5.2 a). The PIV system consists of a TSI $532\ nm$ New Wave Solo 120XT pulsed Nd:YAG laser, issuing a laser sheet in the vertical plane using a $45°$ $532\ nm$ Edmund's high power laser mirror, mounted on a custom-made light arm assembly. A TSI 4 MP (2048 x 2048 pixel^2) CCD camera is positioned orthogonal to the laser plane to capture the flow field. The camera is equipped with a Nikon AF Nikkor 50 mm lens, and an Edmund's $532\ nm$ narrow bandpass filter. The seeding particles used were bis(2-ethylhexyl) sebacate dispersed using a Laskin nozzle generating seeding particle sizes on the order of $1\ \mu$m. For the phase-locked PIV images presented, a TSI LaserPulse 610035 synchronizer, and a custom-made trigger was implemented, where the trigger was fired based on the frequency generator output signal. All phases ϕ in the phase-locked PIV images are relative to the sinusoidal input signal to the top mounted speaker box.

The PIV vector fields were processed with InSight 4G using a first-order deformation-based correlation scheme with a single grid refinement, and with a final window size of 16x16 pixels^2. The validation rate for all vector fields was 99%, and consisted of an ensemble of 200 PIV images. Acceptable convergence of the velocity variance was ensured with this ensemble size. The camera resolution in one direction is 2048 pixels, with 251 velocity data points, revealing a distance between points of Δx = Δz = 8.2 pixels. The spatial resolution of the PIV determined by image calibration in InSight 4G is R = 11.8 pixels/mm, and the time between PIV image pairs is Δt = 23 μs. The displacement gradient error analyzes the error associated with grouping different adjacent velocity vectors into one interrogation region, which is affected essentially by the size of the interrogation regions, and the velocity gradient in the flow. The displacement gradient error in this study was assessed based on the numerical simulation work of Scarano and Riethmuller [50], where different grid-sized PIV processing was performed on a synthetic flow. Their work provides approximate displacement rms error curves as a function of the displacement gradients for two different interrogation window sizes. An error analysis estimate based on these methods indicate a displacement gradient error in our case of under 2% for the mean flow velocity. This will serve as a rough estimate for the mean flow error, whereas real PIV data is also affected by the presence of velocity curvature and noise, which is not accounted for in the present analysis.

PIV also requires the tracking of flow particles in the jet, which are seeded upstream of the nozzle exit. Ideally, the flow particles need to be small enough to follow the gas flow, but large enough to reflect laser light to accurately determine their location, and displacement in the flow. The PIV particle tracking error was performed based on the results of Melling [51]. For high density ratio turbulent flow ($\rho_p/\rho_a = 760$), with approximate particle diameter $d_p \approx 1\mu$m, particle Reynolds number $Re_p = U_{jet}d_p/\nu_a = 0.73$, Stokes number $S_k = d_p\sqrt{2\pi/\tau_k\nu_a} = 0.07$, and maximum frequency based on the Kolmogorov timescales $1/\tau_k$ = 13 kHz, a Reynolds stress error $|\overline{u_p'^2} - \overline{u_a'^2}|/\overline{u_a'^2}$ x $100 \approx 3.7\%$ was estimated.

5.3 Experimental Results

Three frequencies (36 Hz, 70 Hz, and 100 Hz) were used to force the impinging jet in this study. These forcing frequencies correspond to Strouhal numbers St_H = 0.4, 0.76, 1.1 that were based on naturally occurring jet-plate tones, observed experimentally by Arthurs and Ziada [19]. Due to the many different Strouhal numbers assembled using different length scales in the jet literature, we will use dimensional frequency in the results for simplicity. The amplitude of synthetic jet forcing was maintained at approximately 1% of the jet exit velocity U_{jet} with adjustments made to the speaker amplifier output. In this section, we will investigate the general jet response (Section 5.3.1), the fluctuating velocity fields (Section 5.3.2), and the fluctuating kinetic energy (Section 5.3.3) due to synthetic jet forcing.

5.3.1 Forced Jet Response

For relatively low velocity conditions (U_{jet} = 11 m/s), the impinging jet displays different response characteristics dependent on the applied forcing frequency. Figure 5.4 a) shows the mean velocity profiles obtained at a cross-section near the end of the potential core of the impinging jet (z/W = 6). As anti-symmetric forcing is applied by the synthetic jets, the impinging jet oscillates at the applied forcing frequency, and entrains the surrounding fluid. This is evident by the increase in mean velocity profile width, and reduction in centerline velocity under the synthetic jet forcing. An example of the different jet behaviour in response to forcing using the PIV phase-locked vorticity for a single phase (phase ϕ = 0°) is given in Figure 5.4 b), c), and d) for 36 Hz, 70 Hz, and 100 Hz cases, respectively. At 36 Hz anti-symmetric forcing (refer to Figure 5.4 b)), the jet column deflects and oscillates at the forcing frequency, similar to the "linear regime or rocking mode" observed by Arthurs and Ziada [19] on a self-excited impinging jet. At 70 Hz and 100 Hz anti-symmetric forcing (Figure 5.4 c) and d)), the jet column deflects and produces vortex structures that propagate down the impinging shear layers. Coherent vortex structures were identified using the positive second invariant of the phase-locked velocity gradient tensor, or determinant for two-dimensional flows (not shown). A more complete look at the time-series behaviour of the jet response (multiple phases ϕ) of both the vorticity and mean flow field under similar forcing conditions can be found in Ritcey et al. [13]. The 70 Hz and 100 Hz forcing frequencies in the current experiments are also coincidently near frequencies associated with the preferred mode, or most unstable anti-symmetric mode for planar free jets (St_W = $0.12 - 0.19$) confirmed by Iio et al. [11] and Kozlov et al. [39]. We may fall short of this Strouhal number range ($St_W \approx 0.1 - 0.14$) due to the synthetic jet forcing being applied slightly away from the nozzle exit due to the protrusion of the speaker boxes (see Figure 5.3 a)); thus needing to employ a characteristic length slightly greater than the nozzle width W to align with the Strouhal numbers reported in the literature. This unstable anti-symmetric mode is also known to have a subharmonic relationship between the shear layer mode for low-speed laminar plane jets, as discussed by Ho and Hsiao [52], which incorporates similar physics to the subharmonic forcing of mixing layers studied by Ho and Huang [44].

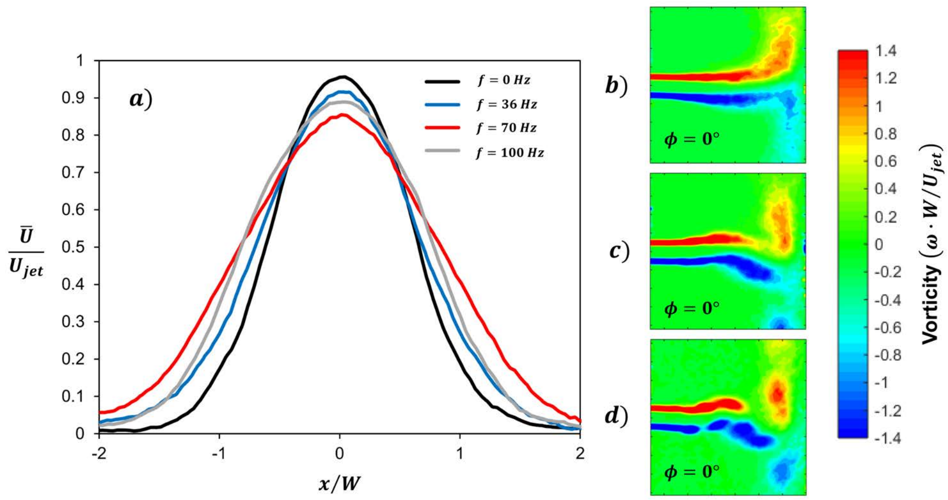

Figure 5.4: a) The mean velocity $\overline{U}$ profiles obtained at z/W = 6 for the different anti-symmetric forcing frequencies tested. Phased-locked PIV vorticity plots (phase ϕ = 0°) under anti-symmetric b) 36 Hz, c) 70 Hz, d) 100 Hz forcing.

5.3.2 Fluctuating Velocity Fields

The rms of the velocity fluctuations were obtained using an ensemble of 200 random PIV images. The velocity fluctuation intensities are defined using the rms velocity fluctuations expressed as a percentage of the jet exit velocity U_{jet}, for the stream-wise u (z-direction), and cross-stream v (x-direction) velocity components, respectively. In Figure 5.5, the stream-wise u-velocity fluctuation intensity flood plots are given for the non-excited case a) 0 Hz, the b) 36 Hz, c) 70 Hz, and the d) 100 Hz anti-symmetrically forced cases. Spatial features of the u-velocity fluctuation intensity flood plots in Figure 5.5 reveal an increased level of u-velocity fluctuations for the 36 Hz case that concentrate in the impinging shear layers, and span most of the impingement distance. As the frequency of anti-symmetric excitation increases to 70 Hz, and 100 Hz, the u-velocity fluctuation intensity distributions in the impinging shear layers effectively shorten in the stream-wise direction, and move away from the impingement plate compared to that of the 36 Hz case. These features in the fluctuating velocity fields may be a result of the periodic jet column dynamics and will be investigated in more detail later. For all the cases, one can also discern a local maximum in the u-velocity fluctuation in the vicinity of the impingement plate ($z/W \approx 7.75$), immediately before these velocity fluctuations are dampened, and re-directed in the stagnation region.

In Figure 5.6, we present the cross-stream v-velocity fluctuation intensity flood plots for the non-excited case a) 0 Hz, the b) 36 Hz, c) 70 Hz, and the d) 100 Hz anti-symmetrically forced cases. The spatial distributions of the flood plots for the v-velocity fluctuation intensities are also altered with anti-symmetric forcing. As 70 Hz and 100 Hz forcing is applied to the jet, there appears to be a merging of v-velocity fluctuation intensity near the jet centerline. This merging of the v-velocity fluctuation intensity distribution eventually leads to a distinct "bib" shape, in Figures 5.6 c) and d), which appears symmetric, and centered about the jet centerline. The jet column dynamics and the presence of coherent vortex structures have been previously argued to transfer energy orthogonally from the u stream-wise, to the v cross-stream fluctuating velocity component, deciphered using two-component PIV [49].

To analyze the fluctuating velocity fields in more detail, the u-velocity fluctuations and v-velocity fluctuations are plotted along the jet centerline (x/W = 0) in Figures 5.7 a) and b). Anti-symmetric forcing amplifies the u-velocity fluctuation intensities along the jet centerline slightly, however, changes in the centerline v-velocity fluctuation intensities are more pronounced. In Figure 5.7 b), the cen-

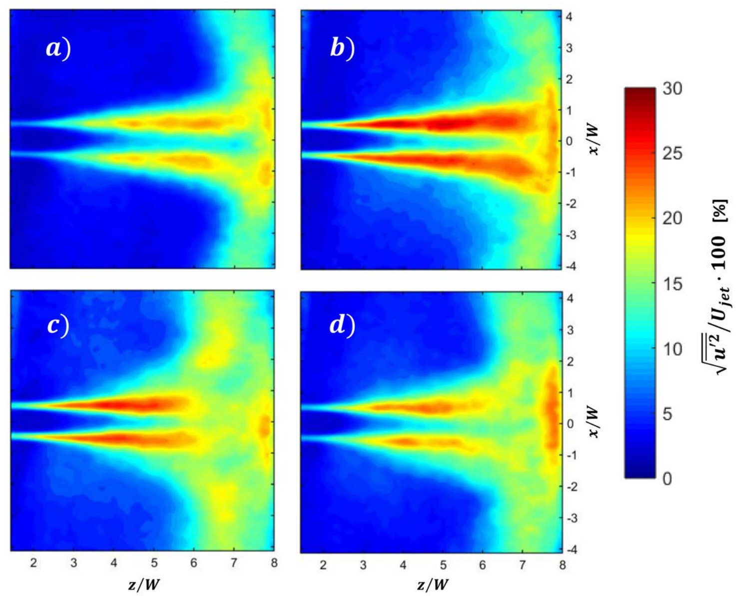

Figure 5.5: Stream-wise u-velocity fluctuation intensity flood plots for the non-excited a) 0 Hz, the b) 36 Hz, c) 70 Hz, and the d) 100 Hz anti-symmetrically forced cases.

terline v-velocity fluctuation increases from 12 % to 22 % at downstream location $z/W \approx 6$ (z/H = 0.75) for the 70 Hz and 100 Hz forced cases. Arthurs and Ziada [49] reported similar v-velocity fluctuation maximums of $\sqrt{v'^2}/U_{jet} \cdot 100 \approx 30$ % at downstream locations $z/H \approx 0.7 - 0.8$ on their high Mach number self-excited impinging gas jet. The maximum fluctuation values in downstream slices within the jet column region ($-1.5 < x/W < 1.5$) are shown for the u and v-velocity fluctuation intensities in Figure 5.7 c) and d), respectively. Interestingly, the u-velocity fluctuation intensity maximums seem to be more affected by forcing, and amplification occurs earlier upstream, compared to that of the maximum v-velocity fluctuation intensities. It appears that the v-velocity fluctuations continue to diffuse towards the jet centerline, as oppose to increasing in absolute magnitude in the jet shear layers. In Figure 5.7 c), the maximum u-velocity fluctuation magnitude

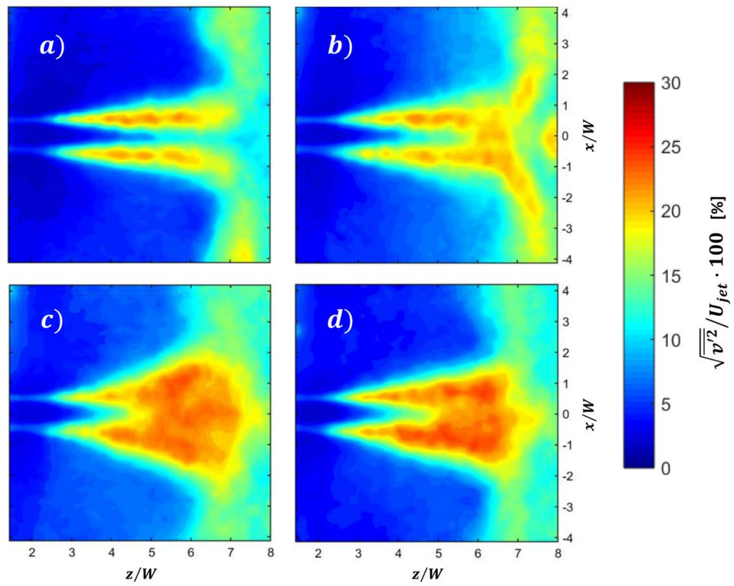

Figure 5.6: Cross-stream v-velocity fluctuation intensity flood plots for the non-excited a) 0 Hz, the b) 36 Hz, c) 70 Hz, and the d) 100 Hz anti-symmetrically forced cases.

for the 70 Hz and 100 Hz cases seem to reside at downstream location $z/W \approx 4$, which was the same maximum amplification location reported by Olsen et al. [26] in their planar free jet study. Another feature to point out in Figure 5.7 c) is that there is a notable local minimum in the u-velocity fluctuation intensity ($\sqrt{u'^2}/U_{jet}$ $\cdot$ $100 \approx 17$ %) at downstream location z/W = 6.75, when the jet is oscillating in the 70 Hz and 100 Hz cases. This feature is not present for the 36 Hz case. The local minimum location also coincides roughly to the local maximum location of the maximum v-velocity fluctuation intensity, shown in Figure 5.7 d) for the 70 Hz and 100 Hz cases.

Fluctuation intensities of the u-component velocity also exhibit another local maximum in the vicinity of the impingement plate shown in Figure 5.7 a) and c) ($z/W \approx 7.75$). Local maximums in the u-velocity fluctuation intensity have been previously reported near impingement surfaces on non-excited planar impinging jets, qualitatively by Maurel et al. [53], and quantitatively by Ritcey et al. [7] ($\sqrt{\overline{u'^2}}/U_{jet} \cdot 100 \approx 20$ %). As we move closer to the impingement plate surface, all velocity fluctuation intensities approach zero, as the velocity fluctuations are dampened by the wall; a result of the no-slip condition. Unfortunately, these zero fluctuation intensity values, and sharp changes in the boundary layer could not be captured with the PIV due to laser light reflection, and are slightly cropped ($\approx$ 1 mm) at the impingement plate location.

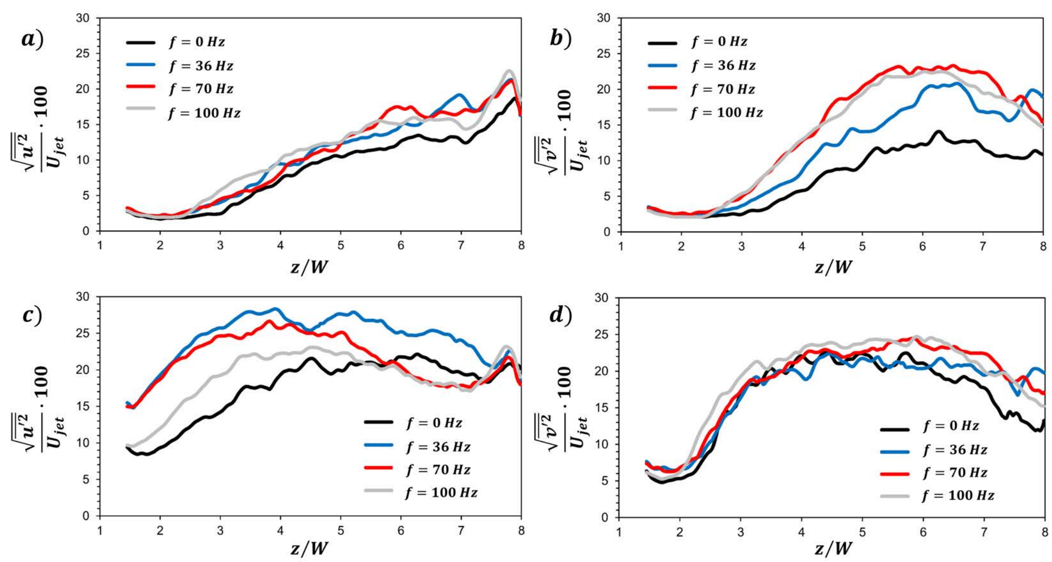

Figure 5.7: a) The stream-wise u-velocity fluctuation intensities along the jet centerline (x/W = 0), b) the cross-stream v-velocity fluctuation intensities along the jet centerline (x/W = 0), c) the maximum stream-wise u-velocity fluctuation intensities in the jet column region ($-1.5 < x/W < 1.5$), and d) the maximum cross-stream v-velocity fluctuation intensities in the jet column region ($-1.5 < x/W < 1.5$) as a function of downstream position (z/W). The 36 Hz, 70 Hz, and 100 Hz cases are under anti-symmetric forcing conditions.

Two important findings can be concluded from this section. First, when the jet is oscillating at 70 Hz and 100 Hz, the fluctuating velocity intensity distributions are clearly different from that of the unexcited jet. This can be best confirmed by the flood plots in Figures 5.5 a) and c) for the u-velocity fluctuations, and Figures 5.6 a) and c) for the v-velocity fluctuations. During 70 Hz anti-symmetric excitation, the u-velocity fluctuation intensity is amplified in the impinging shear layers close to the nozzle, whereas the v-velocity fluctuation intensities tend to populate along the jet centerline forming a “bib”-like shape, which appears symmetric about the jet centerline, shown in Figure 5.6 c). As for the second important finding: When the jet is oscillating at 70 Hz and 100 Hz, the fluctuating velocity fields in Figures 5.5 c) and 5.6 c), are qualitatively similar to the fluctuating velocity fields of a high-speed self-excited planar impinging gas jet under resonance conditions, shown in Figure 5.1. This may suggest that the fluctuating velocity fields are mainly influenced by the jet column dynamics and propagation of coherent vortex structures, even in the absence of a resonating air volume between the jet exit and the impingement plate.

5.3.3 Fluctuating Kinetic Energy (KE')

The fluctuating kinetic energy (KE') is evaluated with the stream-wise and cross-stream fluctuating velocity field, and non-dimensionalized by the square of the jet exit velocity, given in the form $KE' = \frac{1}{2}(\overline{u'^2} + \overline{v'^2})/{U_{jet}}^2$. The KE' flood plots are presented in Figure 5.8 for the no excitation a) 0 Hz, b) 36 Hz, c) 70 Hz, and d) 100 Hz, anti-symmetrically forced cases. These KE' flood plots confirm that the anti-symmetric forcing induced by the planar synthetic jets increases the fluctuating kinetic energy in the impinging shear layers. Another interesting feature revealed in Figure 5.8 c), is that the KE' concentrations in the impinging shear layers migrate away from the impingement plate, diffusing inwards towards the jet centerline, and diffusing outwards in the cross-stream direction, as the jet oscillates at 70 Hz.

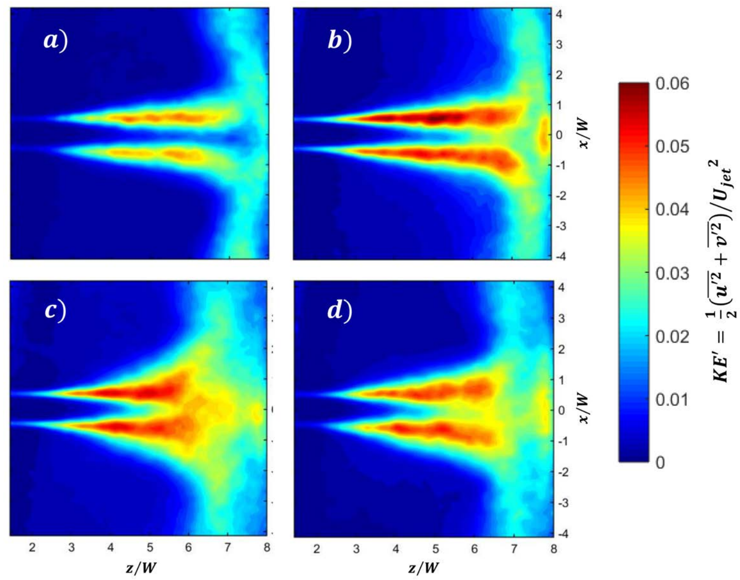

Figure 5.8: The non-dimensional fluctuating kinetic energy ($KE' = \frac{1}{2}(\overline{u'^2} + \overline{v'^2})/{U_{jet}}^2$) for the unexcited jet a) 0 Hz, the b) 36 Hz, c) 70 Hz, and the d) 100 Hz anti-symmetrically forced cases.

Further analysis of the fluctuating kinetic energy distributions in Figure 5.9 a) show an increasing amount of KE' as we progress downstream along the jet centerline. Samimy et al. [36] reported increasing downstream centerline turbulent kinetic energy (TKE) values in their high-speed circular free jet obtained with PIV measurements. The maximum centerline TKE value in their non-excited, baseline case was reported $TKE \approx 0.0175$ approximately eight nozzle diameters downstream. Maximum centerline TKE values reported in the current non-excited case at eight nozzle widths downstream reach a comparable value of $TKE \approx 0.02$. Again, for the unforced condition with the absence of a dominant frequency component, the KE' is representative of the TKE. In Figure 5.9 a), the forced cases seem to reveal a local maximum in the centerline KE' distributions at approximately $6 - 7$ nozzle

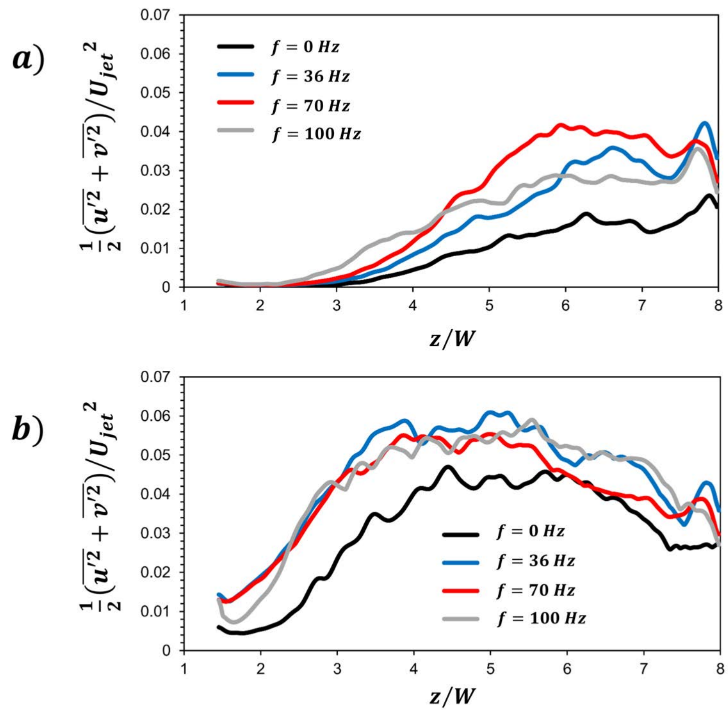

Figure 5.9: a) The non-dimensional fluctuating kinetic energy ($KE' = \frac{1}{2}(\overline{u'^2} + \overline{v'^2})/U_{jet}{}^2$) measured at the jet centerline as a function of downstream direction z/W. b) The maximum non-dimensional fluctuating kinetic energy in the jet column region ($-1.5 < x/W < 1.5$) as a function of downstream direction z/W. All cases are under anti-symmetric forcing.

widths from the jet exit. For the 70 Hz case, the highest KE' value (≈ 0.04) was reached at this downstream location of $z/W \approx 6$. Closer to the impingement plate, at downstream location $z/W \approx 7.75$, another local maximum in the centerline KE' distributions appear of approximately the same magnitude. This local maximum in the centerline KE' distributions is clearly influenced by the local maximums in the u-fluctuations, shown earlier in the Figure 5.5 flood plots. The maximum fluctuating kinetic energy magnitude in the jet column region ($-1.5 < x/W < 1.5$) is plotted as a function of downstream distance in Figure 5.9 b). In this plot, the maximum KE'

values are slightly higher for the 36 Hz case when compared to all other cases. As expected, when the jet column is oscillating under forced conditions, the maximum fluctuating kinetic energy is predominately larger than in the unforced case.

5.4 Triple Decomposition

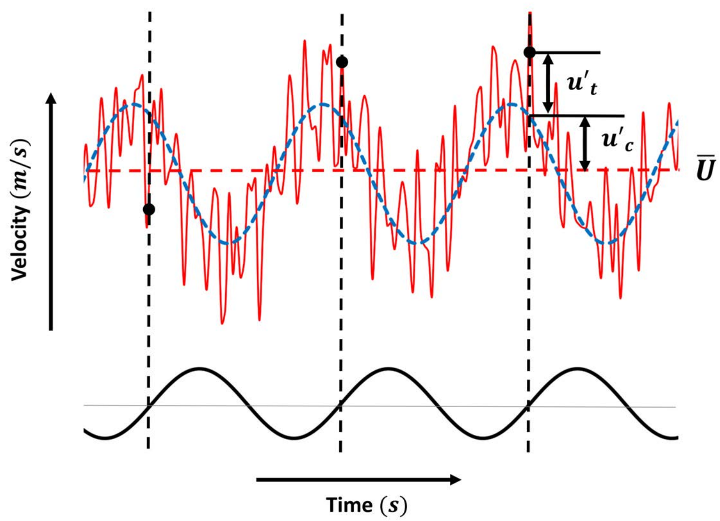

Figure 5.10: A fluctuating velocity signal (red solid line) composed of a coherent velocity u'_c component (blue dashed line) and a turbulent velocity component u'_t. The black signal below is a reference wave of the same coherent frequency used to trigger the PIV at a selected phase.

In this section, an example of a triple decomposition using phase-locked PIV will be examined to further investigate the fluctuating flow field. For a highly periodic flow, the fluctuating velocity u' field will be composed of a coherent fluctuating velocity component u'_c and a turbulent/stochastic fluctuating velocity component u'_t given by Equation 5.3.

$$u' = u'_c + u'_t \tag{5.3}$$

Figure 5.10 graphically illustrates these two components of a fluctuating velocity signal. The red solid line is the fluctuating velocity signal, which contains an organized/coherent wave (blue dotted line) with a superimposed turbulent signal. The black wave is a sinusoidal reference signal of the same frequency (but can be different phase) of the coherent wave motion, which represents our speaker input signal to the synthetic jets. The PIV in this section is triggered at a constant phase using this reference signal (ϕ = 0°), where the fluctuating velocity can be phase-averaged to resolve the coherent velocity on different parts of the wave (blue dashed line). The coherent velocity u'_c can be obtained by subtracting the mean flow velocity $\overline{U}$ from the phase-averaged velocity $<U>$ using the relation: u'_c = $<U>$ - $\overline{U}$. The turbulent part of the fluctuating velocity field can also be obtained at a selected phase by taking the standard deviation of the phase-averaged velocity ensemble. Coherent wave extraction using the triple decomposition method is further detailed in Hussain and Reynolds [54].

In Figure 5.11, 200 phase-locked PIV images for the 100 Hz case is used to determine the coherent and turbulent velocities at a particular instant in the forcing cycle (ϕ = 0°). In Figure 5.11 a) and b), we show the coherent part of the velocity signal for the u and v component, respectively. The spatial distribution of the coherent velocity appears anti-symmetric about the jet centerline for the u-component in 5.11 a), and roughly symmetric about the jet centerline for the v-component in 5.11 b). In Figure 5.11 c) and d), the turbulent part of the fluctuating velocity is extracted using the rms of the phase-locked PIV data for the u and v component,

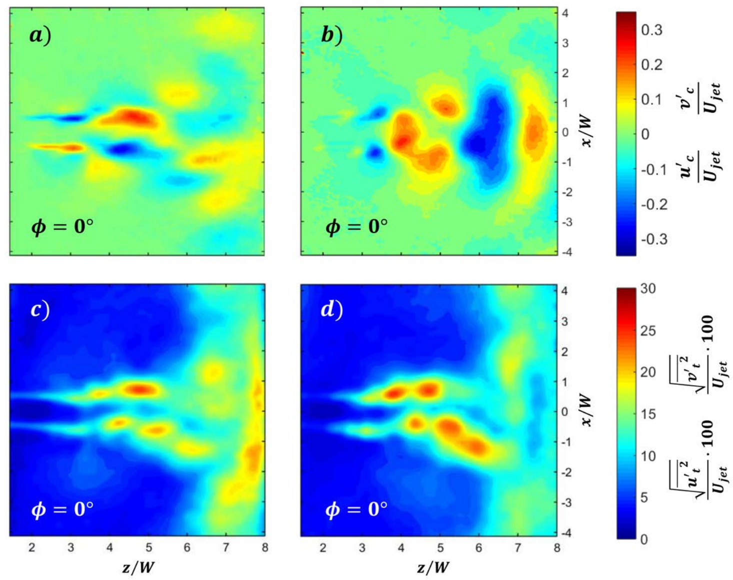

Figure 5.11: a) The coherent u-velocity field of the jet under 100 Hz forcing at phase $\phi = 0°$. b) The coherent v-velocity field under 100 Hz forcing at phase $\phi = 0°$. c) The phase-locked u-turbulence field of the jet under 100 Hz forcing at $\phi = 0°$. d) The phase-locked v-turbulence field under 100 Hz forcing at $\phi = 0°$.

respectively. Here, the turbulence appears to concentrate around regions of strong vorticity with reference to the 100 Hz phase-locked vorticity field given in Figure 5.4 d), and in the vicinity of the wall region for the u-component turbulence. A drawback to the triple decomposition method is that in order to resolve the rms coherent velocity fluctuation fields, many phase-locked cases would be required for each forcing frequency to adequately resolve the time series of the jet response. A different approach to obtain the rms coherent velocity fields will be presented in Section 5.5.3.

5.5 Proper Orthogonal Decomposition (POD)

Proper orthogonal decomposition (POD) is a flow analyzing technique that utilizes pattern recognition in random snapshots of a turbulent flow, to obtain a hierarchy of eigenfunctions that can be used to reconstruct the fluctuating velocity field. These eigenfunctions are ordered in terms of highest mean-square error, and can be interpreted as spatial modes in the flow field contributing the most fluctuating kinetic energy. First implemented in turbulent flows by Lumley [55], it has now been an analysis tool in many different flows, such as reactive flows in combustion chambers [56], unstable swirling jets [57], turbulent jets in cross-flow [58], and circular impinging jets [59]. In some POD studies, large amounts of time-resolved PIV images can also be obtained with high-speed cameras, where a temporal POD analysis can be performed, retrieving Fourier coefficients and frequency spectra.

5.5.1 Snapshot Approach

In the current study, the POD was performed using N=200 random instantaneous PIV images (similar to that of Hammad and Milanovic [59]) to provide the most energetic spatial POD modes in the fluctuating velocity field. These random PIV images are uncorrelated with time. A basic description of the snapshot spatial POD procedure is similar to that found in Meyer et al. [58], and will be given as follows: First, a snapshot matrix S will be constructed with the PIV fluctuating velocity fields configured using Equation 5.4. This matrix takes an instantaneous PIV vector field (mxn pixels) and places all the fluctuating velocities into the first column of S. This process is repeated for each instantaneous PIV snapshot N filling all the columns of the snapshot matrix S.

$$S = [s^1, s^2, ..., s^N] = \begin{bmatrix} {u'}_1^1 & \dots & {u'}_1^N \\ \vdots & \ddots & \vdots \\ {u'}_{mn}^1 & \dots & {u'}_{mn}^N \\ {v'}_1^1 & \dots & {v'}_1^N \\ \vdots & \ddots & \vdots \\ {v'}_{mn}^1 & \dots & {v'}_{mn}^N \end{bmatrix} \tag{5.4}$$

The square covariance matrix C is then constructed using Equation 5.5, containing the transpose, and the original form of the snapshot matrix. This matrix contains information on the joint variability of the fluctuating velocity, with each instantaneous PIV snapshot of the jet flow. The covariance matrix can then be used to solve the eigenvalue problem in Equation 5.6, where eigenvectors Ψ and eigenvalues Λ can be retrieved. The fluctuating velocity field can be expressed as a linear combination of these eigenvectors, thus acting as a series of orthogonal basis functions. The eigenvectors can also be ordered in terms of their associated eigenvalues, from largest to smallest, thus providing a hierarchy of significant contribution to the original fluctuating velocity field.

$$C = S^T S \tag{5.5}$$

$$C\Psi^i = \Lambda^i \Psi^i \tag{5.6}$$

$$\varphi^i = \frac{\sum_{k=1}^{N} \Psi_k^i s^k}{|| \sum_{k=1}^{N} \Psi_k^i s^k ||} \tag{5.7}$$

Finally, the POD modes can be projected onto the original dataset using the eigenvectors in Equation 5.7, where i=$1, 2, ..., N$ represents the mode number. This can be done to retrieve the POD modes for both the u and v-component of fluctuating velocities in Equation 5.7. The relative fluctuating kinetic energy contribution of each mode, from the combined fluctuating velocity components ($\overline{u'^2}$ + $\overline{v'^2}$), can also be evaluated based on its eigenvalue contribution to the whole set N, using Equation 5.8. The relative KE' from each POD mode is evaluated for the first five modes using different numbers of PIV images (50 images, 100 images, 200 images) shown in Figure 5.12 a), b), and c) for the 36 Hz, 70 Hz, and 100 Hz cases, respectively. POD modes for the unforced jet, and all higher POD modes ($i > 2$), each contribute significantly less energy to the fluctuating velocity field, and require more PIV images to obtain convergence.

$$KE'_i = \frac{\Lambda^i}{\sum_{k=1}^{N} \Lambda^k} \tag{5.8}$$

5.5.2 Dominant POD Modes (i=1 and i=2)

Forcing the jet column anti-symmetrically over this range of frequencies produces a strongly periodic flow. As a result, the first two POD modes (φ^1 and φ^2) contribute the largest amount of energy to the fluctuating velocity field compared to the higher modes, and converged using only 200 random PIV images shown in Figure 5.12 a)-c). The cumulative energy content of the first two POD modes are 30.7%, 32.7%,

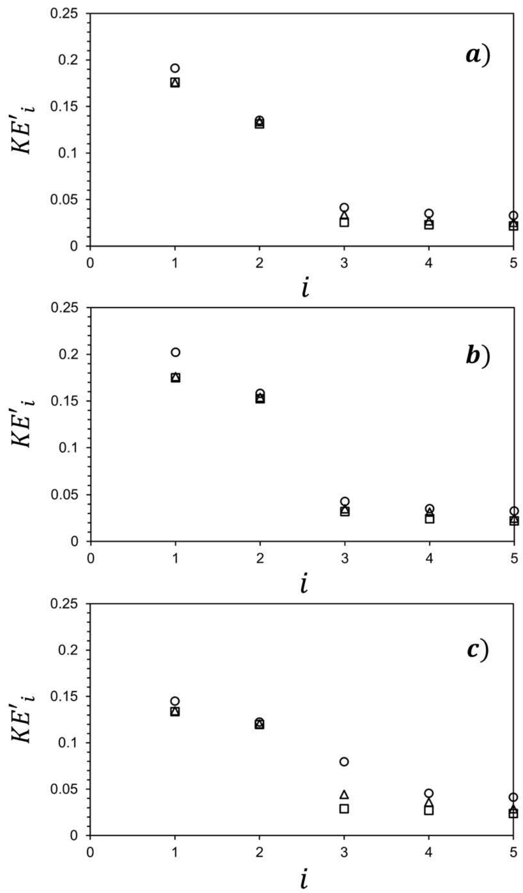

Figure 5.12: The relative fluctuating kinetic energy of the ith POD mode (KE'_i) using different numbers of PIV images for the a) 36 Hz, b) 70 Hz, and c) 100 Hz cases. ◯ 50 images, △ 100 images, and □ 200 images.

25.3% for the 36 Hz, 70 Hz, and 100 Hz cases, respectively. These values can be compared to the cumulative energy content of roughly 9% for the first two POD modes of the unexcited jet (not shown). POD data for an unstable swirling jet by Oberleithner et al. [57] exhibited similar energy grouping in the first two modes. Their POD data are taken from a circular jet exhibiting a swirling instability showed fluctuating kinetic energy levels for their radial velocity modes of 15% for φ^1, and 14.9% for φ^2, totaling $\approx 30\%$ KE' for the first two POD modes. The relatively high

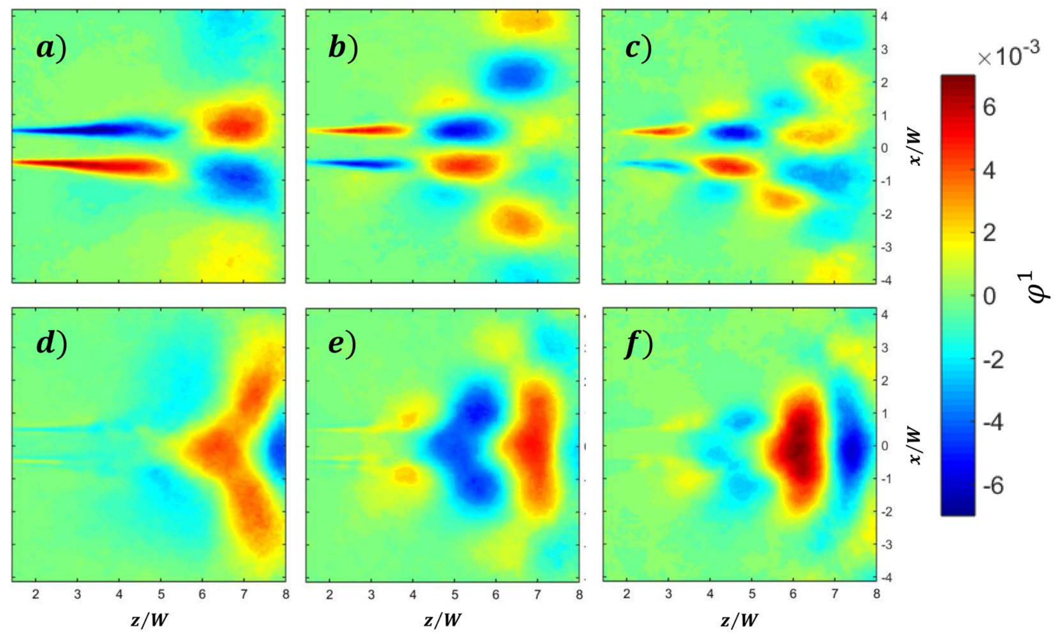

Figure 5.13: The first POD mode φ^1 for the u-component of velocity for the a) 36 Hz, b) 70 Hz, and c) 100 Hz forcing cases. The first POD mode φ^1 for the v-component of velocity for the d) 36 Hz, e) 70 Hz, and f) 100 Hz forcing cases.

energy content of the first two POD modes of the fluctuating velocity field were argued to be associated with a traveling wave feature in the flow [57]. The first and second POD modes for the current u and v fluctuating velocities are displayed in Figures 5.13 and 5.14. The u-component POD mode shapes (Figures 5.13 a)-c) and 5.14 a)-c)) have spatial wavelength features proportional to the forcing frequency, and the v-component of the POD modes (Figures 5.13 d)-f) and 5.14 d)-f)) appear as stacked-liked structures symmetric about the jet centerline. For the 100 Hz case in Figures 5.13 c), f) and 5.14 c), f) note the similarity to the coherent velocity field obtained using the triple decomposition previously in Figure 5.11 a) and b). These first two POD modes encompass the coherent or organized wave motion of the jet flow.

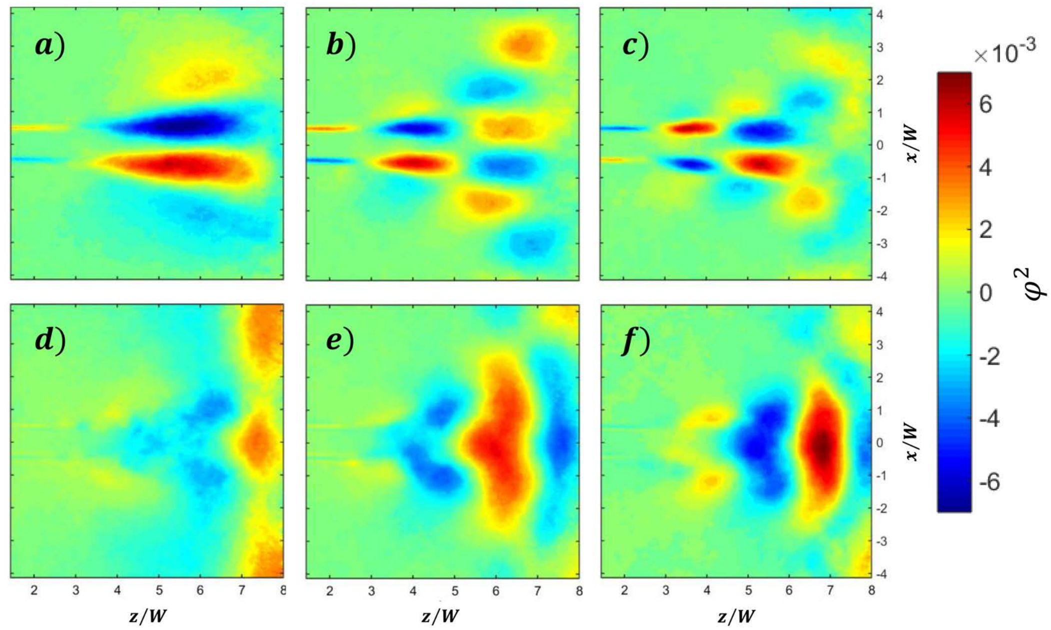

Figure 5.14: The second POD mode φ^2 for the u-component of velocity for the a) 36 Hz, b) 70 Hz, and c) 100 Hz forcing cases. The second POD mode φ^2 for the v-component of velocity for the d) 36 Hz, e) 70 Hz, and f) 100 Hz forcing cases.

5.5.3 Low Order Reconstruction of the Fluctuating Velocity Field

A low order reconstruction of the fluctuating velocity field was performed to assess the amplitude of coherent motion in the jet flow field under forcing conditions. Low order POD reconstructions have been previously employed to approximate the coherent velocity fields in unstable swirling jets [57], and applied to jets in counterflow to determine the dynamic contributions of the individual POD modes [60]. To carry out a low order velocity reconstruction, we first added back the mean flow to the instantaneous PIV snapshots. Next, the POD procedure was repeated (Equations 5.4-5.8) and the amplitude coefficients of the POD were determined using Equation 5.9 (superscript T indicates the transpose). Finally, a low order reconstruction of the instantaneous PIV snapshots $\tilde{S}$ is obtained by projecting the dominant POD modes (φ^1 and φ^2) with their respective amplitude coefficients onto the zeroth mode using Equation 5.10. The low order reconstruction of the velocity fields contain only the zeroth POD mode (i = 0), and the first two POD modes (i = 1 and i = 2) with the remaining higher POD modes nulled.

$$A = [\varphi^0, \varphi^1, \ ... \ \varphi^{N-1}]^T S \tag{5.9}$$

$$\tilde{S} = [\varphi^0, \varphi^1, \varphi^2, 0 \ ... \ 0]A \tag{5.10}$$

The reconstructed instantaneous PIV snapshots are contained within the matrix $\tilde{S}$, which has the same matrix dimensions as S. The fluctuation levels due to only the first two dominant modes (φ^1 and φ^2; in essence the coherent velocity fluctuations) can be obtained by taking the rms of each row within $\tilde{S}$. Figure 5.15 a)-f) display flood plots of the coherent velocity fluctuation levels obtained using the low order reconstruction for the u-component and v-component velocity under different forcing frequencies. The unique features in Figure 5.15 a)-f) include, higher velocity fluctuation levels in the impinging shear layers in the u-component (horizontal streaks on either side of the jet centerline), which decrease towards the impingement plate. Also grouping of the v-component coherent velocity fluctuations (circular shape) emerge near the impingement plate and jet centerline for the 70 Hz and 100 Hz cases. The turbulent or stochastic velocity fields were also approximated in Figure 5.16 by taking the total velocity fluctuations in Figures 5.5 and 5.6, and subtracting the coherent velocity fluctuations determined using the POD in Figure

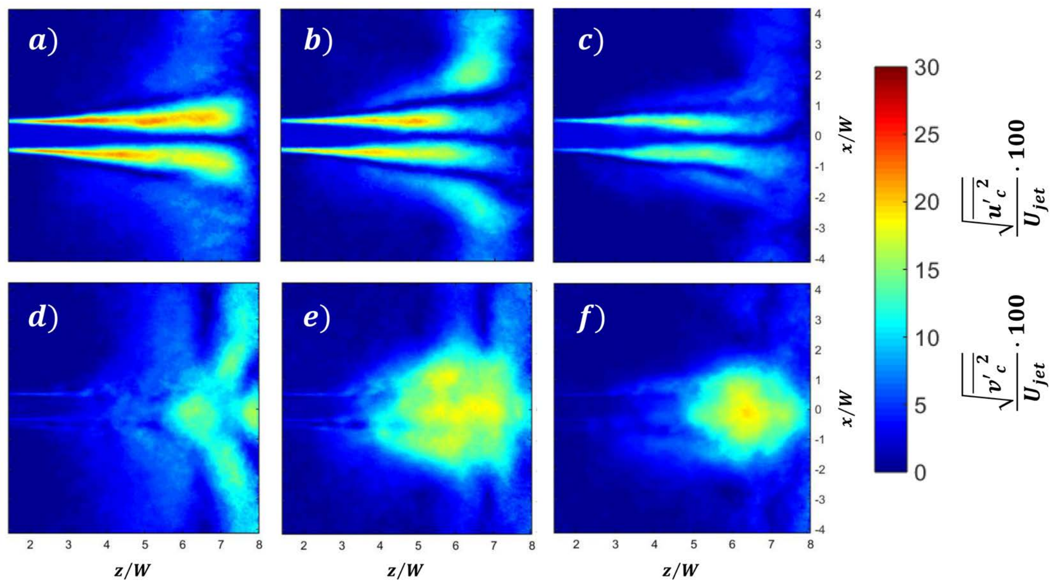

Figure 5.15: The u-component (stream-wise) coherent velocity fluctuations using the low order reconstruction of the velocity field for the a) 36 Hz, b) 70 Hz, and c) 100 Hz forcing cases. The v-component (cross-stream) coherent velocity fluctuations using the low order reconstruction of the velocity field for the d) 36 Hz, e) 70 Hz, and f) 100 Hz forcing cases. These fluctuation levels are associated with the periodic motion of the jet column.

5.15. To perform this operation properly, we subtract variances ($\overline{u_t'^2}$ = $\overline{u'^2}$ - $\overline{u_c'^2}$). The results are an approximation to the u and v turbulence fields in Figure 5.16 for different forcing frequencies. The u-velocity fluctuations in the turbulence fields predominantly concentrate within the impinging jet shear layers, and in a localized region near the impingement plate. Higher u-turbulence near the impingement plate was also verified in the triple decomposition in Figure 5.11 c).

Further examination of the coherent velocity fields in Figure 5.15 a)-f), and turbulent velocity fields in Figure 5.16 a)-f), are presented in Figure 5.17. In Figure 5.17, the maximum fluctuation levels in the jet column region ($-1.5 < x/W < 1.5$) are plotted as a function of downstream z/W position. The maximum coherent ve-

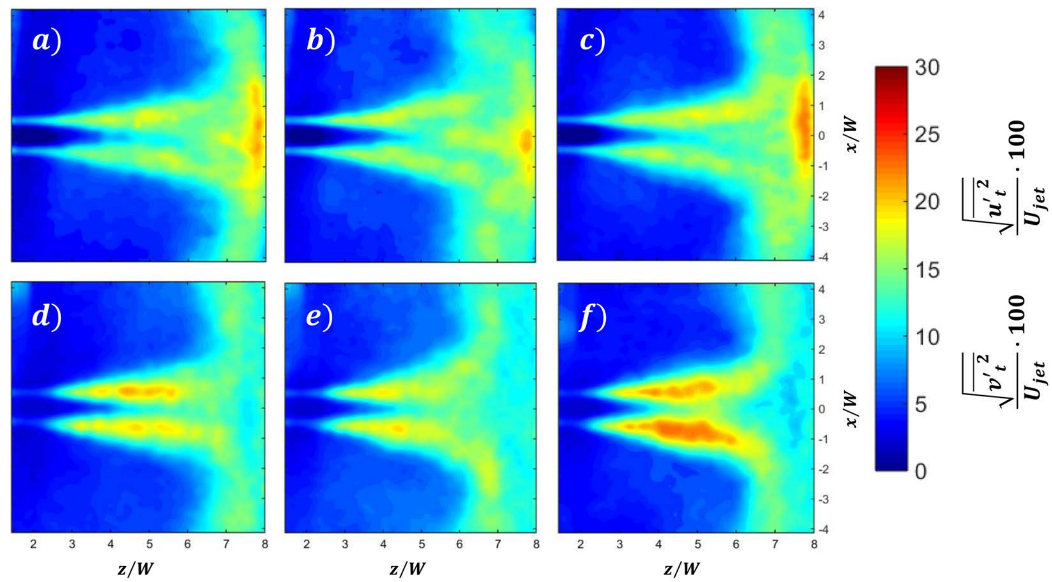

Figure 5.16: The u-component (stream-wise) turbulence field for the a) 36 Hz, b) 70 Hz, and c) 100 Hz forcing cases. The v-component (cross-stream) turbulence field for the d) 36 Hz, e) 70 Hz, and f) 100 Hz forcing cases.

locity fluctuations associated with the periodic motion of the jet column are shown to increase in the u-component in the middle of the impingement distance, and then decrease towards the impingement plate, as shown in Figure 5.17 a). On the contrary, the maximum v-component of the coherent velocity fluctuations is low near the jet exit, and increases as the flow approaches the impingement plate, as depicted in Figure 5.17 b). As the jet column oscillates at the forcing frequency, the flow in the shear layers experience instances where the velocity is high, and instances where the velocity is low (as the core of the jet flow moves away). This would result in a large u-velocity fluctuation level associated with the periodic motion of the jet column. Downstream near the stagnation region of the jet, the v-velocity fluctuations would also experience instances where the flow velocity is high and low due to the mode shape, and oscillation of the jet column.

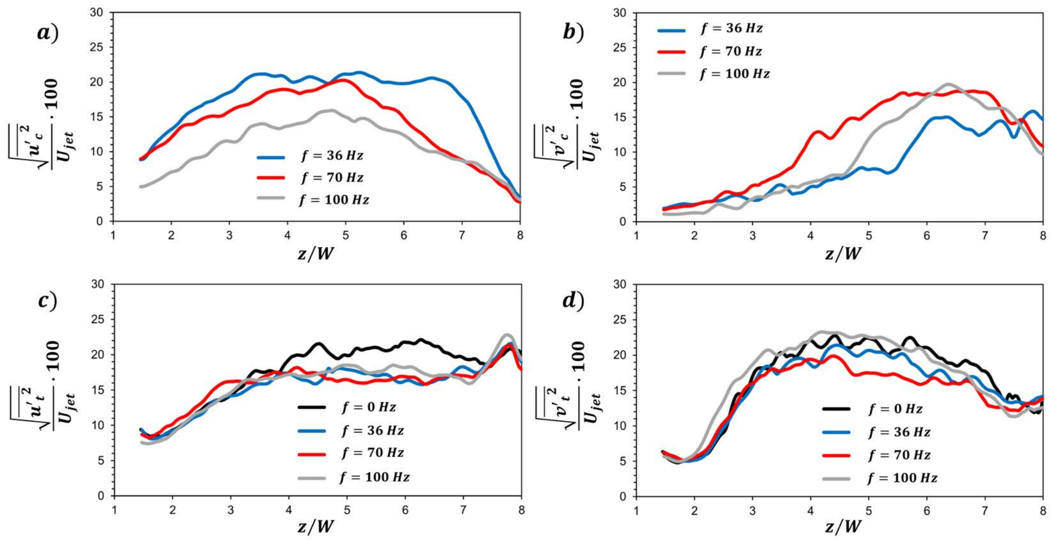

Figure 5.17: a) The maximum coherent u-velocity fluctuation for the 36 Hz, 70 Hz, and 100 Hz cases. b) The maximum coherent v-velocity fluctuation for the 36 Hz, 70 Hz, and 100 Hz cases. c) The maximum u-turbulence fluctuations for the 0 Hz, 36 Hz, 70 Hz, and 100 Hz cases. d) The maximum v-turbulence fluctuations for the 0 Hz, 36 Hz, 70 Hz, and 100 Hz cases. All values are taken within the jet column region ($-1.5 < x/W < 1.5$).

The turbulence field maximums in the jet column region ($-1.5 < x/W < 1.5$) are also presented in Figure 5.17 c) and d) for the u and v component, respectively. The maximum turbulence for the forced cases show similar behaviour to the unforced case, but with a reduction in turbulence ($\approx 23\%$ for the 70 Hz case at z/W = 6), most notably in the u-component between z/W = $4 - 7$ shown in Figure 5.17 c).

5.6 Conclusions

When a planar gas jet impinges on a surface, such as in a wiping operation, a number of jet-plate tones can be produced (dependent on the jet exit velocity and impingement plate distance). The dominant acoustic tone in the frequency spectrum is associated with the oscillation of the jet column, and in some high-speed resonant conditions, impingement of coherent vortex structures. In this study, we have enhanced jet column oscillations (evident by the wider mean velocity profiles and phase-locked vorticity shown in Figure 5.4) in the impinging shear layers by acoustically forcing a low-speed planar impinging gas jet using anti-symmetric forcing at the jet nozzle exit. Previous studies have investigated the acoustics, mean flow field, and impingement plate properties, such as maximum pressure gradients, and maximum skin friction under forced conditions. This study focused on the fluctuating velocity characteristics under forced conditions, such as the fluctuating intensity fields, KE' fields, along with coherent fluctuating velocity, and turbulence fields determined using a low order flow reconstruction with the POD.

Under forcing conditions where the jet is unstable, the initial fluctuation intensity fields appeared to be very different from the unforced jet. In particular for the 70 Hz and 100 Hz cases, the stream-wise u-velocity fluctuation intensity amplifies near the jet exit in the impinging shear layers, and the cross-stream v-velocity fluctuation intensity begins to form a “bib”-shaped feature near the jet centerline. Anti-symmetric vortex structures were also previously found under the 70 Hz and 100 Hz conditions, shedding from side to side of the jet centerline. For these cases, the fluctuation intensity fields are clearly different from that of a unforced jet, and remarkably similar to a high-speed impinging jet under fluid resonant conditions (Figure 5.1). From the KE' analysis, it is apparent that the overall effect of the synthetic jet actuators is an increase in the KE' in the impinging jet shear layers during forcing.

To analyze the effects of the periodic jet column motion on the fluctuating velocity fields, we performed a POD analysis to determine the modes with the largest fluctuating kinetic energy contribution. The spatial features of the dominant POD modes were also complemented with a triple decomposition of the velocity field at a specific phase in Section 5.4. By projecting the two dominant POD modes (φ^1 and φ^2) onto the zeroth mode with their respective amplitude coefficients, a low order reconstruction of the instantaneous PIV images was obtained. An approximation of the rms coherent velocity fluctuation fields is then determined from the rms of these low order velocity reconstructions. The coherent velocity fields reveal that the total fluctuation level increases in the u-component (concentrated in the shear layers near the jet exit), and the central merging of the v-component are in fact a byproduct of the periodic motion of the jet column during forcing. The "bib"-shaped feature in Figures 5.1 and 5.6 c)-d) is a result of the combination of the coherent and turbulence field characteristics. An approximation of the turbulence fields were also obtained by subtracting the coherent velocity fields generated with the POD analysis, from the total fluctuation intensity fields obtained by the random ensemble. The u-turbulence fields displayed similar characteristics, with concentrated turbulence regions in the impinging shear layers and in the vicinity of the impingement plate. A reduction in maximum turbulence was also noted under synthetic jet forcing, predominately in the u-component of the approximated turbulence fields.

5.7 Nomenclature

A	POD amplitude coefficient matrix
C	Covariance matrix
d	Synthetic jet nozzle width
d_p	Mean diameter of seeding particle
D	Diameter of a circular jet nozzle
f	Frequency
H	Impingement distance
H/W	Impingement ratio
i	POD mode number
KE'	Fluctuating kinetic energy
L	Jet span (y-direction)
Ma	Mach number U_{jet}/ speed of sound
m	Number of pixels in x-direction of PIV image
N	Total number of PIV images
n	Number of pixels in z-direction of PIV image
Re_{jet}	Jet Reynolds number $U_{jet}W/\nu_a$
rms	Root mean square
St_ζ	Strouhal number $f\zeta/U_{jet}$
S	PIV snapshot matrix
$\tilde{S}$	Velocity reconstruction matrix
$\hat{S}$	Stokes number
s	Columns of the snapshot matrix
TKE	Turbulent kinetic energy
t	Time
u	Velocity component in the z-direction
u'	Fluctuating velocity component in the z-direction
U_{jet}	Jet exit velocity
v	Velocity component in the x-direction
v'	Fluctuating velocity component in the x-direction
W	Planar jet nozzle width
x	Flow direction along plate (origin at jet stagnation line)
y	Span-wise direction
z	Plate normal direction (origin at jet nozzle exit)
ζ	Characteristic length
Λ	Eigenvalues of the covariance matrix

ν	Kinematic viscosity
ρ	Density
τ	Fluid timescale
ϕ	Phase angle with respect to the speaker input signal
φ	POD mode
Ψ	Eigenvectors of the covariance matrix

Subscripts

a	Based on properties of air
c	Coherent
k	Kolmogorov scale
max	Maximum
p	Pertaining to seeding particle
t	Turbulent

References

[1] D. Arthurs and S. Ziada, "The planar jet-plate oscillator," *Journal of Fluids and Structures*, vol. 27, no. 1, pp. 105–120, 2011.

[2] M. B. Dogruoz, A. Ortega, and R. V. Westphal, "Measurements of skin friction and heat transfer beneath an impinging slot jet," *Experimental Thermal and Fluid Science*, vol. 60, pp. 213–222, 2015.

[3] M. El Hassan, H. Assoum, R. Martinuzzi, V. Sobolik, K. Abed-Meraim, and A. Sakout, "Experimental investigation of the wall shear stress in a circular impinging jet," *Physics of Fluids (1994-present)*, vol. 25, no. 7, p. 077101, 2013.

[4] R. M. Young, M. Hargather, and G. Settles, "Shear stress and particle removal measurements of a round turbulent air jet impinging normally upon a planar wall," *Journal of Aerosol Science*, vol. 62, pp. 15–25, 2013.

[5] J. Long and T. New, "Vortex dynamics and wall shear stress behaviour associated with an elliptic jet impinging upon a flat plate," *Experiments in Fluids*, vol. 57, no. 7, pp. 1–18, 2016.

[6] K. Sodjavi, B. Montagné, P. Bragança, A. Meslem, P. Byrne, C. Degouet, and V. Sobolik, "Piv and electrodiffusion diagnostics of flow field, wall shear stress and mass transfer beneath three round submerged impinging jets," *Experimental Thermal and Fluid Science*, vol. 70, pp. 417–436, 2016.

[7] A. Ritcey, J. R. McDermid, and S. Ziada, "The maximum skin friction and flow field of a planar impinging gas jet," *Journal of Fluids Engineering*, vol. 139, no. 10, p. 101204, 2017.

[8] T. Janetzke, W. Nitsche, and J. Täge, "Experimental investigations of flow field and heat transfer characteristics due to periodically pulsating impinging air jets," *Heat and Mass Transfer*, vol. 45, no. 2, pp. 193–206, 2008.

[9] M. Nirmalkumar, V. Katti, and S. Prabhu, "Local heat transfer distribution on a smooth flat plate impinged by a slot jet," *International journal of heat and mass transfer*, vol. 54, no. 1, pp. 727–738, 2011.

[10] R. Kumar, A. Wiley, L. Venkatakrishnan, and F. Alvi, "Role of coherent structures in supersonic impinging jetsa)," *Physics of Fluids (1994-present)*, vol. 25, no. 7, p. 076101, 2013.

[11] S. Iio, K. Hirashita, Y. Katayama, Y. Haneda, T. Ikeda, and T. Uchiyama, "Jet flapping control with acoustic excitation," *Journal of Flow Control, Measurement & Visualization*, vol. 1, no. 02, p. 49, 2013.

[12] C.-W. Kuo, J. Cluts, and M. Samimy, "Effects of excitation around jet preferred mode strouhal number in high-speed jets," *Experiments in Fluids*, vol. 58, no. 4, p. 35, 2017.

[13] A. Ritcey, J. R. McDermid, and S. Ziada, "Effect of jet oscillation on the maximum impingement plate skin friction," *Journal of Fluids Engineering*, vol. 140, no. 9, p. 091201, 2018.

[14] A. Michalke, "On the inviscid instability of the hyperbolictangent velocity profile," *Journal of Fluid Mechanics*, vol. 19, no. 04, pp. 543–556, 1964.

[15] P. Freymuth, "On transition in a separated laminar boundary layer," *Journal of Fluid Mechanics*, vol. 25, no. 04, pp. 683–704, 1966.

[16] S. C. Crow and F. Champagne, "Orderly structure in jet turbulence," *Journal of Fluid Mechanics*, vol. 48, no. 3, pp. 547–591, 1971.

[17] A. F. Hussain and K. Zaman, "The preferred modeof the axisymmetric jet," *Journal of Fluid Mechanics*, vol. 110, pp. 39–71, 1981.

[18] C.-M. Ho and N. S. Nosseir, "Dynamics of an impinging jet. part 1. the feedback phenomenon," *Journal of Fluid Mechanics*, vol. 105, pp. 119–142, 1981.

[19] D. Arthurs and S. Ziada, "Self-excited oscillations of a high-speed impinging planar jet," *Journal of Fluids and Structures*, vol. 34, pp. 236–258, 2012.

[20] D. Arthurs and S. Ziada, "Effect of nozzle thickness on the self-excited impinging planar jet," *Journal of Fluids and Structures*, vol. 44, pp. 1–16, 2014.

[21] A. Hussain and C. Thompson, "Controlled symmetric perturbation of the plane jet: an experimental study in the initial region," *Journal of Fluid Mechanics*, vol. 100, no. 2, pp. 397–431, 1980.

[22] J. Cohen and I. Wygnanski, "The evolution of instabilities in the axisymmetric jet. part 1. the linear growth of disturbances near the nozzle," *Journal of Fluid Mechanics*, vol. 176, pp. 191–219, 1987.

[23] G. Raman, K. B. Zaman, and E. J. Rice, "Initial turbulence effect on jet evolution with and without tonal excitation," *Physics of Fluids A: Fluid Dynamics*, vol. 1, no. 7, pp. 1240–1248, 1989.

[24] S. Rajagopalan and N. Ko, "Velocity and spanwise vorticity measurements in an excited mixing layer of a plane jet," *Experiments in fluids*, vol. 20, no. 5, pp. 346–357, 1996.

[25] S. Alekseenko, D. Markovich, and V. Semenov, "Turbulent structure of a gas-liquid impinging jet," *Fluid dynamics*, vol. 37, no. 5, pp. 684–694, 2002.

[26] J. Olsen, S. Rajagopalan, and R. Antonia, "Jet column modes in both a plane jet and a passively modified plane jet subject to acoustic excitation," *Experiments in fluids*, vol. 35, no. 3, pp. 278–287, 2003.

[27] A.-L. Birbaud, D. Durox, S. Ducruix, and S. Candel, "Dynamics of free jets submitted to upstream acoustic modulations," *Physics of Fluids (1994-present)*, vol. 19, no. 1, p. 013602, 2007.

[28] H. Sato, "The stability and transition of a two-dimensional jet," *Journal of Fluid Mechanics*, vol. 7, no. 01, pp. 53–80, 1960.

[29] F. Chambers and V. Goldschmidt, "Acoustic interaction with a turbulent plane jet: effects on mean flow," *AIAA Journal*, vol. 20, no. 6, pp. 797–804, 1982.

[30] J.-M. Huang and F.-B. Hsiao, "On the mode development in the developing region of a plane jet," *Physics of fluids*, vol. 11, no. 7, pp. 1847–1857, 1999.

[31] G. Kozlov, G. Grek, A. Sorokin, and Y. A. Litvinenko, "Influence of initial conditions at the nozzle exit on the structure of round jet," *Thermophysics and Aeromechanics*, vol. 15, no. 1, pp. 55–68, 2008.

[32] F.-B. Hsiao and J.-M. Huang, "On the evolution of instabilities in the near field of a plane jet," *Physics of Fluids A: Fluid Dynamics (1989-1993)*, vol. 2, no. 3, pp. 400–412, 1990.

[33] S. Ziada, "Feedback control of globally unstable flows: impinging shear flows," *Journal of Fluids and Structures*, vol. 9, no. 8, pp. 907–923, 1995.

[34] L. Azevedo, B. Webb, and M. Queiroz, "Pulsed air jet impingement heat transfer," *Experimental Thermal and Fluid Science*, vol. 8, no. 3, pp. 206–213, 1994.

[35] Y.-L. Yeh, C.-C. Hsu, C.-H. Chiang, and F.-B. Hsiao, "Vortical structure evolutions and spreading characteristics of a plane jet flow under anti-symmetric long-wave excitation," *Experimental Thermal and Fluid Science*, vol. 33, no. 4, pp. 630–641, 2009.

[36] M. Samimy, J.-H. Kim, J. Kastner, I. Adamovich, and Y. Utkin, "Active control of high-speed and high-reynolds-number jets using plasma actuators," *Journal of Fluid Mechanics*, vol. 578, pp. 305–330, 2007.

[37] M. B. Crawley, C.-W. Kuo, and M. Samimy, "Vortex dynamics and sound emission in an excited high-speed jet," in *22nd AIAA/CEAS Aeroacoustics Conference*, p. 2985, 2016.

[38] E. Gutmark and C.-M. Ho, "Preferred modes and the spreading rates of jets," *Physics of Fluids (1958-1988)*, vol. 26, no. 10, pp. 2932–2938, 1983.

[39] V. V. Kozlov, G. R. Grek, and Y. A. Litvinenko, *Plane Jets Affected by Initial Conditions and Acoustic Perturbations*. Springer, 2016.

[40] A. H. Marsh, "Noise measurements around a subsonic air jet impinging on a plane, rigid surface," *The Journal of the Acoustical Society of America*, vol. 33, no. 8, pp. 1065–1066, 1961.

[41] G. Neuwerth, "Acoustic feedback of a subsonic and supersonic free jet which impinges on an obstacle," *NASA TT F-15719*, 1974.

[42] N. S. Nosseir and C.-M. Ho, "Dynamics of an impinging jet. part 2. the noise generation," *Journal of fluid mechanics*, vol. 116, pp. 379–391, 1982.

[43] D. Arthurs, S. Ziada, and F. Goodwin, "Noise generation by the gas wiping jets of continuous galvanizing lines," *Journal of Fluids and Thermal Sciences*, vol. 1, no. 2, p. 85, 2012.

[44] C.-M. Ho and L.-S. Huang, "Subharmonics and vortex merging in mixing layers," *Journal of Fluid Mechanics*, vol. 119, pp. 443–473, 1982.

[45] D. Rockwell and E. Naudascher, "Self-sustained oscillations of impinging free shear layers," *Annual Review of Fluid Mechanics*, vol. 11, no. 1, pp. 67–94, 1979.

[46] G. Raman, "Supersonic jet screech: half-century from powell to the present," *Journal of Sound and Vibration*, vol. 225, no. 3, pp. 543–571, 1999.

[47] J. Zhe and V. Modi, "Near wall measurements for a turbulent impinging slot jet (data bank contribution)," *Journal of fluids engineering*, vol. 123, no. 1, pp. 112–120, 2001.

[48] K. J. Hammad and I. Milanovic, "Flow structure in the near-wall region of a submerged impinging jet," *Journal of Fluids Engineering*, vol. 133, no. 9, p. 091205, 2011.

[49] D. Arthurs, "Self-excited oscillations of the impinging planar jet," *PhD Thesis*, 2012.

[50] F. Scarano and M. L. Riethmuller, "Advances in iterative multigrid piv image processing," *Experiments in Fluids*, vol. 29, no. 1, pp. S051–S060, 2000.

[51] A. Melling, “Tracer particles and seeding for particle image velocimetry,” *Measurement Science and Technology*, vol. 8, no. 12, p. 1406, 1997.

[52] C.-M. Ho and F.-B. Hsiao, “Evolution of coherent structures in a lip jet,” in *Structure of Complex Turbulent Shear Flow*, pp. 121–136, Springer, 1983.

[53] S. Maurel and C. Solliec, “A turbulent plane jet impinging nearby and far from a flat plate,” *Experiments in Fluids*, vol. 31, no. 6, pp. 687–696, 2001.

[54] A. K. M. F. Hussain and W. C. Reynolds, “The mechanics of an organized wave in turbulent shear flow,” *Journal of Fluid Mechanics*, vol. 41, no. 2, pp. 241–258, 1970.

[55] J. L. Lumley, *The structure of inhomogeneous turbulent flows*. Nauka, 1967.

[56] S. Gadiraju, S. Park, D. Gomez-Ramirez, S. V. Ekkad, K. T. Lowe, H.-K. Moon, Y. Kim, and R. Srinivasan, “Application of proper orthogonal decomposition to high speed imaging for the study of combustion oscillations,” in *ASME Turbo Expo 2017: Turbomachinery Technical Conference and Exposition*, pp. V04BT04A031–V04BT04A031, American Society of Mechanical Engineers, 2017.

[57] K. Oberleithner, M. Sieber, C. Nayeri, C. Paschereit, C. Petz, H.-C. Hege, B. Noack, and I. Wygnanski, “Three-dimensional coherent structures in a swirling jet undergoing vortex breakdown: stability analysis and empirical mode construction,” *Journal of Fluid Mechanics*, vol. 679, pp. 383–414, 2011.

[58] K. E. Meyer, J. M. Pedersen, and O. Özcan, “A turbulent jet in crossflow analysed with proper orthogonal decomposition,” *Journal of Fluid Mechanics*, vol. 583, pp. 199–227, 2007.

[59] K. J. Hammad and I. M. Milanovic, “A pod study of an impinging jet flowfield,” in *ASME 2009 Fluids Engineering Division Summer Meeting*, pp. 1477–1485, American Society of Mechanical Engineers, 2009.

[60] S. Bernero and H. Fiedler, “Application of particle image velocimetry and proper orthogonal decomposition to the study of a jet in a counterflow,” *Experiments in Fluids*, vol. 29, no. 1, pp. S274–S281, 2000.

Chapter 6

Discussion

The experimental results presented in Chapters 3, 4, and 5 provide contributions to the fluid dynamics literature by investigating the wiping ability, and flow field of a planar impinging gas jet. This chapter will be devoted to summarizing these contributions and connecting the work together.

In Chapter 3, oil film interferometry (OFI) was implemented on the impingement plate of a planar impinging gas jet to assess the maximum skin friction produced in the stagnation region. The maximum skin friction is an important input parameter in industrial coating weight models, which is used to predict the final coating thicknesses in continuous hot-dip galvanizing. The experimental planar impinging gas jet served as a scaled-up model of an industrial air-knife, which assumes a stationary impingement plate, due to the gas velocities typically being much higher than the steel strip velocities during wiping. The wiping ability of air-knives is sensitive to operating conditions, mainly jet Reynolds number, and impingement distance. The objectives of this study focused on testing the air-knife model wiping ability under a range of these commonly employed parameters

(Re_{jet} = $11000 - 40000$ and H/W = $4 - 10$). OFI was chosen to measure the wall shear stress at the impingement plate because it has previously been shown to be a more robust wall shear stress measuring technique in gas flows, compared to other commonly employed techniques, such as the velocity gradient method, and Preston/Stanton tube methods. These other methods have many intrinsic errors due to their calibration and indirect nature associated with them. The measured skin friction distributions were obtained and used to construct an overall characteristic map of the maximum skin friction as a function of jet Reynolds number and impingement ratio, as presented in Figure 3.18. These maximum skin friction values can be implemented in coating weight models under a range of different air-knife operating conditions, and can also be used to validate CFD model results.

The maximum skin friction map provided in Figure 3.18 highlights how the OFI data behaves in comparison to the semi-empirical maximum skin friction correlations of Phares et al. [29]. Due to the difficulty in measuring skin friction on impinging jets, these semi-empirical correlations have previously served as a benchmark for wall shear stress values in the jet literature. Thus, it was important to compare our results to these prediction curves. The OFI data obtained showed the same decreasing maximum skin friction trends as Phares et al. [29] with jet Reynolds number (scaling with $\sim {Re_{jet}}^{1/2}$). However, the measured OFI data was less sensitive to the jet impingement ratio, particularly when the jet standoff distance was within the potential core length of the jet (i.e $H/W \approx 4 - 6$). Further inspection of Figure 3.18, showed that all of the maximum skin friction OFI data clustered along a band within the maximum skin friction predictions of Phares et al [29], which can agree quite well in some cases (within 5% for H/W = 6), but can also exhibit errors of up to 28% depending on the operating condition of the air-knife.

In Chapter 4, the maximum mean skin friction produced by an air-knife model with the addition of external forcing at the jet nozzle exit was determined. Under some high-speed jet operating conditions, planar impinging gas jets have been previously shown to produce self-excited, large amplitude oscillatory features in the flow and sound field. These features are characterized based on the fluid dynamic, and fluid-resonant regimes associated with impingement plate feedback. The goal of this chapter was to assess the maximum mean skin friction along the impingement plate using OFI under enhanced oscillatory jet response provided by planar synthetic jet actuators. The synthetic jet actuators were employed to force the jet column both anti-symmetrically, and symmetrically at the jet nozzle exit. Under some forcing conditions, the oscillatory response of the jet was amplified, which resulted in large amplitude jet column deflections, and coherent vortex structure propagation down the impinging shear layers. Both of these flow field features were shown to cause increased levels of fluid entrainment into the jet column, and reductions in the centerline velocity of the jet. The changes in the flow field due to forcing also initiated downstream effects at the impingement plate surface. External forcing resulted in decreased maximum mean skin friction values for the frequencies and amplitudes tested, as summarized in Figures 4.19 and 4.20. Reductions in the maximum mean pressure gradient along the impingement plate was also confirmed under forcing conditions, shown in Figure 4.14. By analyzing the maximum skin friction reductions under anti-symmetric and symmetric conditions separately, it was determined that jet column deflection was the main contributor to fluid entrainment, as oppose to the enhancement of vortex structures in the impinging shear layers. The reductions in maximum skin friction and maximum pressure gradient correspond to a lower wiping efficiency, and a higher average coating weight on the impingement plate when compared to the same jet without external forcing. The experimental results of the oscillating air-knife model suggest that if an air-knife was operating in a resonance condition, or exhibiting similar enhanced oscillation features due to external disturbances, the wiping performance of the air-knife will be compromised.

In Chapter 5, the fluctuating velocity field of the oscillatory jet was further analyzed using particle image velocimetry (PIV) and proper orthogonal decomposition (POD). It was found that under anti-symmetric forcing conditions near frequencies close to those associated with jet instabilities, that the oscillatory motion of the jet column was enhanced. In particular, under 70 Hz and 100 Hz anti-symmetric forcing, the resulting fluctuating velocity fields exhibited **i)** a unique amplified u-component fluctuation closer to the jet nozzle exit in the impinging shear layers (shown in Figures 5.5 c and d), as well as **ii)** a widening, and central merging of the v-component fluctuation downstream at the jet centerline (shown in Figures 5.6 c and d). A POD analysis was also performed on the PIV images in the random ensemble. The POD revealed that under the anti-symmetrically-forced cases tested, the first two POD modes contained the largest amount of fluctuating kinetic energy, and represented the periodic motion of the jet column (this was also verified using a triple decomposition of the phase-locked PIV in Figure 5.11). These two dominant POD modes were incorporated into a low order reconstruction of the fluctuating velocity field, as shown in Figures 5.15 a)-f). The low order reconstruction from the

POD analysis showed that the unique features in the fluctuating velocity fields mentioned above, **i)** and **ii)**, are also present in the low order reconstruction, indicating that these features are produced as a result of the coherent motion of the jet column under forcing. The fluctuating velocity fields of the low speed air-knife model (Figures 5.5 c and 5.6 c) was also qualitatively similar to that previously investigated on a high-speed self-excited impinging gas jet, shown in Figure 5.1. These observations suggest that the fluctuating velocity field of a forced jet has similar features regardless of the forcing method (either external or self-excited), and these features are dominated by the periodic jet column dynamics. Additionally, subtracting the coherent velocity fluctuation levels from the total velocity fluctuation levels in the random ensemble allowed for an approximation of the turbulence fields to be obtained, displayed in Figure 5.16 a)-f). These turbulence fields had similar characteristics to the unforced jet (Figure 5.16 a). However, a reduction in turbulence levels near the middle of the impingement distance was noted, predominantly in the random u-component velocity.

Chapter 7

Conclusions

This thesis is a comprehensive investigation of the maximum skin friction and flow field developed by a planar impinging gas jet using oil film interferometry and particle image velocimetry. Specific conclusions are provided in each paper (Chapters 3-5), but here we give a summary of those which are relevant to the hot-dip galvanizing process. Due to the limited amount of reliable skin friction data available for planar impinging gas jets, measurements using a more robust technique called oil film interferometry (OFI) were performed, and were compared to existing skin friction correlations in the literature. A maximum skin friction map was also developed for different air-knife Reynolds numbers and impingement ratios (Re_{jet} = $11000 - 40000$ and H/W = $4 - 10$), which can be used as inputs to coating weight models implemented in continuous hot-dip galvanizing.

Impinging jets are also known to be sensitive to external disturbances, and can become self-excited at higher flow speeds due to established (and amplified) impingement plate feedback loops. The jet response under these conditions exhibit large amplitude jet column oscillations and enhanced vortex structures propagating down the impinging shear layers. For the first time, the effect of jet oscillation on the maximum impingement plate skin friction using oil film interferometry was determined. Enhanced jet oscillations were achieved using planar synthetic jet forcing at the jet nozzle exit using different frequencies ($f = 36, 70, 100$ Hz corresponding to $St_H = 0.39, 0.76, 1.1$, respectively), and forcing amplitudes (1%, 10% of U_{jet}), both in the anti-symmetric and symmetric configuration. The maximum mean skin friction was found to be reduced for all externally-forced cases tested when compared to that of the unforced case. During forcing, the maximum skin friction reductions are facilitated by increased levels of fluid entrainment caused by jet column deflection, and by the enhancement of coherent vortex structures in the impinging shear layers. The increased fluid entrainment levels slowed the jet centerline velocity, and reduced the jets ability to wipe coatings in the stagnation region.

Under jet forcing conditions, the jet flow field statistics, and the proper orthogonal decomposition results revealed strong coherent motions existed in the jet column of the model air-knife. It was also found that the fluctuating velocity fields of a low-speed externally-forced jet have qualitatively similar features to a high-speed self-excited jet. Due to the dynamic similarity between these cases, this may further suggest similar downstream flow effects occur at the impingement plate, such as maximum mean skin friction reductions, and maximum mean pressure gradient reductions for the high-speed self-excited jet. The results of this investigation concluded that mitigating air-knife disturbances, or operating air-knives outside fluid-resonant regimes, would be beneficial to the overall wiping power of air-knives as applied to the continuous hot-dip galvanizing process.

7.1 List of Contributions

(i) A more extensive experimental skin friction data set was provided for a planar impinging gas jets using OFI. The OFI technique is known to be a more robust skin friction measuring technique for gas flows. A parametric map of the maximum skin friction was developed for various air-knife Reynolds numbers Re_{jet} and impingement ratios H/W, which can be implemented as an input parameter to coating weight models used in continuous hot-dip galvanizing.

(ii) The maximum skin friction was shown to be less sensitive to the impingement ratio when the jet standoff distance was within the potential core length of the jet than that suggested by the semi-empirical correlations of Phares et al. [29]. However, similar jet Reynolds number scaling ($C_f \sim {Re_{jet}}^{-1/2}$) was observed consistent with laminar boundary layer skin friction development.

(iii) The effect of jet oscillation on the maximum mean impingement plate skin friction was determined using OFI. The maximum mean skin friction, and maximum pressure gradient on the impingement plate was reduced during jet forcing conditions due to reductions in jet centerline momentum, which were directly correlated to increased levels of surrounding fluid entrainment.

(iv) The maximum mean skin friction was more effectively reduced during anti-symmetric forcing compared to symmetric forcing. This result suggests that jet column deflection was a larger contributor to entrainment compared to the enhancement of vortex structures in the impinging shear layers.

(v) When forcing a jet near jet instability frequencies, a unique amplification of the u-component fluctuation level near the jet exit was found in the impinging shear layers, along with a merging of the v-component fluctuation at the jet centerline. These features in the fluctuating velocity fields were determined to be a result of the coherent motion of the jet column under forcing conditions.

(vi) The fluctuating velocity fields of a low-speed externally-forced planar impinging gas jet was found to have qualitatively similar characteristics to that of a high-speed self-excited planar impinging gas jet. This suggests that the low-speed air-knife model was able to capture comparable jet column dynamics to that of a self-excited high-speed planar impinging gas jet.

(vii) Enhanced jet column oscillations degraded the wiping performance of the model air-knife due to the subsequent reductions in maximum mean skin friction, and maximum pressure gradients developed along the impingement plate. This was observed directly during OFI testing by the increased amount of experiment time required to thin the silicon oil (obtain equivalent fringe spacing) under jet forcing conditions.

7.2 Recommendations for Future Work

(i) Investigate the effects of Mach number and compressibility on the skin friction distributions using OFI. There is very little skin friction research on higher speed planar impinging gas jet flows $Ma>0.3$. The OFI analysis would require the use of calibrated higher viscosity oils ($>$ 50 cSt), and adequate camera magnification or jet scaling to resolve the skin friction distributions along the impingement plate.

(ii) Investigate the effects of air-knife nozzle shape and turbulence intensity at the jet exit on the maximum skin friction developed on the impingement plate using OFI. There may be some nozzle geometries that out-perform traditional nozzle shapes due to differences in boundary layer development, vena contracta effects, fluctuating velocity fields and entrainment effects. The extent of this has not been well investigated.

(iii) Explore pressure sensitive paint (PSP) on planar impinging gas jets. The mean Gaussian pressure profiles and/or the time-resolved pressure effects (Fast PSP) can be obtained at the impingement plate.

(iv) Investigate edge effects on the pressure and skin friction distributions at the impingement plate. This may have applications in air-knife wiping near the sides of the steel strip.

(v) Explore the skin friction developed by a multiple slot air-knife using OFI.

References

[1] C. Ellen and C. Tu, “An analysis of jet stripping of liquid coatings,” *Journal of fluids engineering*, vol. 106, no. 4, pp. 399–404, 1984.

[2] D. Lacanette, A. Gosset, S. Vincent, J.-M. Buchlin, and É. Arquis, “Macroscopic analysis of gas-jet wiping: Numerical simulation and experimental approach,” *Physics of Fluids*, vol. 18, no. 4, p. 042103, 2006.

[3] P. Tamadonfar, *Numerical Investigation of Multiple-Impinging Slot Jets in the Gas-Jet Wiping of Liquid Zinc Coatings*. PhD thesis, 2010.

[4] A. Y. Soufiani, J. McDermid, A. Hrymak, and F. Goodwin, “Numerical investigation of multiple-slot jets in air-knife wiping,” *Journal of Coatings Technology and Research*, vol. 14, no. 5, pp. 1015–1028, 2017.

[5] S. B. Pope, “Turbulent flows,” 2001.

[6] W. J. Dahm and P. E. Dimotakis, “Mixing at large schmidt number in the self-similar far field of turbulent jets,” *Journal of Fluid Mechanics*, vol. 217, pp. 299–330, 1990.

[7] R. D. Blevins, *Applied Fluid Dynamics Handbook*. Transactions of the ASME, New York, Van Nostrand Reinhold Co., pg. 236, 1984.

[8] Michalke, A., 1964. “On the inviscid instability of the hyperbolictangent velocity profile”. *Journal of Fluid Mechanics,* **19**(04), pp. 543–556.

[9] Freymuth, P., 1966. “On transition in a separated laminar boundary layer”. *Journal of Fluid Mechanics,* **25**(04), pp. 683–704.

[10] Kozlov G, Grek G, Sorokin A, et al. Influence of initial conditions at the nozzle exit on the structure of round jet. Thermophysics and Aeromechanics. 2008; 15(1):55–68.

[11] Pritchard, P. J., 2011. *Fox and McDonald's Introduction to Fluid Mechanics*, 8th Edition. John Wiley & Sons New York, pg.444.

[12] V. V. Kozlov, G. R. Grek, and Y. A. Litvinenko, "Plane jets affected by initial conditions and acoustic perturbations," in *Visualization of Conventional and Combusting Subsonic Jet Instabilities*, pp. 51–63, Springer, 2016.

[13] C. B. da Silva, J. C. Hunt, I. Eames, and J. Westerweel, "Interfacial layers between regions of different turbulence intensity," *Annual review of fluid mechanics*, vol. 46, pp. 567–590, 2014.

[14] I. Wygnanski and H. Fiedler, "Some measurements in the self-preserving jet," *Journal of Fluid Mechanics*, vol. 38, no. 03, pp. 577–612, 1969.

[15] G. Heskestad, "Hot-wire measurements in a plane turbulent jet," *Journal of Applied Mechanics*, vol. 32, no. 4, pp. 721–734, 1965.

[16] D. Arthurs and S. Ziada, "Self-excited oscillations of a high-speed impinging planar jet," *Journal of Fluids and Structures*, vol. 34, pp. 236–258, 2012.

[17] S. Beltaos and N. Rajaratnam, "Plane turbulent impinging jets," *Journal of Hydraulic Research*, vol. 11, no. 1, pp. 29–59, 1973.

[18] E. Gutmark, M. Wolfshtein, and I. Wygnanski, "The plane turbulent impinging jet," *Journal of Fluid Mechanics*, vol. 88, no. 04, pp. 737–756, 1978.

[19] K. Selvam, E. Öngüner, J. Peixinho, E.-S. Zanoun, and C. Egbers, "Wall pressure in developing turbulent pipe flows," *Journal of Fluids Engineering*, vol. 140, no. 8, p. 081203, 2018.

[20] Hussain A, Thompson C. Controlled symmetric perturbation of the plane jet: an experimental study in the initial region. Journal of Fluid Mechanics. 1980; 100(2):397–431.

[21] S. C. Crow and F. Champagne, "Orderly structure in jet turbulence," *Journal of Fluid Mechanics*, vol. 48, no. 3, pp. 547–591, 1971.

[22] Iio, S., Hirashita, K., Katayama, Y., Haneda, Y., Ikeda, T., and Uchiyama, T., 2013. "Jet flapping control with acoustic excitation". *Journal of Flow Control, Measurement & Visualization,* **1**(02), p. 49.

[23] C. Ball, H. Fellouah, and A. Pollard, "The flow field in turbulent round free jets," *Progress in Aerospace Sciences*, vol. 50, pp. 1–26, 2012.

[24] C.-M. Ho and F.-B. Hsiao, "Evolution of coherent structures in a lip jet," in *Structure of Complex Turbulent Shear Flow*, pp. 121–136, Springer, 1983.

[25] H. Sadeghi and A. Pollard, "The preferred and shear layer modes in a jet under passive controls," in *Proceedings of 18th Australasian Fluid Mechanics Conference*, pp. 3–7, 2012.

[26] P. Burattini, R. Antonia, S. Rajagopalan, and M. Stephens, "Effect of initial conditions on the near-field development of a round jet," *Experiments in fluids*, vol. 37, no. 1, pp. 56–64, 2004.

[27] Gutmark E, Ho CM. Preferred modes and the spreading rates of jets. Physics of Fluids (1958-1988). 1983;26(10):2932–2938.

[28] J. W. Naughton and M. Sheplak, "Modern developments in shear-stress measurement," *Progress in Aerospace Sciences*, vol. 38, no. 6, pp. 515–570, 2002.

[29] D. J. Phares, G. T. Smedley, and R. C. Flagan, "The wall shear stress produced by the normal impingement of a jet on a flat surface," *Journal of Fluid Mechanics*, vol. 418, pp. 351–375, 2000.

[30] H. Schlichting, "Boundary-layer theory," 1968.

[31] D. J. Phares, G. T. Smedley, and R. C. Flagan, "The inviscid impingement of a jet with arbitrary velocity profile," *Physics of Fluids (1994-present)*, vol. 12, no. 8, pp. 2046–2055, 2000.

[32] G. N. Abramovich, T. Girshovich, S. I. Krasheninnikov, A. Sekundov, and I. Smirnova, “The theory of turbulent jets,” *Moscow Izdatel Nauka*, vol. 1, 1984.

[33] M. El Hassan, H. H. Assoum, V. Sobolik, J. Vétel, K. Abed-Meraim, A. Garon, and A. Sakout, “Experimental investigation of the wall shear stress and the vortex dynamics in a circular impinging jet,” *Experiments in fluids*, vol. 52, no. 6, pp. 1475–1489, 2012.

[34] S. Alekseenko and D. Markovich, “Electrodiffusion diagnostics of wall shear stresses in impinging jets,” *Journal of applied electrochemistry*, vol. 24, no. 7, pp. 626–631, 1994.

[35] K. Kataoka, Y. Kamiyama, S. Hashimoto, and T. Komai, “Mass transfer between a plane surface and an impinging turbulent jet: the influence of surface-pressure fluctuations,” *Journal of fluid Mechanics*, vol. 119, pp. 91–105, 1982.

[36] M. El Hassan, H. Assoum, R. Martinuzzi, V. Sobolik, K. Abed-Meraim, and A. Sakout, “Experimental investigation of the wall shear stress in a circular impinging jet,” *Physics of Fluids (1994-present)*, vol. 25, no. 7, p. 077101, 2013.

[37] L. P. Reiss and T. J. Hanratty, “Measurement of instantaneous rates of mass transfer to a small sink on a wall,” *AIChE Journal*, vol. 8, no. 2, pp. 245–247, 1962.

[38] T. J. Hanratty, “Study of turbulence close to a solid wall,” *Physics of Fluids (1958-1988)*, vol. 10, no. 9, pp. S126–S133, 1967.

[39] T. Mizushina, “The electrochemical method in transport phenomena,” *Advances in heat transfer*, vol. 7, pp. 87–161, 1971.

[40] K. Kataoka and T. Mizushina, “Local enhancement of the rate of heat-transfer in an impinging round jet by free-stream turbulence,” in *Heat transfer 1974; Proceedings of the Fifth International Conference, Tokyo, Volume 2*, vol. 2, pp. 305–309, 1974.

[41] J. Preston, "The determination of turbulent skin friction by means of pitot tubes," *JR Aeronaut. Soc*, vol. 58, pp. 109–121, 1954.

[42] S. Beltaos and N. Rajaratnam, "Impinging circular turbulent jets," *Journal of the hydraulics division*, vol. 100, no. 10, pp. 1313–1328, 1974.

[43] P. Bradshaw and E. M. Love, *The normal impingement of a circular air jet on a flat surface*. HM Stationery Office, 1961.

[44] L. East, "Measurement of skin friction at low subsonic speeds by the razor-blade technique," 1968.

[45] V. Patel, "Calibration of the preston tube and limitations on its use in pressure gradients," *Journal of Fluid Mechanics*, vol. 23, no. 01, pp. 185–208, 1965.

[46] V. Patel and M. R. Head, "Reversion of turbulent to laminar flow," *Journal of Fluid Mechanics*, vol. 34, no. 02, pp. 371–392, 1968.

[47] C. Ching *et al.*, "Effect of tube diameter on preston tube calibration curves for the measurement of wall shear stress," *Experimental Thermal and Fluid Science*, vol. 24, no. 3, pp. 93–97, 2001.

[48] C. Tu and D. Wood, "Wall pressure and shear stress measurements beneath an impinging jet," *Experimental thermal and fluid science*, vol. 13, no. 4, pp. 364–373, 1996.

Appendix A

Preliminary OFI Testing

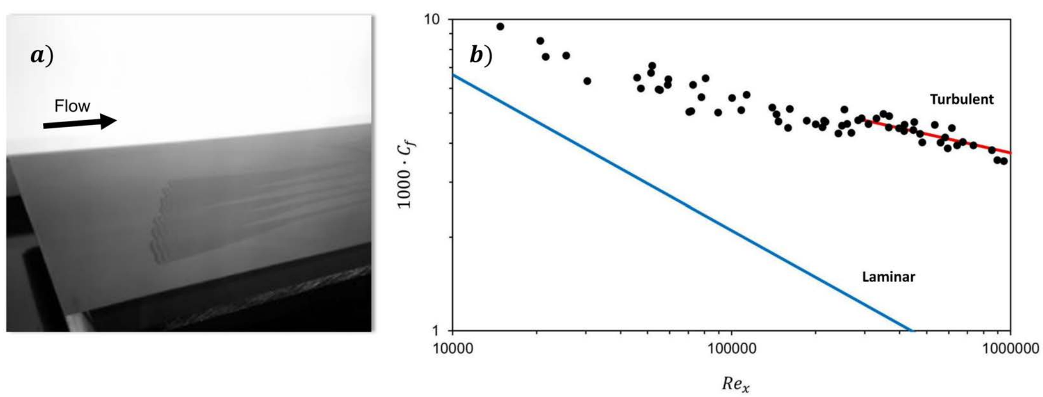

Figure A.1: a) Flat plate mounted parallel to wind-tunnel exit flow for preliminary OFI measurements. b) The Fanning skin friction factor versus the local Reynolds number for a flat plate with zero pressure gradient is plotted. The turbulent boundary layer is tripped from the leading edge, and the data follows the turbulent skin friction relation $C_f = \frac{0.059}{{Re_x}^{1/5}}$.

OFI testing was first performed at McMaster University on flat plates situated at the exit of an open-loop wind-tunnel, shown in Figure A.1 a). Oil lines were applied at different distances from the leading edge of the plate, and the local Reynolds number and skin friction coefficients were measured, and compared to existing well-known skin friction coefficient relations for flat plates in a zero pressure gradient, shown in Figure A.1 b). These OFI measurements were eventually transferred to a more complicated setup; on the impingement plate of a planar impinging gas jet shown in Figure A.2 a). The single image interferometry method allowed for the removal of the impingement plate immediately after testing, and for the image capture procedure to be performed in a less confined environment. The interferogram shown in Figure A.2 b) is the result of an angled oil line spread along the impingement plate during jet flow conditions. The red line in Figure A.2 b) indicates a location of where a single skin friction measurement would take place by analyzing the pixel intensity distribution along the fringes.

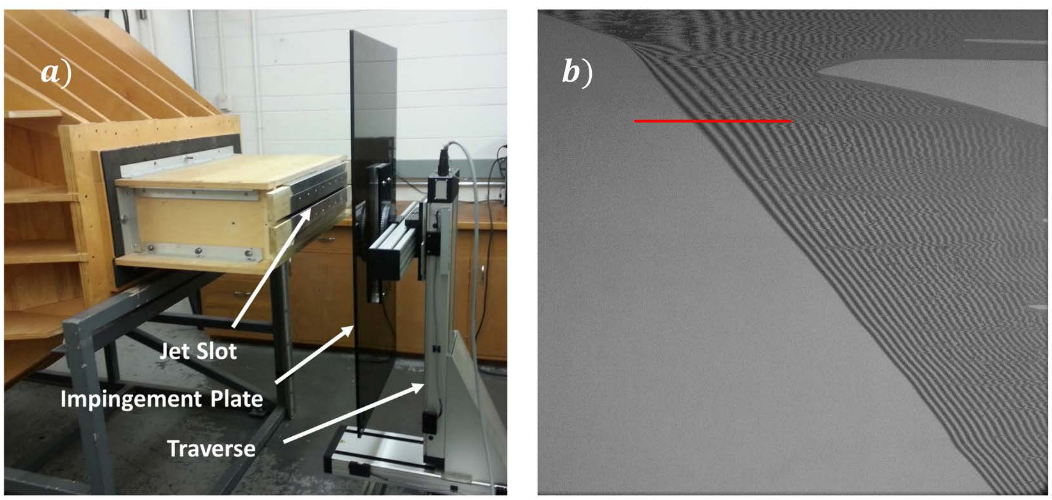

Figure A.2: a) Flat plate mounted orthogonal to planar gas jet flow positioned at the exit of the open-loop wind-tunnel. b) Interferogram obtained on the impingement plate using the angled oil line approach. The red line indicates an example of where a skin friction measurement will be performed using the pixel intensity distribution.

The single interferogram method was used to determine the applied wall shear stress based on the slope of the oil surface over a certain amount of time, which is inferred from the fringe spacing in the interferogram (See Equation 3.7). The thin film equations use the height of the oil at the leading edge (h= 0), and the height

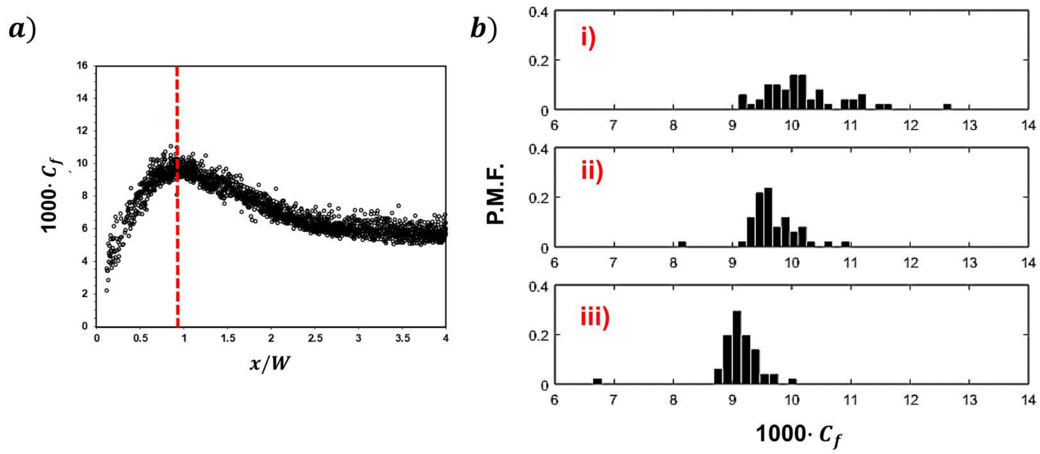

Figure A.3: a) The skin friction distribution along the impingement plate obtained at Re_{jet} = 20000 H/W = 6. b) The probability mass function obtained along the red dashed line using the first i), second ii), and third iii) fringe in the pixel intensity distribution. Notice the compromise between the random error in the measurement, and the systematic error due to spatial averaging.

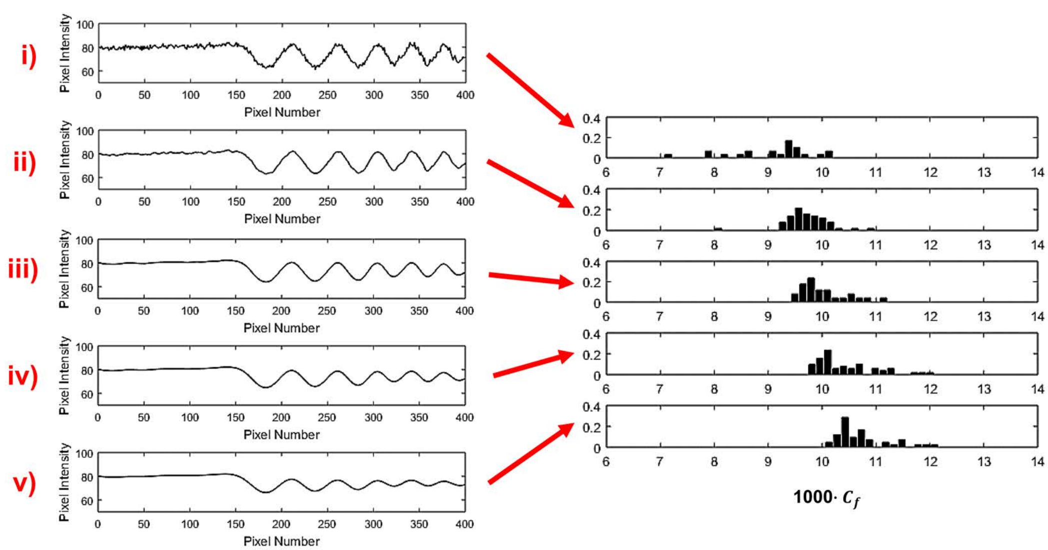

Figure A.4: The effect of number of smoothing operations i) 2, ii) 5, iii) 10, iv) 20, v) 40 on the pixel intensity distributions (left), and the resulting skin friction probability mass functions (right).

of the oil at a specific fringe location to calculate the slope. In Figure A.3 a), the skin friction distributions are analyzed near the maximum skin friction location in the vicinity of the red dashed line. In Figure A.3 b), the probability mass function of the measured skin friction data is presented for the OFI calculations based on the first i), second ii), and third iii) fringe in the interferogram. The trends to highlight are as follows: using the first fringe in the wall shear stress calculation results in a larger random error, due to the small x' distance measurement from the fringe location to the oil leading edge. As fringes are selected further from the oil leading edge, the random error is less, but a systematic error is introduced. This systematic error is caused by spatial averaging, and results in a lower maximum mean skin friction reading. Therefore, there is a compromise between the associated random and systematic errors. This thesis evaluated the skin friction using the second fringe in the interferograms, with the combined random and systematic error estimated at $\approx 9\%$. During preliminary OFI analysis, there was also a systematic error found in the level of smoothing of the pixel intensity distribution, shown in Figure A.4. Initially, some level of smoothing helps distinguish the peaks in the pixel intensity distribution by increasing the signal to noise ratio. However, over-smoothing the interferogram results in pushing the leading edge peak back further upstream, resulting in a larger skin friction value. The further the fringes are spaced, in the same amount of time, means better wiping, and higher wall shear stress. Another interesting feature is the positive skewness in the probability mass functions for the skin friction in Figure A.4. This positive skewness arises when the leading edge peak is over-smoothed, and any upstream irregularities in the pixel intensity take precedence in the peak detection program. This skewness becomes more prominent as the number of smoothing operations is increased. Typically, the pixel intensity distributions underwent five smoothing operations in MATLAB before the OFI analysis was performed.

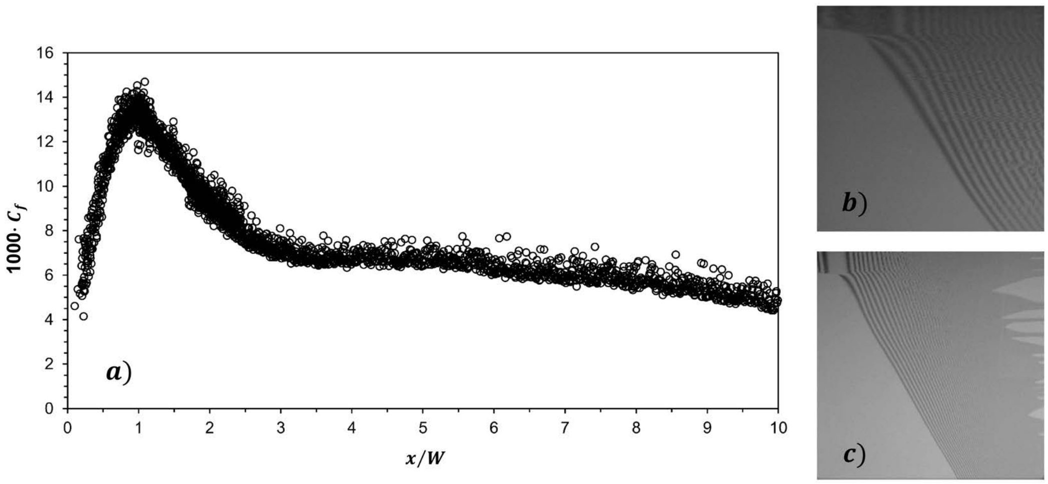

Figure A.5: a) A skin friction distribution measured out to x/W = 10 for Re_{jet} = 11000 and H/W = 6. The skin friction distribution is composed of multiple OFI tests, with interferograms obtained using different camera lens magnifications, shown in b), and c).

In Figure A.5 a), a skin friction distribution is presented with the tails extending to x/W = 10 for Re_{jet} = 11000 and H/W = 6. Typically, the maximum skin friction value within the stagnation region was of interest, so most of the skin friction profiles were only evaluated out to four nozzle widths. With different positioning of the camera, and different camera lens magnifications, different OFI tests (Figure A.5 b-c) can be overlaid to obtain a more extended profile, as shown in Figure A.5 a). Skin friction coefficients tend to monotonically decrease outside the stagnation region, with the exception of some closer impingement ratios where a secondary local maximum can sometimes occur, around $x/W \approx$ 4-5, due to turbulent boundary layer transition.

In Figure A.6 a) and b), the effect of jet nozzle width (W= 12 mm and W= 25 mm) is also explored on the skin friction distributions, while maintaining non-dimensional similarity under two different jet Reynolds numbers, and impingement ratios.

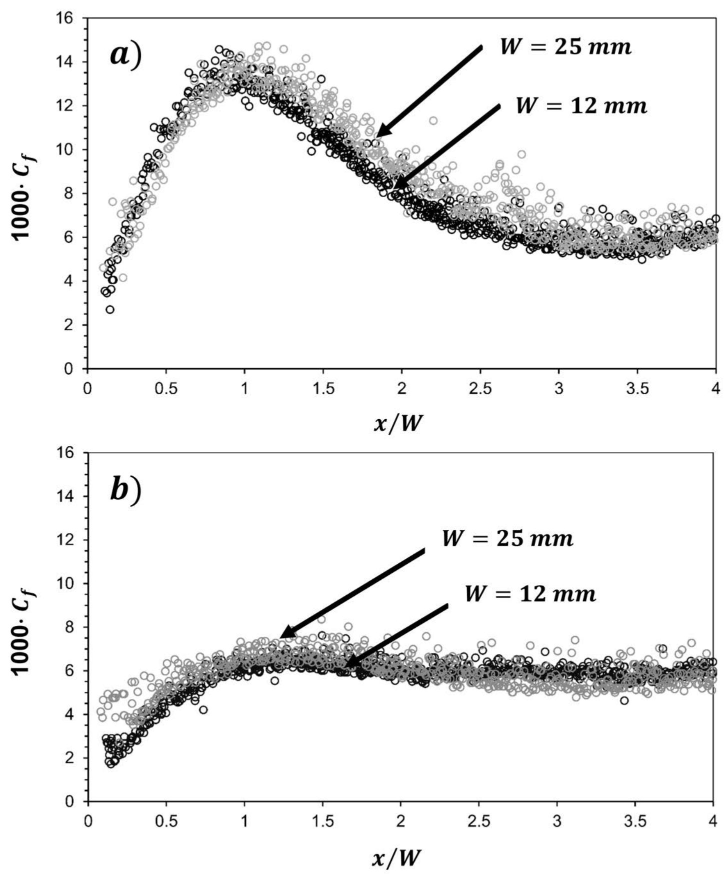

Figure A.6: Skin friction distributions obtained at a) Re_{jet} = 11000 and H/W = 4 and b) Re_{jet} = 40000 and H/W = 8 for two different jet nozzle widths W = 12 mm, and W = 25 mm. These tests explored the non-dimensional arguments due to scaling of the experimental setup.

Appendix B

Fluctuating Kinetic Energy Production

The fluctuating kinetic energy production was evaluated using the Reynolds stresses, and velocity gradients obtained with the PIV measurements for the 36 Hz, 70 Hz, and 100 Hz anti-symmetrically forced cases in Chapter 5. The KE' production ξ, which can be derived from the fluctuating velocity transport equation is given in Equation B.1:

$$\xi = -\overline{u_i'u_j'}\frac{\partial \overline{U_i}}{\partial x_j} = -\left(\overline{u'v'}\frac{\partial \overline{U}}{\partial x} + \overline{v'u'}\frac{\partial \overline{V}}{\partial z} + \overline{u'u'}\frac{\partial \overline{U}}{\partial z} + \overline{v'v'}\frac{\partial \overline{V}}{\partial x}\right) \tag{B.1}$$

When expanding the tensor product, four terms are obtained for the KE' production. The first two terms on the right hand side of the equation is the KE' shear production. It is well known that mean shear produces fluctuating kinetic energy, which appears directly in the derivation of the KE' transport equation. The third and fourth terms are the KE' normal production. These terms are a result of the normal stresses interacting with the mean velocity gradients in their aligned directions. The KE' production ξ is non-dimensionalized using the jet nozzle width W, and the jet exit velocity U_{jet} in the form: $100 \cdot (\xi \cdot W)/{U_{jet}}^3$. The non-dimensional KE' production is displayed in flood plots in Figure B.1 for the no-excitation a) 0 Hz, b) 36 Hz, c) 70 Hz, and d) 100 Hz anti-symmetric cases.

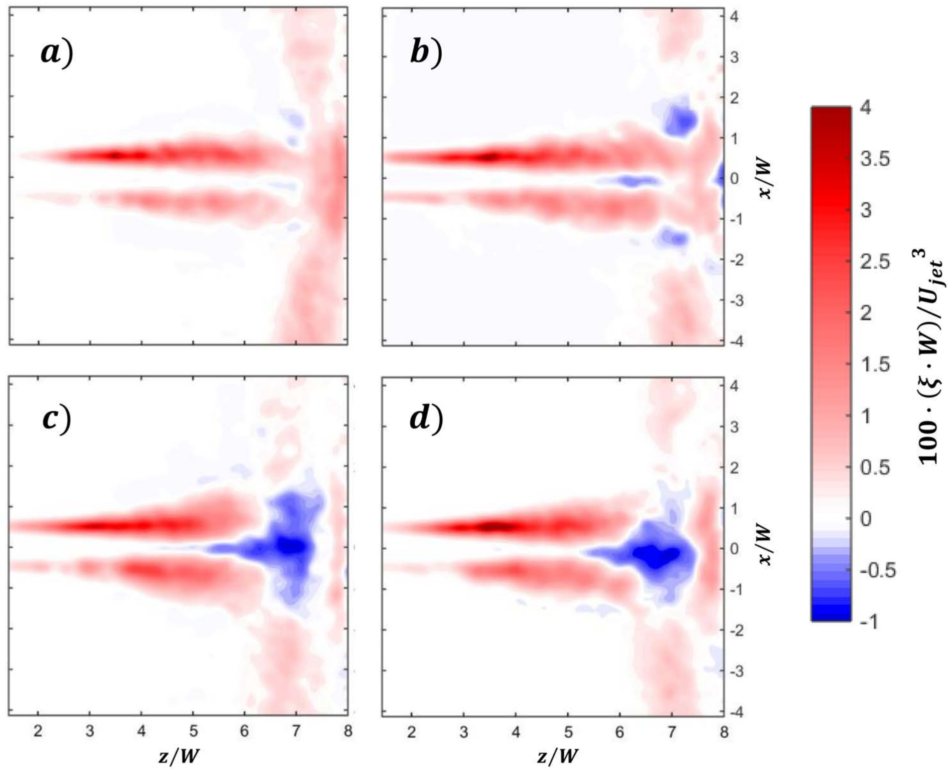

Figure B.1: The non-dimensional KE' production flood plots for the non-exited jet a) 0 Hz, b) 36 Hz, c) 70 Hz, and d) 100 Hz anti-symmetric 1% amplitude cases.

In Figure B.1 there is relatively high KE' production in the impinging shear layers for all cases, and regions of the negative KE' production become more prominent in the impingement region under forcing conditions. For the 36 Hz case, the negative KE' production regions appear as small circular zones near the vortex impingement locations ($x/W \pm 1$), and at the jet centerline ($z/W \approx 6 - 7$). As the frequency of forcing is increased to 70 Hz and 100 Hz, the negative KE' production regions merge and conglomerate into a larger zone near the jet centerline at

$z/W \approx 6 - 7$. Some care must be taken into account with the measurement error in the PIV data, to ensure we can differentiate slightly negative regions from approximately zero KE' production regions (such as background KE' production $100 \cdot (\xi \cdot W)/{U_{jet}}^3 \approx 0$). A KE' production uncertainty analysis can be found in Appendix E.

Negative turbulent kinetic energy production has been reported previously in the literature in stagnating flows [1, 2, 3]. A paper by Hussain [4] highlights that most flows possess Reynolds shear stresses ($\overline{u'v'}$), and the mean velocity gradients, that are opposite-signed in the flow field. In addition to this, both of these flow quantities are multiplied by negative one in Equation B.1, and therefore the product will result in a positive value for TKE production. Therefore, shear layers generally possess positive TKE production due to the dominant shear production terms, and the energy from the mean flow is transferred to the turbulence. In a channel flow, for instance, the Reynolds shear stresses and velocity gradients, have opposite signs, and their respective profiles are zero at the channel centerline. In a case where a channel flow may have a different surface roughness on the top or bottom wall, flow asymmetry is introduced, which may give rise to a particular spatial region where the Reynolds shear stresses, and velocity gradients have the same sign; resulting in negative TKE production. Physically, negative TKE production means that energy is being taken from the turbulence, and transferred to the mean flow; establishing a "reverse" energy cascade. Hussain [4] has also shown that the process of vortex pairing can induce vortex configurations, where negative TKE production can be generated due to the signs of the Reynolds stresses, and local velocity gradients. The randomness of vortex pairing, however, and this negative production configuration, is said to generally not be felt in the time-average, unless the coherent vortex structures can exist at fixed spatial locations. Deterministic pairing locations can be achieved with external excitation, or resonance effects, thus explaining why the current jet excitation cases may give rise to regions of negative KE' production downstream in the flow. To better understand the regions of negative KE' production in Figure B.1, we will analyze the Reynolds stresses, and mean velocity gradients, at the z/W = 4, and z/W = 7 downstream distances, for the unexcited 0 Hz, and 70 Hz anti-symmetric cases.

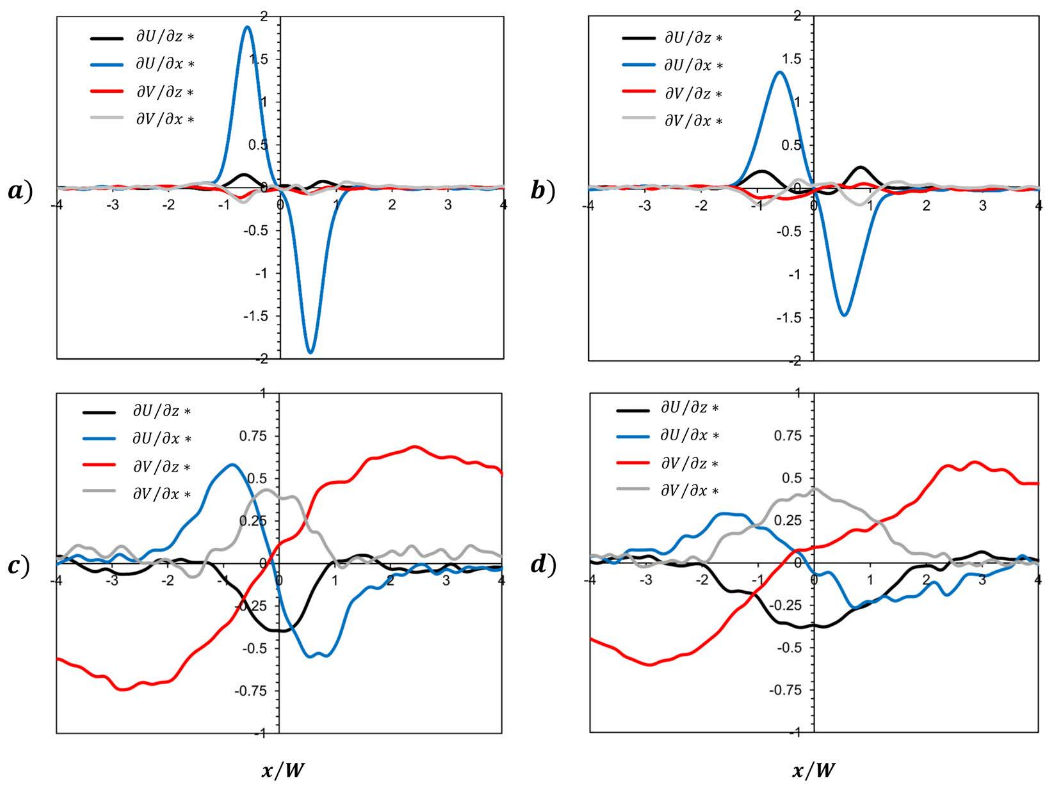

Figure B.2: The non-dimensional mean velocity gradients ($\frac{\partial \overline{U}}{\partial x} * = \frac{\partial \overline{U}}{\partial x} \cdot \frac{W}{U_{jet}}$) for the unexcited jet a) 0 Hz, and the b) 70 Hz excited jet, at downstream location z/W = 4. The non-dimensional mean velocity gradients for the unexcited jet c) 0 Hz, and the d) 70 Hz excited jet at downstream location z/W = 7. Note that for c) and d) the abcissa is half the scale as a) and b) to help observe the trends.

As a reminder to the reader, in this study the downstream flow direction is z, with corresponding velocity component U, and the cross-stream coordinate is x, with velocity component V. In Figure B.2 a), the mean velocity gradients are plotted at downstream location z/W = 4 for the unexcited jet. The dominant gradient at this cross section is the $\partial\overline{U}/\partial x$ term at impinging shear layer locations $x/W \pm 0.5$, whereas the other gradients are an order of magnitude lower. In Figure B.2 b), we show the same downstream location, but with the jet forced anti-symmetrically at 70 Hz. The $\partial\overline{U}/\partial x$ term decreased in magnitude as a result of forcing, and broadly diffused in the x-direction as the jet spread rate increases. The KE' production is positive in the shear layer locations, and is dominated by the $\partial\overline{U}/\partial x$ velocity gradient, which appears in the first term on the right hand side of Equation B.2. In Figure B.2 c), the mean velocity gradients are plotted at downstream location z/W = 7 for the unexcited jet. In this plot, all velocity gradients are the same order of magnitude, with the $\partial\overline{U}/\partial z$ and $\partial\overline{V}/\partial x$ term being equal, and opposite in magnitude. Again, with anti-symmetric 70 Hz excitation at z/W = 7, a lower $\partial\overline{U}/\partial x$ term is observed, and more spread in the gradient profiles associated with fluid entrainment during anti-symmetric oscillation in Figure B.2 d).

Next, the Reynolds stresses are investigated. In Figure B.3 a), the Reynolds stresses are plotted for the unexcited jet at downstream location z/W = 4. Although the normal stresses are much larger than the shear stresses in Figure B.3 a), the overpowering $\partial\overline{U}/\partial x$ gradient in Equation B.1 determined the sign. Additionally, the Reynolds shear stresses (in this case plotted -$\overline{u'v'}$) are the same sign as the $\partial\overline{U}/\partial x$ gradient, therefore resulted in positive KE' production. Similar conclusions can be drawn when the jet is excited at 70 Hz at this z/W = 4 location, as shown in Fig-

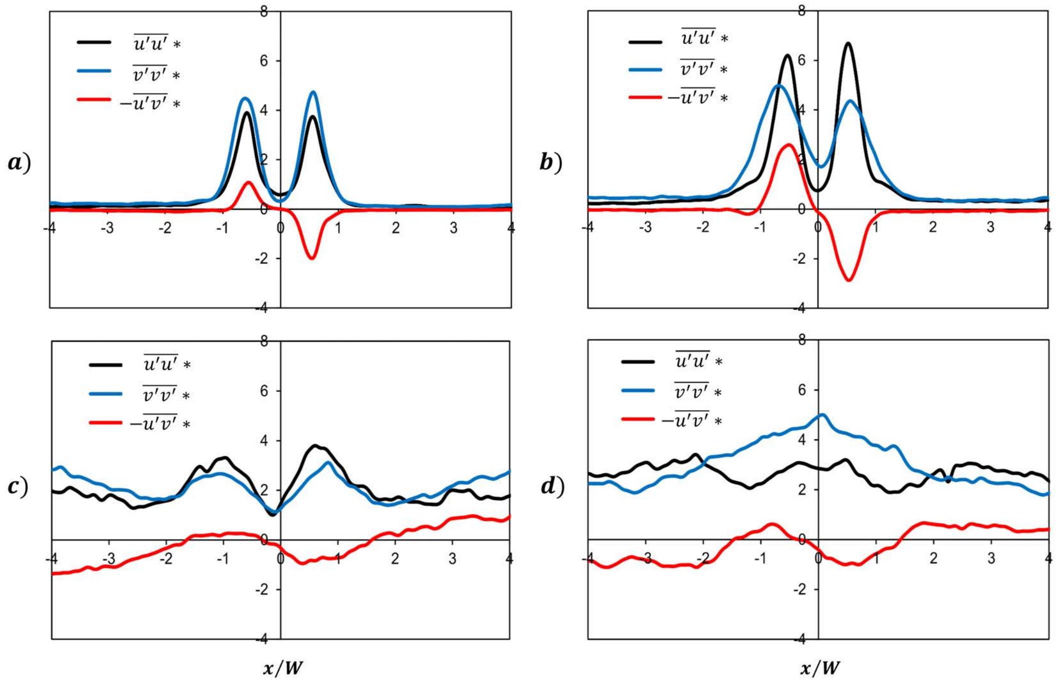

Figure B.3: The non-dimensional Reynolds stresses ($\overline{u'u'}*$ = $100 \cdot \overline{u'u'}/{U_{jet}}^2$) for the unexcited jet a) 0 Hz, and the b) 70 Hz excited jet at downstream location z/W = 4. The non-dimensional Reynolds stresses for the unexcited jet c) 0 Hz, and the d) 70 Hz excited jet at downstream location z/W = 7.

ures B.2 b), and B.3 b). We will now analyze these terms further downstream at the z/W = 7 location. In Figure B.3 c) and d), the Reynolds stresses are plotted for the unexcited 0 Hz, and 70 Hz cases, respectively. In these plots, the Reynolds shear stresses show insignificant changes, however, some interesting features are shown with the normal stresses. When the jet is not excited, in Figure B.3, the normal stresses are nearly isotropic (nearly equal), forming distinct peaks at plate locations $x/W \approx \pm 1$. At 70 Hz excitation, in Figure B.3 b), the u-fluctuation intensities (or stream-wise normal stress) become inverted, now showing local minimums at plate locations $x/W \approx \pm 1$. As mentioned previously, during vortex structure presence, KE' is transferred orthogonally, moving energy from the stream-wise direction to the cross-stream direction, with the propensity for the v-fluctuation intensities to migrate towards the jet centerline. In Figure B.3 d), the v-fluctuation intensity (or cross-stream normal stress) exhibited a maximum at the jet centerline, with an approximate six-fold increase from that of the unexcited case. Since the mean velocity gradients for this excited case show comparable order of magnitude (Figure B.2 d)), and because the Reynolds shear stresses are very low at the jet centerline ($|\overline{u'v'}| < 1\ m^2/s^2$), thus the KE' shear production is very small (term 1 and 2 on the right hand side of Equation B.1). The main contributors in Equation B.1, at this z/W = 7 location near the jet centerline, is the normal KE' production terms, 3 and 4. At the jet centerline location, the mean velocity gradients $\partial\overline{U}/\partial x$, $\partial\overline{V}/\partial z$ are equal and opposite at this location, shown in Figure B.2 d). Therefore, the stream-wise and cross-stream normal stresses are in competition with each other to determine the sign of the KE' production. In Figure B.3 d), the cross-stream normal stresses dominate near the jet centerline (approximately $-2 < x/W < 2$), thus enforcing negative KE' production at this z/W=7 downstream location.

In Figure B.4, the KE' production is plotted for the unexcited jet at downstream locations z/W = 4 (curve 1), and z/W = 7 (curve 3), and for the excited jet at 70 Hz at downstream locations z/W = 4 (curve 2), and z/W = 7 (curve 4). Curve 4 indicates the KE' production forms a minimum at the jet centerline ($100 \cdot (\xi \cdot W)/{U_{jet}}^3 \approx -1$) when the jet is excited anti-symmetrically at 70 Hz. The negative KE' production is statistically significant near the jet centerline, and data markers are inserted along curve 4 at x/W locations -1,-0.5, 0, 0.5, 1 to represent the size of the error bars. At the z/W = 4 location for the unexcited jet (curve 1), asymmetry is noted in the KE' production at the impinging shear layer locations $x/W \pm 0.5$,

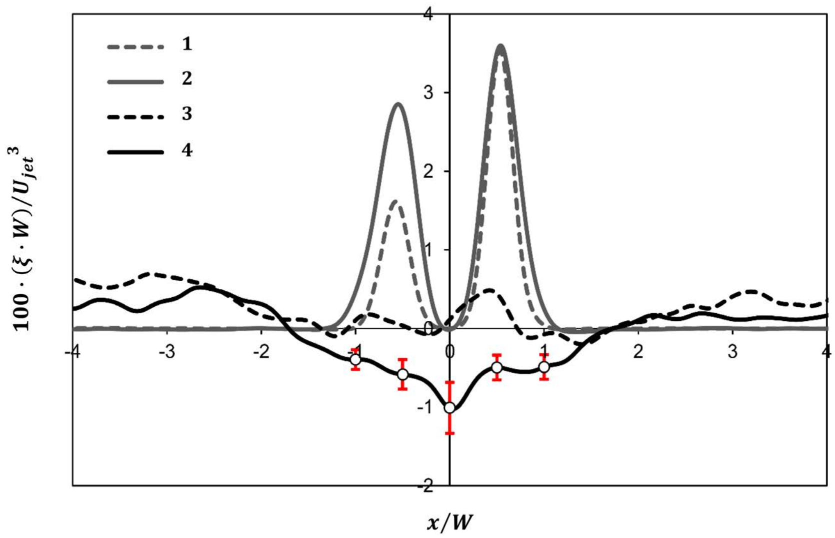

Figure B.4: The KE' production for the unexcited jet at downstream locations $z/W = 4$ (curve 1) and $z/W = 7$ (curve 3). The KE' production for the jet excited at 70 Hz at downstream locations $z/W = 4$ (curve 2) and $z/W = 7$ (curve 4). For curve 4, data markers are inserted at -1,-0.5, 0, 0.5, 1 x/W locations with the red error bars used to indicate the estimated standard uncertainty (See Appendix E).

which is predominantly due to the slight asymmetry in the mean velocity gradient $\partial\overline{U}/\partial x$ at this location (Figure B.2 a)). This slight asymmetry can also be seen in the KE' flood plots for the turbulent kinetic energy in Figure 5.8 a). As the jet is exposed to 70 Hz anti-symmetric excitation at $z/W = 4$ (curve 2 in Figure B.4), the positive KE' production becomes more balanced in the impinging shear layers.

To understand the flow physics, and how negative fluctuating kinetic energy production plays a role in the excited impinging gas jet, the following chain of events is proposed: The effect of forcing at the jet nozzle exit, whether instigated by upstream feedback, a resonance condition, or external synthetic jet forcing, caused the KE' in the impinging shear layers to increase from that of the unforced condition. If the jet column is sensitive to this forcing frequency (in particular in the current

70 Hz anti-symmetric configuration), then the jet column can oscillate periodically, and produce coherent vortex structures that propagate downstream towards the impingement plate. Due to the periodic motion of the jet column, the cross-stream normal stresses dominated downstream at the jet centerline location, and the normal cross-stream production (term 4 of Equation B.1) determined the sign change; the KE' production became negative at that location. This negative KE' production dictated the flow of energy; from the velocity fluctuations back to the mean flow. This transfer of energy must go into the mean flow in the form of rotation, or pairing of large-scale vortex structures, because previous experiments in Chapter 4 have shown reductions in momentum near the jet centerline with anti-symmetric excitation. This rotation of the mean flow increased the entrainment rate of the surrounding fluid causing downstream centerline velocity decay, and repercussions at the impingement plate, such as maximum skin friction reductions, and maximum pressure gradient reductions.

Appendix C

Symmetric Jet Forcing

In Figure C.1 a) and b), the centerline fluctuation intensity is given for the streamwise fluctuation intensity, and cross-stream fluctuation intensity, respectively. The magnitude of the u and v-fluctuation intensities along the jet centerline are comparable at some locations to the fluctuation intensity magnitudes for the no-excitation case (maximum difference between the centerline v-component for the 70 Hz symmetric case, and no-excitation case, being $\approx 46\%$, compared to 150% for the anti-symmetric forcing). In Figure C.1 c) and d), the maximum magnitude of the streamwise and cross-stream fluctuation intensity are shown in the jet column region ($-1.5 < x/W < 1.5$). Similarly, minor changes in the magnitude of the fluctuation intensities are found. In Figure C.1 c), we also observe some instances of where the fluctuation intensity is suppressed below the baseline no-excitation case ($\approx 16\%$ reduction for the 70 Hz symmetric case at $z/W \approx 6.25$). Although planar gas jets may be susceptible to symmetric forcing at higher frequencies, these large amplitude, high frequency forcing conditions could not be achieved with the current synthetic jet actuators. Hussain and Thompson [5] excited a planar free gas jet using a loudspeaker inside the plenum, which is essentially inducing disturbances symmetrically around the perimeter of the nozzle. Their reported total fluctuation intensity showed comparable results of $\approx 20\%$ of the jet exit velocity at $z/W \approx 4$ for their preferred mode Strouhal number of $St_W \approx 0.18$. The relatively small changes in the fluctuation intensities for the symmetrically-forced cases are due to insignificant changes in the jet column dynamics (deflection and entrainment mainly) under these forcing conditions. The jet is clearly more susceptible to anti-symmetric forcing in the lower frequency range tested.

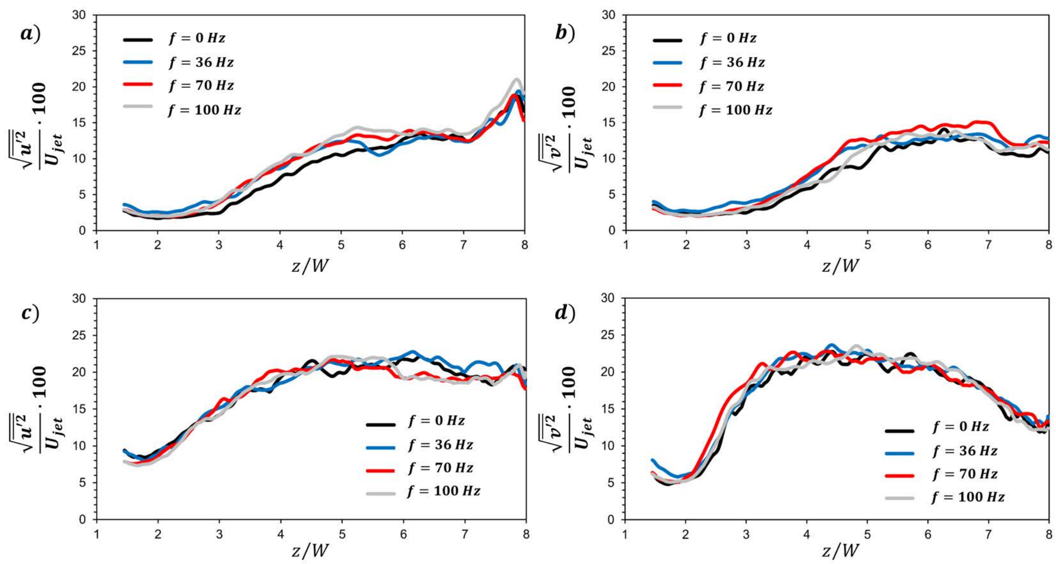

Figure C.1: a) The stream-wise u-fluctuation intensities along the jet centerline (x/W = 0), b) the cross-stream v-fluctuation intensities along the jet centerline (x/W = 0), c) the maximum stream-wise u-fluctuation intensities in the jet column region ($-1.5 < x/W < 1.5$), and d) the maximum cross-stream v-fluctuation intensities in the jet column region ($-1.5 < x/W < 1.5$) as a function of downstream position (z/W). The 36 Hz, 70 Hz, and 100 Hz cases are under symmetric forcing conditions.

Appendix D

Higher Frequency Jet Forcing

As gas separates from the nozzle edge, the flow becomes unstable and susceptible to a particular range of frequencies due to an inflection point in the velocity profile. This particular range of sensitive frequencies has been both experimentally, and mathematically determined (using linear instability analysis) to be a function of the momentum thickness θ at the nozzle edge; the shear layer mode frequencies for planar gas jets $St_\theta = \frac{f\theta}{U_{jet}} \approx 0.01\text{-}0.015$ between jet exit velocities U_{jet} = 15-100 ft/s [6].

The momentum thickness and dominant frequency in the hot-wire signal at the jet exit was evaluated under $U_{jet} = 11\ m/s$ conditions and presented in Figure D.1. The dominant frequency is dependent on the measurement location in the jet flow. Figure D.2, shows the dominant frequency in the hot-wire spectra measured along the jet centerline, and jet shear layer location, at different z/W downstream positions of the unforced jet. Symmetric forcing was then applied to the jet exit under f_0 = 500 Hz, and f_1 = 200 Hz (similar to the dominant frequencies shown in Figure D.2) using planar synthetic jets at the nozzle exit, and the flow-field and impinge-

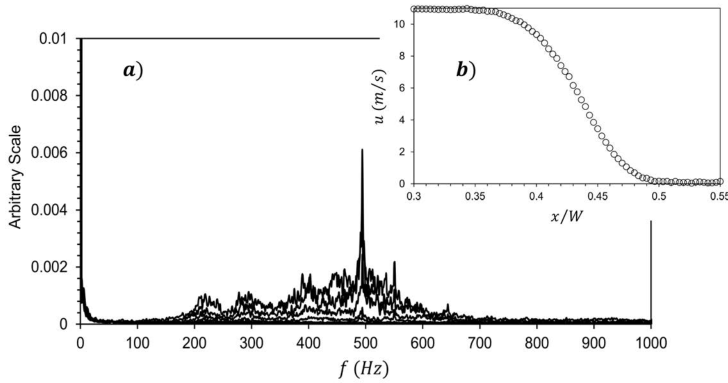

Figure D.1: a) Hot-wire frequency spectra measured in the jet exit shear layer ($x/W = 0.5$, $z/W = 1 - 2$) revealing a shear layer mode frequency of $f_0 \approx 494$ Hz. b) The jet exit boundary layer measured with a hotwire to evaluate the momentum thickness ($\theta = 0.282$ mm), and Strouhal number $St_\theta = 0.0126$.

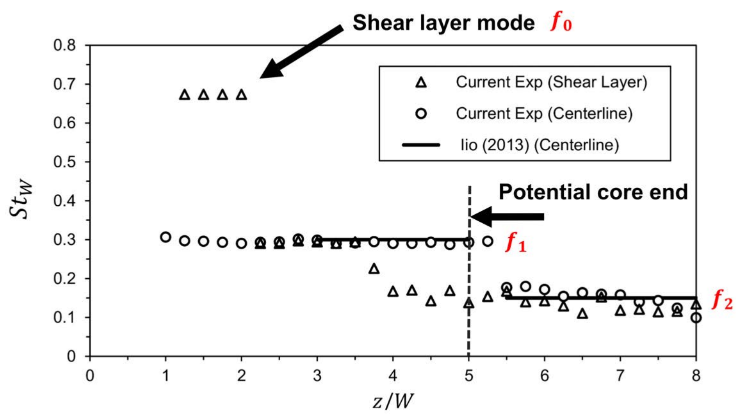

Figure D.2: The dominant frequency in the hot-wire spectra represented as $St_W = \frac{fW}{U_{jet}}$ measured at the jet centerline $x/W = 0$, and shear layer $x/W = 0.5$ locations as a function of the downstream z/W position.

ment plate skin friction was investigated. Due to the amplitude limitations of the synthetic jets, the forcing amplitude at the jet nozzle exit for these cases ($< 0.1\%$ of U_{jet}) could not be brought to comparable values to those in Chapter 4 and 5 (1%), and therefore the results cannot be compared directly. In Figure D.3 the normalized velocity magnitudes for the symmetrically-forced $f = f_0$ and $f = f_1$ cases are presented using phase-locked PIV at phase ϕ = 0. In Figure D.4, the non-dimensional phase-locked vorticity fields are shown for the two forcing frequencies (f_0, f_1) at different phases. Free shear layer forcing at subharmonics of the fundamental disturbance frequency, resulted in pairing of the fundamental disturbance upstream, subsequently forming larger vortex structures in the jet flow field. For Figures D.5 and D.6 we utilized a triple decomposition of the jet flow-field. In Figure D.5 the coherent component of the velocity is obtained by subtracting the phase-locked velocity $<U>$ from the average velocity $\overline{U}$. This is done for the stream-wise and cross-stream components of velocity for a constant phase ϕ = 0. In Figure D.6, the turbulent kinetic energy is shown, and obtained by calculating the rms of the phase-locked PIV data for different forcing frequencies (f_0, f_1) and different phases (ϕ = 0, ϕ = π). Note that the turbulent kinetic energy, in the instantaneous sense, concentrates in the vortex centers or regions of high vorticity in reference to Figure D.4.

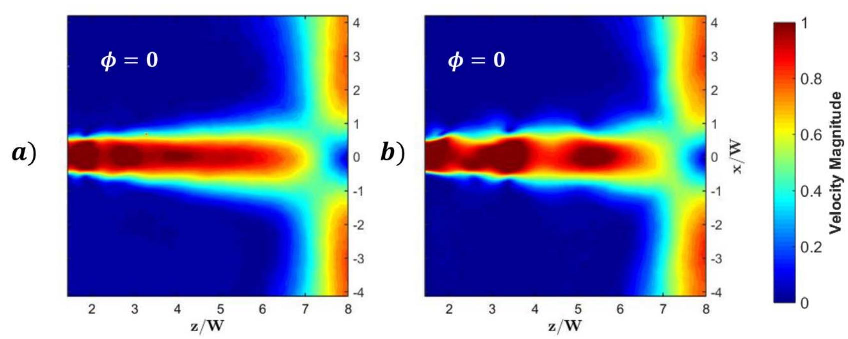

Figure D.3: Normalized velocity magnitude fields for symmetrically-forced a) f_0 = 500 Hz and b) f_1 = 200 Hz using phase-locked PIV at ϕ = 0.

In Figure D.7, the proper orthogonal decomposition (POD) results are shown for a set of 200 random images for the f_1 = 200 Hz case. The energy distribution

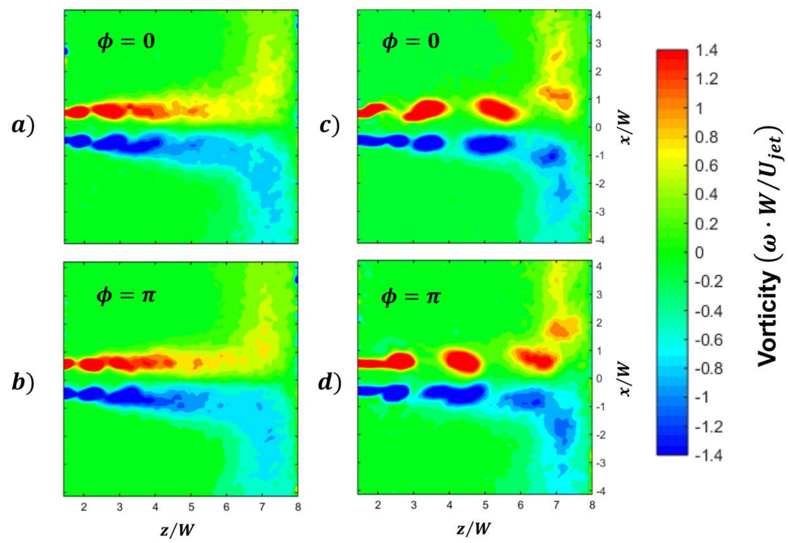

Figure D.4: Non-dimensional phase-locked vorticity fields for two different phases a) $\phi = 0$ and b) $\phi = \pi$ for the $f_0 = 500$ Hz forcing frequency. Phase-locked vorticity fields for two different phases c) $\phi = 0$ and d) $\phi = \pi$ for the $f_1 = 200$ Hz forcing frequency.

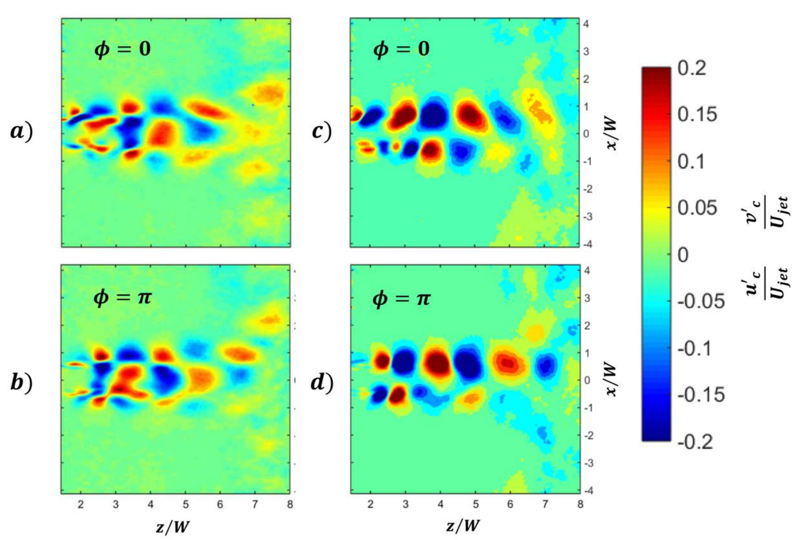

Figure D.5: The coherent u component velocity (stream-wise) under 200 Hz forcing for phase a) $\phi = 0$ and b) $\phi = \pi$. The coherent v component velocity (cross-stream) under 200 Hz forcing for phase c) $\phi = 0$ and d) $\phi = \pi$.

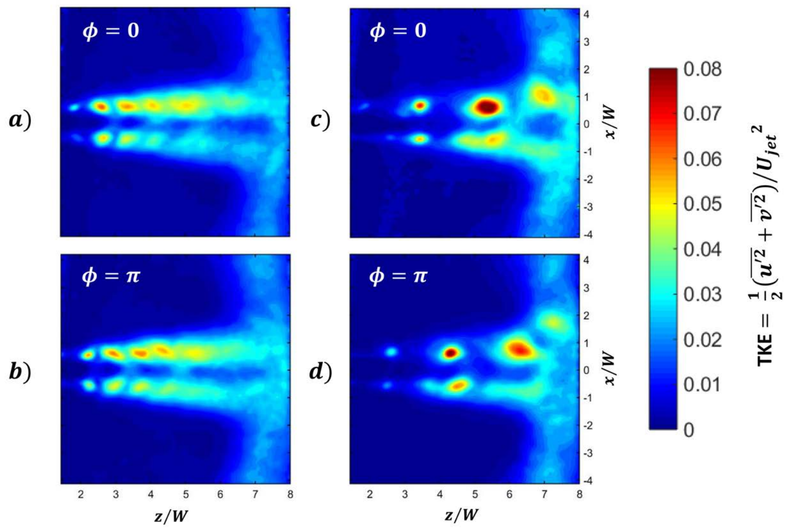

Figure D.6: The turbulent kinetic energy of the jet under f_0 = 500 Hz forcing for phase a) $\phi = 0$ and b) $\phi = \pi$. The turbulent kinetic energy of the jet under f_1 = 200 Hz forcing for phase c) $\phi = 0$ and d) $\phi = \pi$.

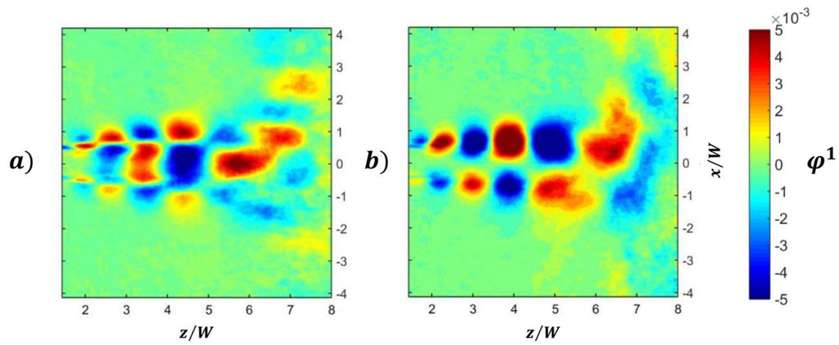

Figure D.7: The first POD mode φ^1 under f_1 = 200 Hz forcing for the a) u-component velocity and b) the v-component velocity.

is decreasing with POD mode number and is not yet fully converged for the 200 images. The first POD mode φ^1 containing most the relative fluctuating kinetic energy ($\approx 10\%$) is shown for the u-component velocity and the v-component velocity in Figure D.7 a) and b), respectively. In Figure D.8, the impingement plate skin friction distributions obtained with oil film interferometry (OFI) are shown under

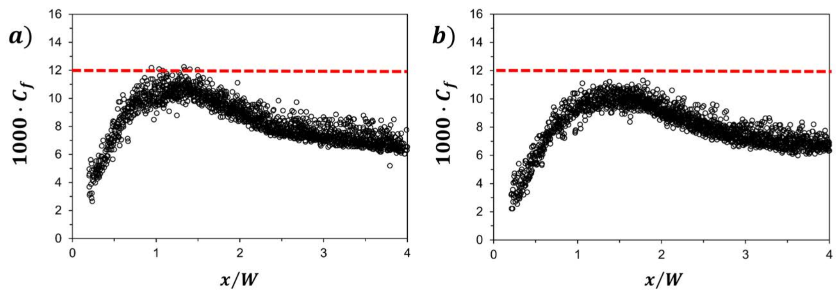

Figure D.8: The skin friction distributions for the a) f_0 = 500 Hz case, and the b) f_1 = 200 Hz case. The red dashed line indicates the maximum skin friction from the unforced condition for reference.

a) f_0 = 500 Hz case, and the b) f_1 = 200 Hz jet forcing. Note the reductions in maximum skin friction from the unforced case (red dashed line) due to increased levels of fluid entrainment under jet forcing conditions.

Appendix E

PIV Error

E.0.1 PIV Error Sources

Like any measurement technique, Particle Image Velocimetry (PIV) is subject to systematic and random errors. In general, these errors come from **i)** flow tracking errors induced by the seeding particles not following the flow accurately (particle slip or lag) due to excessive particle size, high flow speed, or flow acceleration, **ii)** improper flow seeding (either too sparse or too much causing particle agglomeration), **iii)** insufficient illumination intensity from the laser, **iv)** laser glare interrupting particle paths near solid surfaces, **v)** insufficient spatial resolution for the discretization of the cross-correlation function (peak locking errors), **vi)** insufficient resolution in the presence of shear causing spatial averaging (displacement gradient error), **vii)** out-of-plane motion causing missing particle pairs or skewed 2D velocity components, **viii)** insufficient or excessive particle travel within the interrogation region, and **ix)** poor image quality caused by laser alignment or camera focus, to name a few.

E.0.2 Experimental PIV Details

The 2C-2D (two component two dimensional) PIV was implemented in this research to analyze the flow field issuing from a 2D planar impinging jet. The laser plane was oriented vertically using a custom light-arm assembly and a $45°$ laser mirror. PIV vector fields were processed with InSight 4G using a first-order deformation-based correlation scheme with a single grid refinement, and a final window size of 16x16 pixels^2. The spatial resolution of the PIV determined by image calibration in InSight 4G was R = 16 pixels/mm in Chapter 3, and R = 11.8 pixels/mm in Chapters 4 and 5, with the time between image pairs set to Δt = 23 μs for all cases at U_{jet} = 11 m/s. This allowed particles in the jet flow to travel $18 - 25\%$ of the interrogation region in between frames. The validation rate for all vector fields was 99%, and consisted of an ensemble of N = 200 PIV images. Acceptable convergence of velocity statistics was checked by doubling the amount of PIV images (400 images). The camera resolution is 4 mega-pixels, with 63001 velocity vectors provided from each PIV image, resulting in an exported grid size of Δx = Δz = 8.2 pixels. A TSI Laser Pulse synchronizer was employed, along with a custom made trigger used for phase-locking.

E.0.3 Particle Tracking Error

PIV requires the tracking of flow particles in the jet, which are seeded upstream of the nozzle exit. Ideally, the flow particles need to be small enough to propagate with the gas flow, but large enough to reflect laser light to accurately determine their position, and displacement in the flow. The PIV particle tracking error was performed based on the results of Melling [7]. For high density ratio turbulent flow (ρ_p/ρ_a = 760), with approximate particle diameter $d_p \approx 1\mu$m, particle Reynolds number Re_p = $U_{jet}d_p/\nu_a$ = 0.73, Stokes number S_k = $d_p\sqrt{2\pi/\tau_k\nu_a}$ = 0.07, and maximum frequency based on the Kolmogorov timescales $1/\tau_k$ = 13 kHz, a Reynolds stress error $|\overline{u_p'^2} - \overline{u_a'^2}|/\overline{u_a'^2}$ x $100 \approx 3.7\%$ is estimated.

Individual particle tracking can also be affected by a systematic error called peak locking. Peak locking is a phenomenon introduced when a particle is displaced within a sub-pixel region in the flow, and due to the corresponding discretization of the cross-correlation function, the confirmed particle displacement will always be shifted to the nearest pixel center. This shift to the nearest pixel center is due to the maximum peak intensity in the cross-correlation function obtained at that location. To dissolve this error for individual particle displacement, adequate grid resolution is required, where the particle image diameter divided by the distance between pixels should be greater or equal to approximately 2 [8]. However, with PIV, multiple particles in randomly placed positions will exist within each interrogation region. If these particles are displaced by the same amount, depending on their initial positions, they will land on integer pixel values (pixel centers) or perhaps be shifted negatively to the nearest pixel center location. The combined effect of this displacement bias is essentially zero in PIV with enough seeding particles because the systematic error introduced by peak locking tends to be randomly distributed. Keane and Adrian [9] have determined that an excess of 15 or more particle pairs displaced $10 - 20\%$ of the interrogation spot size results in valid detection probabilities of $\approx 99\%$.

E.0.4 Cross-Correlation Peak Ratio (PR)

A study by Charonko and Vlachos [10] examined the rms displacement error of seeding particles (both in simulation and on a real impinging flow) related to the peak ratio (PR) of the PIV cross-correlation function; this is the peak intensity of the cross-correlation function divided by the second largest peak within the same interrogation region. Essentially the peak ratio deciphers the signal-to-noise ratio in the instantaneous PIV image. Cross-correlation statistics have shown to be a useful tool for analyzing PIV error, and error analysis packages using peak ratios can now be purchased as an upgrade to the InSight 4G software. In our current software package, we can manually monitor the cross-correlation statistics during PIV processing. In Figure E.1, we show the cross-correlation function peaks (with PR values given in the caption) at four points in the impinging jet shear layer (Figure E.1 a)-d)), and four points along the jet centerline (Figure E.1 e)-h)). In the background of Figure E.1, an instantaneous raw PIV image is shown with the jet exit on the left, impingement plate on the right (jet flow moving from left to right), and seeding particles illuminated by the vertical laser sheet.

200 random peak ratios were evaluated manually from the instantaneous PIV images, with the PR statistics extracted (sample mean $\overline{PR}$ = 4.8, sample standard deviation $\overline{\sigma}$ = 0.98), and the average value inserted into Equation E.1. Equation E.1 represents the absolute displacement error $\hat{\epsilon}_d$ (in pixels) for a given peak ratio derived from an empirical fit for the synthetic flows studied using a standard Fourier-based cross-correlation (SCC) processing technique in Charonko and Vlachos [10]:

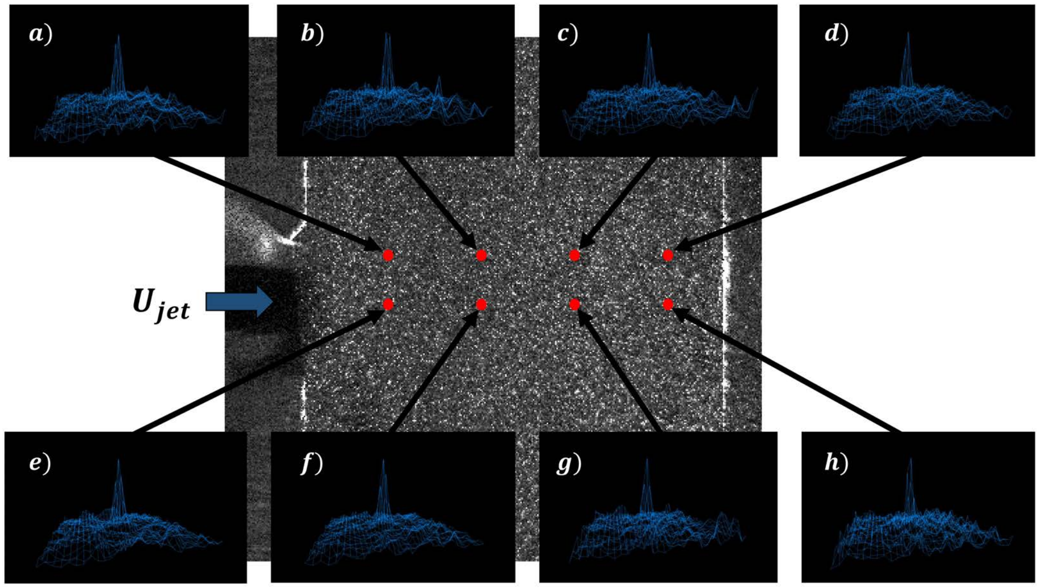

Figure E.1: An instantaneous raw PIV image of the impinging jet flow with the cross-correlation function peaks from the PIV processing at four points in the impinging shear layers a)-d), and at four points along the jet centerline e)-h). The peak ratio values: a) PR = 5.8, b) PR = 3.4, c) PR = 4.6, d) PR = 5.5, e) PR = 5.4, f) PR = 6.8, g) PR = 5.0, h) PR = 4.4.

$$\hat{\epsilon}_d^2 = (13.1 \cdot e^{-\frac{1}{2}\left(\frac{PR-1}{0.317}\right)^2})^2 + (0.226 \cdot PR^{-1})^2 + (0.08)^2 \tag{E.1}$$

A rough estimate of the rms standard uncertainty in the particle displacements is evaluated at $9.3/100$ pixels or $\epsilon_d \approx 3.1\%$ ($\epsilon_d = \frac{\hat{\epsilon}_d}{U_{jet} \cdot \Delta t \cdot R} \cdot 100$). Although Equation E.1 is derived from an empirical fit using synthetic flows, their empirical fit functions for the robust phase correlation (RPC) processing technique was tested using real PIV on a carefully controlled 2D stagnating flow [10]. 1000 PIV images were taken with 5.1 million instantaneous vectors sorted for their respective errors, and binned according to pass or fail within the predicted uncertainty intervals. It was found that all of their empirical fits over-predicted the particle displacement uncertainty levels. This standard uncertainty value ($\epsilon_d \approx$ 9.3/100 pixels) will serve as an upper limit for the instantaneous particle displacement error. For ensemble PIV techniques (unlike individual particle tracking), PIV noise and randomly distributed errors can be less influential when concerning the sample mean statistic. The expected value of the sample mean particle displacement is equal to the population mean displacement, and the standard deviation of the sample mean displacement decreases as $\sim 1/\sqrt{N}$, where N is the number of PIV images in the ensemble. Using the rms uncertainty value as an estimate for the population standard deviation, the error in the mean displacement statistic can be estimated $\hat{\epsilon}_d \approx \overline{\sigma}/\sqrt{N}$ = $(9.3/100$ pixels)/$\sqrt{200}$ = $6.6/1000$ pixels. In the next section, we will estimate the systematic error in the ensemble PIV data due to the presence of shear given a defined spatial resolution.

E.0.5 Displacement Gradient Error

The displacement gradient error is associated with grouping vastly different particle displacements (sharp velocity gradient) into one interrogation region, which causes spatial averaging due to insufficient spatial resolution. This error is affected by the size of the interrogation regions, and the velocity gradient in the flow. The displacement gradient error in this study was assessed based on the simulation work of Scarano and Riethmuller [11], where different grid-sized PIV processing was performed on a synthetic flow. Their work provided rms displacement error $\hat{\epsilon}_d$ curves, as a function of the displacement gradients, for two different interrogation window sizes. The displacement gradients in the current experiments were obtained along three locations in the impinging jet flow domain, represented as black dashed lines in Figure E.2.

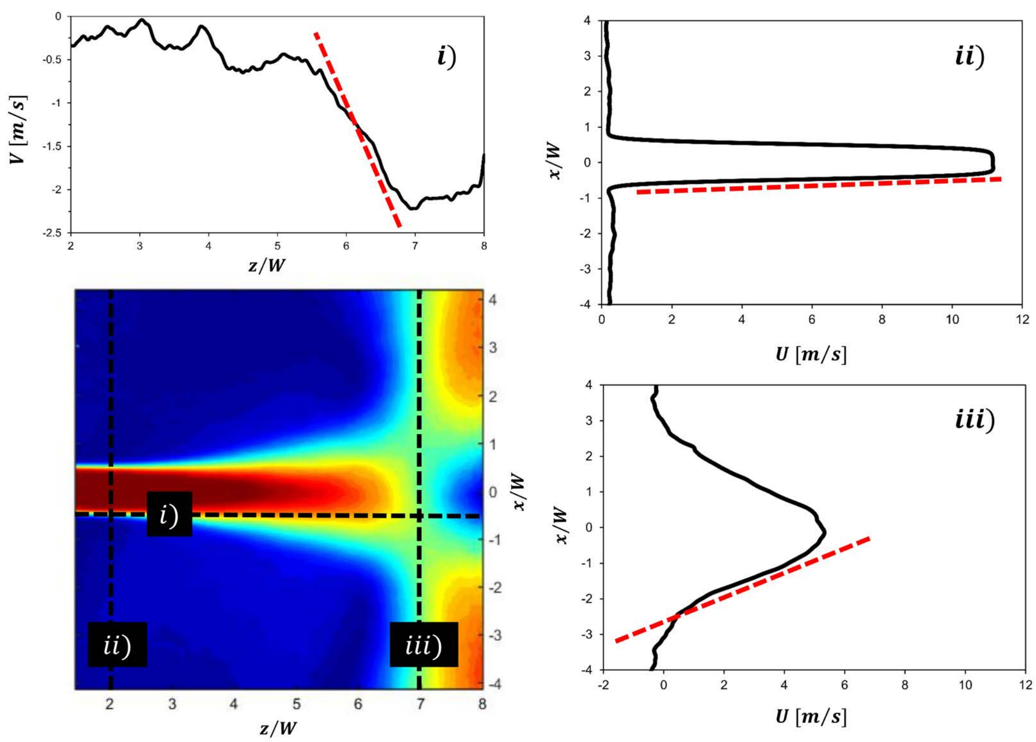

Figure E.2: The velocity profiles and maximum displacement gradients measured in the impinging jet flow field under 70 Hz anti-symmetric excitation. The three plots i), ii), and iii) correspond to the measurement locations shown by the black dashed lines in the lower left corner plot. The red dashed lines are the maximum velocity gradients obtained from their corresponding velocity profiles.

In the following analysis we assume no error in the laser timing and synchronizer equipment (Δt measurement), and thus the mean particle displacement error is equal to the mean particle velocity error $\epsilon_d = \epsilon_u$. The maximum displacement gradients are calculated from the maximum velocity gradients (red dashed lines) in Figure E.2, which correspond to the locations along the black dashed line i) $\frac{\partial \overline{V}}{\partial z}|_{max} \cdot \Delta t = 2.85 \times 10^{-3}$ pixels/pixels, line ii) $\frac{\partial \overline{U}}{\partial x}|_{max} \cdot \Delta t = 5.36 \times 10^{-2}$ pixels/pixels at $z/W = 2$, and line iii) $\frac{\partial \overline{U}}{\partial x}|_{max} \cdot \Delta t = 4.90 \times 10^{-3}$ pixels/pixels at $z/W =$

7. The relative $\overline{U}$ velocity error ϵ_u is obtained by dividing the absolute displacement error $\hat{\epsilon}_d$ by the local downstream displacement δ_d. The local downstream displacement is evaluated by multiplying the local flow velocity at the maximum velocity gradient location by the time between laser pulses Δt, and the spatial resolution R given by: $\delta_d = \overline{U} \cdot \Delta t \cdot R$. The PIV error analysis is presented in Table $E.1$ for the u-component velocity at the two cross-sections in the jet flow, $z/W = 2$ and $z/W = 7$, corresponding to the dashed lines ii) and iii) in Figure E.2, respectively.

Location	$z/W = 2$	$z/W = 7$
Displacement gradient $\frac{\partial \overline{U}}{\partial x}\|_{max} \cdot \Delta t$	5.36×10^{-2} px/px	4.90×10^{-3} px/px
Absolute displacement error $\hat{\epsilon}_d$	2.00×10^{-2} px	3.04×10^{-3} px
Local flow velocity	5.93 m/s	2.35 m/s
Relative velocity error $\epsilon_u = \frac{\hat{\epsilon}_d}{\delta_d}$	1.24%	0.47%

Table E.1: Error analysis for the u-component velocity at the location of maximum velocity gradient along dashed lines ii) and iii) in Figure E.2.

The flow velocity error, and the velocity gradient error will be analyzed at the intersection of dashed lines i) and iii), shown in the bottom left corner of Figure E.2, for the KE' production calculations (regions of negative production). This spatial location corresponds to the coordinates $z/W = 7$ and $x/W = -0.5$. The absolute error in the velocity gradients are tabulated in Table $E.2$ and are evaluated using the error propagation through the central differencing scheme, outlined in Raffel et al. [12] using the following expression: $\hat{\epsilon}_{grad} = 0.7 \cdot \hat{\epsilon}_d / \Delta x$.

To incorporate the random error (PIV noise) from Section $E.0.4$ into this worst case velocity gradient $\frac{\partial \overline{U}}{\partial x}$ in Table E.2, we can combine the absolute displacement errors from the random and systematic components using Equation E.2:

Parameter	Displacement gradient (px/px)	$\hat{\epsilon}_d$ (px)	$\hat{\epsilon}_{grad}$ (px/px)	ϵ_{grad}
$\frac{\partial \overline{U}}{\partial x}$	1.84×10^{-3}	1.97×10^{-3}	1.69×10^{-4}	9.2%
$\frac{\partial \overline{U}}{\partial z}$	6.05×10^{-3}	3.45×10^{-3}	2.96×10^{-4}	4.8%
$\frac{\partial \overline{V}}{\partial x}$	6.24×10^{-3}	3.51×10^{-3}	3.02×10^{-4}	4.8%
$\frac{\partial \overline{V}}{\partial z}$	1.81×10^{-4}	1.40×10^{-3}	2.00×10^{-4}	7.0%

Table E.2: Error analysis for the velocity gradients at spatial coordinates z/W = 7 and x/W = -0.5, which corresponds to the intersection of black dashed lines i) and iii) in Figure E.2.

$$\hat{\epsilon}_d = \sqrt{\hat{\epsilon}_{d1}^2 + \hat{\epsilon}_{d2}^2} = \sqrt{\left(\frac{1.97}{1000}\right)^2 + \left(\frac{6.6}{1000}\right)^2} = \left(\frac{6.9}{1000}\right)px \tag{E.2}$$

Utilizing this absolute displacement error estimate into the relative gradient error calculation reveals substantial error in the $\frac{\partial \overline{U}}{\partial x}$ term $\epsilon_{grad} \approx 32\%$. The presence of PIV noise effectively triples the standard uncertainty in the velocity gradients.

E.0.6 Fluctuating Kinetic Energy Production Error

The error in the fluctuating kinetic energy production (KE') in Appendix B was estimated using the Taylor Series Method (TSM) outlined in Coleman and Steele [13]. This analysis incorporates the errors in the Reynolds stresses and PIV velocity gradients previously assessed in Appendix $E.0.3$ and $E.0.5$. Assuming the error in all of the velocity gradients are worse case scenario $\epsilon_{\Omega_1} \approx 32\%$ (Appendix $E.0.5$), and assuming the error in all the Reynolds stresses are equal $\epsilon_{\Omega_2} \approx 3.7\%$ (Appendix $E.0.3$), the KE' production in Equation B.1, can be grouped and simplified leading to Equation E.3.

$$\xi \approx 4 \cdot \Omega_1 \Omega_2 \tag{E.3}$$

$$\epsilon_\xi = \frac{\hat{\epsilon}_\xi}{\xi} = \sqrt{\left(\frac{\Omega_1}{\xi} \cdot \frac{\partial \xi}{\partial \Omega_1}\right)^2 \cdot (\epsilon_{\Omega_1})^2 + \left(\frac{\Omega_2}{\xi} \cdot \frac{\partial \xi}{\partial \Omega_2}\right)^2 \cdot (\epsilon_{\Omega_2})^2} \tag{E.4}$$

$$\epsilon_\xi = \sqrt{(\epsilon_{\Omega_1})^2 + (\epsilon_{\Omega_2})^2} \approx 32\% \tag{E.5}$$

Using the data reduction equation in $E.3$, the error for the approximated KE' production ϵ_ξ can be assessed by the assembled partial derivatives in Equation E.4, which can be further mathematically reduced to Equation E.5. The relative standard uncertainty in the KE' production using the PIV velocity gradients and Reynolds stresses in the presence of shear and noise is estimated at approximately $\epsilon_\xi \approx 32\%$ in a region of negative KE' production ($z/W = 7$ and $x/W = -0.5$). The error in the KE' production is clearly dominated by the errors in the velocity gradients. This estimation for the rms standard uncertainty in the KE' production has also been incorporated as error bars in Figure B.4 of Appendix B.

References

[1] K. Nishino, M. Samada, K. Kasuya, and K. Torii, “Turbulence statistics in the stagnation region of an axisymmetric impinging jet flow,” *International Journal of Heat and Fluid Flow*, vol. 17, no. 3, pp. 193–201, 1996.

[2] T. Cziesla, G. Biswas, H. Chattopadhyay, and N. Mitra, “Large-eddy simulation of flow and heat transfer in an impinging slot jet,” *International Journal of Heat and Fluid Flow*, vol. 22, no. 5, pp. 500–508, 2001.

[3] H. Chattopadhyay and S. K. Saha, “Turbulent flow and heat transfer from a slot jet impinging on a moving plate,” *International Journal of Heat and Fluid Flow*, vol. 24, no. 5, pp. 685–697, 2003.

[4] A. F. Hussain, “Coherent structures and turbulence,” *Journal of Fluid Mechanics*, vol. 173, pp. 303–356, 1986.

[5] A. Hussain and C. Thompson, “Controlled symmetric perturbation of the plane jet: an experimental study in the initial region,” *Journal of Fluid Mechanics*, vol. 100, no. 2, pp. 397–431, 1980.

[6] C.-M. Ho and F.-B. Hsiao, “Evolution of coherent structures in a lip jet,” in *Structure of Complex Turbulent Shear Flow*, pp. 121–136, Springer, 1983.

[7] A. Melling, “Tracer particles and seeding for particle image velocimetry,” *Measurement Science and Technology*, vol. 8, no. 12, p. 1406, 1997.

[8] A. Prasad, R. Adrian, C. Landreth, and P. Offutt, “Effect of resolution on the speed and accuracy of particle image velocimetry interrogation,” *Experiments in Fluids*, vol. 13, no. 2-3, pp. 105–116, 1992.

[9] R. D. Keane and R. J. Adrian, "Optimization of particle image velocimeters. i. double pulsed systems," *Measurement science and technology*, vol. 1, no. 11, p. 1202, 1990.

[10] J. J. Charonko and P. P. Vlachos, "Estimation of uncertainty bounds for individual particle image velocimetry measurements from cross-correlation peak ratio," *Measurement Science and Technology*, vol. 24, no. 6, p. 065301, 2013.

[11] F. Scarano and M. L. Riethmuller, "Advances in iterative multigrid piv image processing," *Experiments in Fluids*, vol. 29, pp. S051–S060, 2000.

[12] M. Raffel, C. E. Willert, S. T. Wereley, and J. Kompenhans, *Particle image velocimetry: a practical guide*. Springer, 2013.

[13] H. W. Coleman and W. G. Steele, *Experimentation, validation, and uncertainty analysis for engineers*. John Wiley & Sons, 2009.